Through a lens darkly: magnified views of massive galaxy formation

Stacey, Hannah

DOI:
10.33612/diss.118594120

rijksuniversiteit
groningen

Through a lens darkly: magnified views of massive galaxy formation

Proefschrift

ter verkrijging van de graad van doctor aan de
Rijksuniversiteit Groningen
op gezag van de
rector magnificus prof. dr. C. Wijmenga
en volgens besluit van het College voor Promoties.

De openbare verdediging zal plaatsvinden op

vrijdag 11 september 2020 om 12:45 uur

door

Hannah Ruth Stacey

geboren op 30 maart 1989
te Manchester, Verenigd Koninkrijk

Promotores
Prof. dr. J. P. McKean
Prof. dr. L. V. E. Koopmans

Beoordelingscommissie
Prof. dr. K. I. Caputi
Prof. dr. F. Combes
Prof. dr. K. K. Knudsen

Kapteyn Institute - PhD thesis 2020
ISBN: 978-94-034-2492-7
ISBN: 978-94-034-2491-0 (electronic version)

The work described in this thesis was performed in the research groups at the Kapteyn Astronomical Institute at the University of Groningen and the Netherlands Institute for Radio Astronomy (ASTRON).

Cover design by H. R. Stacey, based on a snapshot of the formation of a massive elliptical galaxy in the Illustris TNG50 simulation.

Printed by Ipskamp Printing using 100% recycled paper

Arthur lay in startled stillness on the acceleration couch. He wasn't certain whether he had just got space-sickness or religion.

— Douglas Adams, 'Life, the Universe and Everything'

Contents

List of Figures

List of Tables

Samenvatting

Het ontstaan en vergaan van massieve sterrenstelsels

Het heelal bevat miljarden sterrenstelsels met een verscheidenheid aan vormen en afmetingen. Een fractie van de sterrenstelsels die in het huidige universum worden gezien, staan bekend als it elliptische sterrenstelsels. Zij zijn dichte, bolvormige groepen van oude sterren zijn. De meest massieve sterrenstelsels zijn elliptische sterrenstelsels. Ze lijken misschien weinig opmerkelijk, maar hebben naar alle waarschijnlijkheid een dramatisch leven geleid. Naar onze huidige kennis hebben gewelddadige processen, waaronder botsingen van meerdere sterrenstelsels, deze stelsels in een vroeg stadium van het heelal gecreëerd. Het grootste deel van hun waterstofgas wordt in een korte burst omgezet in sterren, dus elliptische sterrenstelsels 'live fast and die young'.

Zoals de meeste sterrenstelsels bevatten elliptische sterrenstelsels in hun midden it superzware zwarte gaten. Deze zwarte gaten zijn miljoenen tot miljarden keren massiever dan onze zon. Astronomen geloven dat er een soort symbiotisch verband bestaat tussen elliptische sterrenstelsels en hun superzware zwarte gaten, en deze relatie speelt een belangrijke rol in de evolutie van sterrenstelsels. Superzware zwarte gaten hebben de mogelijkheid om enorme krachten te produceren door materiaal te verzamelen en om te zetten in energie. Deze krachten kunnen het waterstofgas uit het stelsel werpen, of het opwarmen en voorkomen dat het samenklontert om nieuwe sterren te vormen. Figuur 1 toont een voorbeeld van een elliptisch sterrenstelsel en een straal plasma geproduceerd door het superzware zwarte gat.

Een groot deel van de astronomie is bezig om te begrijpen hoe enorme sterrenstelsels zich vormden en zijn gegroeid in combinatie met hun superzware zwarte gaten. In dit proefschrift heb ik heel verre sterrenstelsels bestudeerd met snelgroeiende superzware zwarte gaten (ook wel it quasars genoemd) om te testen hoe deze sterrenstelsels elliptische sterrenstelsels worden. Hoofdstukken 2 en 3 onderzoeken hoeveel nieuwe sterren zich vormen in deze sterrenstelsels. Ik ontdekte dat deze sterrenstelsels veel nieuwe sterren vormen, wat in overeenstemming is met de verwachtingen van hoe massieve sterrenstelsels en hun superzware zwarte gaten samen groeien. Hoofdstuk 4

onderzoekt de grootte en structuur van de sterren en het gas om de processen te begrijpen waardoor elliptische sterrenstelsels compacte sferoïden werden in plaats van schijven. Ik ontdekte dat de sterrenstelsels die snel groeiende superzware zwarte gaten hebben erg klein en compact zijn, waaruit blijkt dat hun gas in een klein gebied is ingestort en dat ze hun gas snel in sterren zullen veranderen. Mijn bevindingen suggereren dat de gewelddadige processen die ervoor zorgen dat de sterren zich snel vormen, ook leiden tot superzware zwarte gaten die snel groeien. In hoofdstuk 6 combineer ik gegevens uit het hele elektromagnetische spectrum om een beeld te maken van de gasschijf en de straal van een superzwaar zwart gat in het verre heelal. Een aspect van mijn toekomstige onderzoek zal zijn om de studies van hoofdstuk 4 en 6 uit te breiden om te onderzoeken hoe de structuur van het gas kan helpen het superzware zwarte gat efficiënt te laten groeien, en hoeveel het superzware zwarte gat het gas opwarmt.

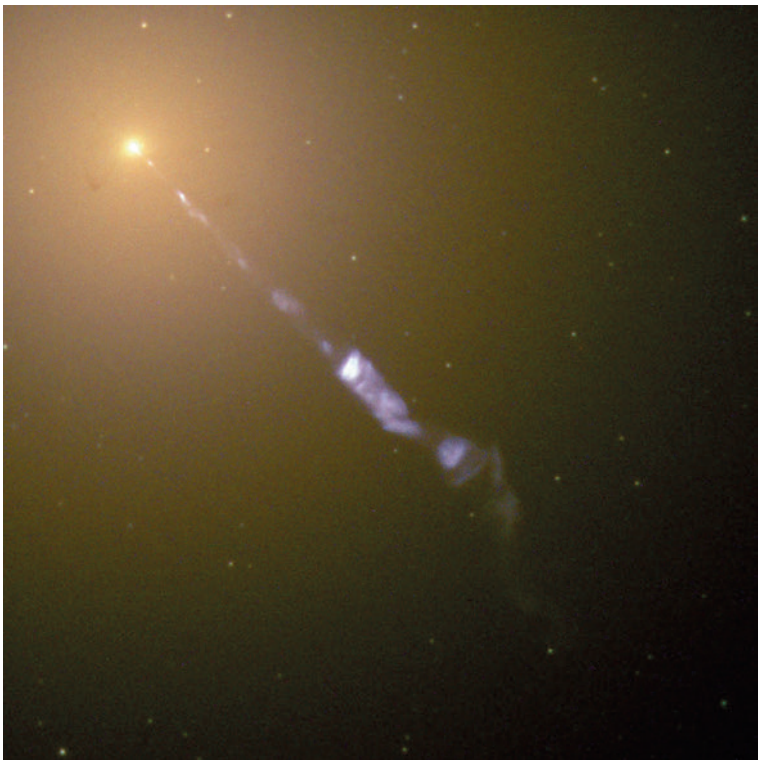

Figuur 1 | Een iconisch beeld van de elliptische melkweg M87, dat een groeiend superzwaar zwart gat bevat. Het superzware zwarte gat produceert een straal van plasma uit het stelsel, gezien in het blauw. Beeld met dank aan: NASA / ESA Hubble Space Telescope.

Figuur 2 | 'Het is belangrijk op te merken dat hoewel de effectieve grootte van de hond willekeurig groot kan zijn, het niet een betere hond dan de twee originele honden', Munroe (2005), vertaald uit het engels.

Het verkennen van het onzichtbare universum

Als we naar de nachtelijke hemel kijken, kunnen we duizenden sterren zien, en misschien enkele sterrenstelsels. Met telescopen kunnen we miljoenen sterrenstelsels zien in zichtbaar licht. Het grootste deel van het universum is echter onzichtbaar. In het verre heelal wordt het meeste licht van sterren uitgezonden bij lagere energieën, in de vorm van sub-millimeter golflengten (100 μm tot 1 mm), geproduceerd door kleine stofkorrels die worden verwarmd door de ultraviolette straling van jonge sterren. Op radiogolflengten licht de lucht op met energieke stralen uit superzware zwarte gaten. Als we de details van deze sterrenstelsels op dezelfde schaal willen zien als we kunnen zien met telescopen die zichtbaar licht zien, moeten we een techniek gebruiken die it interferometry wordt genoemd. Deze techniek combineert de signalen van meerdere telescopen (antennes) om beelden met een zeer hoge resolutie te produceren: het kan functioneren als een telescoop met een diameter zo groot als de afstand tussen de antennes (zie figuur 2). In hoofdstuk 4, 5 en 6 heb ik interferometrie gebruikt om de gedetailleerde structuur van stof-, gas- en radiostralen rond superzware zwarte gaten in verre sterrenstelsels waar te nemen.

Maar er is ook een andere kant van het universum die niet direct met een telescoop te zien is: it donkere materie. De meeste materie in het universum is donkere materie, die geen licht absorbeert, uitzendt of reflecteert. Computatiesimulaties vertellen ons dat donkere materie een essentieel onderdeel van de kosmos is omdat het de beginpunten creéert van waaruit sterrenstelsels worden gevormd, maar we hebben momenteel geen idee uit welke fundamentele deeltjes donkere materie bestaat. De kleinste structuren die donkere materie vormt, kunnen ons hints geven over wat deze deeltjes kunnen zijn.

Het universum als een telescoop

De informatie die we over het heelal kunnen verzamelen, hangt af van hoe ver we kunnen kijken en van het bereik van fysieke schalen die we kunnen onderscheiden. Dit wordt praktisch beperkt door de kracht van telescopen om licht van zwakke sterrenstelsels te detecteren en hoe ver we de afzonderlijke componenten van een interferometer kunnen plaatsen. We verbeteren deze naarmate de technologie verbetert, maar we kunnen het altijd beter doen door gebruik te maken van een fenomeen dat bekend staat als it zwaartekrachtlenzen. Zwaartekrachtlenzen zijn zeldzame objecten waarbij een ver sterrenstelsel wordt uitgerekt en vervormd door de zwaartekracht van een massieve melkweg (of groep sterrenstelsels) langs de gezichtslijn (zie bijvoorbeeld figuur 3). Dit heeft ook het effect van het vergroten van verre sterrenstelsels. In dit proefschrift heb ik zwaartekrachtlensstelsels onderzocht om de kracht van de telescopen die ik gebruikte te vergroten. Dit heeft me in staat gesteld om licht te detecteren van sterrenstelsels die anders te zwak zouden zijn om te detecteren (hoofdstuk 2 en 3), en om structuren te observeren die kleiner zijn dan de telescoop anders zou kunnen onderscheiden (hoofdstuk 4 en 6).

Aan de andere kant geeft de manier waarop licht wordt vervormd door een zwaartekrachtlens ook informatie over de structuur van het lensstelsel (of sterrenstelsels). Net zoals licht door een optische lens onvolkomenheden in het glas kan onthullen, kunnen kenmerken in het lenslicht de zwaartekrachtskenmerken van kleine sterrenstelsels en substructuren laten zien die anders niet te zien zijn. Zwaartekracht is ongevoelig voor het soort materie, dus het zwaartekrachteffect van donkere materie kan op dezelfde manier worden waargenomen als voor gewone materie. In de afgelopen twee decennia is dit een gevestigde methode geworden om onzichtbare structuren van donkere materie te detecteren en modellen van donkere materie te testen. In hoofdstuk 5 stel ik een nieuwe aanpak voor met observaties op sub-millimeter golflengten met interferometers. Een aspect van mijn toekomstig onderzoek zal zijn om deze aanpak te testen met nieuwe gegevens van zwaartekrachtlenzen, die kunnen helpen beperken tot welke fundamentele deeltjes donkere materie vormen.

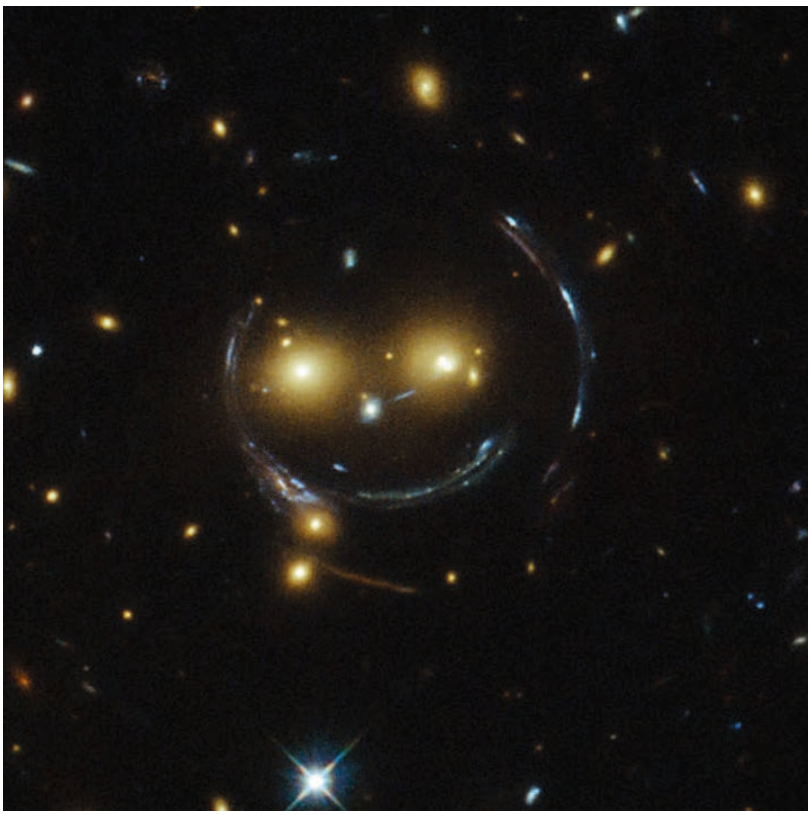

Figuur 3 | Voorbeeld van een zwaartekrachtlens: een groep sterrenstelsels vervormt het licht van verder weg gelegen sterrenstelsels om een illusie van een lachend gezicht te creëren. Met dank aank: NASA / ESA Hubble Space Telescope.

Summary for non-experts

The birth and death of massive galaxies

The Universe is populated with billions of galaxies with a diversity of shapes and sizes. A fraction of the galaxies seen in the present-day Universe are known as *elliptical galaxies* which are dense, spheroidal groups of old stars. The most massive galaxies are elliptical galaxies. They may appear to be unremarkable, but, in all likelihood, have lived dramatic lives. The popular belief is that violent processes, including collisions of multiple galaxies, created them at a much earlier time in the life of the Universe. Most of their Hydrogen gas is converted into stars in a short burst so, in effect, elliptical galaxies 'live fast and die young'.

Like most galaxies, elliptical galaxies contain *supermassive black holes* at their centres. These black holes are millions to billions of times more massive than our Sun. Astronomers believe that there is a kind of symbiotic link between elliptical galaxies and their supermassive black holes, and this relationship plays an important role in how galaxies evolve. Supermassive black holes have the ability to produce huge amounts of power by accreting material and converting it into energy. This can eject or heat up the Hydrogen gas in the galaxy and prevent its clumping together to form new stars. Figure 4 shows an example of an elliptical galaxy and a jet of plasma produced by its supermassive black hole.

A large area of astronomy research is in pursuit of understanding how massive galaxies formed and grew alongside their supermassive black holes. In this thesis, I studied very distant galaxies that have rapidly growing supermassive black holes (referred to as *quasars*) to test how these galaxies turn into elliptical galaxies. Chapters 2 and 3 investigate how many new stars are forming in these galaxies. I found that these galaxies are forming many new stars, which is in agreement with expectations of how massive galaxies and their supermassive black holes grow together. Chapter 4 investigates the size and structure of the stars and gas to understand the processes that caused elliptical galaxies to become dense spheroids, rather than discs. I found that the galaxies that have rapidly growing supermassive black holes are very small and dense, showing that their gas has collapsed into a small region and that they will quickly turn

their gas into stars. My findings suggest that the violent processes that cause the stars to form quickly also cause supermassive black holes to grow quickly. In Chapter 6, I combine data from across the electromagnetic spectrum to construct a picture of the gas disc and jets around a supermassive black hole in the distant Universe. An aspect of my future research will be to expand the studies of Chapter 4 and 6 to investigate how the structure of the gas may help the supermassive black hole to grow efficiently, and how much the supermassive black hole is heating up the gas.

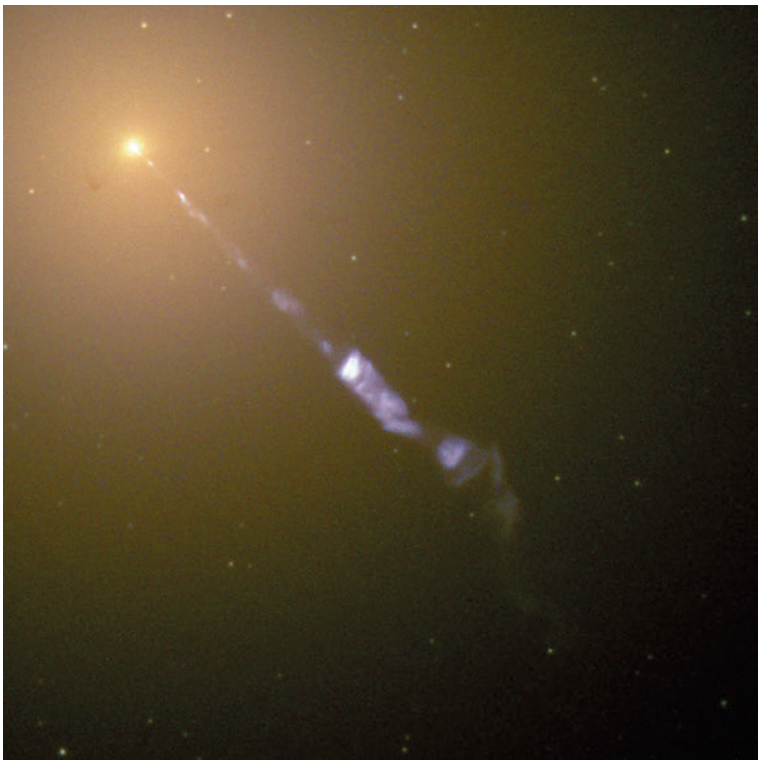

Figure 4 | An iconic image of the elliptical galaxy M87, which contains an accreting supermassive black hole. The supermassive black hole produces a jet of plasma from the galaxy, seen in blue. Image credit: NASA/ESA Hubble Space Telescope.

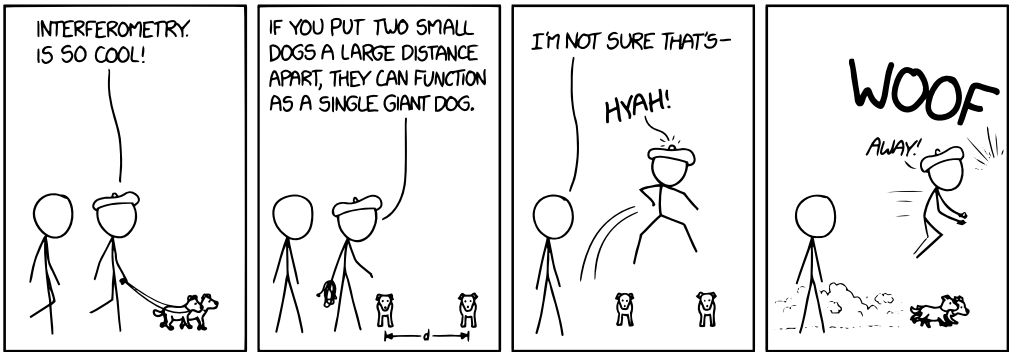

Figure 5 | 'It's important to note that while the effective size of the dog can be arbitrarily large, it's not any more of a good dog than the two original dogs', Munroe (2005).

Exploring the invisible Universe

When we look at the night sky we can see thousands of stars, and maybe a few galaxies. With telescopes we can see millions of galaxies in visible light. However, most of the Universe is invisible. In the distant Universe, most of the light from stars is emitted at lower energies, at sub-millimetre wavelengths (100 μm to 1 mm), produced by tiny dust grains that are heated by the ultraviolet radiation from young stars. At radio wavelengths, the sky lights up with energetic jets from supermassive black holes. If we want to see the details of these galaxies on the same scales as we can see with telescopes that see visible light, we need to use a technique called *interferometry*. This technique combines the signals from multiple telescopes (antennas) to produce very high resolution images: it can function as a telescope with a diameter as large as the distance between the antennas (see Figure 5). In Chapter 4, 5 and 6 I used interferometry to resolve the detailed structure of dust, gas and radio jets around supermassive black holes in distant galaxies.

But there is also another side the Universe that cannot be seen directly with any telescope: *dark matter*. Most of the matter in the Universe is dark matter, which does not absorb, emit or reflect light. Computational simulations tell us that dark matter is an essential ingredient of the cosmos as it creates the seeds in which galaxies form, but we currently have no idea what fundamental particles make up dark matter. The smallest structures that dark matter forms can give us hints as to what these particles might be.

The Universe as a telescope

The information we can gather about the Universe depends on how deep we can see and the range of physical scales we can resolve. This is practically limited by the power of telescopes to detect light from faint galaxies, and how far apart we can place the individual components of an interferometer. We improve these as technology improves, but we can always do better by exploiting a phenomenon known as *gravitational lensing*. Gravitational lenses are rare objects whereby a distant galaxy is stretched and distorted by the gravity of a massive galaxy (or group of galaxies) along the line-of-sight (see Figure 6, for example). This also has the effect of magnifying distant galaxies. In this thesis, I investigated gravitationally lensed galaxies to boost the power of the telescopes I used. This has allowed me to detect light from galaxies that would otherwise be too faint to detect (Chapter 2 and 3), and to observe structures smaller than the telescope could otherwise resolve (Chapter 4 and 6).

The other side of the coin is that the way light is distorted by a gravitational lens also gives information about the structure of the lensing galaxy (or galaxies). Just as light through an optical lens can reveal imperfections in the glass, features in the lensed light can show the gravitational signatures of small galaxies and substructures that cannot otherwise be seen. Gravity is insensitive to the type of matter, so the gravitational effect of dark matter can been observed in the same way as for ordinary matter. In the past two decades this has become an established method to detect invisible dark matter structures and test models of dark matter. In Chapter 5, I propose a new approach for this using observations at sub-millimetre wavelengths with interferometers. An aspect of my future research will be to test this approach with new data of gravitational lenses, which could help narrow down what fundamental particles make up dark matter.

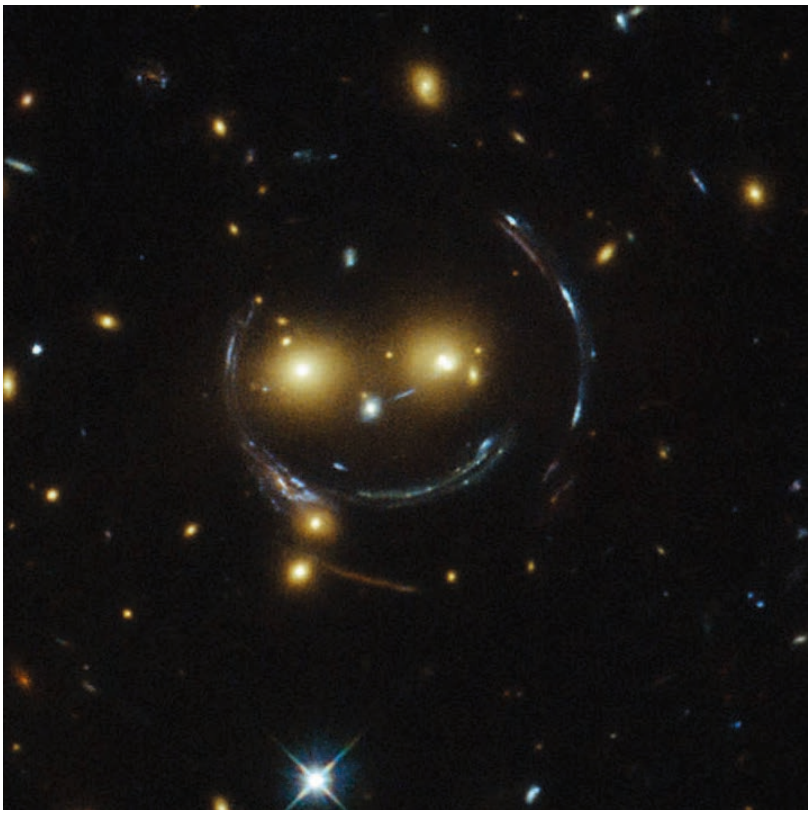

Figure 6 | Example of a gravitational lens: a group of galaxies warps the light from more distant galaxies to create an illusion of a smiling face. Image credit: NASA/ESA Hubble Space Telescope.

Through a glass bitterly

30 ml Campari
60 ml brandy
30 ml vermouth

Shake the Campari, brandy and vermouth with ice. Strain into an old-fashioned glass over fresh ice and garnish with an orange peel.

1

Introduction

1.1. Active galactic nuclei

1.1.1. Morphology and classification

It has now been well established that most galaxies host supermassive black holes (SMBHs) with masses in excess of 10^6 $M_\odot$ (Magorrian et al., 1998). SMBHs grow through the accretion of matter, which liberates huge amounts of energy in a phenomenon known as an active galactic nucleus (AGN). While AGN are among the most luminous objects in the Universe, often outshining their host galaxies, their morphology, formation, evolution and interaction with their host galaxies are all poorly understood.

The first indication of AGN was the detection of broad emission lines from spiral 'nebulae' by Seyfert (1943) and from the Cygnus A radio source by Baade & Minkowski (1954). However, it was the discovery of a *quasar* (quasi-stellar object or QSO) by Schmidt (1963) – an extremely luminous object at cosmological distance – that motivated a rapidly expanding sub-field of astrophysics and, ultimately, led to the consensus that quasars are powered by accreting SMBHs. Since that time, many different classifications of AGN have been established to associate those with distinct observational properties: for example, the (non-)detection of broad emission lines (AGN Type 1 or 2), the clear detection of a host galaxy (Seyfert galaxy), or the presence of a radio jet

(Fanaroff-Riley class radio source). Forming a coherent evolutionary framework has been a major challenge in astronomy, as it remains unclear whether these sub-types represent different nuclear morphology, or to what extent their taxonomic properties are a consequence of orientation, level of dust obscuration or evolutionary stage (Padovani et al. 2017, for review). The term *quasar* typically refers to the most optically luminous, unobscured AGN (e.g. Schmidt & Green, 1983), which have been the focus of this thesis.

A small fraction of quasars (5–10 percent) are *radio-loud*, with dramatic radio jets (Strittmatter et al., 1980). These jets are produced by collimated outflows of plasma from near the accretion disc of the black hole (see Fig. 1.1). At radio frequencies, synchrotron emission is produced from relativistic electrons that are accelerated by magnetic fields. At GHz frequencies, this emission has a characteristic flat spectrum from the optically thick core and steep-spectrum emission (flux density increasing towards lower frequencies) from optically thin jets.

The majority of quasars are *radio-quiet*, with very faint radio counterparts, and it is not clear whether the same emission mechanisms can be applied to the population in general. There is some evidence that radio-loud quasars are hosted in more massive galaxies (Mandelbaum et al., 2009), and have less efficient black hole accretion associated with a different nuclear morphology (Ho, 2008). Whether these differences point to a true bimodality, in which there are two types of quasars governed by different physical processes, has been a subject of long debate. Do radio-quiet quasars also produce radio jets? Do these represent a continuous population of quasars, but observed at a different period in their duty cycle, or with different local environments? Are the production of radio jets a consequence of different nuclear properties (e.g. black hole spin) or host galaxy properties (e.g. second-generation mergers)? Investigations of the radio properties of radio-quiet AGN can provide insight into these open questions.

1.1.2. The role of AGN in galaxy evolution

Until the last two decades, observations of the electromagnetic spectrum in the far-infrared to sub-millimetre regime (100 μm to 1 mm) have been severely limited by the effects of Earth's atmosphere, which require detectors to observe at high altitudes or in space. The Sub-millimeter Common-User Bolometer Array (SCUBA; Holland et al. 1999) and the Max-Planck-Millimeter-Bolometer (MAMBO; Kreysa et al. 1999) detected a new population of galaxies that are extremely luminous at sub-mm wavelengths. These are high-redshift galaxies with extreme levels star formation, largely undetected in optical surveys as their ultraviolet emission is obscured by dust.

The discovery of these galaxies has since revolutionised our understanding of

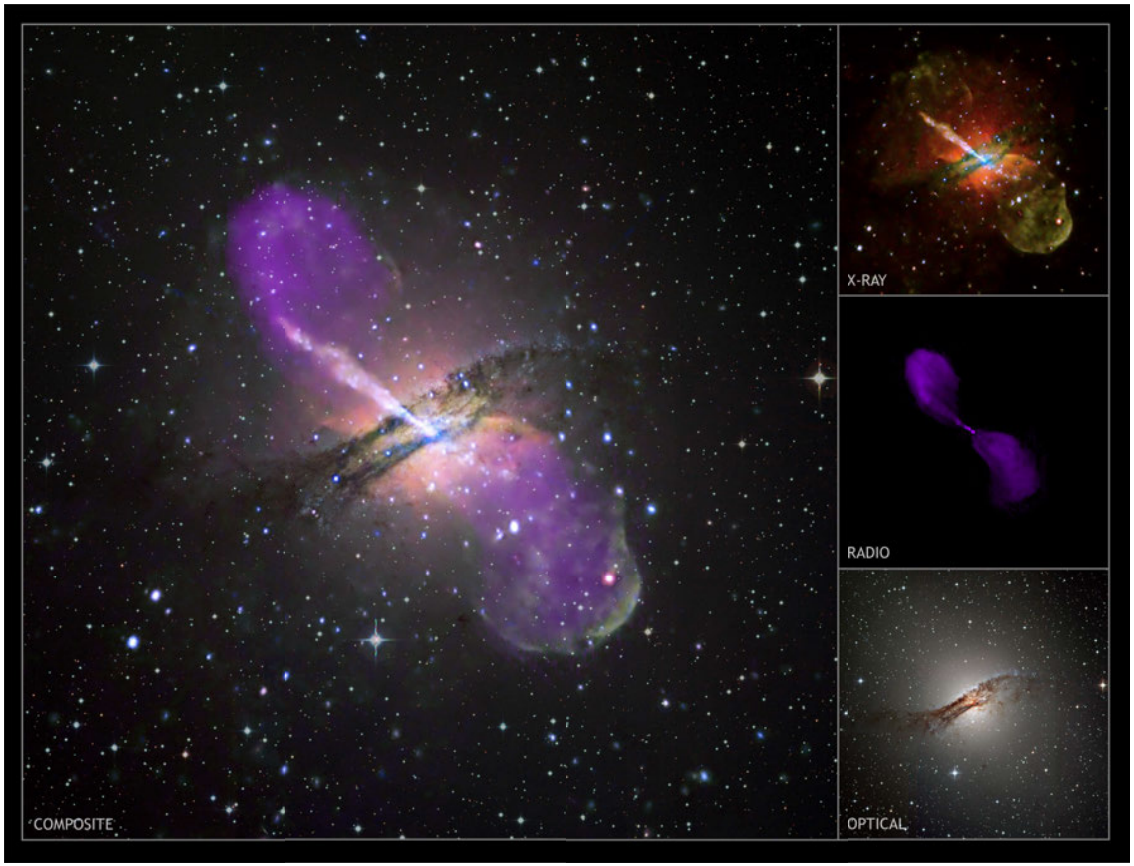

Figure 1.1 | Composite image of the nearby radio galaxy Centaurus A. Inset panels show the X-ray emission, radio jets and the optical host galaxy. Image credit: NASA/CXC.

galaxy formation and evolution: the bulk of star formation takes place in these extremely luminous and compact dusty star-forming galaxies (DSFGs)* (Blain et al. 2002; Casey et al. 2014, for review). These are believed to be the progenitors of present-day elliptical galaxies, which have dense, dispersion-dominated stellar distributions, low star formation rates and old stellar populations.

Many studies of galaxy evolution are in the pursuit of understanding the mechanisms by which spheroids form such high stellar densities and rapidly shut off their star formation. Over the past 20 years there has been a growing consensus that this evolution is closely tied to that of their central SMBHs. Observations of high redshift galaxies show that the cosmic star formation history and SMBH accretion are closely correlated (see Fig. 1.2), suggesting that there is a common physical process driving both phenomena. Further evidence is the correlation between black hole mass and host galaxy stellar mass, supported by both observations and hydro-dynamical simulations (see Fig. 1.3, Weinberger et al. 2018), despite a difference of several orders of magnitude in size scales.

From the perspective of simulations, it is clear that some mechanism must inject large amounts of energy into the interstellar medium (ISM) of galaxies to prevent cooling of gas and reduce the star forming efficiency of the most massive galaxies (see Somerville & Davé (2015) for review). As shown in Fig. 1.3, there is a significant reduction in the star formation efficiency of galaxies with black hole mass $> 10^8$ $M_\odot$and stellar mass $> 10^{11}$ $M_\odot$. Feedback from star formation alone appears to be unable to reproduce these effects (Somerville et al., 2008). However, the findings of these models depend on their prescription of AGN and stellar feedback. The fact that black hole mass correlates weakly with the size of the dark matter halo and not at all for disk galaxies may indicate that the observed black-hole–stellar mass correlation is simply a consequence of the common supply of cold gas, underlining the need to test theory with a variety of observations (see Kormendy & Ho 2013, for review).

Observational studies of the local Universe have shown that AGN are able to inject large amounts of energy into the ISM and circumgalactic medium of their host galaxies. This feedback may be kinetic, in which gas is expelled by radio jets and prevented from re-cooling to form stars (e.g. Nesvadba et al. 2010; Querejeta et al. 2016; see Fig. 1.1). Radiative feedback, in which radiatively driven winds provide the main source of energy (e.g. Feruglio et al., 2010; Alatalo et al., 2011, 2015), may be associated with high-luminosity rapidly accreting AGN, but the separation between these two modes is unlikely to be unequivocal (see Alexander & Hickox 2012 for review). These feedback mechanisms are believed to be how AGN regulate star formation in massive galaxies,

*Also referred to as a sub-millimetre galaxy (SMG), or commonly as an ultra-luminous infrared galaxy (ULIRG) at low redshifts.

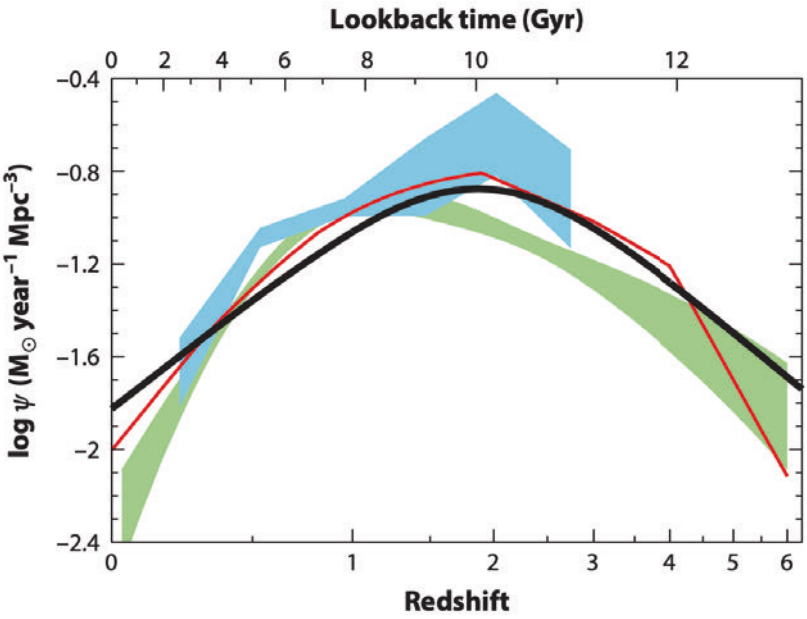

Figure 1.2 | A comparison of cosmic star formation history (black curve) with black hole accretion history (red curve, scaled up by a factor of 3300). The blue and green shaded regions show black hole accretion and 1σ uncertainty inferred from X-ray and infrared data, respectively. Figure from Madau & Dickinson (2014).

and one of the most important processes that shapes their evolution. Hopkins et al. (2008), supported by simulations (e.g. Di Matteo et al., 2005; Hopkins et al., 2005) and observational studies (e.g. Page et al., 2004; Stevens et al., 2005), encode these processes into a unified evolutionary framework that links high-redshift star-forming galaxies to present-day elliptical galaxies (Fig. 1.4).

1.1.3. Observing AGN feeding and feedback at high redshift

At high redshift, obscured star formation, AGN accretion and feedback phenomena are challenging to study due to the required sensitivity and spatial resolution. The *Herschel Space Observatory* (Pilbratt et al., 2010), launched in May 2009, was the first space satellite to observe wavelengths between 100 and 500 μm. This could reach much shorter wavelengths and higher sensitivities than previously capable from the Earth,

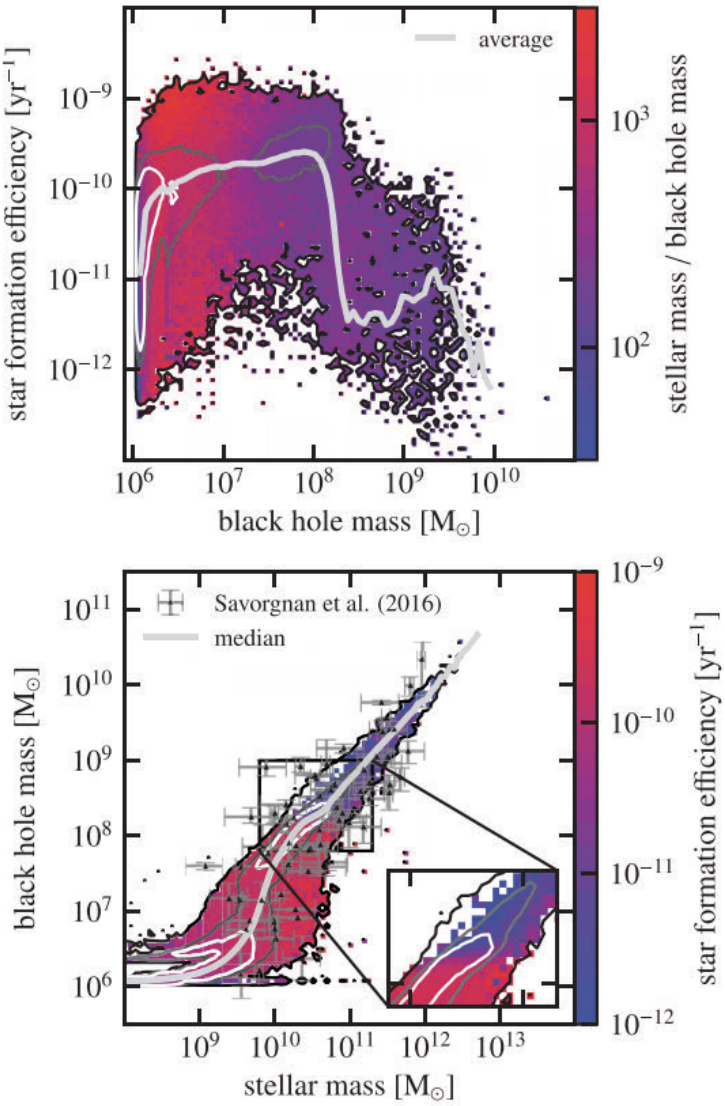

Figure 1.3 | Top: star formation efficiency with black hole mass for galaxies in the Illustris TNG simulation, colour-coded by the ratio of stellar to black hole mass. The star formation efficiency decreases with increased black hole mass. Bottom: black hole mass with host galaxy stellar mass for galaxies in the Illustris TNG simulation, colour-coded by star formation efficiency. Both simulations and observations show a tight correlation between black hole mass and stellar mass, and a decreased star formation efficiency at high stellar masses. Observational data are shown with grey scatter points. Figures from Weinberger et al. (2018).

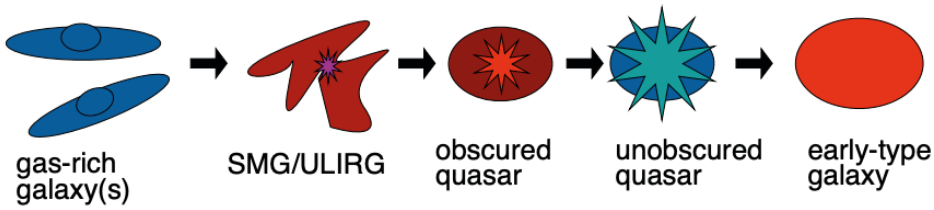

Figure 1.4 | Illustration of the evolutionary sequence of a massive elliptical galaxy, first proposed by Sanders et al. (1988). Here, a DSFG (or SMG/ULIRG) is formed as a result of a major merger, which evolves into a quasar host, and ultimately an elliptical (early-type) galaxy. Figure from Alexander & Hickox (2012).

enabling the large population of high-redshift galaxies to be efficiently characterised. However, many aspects still remain unclear. To what extent is star formation ongoing in the host galaxies of quasars? Is star formation suppressed in quasar host galaxies? To what spatial extent do accretion discs radiatively heat their host galaxies? Are AGN able to drive outflows of molecular gas and, if so, how? Are different feedback processes at play in galaxies that host radio-loud AGN? How strongly do these feedback mechanisms couple to the molecular gas?

Accessing the small scales required to investigate the structure of quasars and their host galaxies at sub-mm to radio wavelengths requires different observational techniques than at shorter wavelengths, such as in the optical. The angular resolution of a telescope is determined by the number of wavelengths across the aperture, $\theta \sim \lambda / D$ (where D is the diameter of the telescope), implying unfeasibly large antennas to achieve a resolution comparable to those at optical wavelengths. This resolution can only be achieved with interferometry, which measures the interference of radio signals between pairs of radio antennas to synthesise an aperture with a size that is equivalent to the distance between them.

The Atacama Large (sub-)Millimetre Array (ALMA; Brown et al. 2004), an interferometric array of 66 antennas, has improved the resolution and sensitivity of observations at sub-mm/mm wavelengths by orders of magnitude. Sub-arcsecond resolution and sub-mJy point-source sensitivity can investigate the dust and molecular gas with new levels of detail. In the local Universe, ALMA has been used to investigate the structure and kinematics of molecular gas in the central kpc of galaxies that directly fuels black hole accretion. These studies have revealed bars and spiral arms (García-Burillo et al., 2016; Maccagni et al., 2018; Combes et al., 2013) and evidence of AGN-driven molecular outflows (Morganti et al., 2015; Combes et al., 2019; Audibert et al., 2019). Fig. 1.5 shows

1

ALMA imaging of CO (2–1) emission from the inner ~ 1 kpc of a nearby AGN host galaxy with a spatial resolution of 20 pc, that shows molecular gas structures that could help regulate the inflow of gas onto the SMBH (Audibert et al., 2019). The key tests of the evolutionary mechanisms of galaxies require observations of star formation, accretion and feedback at high redshift with equivalent spatial resolution to the local Universe, during the cosmic peak of galaxy growth ($z \sim 2$). This thesis aims to probe these scales at high redshift by exploiting the magnification effect of gravitational lensing.

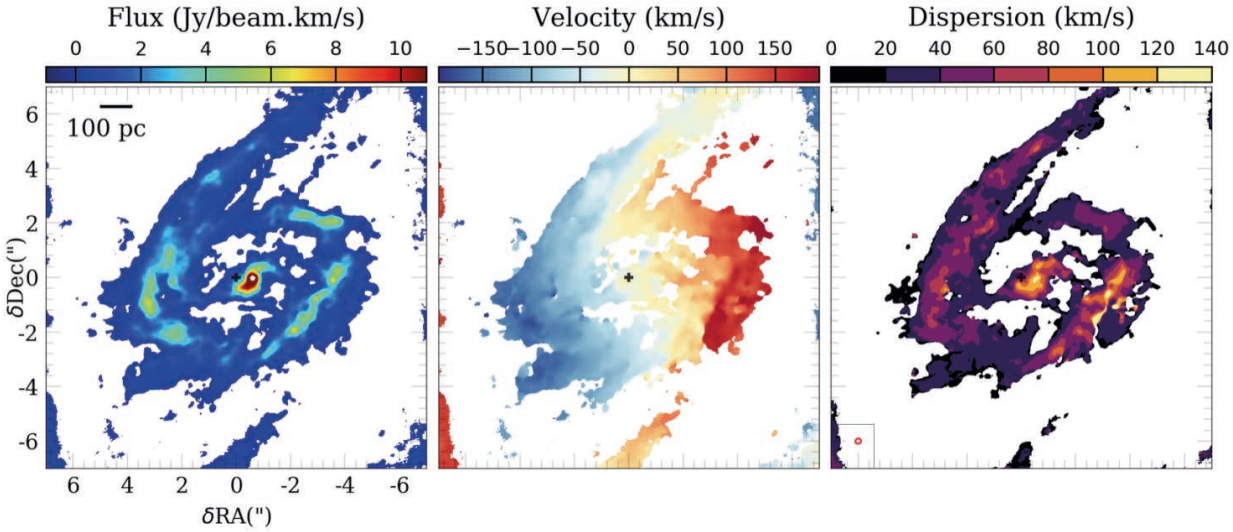

Figure 1.5 | Example of investigations of the central ~ 1 kpc of an AGN host galaxy in the local Universe: CO (2–1) emission from Seyfert galaxy NGC 613 is imaged with ALMA at a spatial resolution of about 20 pc (Audibert et al., 2019). These data show nuclear spiral arms that allows efficient inflow towards the central SMBH and a small outflow driven by the AGN.

1

1.2. Magnifying the high-redshift Universe

Despite the advances in technology and observational techniques, accessing the small scales and high sensitivity required to investigate AGN feedback may still be challenging or inefficient at cosmologically interesting redshifts. These limitations may be improved by using the Universe itself as a telescope, through investigation of gravitational lens phenomena.

General relativity describes gravity as a geometric property of space-time, that is, the curvature of space is determined by the mass within it (Einstein, 1916). As a consequence, if a source and a foreground massive galaxy are closely aligned along the line-of-sight, light from the source is lensed by the foreground galaxy. Depending on the alignment and the properties of lens and source, the source may be observed as a ring or arc, or be seen as multiple images (see Figs. 1.6 and 1.7). The first gravitational lens, Q0957+561, a quasar with two lensed images separated by 6 arcsec, was discovered with radio interferometric observations (Walsh et al., 1979). Technological advances have since allowed many more gravitational lenses with much smaller image separations to be discovered. This regime, where multiple imaging occurs, is known as *strong lensing* as opposed to *weak lensing*, which is a statistical shearing effect due to the distribution of matter on cosmological scales, and *microlensing*, which is a lensing effect produced by transiting stars and planets (see Schneider et al. 2006 for overview).

1.2.1. Gravitational lensing formalism

This section gives a brief overview of gravitational lensing formalism. More detailed reviews can be found by Meylan et al. (2006) and Congdon & Keeton (2018).

General relativity field equations describe how light propagates through curved space-time, however, in gravitational lens theory, we can approximate these paths as linear by assuming the gravitational field is weak at the point of deflection. Furthermore, as the distance between source, lens and observer are extremely large, we can assume the mass distribution of the lens is a 2-dimensional distribution (i.e. *thin screen* approximation) and assume small-angle approximation (i.e. $\sin\alpha \simeq \tan\alpha \simeq \alpha$).

An illustration of the geometry of a lens system is shown in Fig. 1.6. The radial deflection of light rays by angle $\hat{\alpha}$ at a distance θ from the centre of the lens with a mass M contained within impact parameter ξ, is described by

$$\hat{\alpha}(\xi) = \frac{4GM(<\xi)}{c^2\xi}\frac{D_{ls}}{D_s}, \tag{1.1}$$

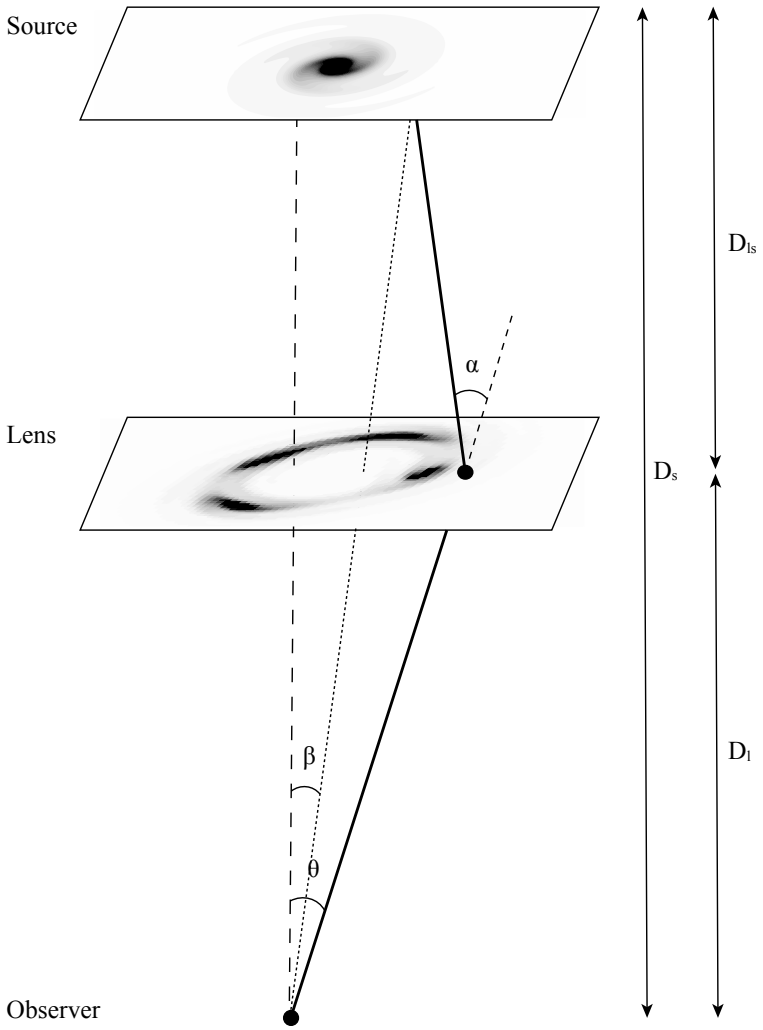

Figure 1.6 | Diagram of gravitational lens geometry.

where D_s, D_l and D_{ls} are the angular diameter distances from observer to source, observer to lens and from lens to source, respectively. A position on the source-plane is related to a position on the lens plane via the *lens equation*,

$$D_s\boldsymbol{\beta} = D_l\boldsymbol{\theta} - D_{ls}\hat{\boldsymbol{\alpha}}. \tag{1.2}$$

By defining the reduced deflection angle as

$$\alpha(\boldsymbol{\theta}) = \frac{D_{ls}}{D_s}\hat{\boldsymbol{\alpha}}(D_l\boldsymbol{\theta}), \tag{1.3}$$

Eq. 1.2 reduces to the standard form of the lens equation,

$$\boldsymbol{\beta} = \boldsymbol{\theta} - \alpha(\boldsymbol{\theta}), \tag{1.4}$$

which relates an angular position β on the source plane to an angular position θ on the lens plane.

Multiple images of the source will be produced where there are multiple solutions to the lens equation. For a circularly symmetric lens where the lens and source are perfectly aligned (that is, the deflection angle is equal to the impact parameter) a source is lensed into an *Einstein ring* with a radius defined as the *Einstein radius*, θ_E. The Einstein radius of an axisymmetric lens depends both on the enclosed mass, M, and the relative distance between source and lens,

$$\theta_E = \sqrt{\frac{4GM}{c^2}\frac{D_s}{D_l D_{ls}}}. \tag{1.5}$$

As the typical image separation of a gravitational lens is twice the Einstein radius, the mass enclosed within the Einstein radius can be estimated if the lens and source distance (redshift) are known.

For a three-dimensional mass distribution, the surface mass density is $\Sigma(D_l\theta)$. The *critical surface mass density*, Σ_{cr}, is the characteristic scale for which multiple images of the source are produced, defined as

$$\Sigma_{cr} \equiv \frac{c^2}{4\pi G}\frac{D_s}{D_l D_{ls}}. \tag{1.6}$$

We define the *convergence*, κ, or dimensionless surface density, as the ratio of surface mass density to the critical density,

$$\kappa(\boldsymbol{\theta}) \equiv \frac{\Sigma(D_l\boldsymbol{\theta})}{\Sigma_{cr}}. \tag{1.7}$$

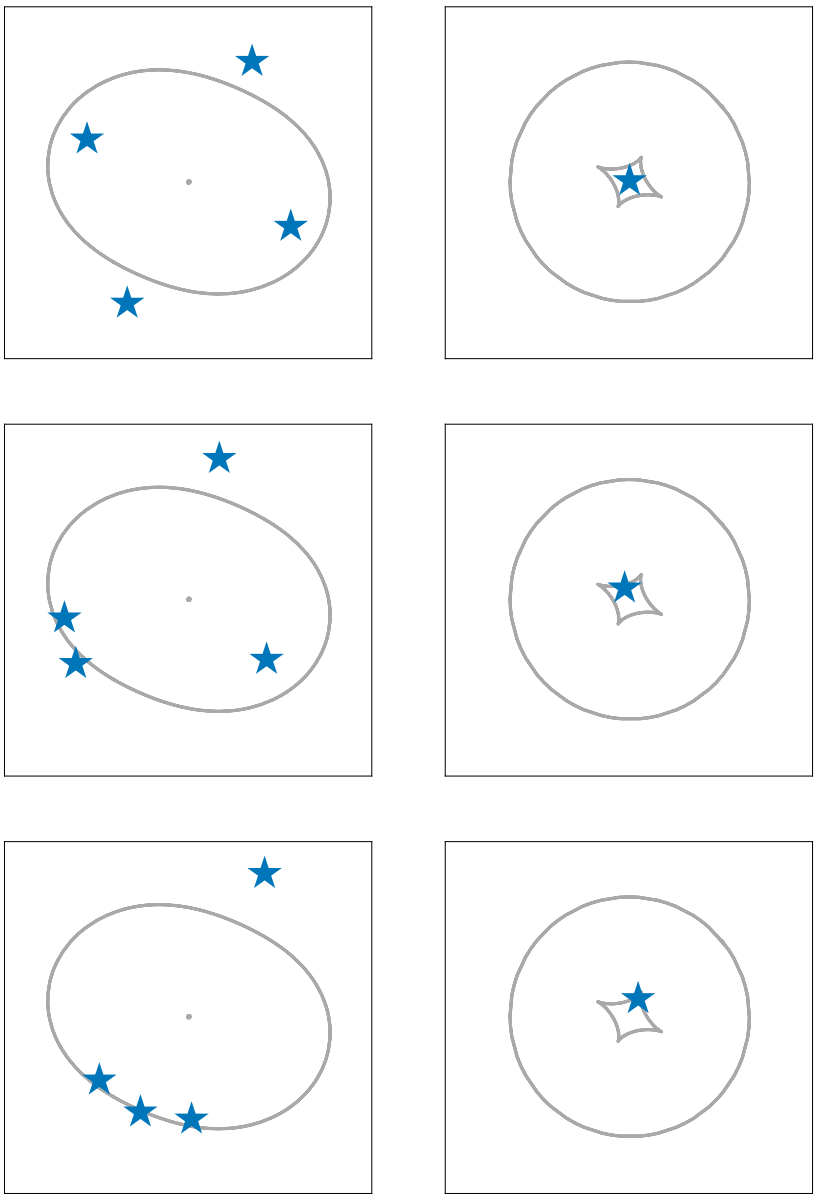

Figure 1.7 | An illustration of image configurations produced for a source lensed by a singular isothermal sphere with external shear. The columns show the resulting images produced on the lens plane (left) by a source in different positions relative to the tangential caustic (right). Top to bottom, the rows show a characteristic Einstein cross configuration, a fold configuration and a cusp configuration.

1

By using angular sizes in arcseconds and the dimensionless convergence, we can also define a dimensionless *lens potential*, ψ, such that the deflection angle is the gradient of the potential,

$$\boldsymbol{\alpha} = \nabla \boldsymbol{\psi}, \tag{1.8}$$

and the convergence is the Laplacian (divergence of the gradient) of the potential,

$$\boldsymbol{\kappa} = \nabla^2 \boldsymbol{\psi}. \tag{1.9}$$

It follows from Eq. 1.7 that $\kappa = 1$ where θ is equal to the Einstein radius, which denotes the *critical curve* in the lens plane. As shown in Fig. 1.7, the critical curve maps to the source plane as an astroid caustic. For axisymmetric lenses, the average surface density inside the Einstein radius is the critical density, so the surface density must be larger than the critical surface density for multiple images to be produced.

The solutions to the lens equation denote the positions of the lensed images under the assumption of a point-like source (i.e. a light ray has a single point of deflection). The magnification of a lensed image depends on the convergence, expressed as

$$\mu = \frac{1}{(1-\kappa)^2 - \gamma^2}, \tag{1.10}$$

where $gamma$ is the total shear ($\gamma^2 = \gamma_1^2 + \gamma_2^2$), which quantifies an overall stretching and squeezing due to mass contributions external to the lens. μ can be either positive or negative, where $\mu > 0$ is defined as even parity and $\mu < 0$ as odd parity. The critical curves on the lens plane, or *tangential caustics* on the source plane, denote the boundaries where $|\mu| \to \infty$ (for an infinitely small source). A source outside the tangential caustic (inside the radial caustic) produces three images, where the number of even parity images is always larger. Inside the tangential caustic, five images are produced. While an odd number of images is always produced theoretically, the central image is highly demagnified as $\kappa \gg 1$ near the centre of the lens[†]. The central image is also strongly affected by propagation effects due to the density of dust and ionised gas in the inner part of the lensing galaxy, so central images are very rarely observed for galaxy-scale lens systems (PMN J1632−0033 is probably the only example; Winn et al. 2003). Thus, these are referred to as two- or four-image lens systems (commonly known as doubles or quads) in this thesis.

In reality, sources have a size and structure such that each light ray has a different point of deflection, making lensed images differentially stretched and distorted. A key aspect of gravitational lensing is the *conservation of surface brightness*: as only the solid

[†]This is not necessarily the case if galaxies have a high concentration of mass in the central region, such as from a SMBH, but the images will be very faint in any case.

angle through which the source is observed changes, the source magnification is the ratio of the solid angle of the source on the lens plane to the source plane,

$$\mu(\boldsymbol{\theta}) = \left| \det\left(\frac{\delta\beta}{\delta\boldsymbol{\theta}} \right) \right|^{-1}. \tag{1.11}$$

1.2.2. Lens modelling and applications

As the position, brightness and structure of gravitationally lensed images are probes of the enclosed mass, lens modelling can investigate the distribution of mass. This makes the phenomenon an important means to investigate the properties of galaxies, such as their dark matter content and stellar initial mass function (e.g. Koopmans et al., 2009; Sonnenfeld et al., 2012; Dutton et al., 2013; Oldham et al., 2017; Oldham & Auger, 2018) or mass substructure (e.g. Hsueh et al., 2016, 2017), or to measure the Hubble constant from the time delays between lensed images (e.g. Fassnacht et al., 2002; Suyu et al., 2010; Rusu et al., 2019; Wong et al., 2019). These are all important tests of cosmological models and models of galaxy evolution, particularly when compared to predictions from simulations.

Gravitational lens modelling involves fitting a parameterised gravitational potential, which is typically a single power law ellipsoid. This is described by a density profile $\rho(r) \propto r^{-\gamma}$, where r is radius and $\gamma = 2$ for an isothermal profile. Observations have found that lens systems are usually well-fit by a power-law model that is close to isothermal (e.g. Koopmans et al., 2006, 2009; Auger et al., 2010; Sonnenfeld et al., 2013), perhaps due to a 'conspiracy' between the baryonic and dark matter mass components near the Einstein radius. The number of model constraints on the mass profile depends on the degree of information provided by each lensed image. For a two-image lensed quasar (a point source) the maximum number of constraints is five, given two positions (x,y) and a flux ratio: fewer than the number of lens parameters (7 for an isothermal ellipsoid model with external shear[‡]). Arcs and rings probe the lens potential at many more positions, enabling the parameters of the smooth mass profile (*macro-model*) to be determined more robustly.

The recent development of sophisticated grid-based lens modelling techniques (Warren & Dye, 2003) has advanced the study of gravitational lenses by enabling the extended surface brightness distribution to constrain the lens potential (e.g Dye & Warren, 2005; Suyu et al., 2006; Nightingale & Dye, 2015). While the optimisation of the lens parameters required to model the mass distribution is a non-linear problem,

[‡]These include lens position (x,y), lens strength, ellipticity (magnitude and position angle) and shear (magnitude and position angle).

for a given set of lens parameters the inversion to obtain the deconvolved source brightness distribution is a linear step (Warren & Dye 2003). The lens equation can then be written in the matrix form

$$\boldsymbol{FLs} + \boldsymbol{n} = \boldsymbol{d}, \tag{1.12}$$

where $\boldsymbol{L}$ is the lensing operator (defined by the lens potential) that acts on the matrix $\boldsymbol{s}$ describing the source surface brightness distribution. This, plus a noise covariance matrix $\boldsymbol{n}$, produces the matrix $\boldsymbol{d}$ that describes the lensed surface brightness distribution. For lens modelling in image-space, the term $\boldsymbol{F}$ is a sparse matrix that describes the point spread function of the telescope, while for visibility-plane modelling it includes Fourier transform and gridding operators to convert the lensed surface brightness into model visibilities. This allows a pixellated reconstruction of the deconvolved source structure to be generated. Furthermore, as the lens potential is well constrained by the complex surface brightness distributions with grid-based modelling, it is possible to infer deviations from a smooth model, such as from a low-mass halo (Koopmans, 2005; Vegetti & Koopmans, 2009; Hezaveh et al., 2016b). This is particularly powerful, as the detection and characterisation of low-mass galaxies at cosmological distances can constrain the halo mass function and discriminate between models of dark matter (e.g. Ritondale et al. 2019; Hsueh et al. 2019).

1.3. Thesis outline

In addition to the lenses themselves, gravitational magnification of the background source allows new insights into the high-redshift Universe. Where a lens system is unresolved, there is an overall apparent magnification of the source flux density: this can allow emission to be detected that would otherwise be too faint (Riechers et al. 2006; Impellizzeri et al. 2008; Riechers et al. 2011b) and also for efficient selection of lensed objects (Negrello et al., 2010). With resolved studies, the gravitational lens acts as a natural telescope by stretching and enlarging source structure such that it can be resolved on scales below the resolution limit (Rybak et al. 2015a,b; Paraficz et al. 2018; Massardi et al. 2018; Yang et al. 2019). Fig. 1.8 shows dust emission from a star-forming galaxy at $z = 3$, reconstructed with an effective resolution < 50 pc using grid-based lens modelling (Rybak et al., 2015a).

As discussed in Section 1.1.2, the star-forming properties of quasar host galaxies are an important test of the evolutionary paradigm. According to this model, as quasars are expected to be triggered following a merger-driven starburst, extreme levels of dust-obscured star formation should still be ongoing in the host galaxies of quasars.

In Chapter 2, we address this question with a survey of the FIR/sub-mm properties of quasar systems to constrain the level of thermal dust emission from the quasar host galaxies by exploiting the magnification effect of gravitational lensing. In the analysis, we investigate the contribution to radio and dust-heating measurements from AGN-associated emission to address the mechanisms of AGN feedback from these quasars.

In Chapter 3, the question of the feedback mechanisms of radio-quiet quasars is explored further with detections of emission at low radio frequencies. Exploiting the sensitivity of the Low Frequency Array (LOFAR; van Haarlem et al. 2013), we detect faint radio emission to search for any excess radio emission associated with low-luminosity radio jets. We predict future LOFAR surveys to be useful for characterising the global properties of radio-quiet quasars.

The remaining science chapters of this thesis (Chapters 4, 5 and 6) focus on high-resolution observations with ALMA of lensed quasar systems from the parent sample of Chapter 2. Chapter 4 we study the dust and molecular gas in six systems with equivalent resolution of 100–300 pc, which allows us to resolve the structure of these extremely compact galaxies and compare our findings to models of massive galaxy formation.

In Chapters 5 and 6 we investigate dust and molecular gas from a lensed quasar at $z = 2.64$. In Chapter 5, we suggest that these observations of high-excitation CO emission represent a new approach to find lensing mass substructures, and test models of dark matter and galaxy formation. In Chapter 6, we combine the CO data from Chapter 5 with H_2O data and global VLBI imaging of the radio jet structure to construct a model for this distant galaxy. We use our model to explain the previously reported detection of a water megamaser from this system.

In Chapter 7 we summarise the findings of this thesis and consider how our understanding of galaxy formation and evolution may benefit from future studies of gravitational lenses at sub-mm and radio wavelengths.

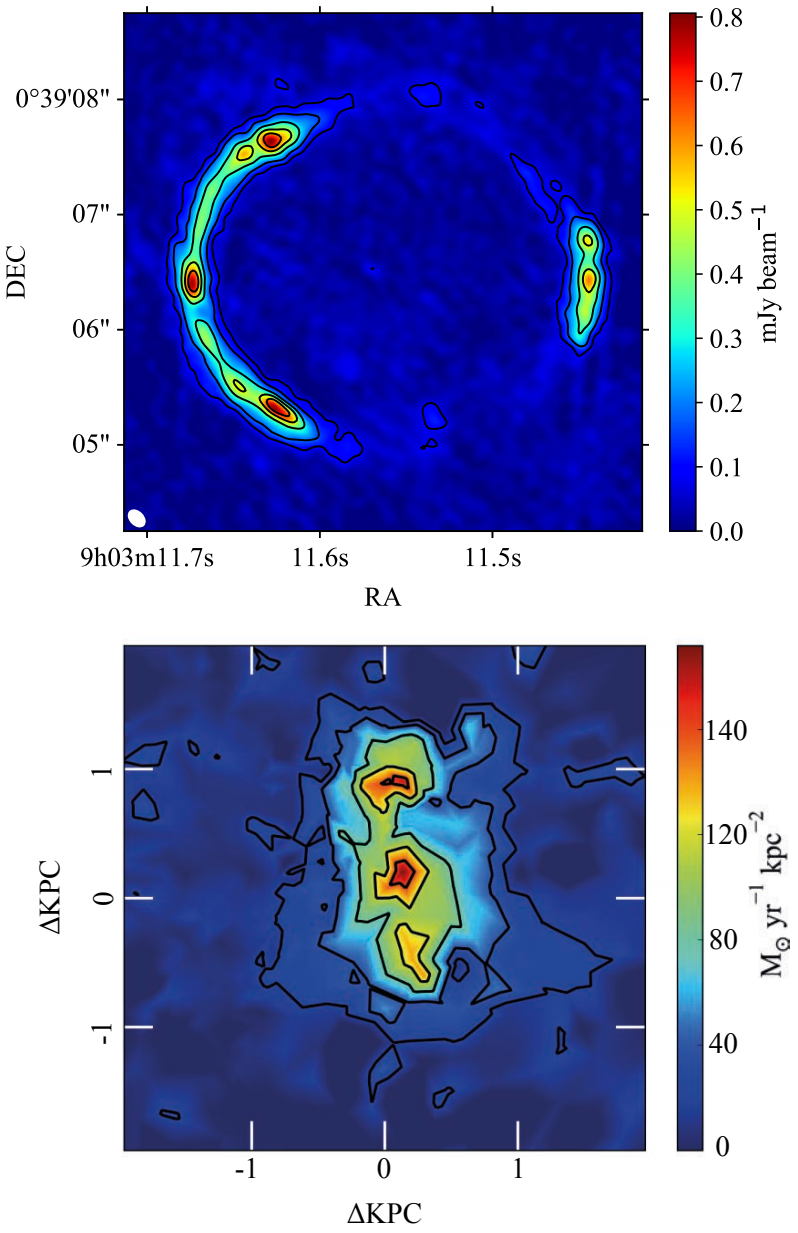

Figure 1.8 | Top: lensed dust emission from star-forming galaxy SDP81, observed with ALMA. Emission from the lensing galaxy is marginally detected. The synthesised beam is shown in the lower left corner. Bottom: the reconstructed source, where the colour-coding is star formation rate surface density (Rybak et al., 2015a).

Dust-obscured starburst

60 ml mezcal
30 ml lime juice
20 ml agave syrup
7 blackberries

Muddle together the mezcal, lime, agave and four blackberries. Shake with ice. Serve in an old-fashioned glass over fresh ice, garnished with the remaining blackberries.

2

Surveying quasar host galaxies with gravitational lensing

I. Detecting dust-obscured star formation in quasar host galaxies

H. R. Stacey, J. P. McKean, N. C. Robertson, R. J. Ivison, K. G. Isaak, D. R. G. Schleicher, P. P. van der Werf, W. A. Baan, A. Berciano Alba, M. A. Garrett and A. F. Loenen

Based on "Gravitational lensing reveals extreme dust-obscured star formation in quasar host galaxies"
Stacey et al. 2018, Monthly Notices of the Royal Astronomical Society, Volume 476, 5075

2

Abstract

We have observed 104 gravitationally-lensed quasars at $z \sim 1$–4 with *Herschel*/SPIRE, the largest such sample ever studied. By targeting gravitational lenses, we probe intrinsic far-infrared (FIR) luminosities and star formation rates (SFRs) more typical of the population than the extremely luminous sources that are otherwise accessible. We detect 72 objects with *Herschel*/SPIRE and find 66 percent (69 sources) of the sample have spectral energy distributions (SEDs) characteristic of dust emission. For 53 objects with sufficiently constrained SEDs, we find a median effective dust temperature of 38^{+12}_{-5} K. By applying the radio–infrared correlation, we find no evidence for an FIR excess which is consistent with star-formation-heated dust. We derive a median magnification-corrected FIR luminosity of $3.6^{+4.8}_{-2.4} \times 10^{11}$ $L_\odot$ and median SFR of 120^{+160}_{-80} $M_\odot$ yr^{-1} for 94 quasars with redshifts. We find $\sim$ 10 percent of our sample have FIR properties similar to typical dusty star-forming galaxies at $z \sim 2$–3 and a range of SFRs < 20–10000 $M_\odot$ yr^{-1} for our sample as a whole. These results are in line with current models of quasar evolution and suggests a coexistence of dust-obscured star formation and AGN activity is typical of most quasars. We do not find a statistically-significant difference in the FIR luminosities of quasars in our sample with a radio excess relative to the radio–infrared correlation. Synchrotron emission is found to dominate at FIR wavelengths for < 15 percent of those sources classified as powerful radio galaxies.

2.1. Introduction

Key to the study of galaxy formation and evolution is understanding the physical processes that drive star formation and the growth of active galactic nuclei (AGN). The concurrence of these phenomena is thought to relate a coevolution driven by feedback from the AGN, which may quench or induce star formation in the host galaxy through interactions with the interstellar medium. The mechanism of feedback may involve mechanical energy injection via AGN-driven jets, called 'jet mode' or 'radio mode' (Bicknell et al., 2000; Klamer et al., 2004), or radiative energy injection via winds, called 'quasar mode', although these processes are not well understood (see Alexander & Hickox, 2012, for review).

Hydrodynamical simulations of galaxy formation (Di Matteo et al., 2005; Hopkins et al., 2005; Bower et al., 2006) and various observational studies (for example Page et al., 2004; Stevens et al., 2005; Coppin et al., 2008) support an evolutionary model, initially proposed by Sanders et al. (1988) and developed more recently by Hopkins et al. (2008), in which quasars are formed as a result of gas-rich major mergers. According to this scenario, luminous dusty star-forming galaxies (DSFGs) are merger-driven starbursts that represent a transition phase into dust-obscured quasars. Over time, feedback effects strip the quasar host galaxies of gas and dust, and the quasars become unobscured and ultraviolet (UV) luminous. These leave passive spheroidal galaxies when the quasar exhausts its supply of cold gas.

Quasars that are luminous in the far-infrared (FIR) to mm regime are therefore predicted to be in a transition phase of their evolution with high rates of dust-obscured star formation. Studying the properties of these sources can provide important information about the evolutionary process, particularly when compared to the large population of extreme starburst galaxies that were discovered through blind surveys with the Submillimetre Common-User Bolometer Array (SCUBA), *Herschel Space Observatory* and now the Atacama Large Millimetre/sub-millimetre Array (ALMA).

Studies of FIR-luminous quasars, such as those in the SCUBA Bright Quasar Survey (Isaak et al., 2002; Priddey et al., 2003) and MAMBO/IRAM-30 m Survey (Omont et al., 2001, 2003), and more recent studies of quasars detected with *Herschel*/SPIRE (Pitchford et al., 2016, for example) have found that these quasars are embedded within gas- and dust-rich starbursting galaxies, with star formation rates of $\sim$1000 $M_\odot$ yr^{-1}, comparable to FIR-detected DSFGs. The low spatial density of FIR-luminous quasars, relative to DSFGs and UV-luminous quasars, has led some to argue for a quick transition from starbursting DSFG to an AGN-dominated quasar, with the FIR-luminous quasar phase being less than 100 Myr, and perhaps as short as $\sim$1 Myr (Simpson et al., 2012, for example). However, studies of individually-detected quasars have mostly focused on significantly bright sources due to limitations in sensitivity or source confusion. While

some recent progress has been made with the improved sensitivity and resolution of ALMA (Harrison et al., 2016; Banerji et al., 2017; Scholtz et al., 2018), resolutions of 100-pc are required to spatially resolve regions of star formation and AGN-heating, which are still difficult to attain for the high-redshift Universe.

Other studies have instead used stacking to investigate the mean star formation properties of quasar host galaxies. These studies, which account for redshift and stellar mass, find no significant correlation between star formation and AGN activity, and find SFRs comparable to normal star-forming galaxies that lie on the galaxy main sequence (Rosario et al., 2013; Azadi et al., 2015; Stanley et al., 2017).

The next logical step in understanding the properties of quasar host galaxies at all luminosities requires an investigation of lower surface-brightness sources. Many of the limitations of confusion and sensitivity can be mitigated by observing quasars that have been magnified by a gravitational lens.

The advantages of observing strong gravitationally-lensed quasars are three-fold. The first is that magnification effects increase the apparent flux-density such that a magnification factor of ∼10 the reduces integration time by a factor of ∼100. Sources with intrinsic flux densities below the confusion limit of field quasars can therefore be observed, probing the fainter end of the luminosity function (Impellizzeri et al., 2008, for example). The second advantage is the increase in apparent surface area, which combined with source reconstruction methods, allow source structure to be probed on much smaller physical scales (Rybak et al., 2015a,b, for example). A third advantage is that gravitational lensing has different systematic biases compared to field sources; while field observations tend to bias high luminosity or low-redshift sources, gravitationally-lensed sources are more biased towards compact higher redshift sources (typically $z > 1$) and less biased towards high intrinsic luminosities* (Swinbank et al., 2010, for example). In combination, these methodologies allow for a more complete view of the quasar population to be constructed.

In this chapter, we have targeted a sample of strong gravitationally-lensed quasars with the *Herschel Space Observatory* (Pilbratt et al., 2010) and derive their dust temperatures, intrinsic FIR luminosities and dust-obscured SFRs. Previous work in this area has been undertaken by Barvainis & Ivison (2002), who detected 23 of 40 gravitationally-lensed quasars and radio galaxies in their sample at 850 μm with SCUBA. They found dust emission broadly comparable to radio galaxies, in line with the AGN unification model, and no statistically-significant difference AGN classified as powerful radio galaxies, as would be expected if they have the same host galaxy properties. We have observed 104 lensed quasars, including 37 of the Barvainis & Ivison sample, detecting

*Although these biases are dependent on whether the gravitational lens systems are selected via the lens or source populations.

72 sources in at least one band with the *Herschel*/SPIRE. As our data cover shorter wavelengths, we are also able to determine the dust temperatures for the first time and infer whether the heated dust is due to star formation or AGN activity.

In Section 2.2, we present our sample selection, the relevant properties of the quasars in our sample, the parameters of the observations, and our data reduction methods. In Section 2.3, we report the results of the photometric measurements and the analysis of the radio-to-FIR spectral energy distributions (SEDs) of the sources. In Section 2.4, we show that the SEDs are consistent with dust heating due to star formation in the quasar host galaxies, and we compare our results with a sample of DSFGs at similar redshifts. Here, we also consider the contribution to the total radio emission from star formation processes for these quasars by considering the infrared–radio correlation. Finally, in Section 2.5 we present a summary of our results and discuss the future work that we will carry out with this sample.

Throughout, we assume the Planck Collaboration et al. (2016) instance of a flat ΛCDM cosmology with $H_0 = 67.8\ \mathrm{km\,s^{-1}\ Mpc^{-1}}$, $\Omega_M = 0.31$ and $\Omega_\Lambda = 0.69$.

2.2. Sample and observations

In this section, we describe our sample of gravitationally-lensed quasars and present the observations that were carried out using the *Herschel Space Observatory*.

2.2.1. Sample selection

Our sample consists of all of the gravitationally-lensed quasars that were observed with the *Herschel Space Observatory* (Pilbratt et al., 2010) using the Spectral and Photometric Imaging Receiver (SPIRE) instrument (Griffin et al., 2010). The vast majority of the observations came from our own open time project (Proposal ID: OT1_abercian_1). At the time of the proposal, these included all known quasars lensed by foreground galaxies. The majority of the sample are identified spectroscopically to be quasars, although some are identified as powerful radio galaxies without detections of prominent emission lines[†]. These sources are listed in the Sloan Digital Sky Survey Quasar Lens Search (SQLS) catalogue and CASTLES database (Inada et al., 2012; Kochanek et al., 1999) and come from a variety of surveys at optical and radio wavelengths. Our sample is quite heterogeneous given the nature of the different surveys from which the targets were selected, but its size will allow us to draw representative conclusions on the

[†]We refer to all these objects as quasars in this chapter, for simplicity.

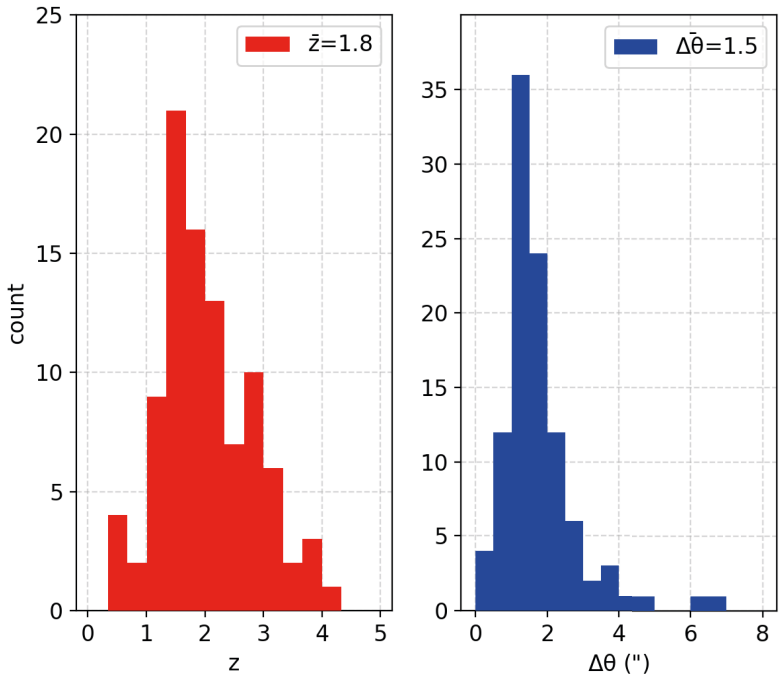

Figure 2.1 | (left) The redshift distribution of 94 objects in our sample with known redshift, which has a median redshift of 1.8. (right) The lensed image separations, in arcsec, which have a median of 1.5 (excluding SDSS J1029+2623 which has a maximum image separation of 22.5 arcsec).

relative FIR properties of jet-dominated and SF-dominated quasars, and provides a large parent sample from which further higher resolution observations of interesting individual objects can be made.

In total, there are 104 lensed quasars in our sample, the relevant properties of which are presented in Table 2.6 of the Appendix. The redshift distribution and maximum image separations of the lensed quasars in our sample are presented in Fig. 2.1. The full width at half maximum (FWHM) of the point spread function (PSF) in each band is 18, 24 and 35 arcsec for the 250, 350 and 500 μm bands, respectively. Therefore, all but 3 of our sample (Q0957+561, RX J0921+4529 and SDSS J1029+2623) have separations between the lensed images that are <1/3 of the smallest *Herschel*/SPIRE beam size, and can therefore be considered point sources for our study. The sample was observed in small map mode with one scan repetition per source, with a total integration time of 2–3 min per target, such that a source of 50 mJy will be detected at the 5σ level in the 500 μm band.

Of our quasar sample, 21 have 850 μm detections and 11 have 450 μm detections with SCUBA by Barvainis & Ivison (2002). Assuming magnifications from the literature and spectral energy distributions (SEDs) described by Yun & Carilli (2002) ($T_{\rm d}$ = 58 K, β = 1.35), nearly all of these detected sources (15 at 250 and 350 μm, 18 at 500 μm) would be below the confusion limits of *Herschel*/SPIRE were they not gravitationally-lensed. It is therefore likely that the quasar population with intrinsic fluxes below those of previously detected field sources will be revealed in this study. Moreover, while SCUBA measurements lie on the Rayleigh-Jeans side of the thermal SED, the *Herschel*/SPIRE bands allow for better constraints on the peak of the SED, and thus, more accurate estimates of the characteristic FIR-luminosities and dust temperatures of the sample. We note that the previous study by Barvainis & Ivison assumed a dust temperature of 30 K for their sample, which may have biased their estimates of the FIR luminosities and inferred star formation rates.

2.2.2. Radio properties

Radio emission from quasars may be associated with AGN (synchrotron) or star formation (synchrotron, free-free) processes. Quasars with radio jets are associated with jet-mode feedback, whereas quasars without these features are primarily radiative, so it is convenient to classify our sample based on their radio properties. There is a range of terminology and methods of classification employed in the literature to distinguish these groups, typically radio-'loud' and radio-'quiet' based on radio luminosity or radio-optical ratio. However, we find it more appropriate to group these by considering the operative feedback mechanisms. We have divided the sample into jetted (quasars with known jet-dominated radio emission) and non-jetted (quasars with star-formation-dominated radio emission and those where the dominant radio emission mechanism is unknown) dependent on whether there has been confirmation of the existence of a radio jet component with high-resolution radio data. For this, we have used the data from targeted observations for individual objects in the literature. Of the 34 quasars within the sample that we classify as jet-dominated radio sources, 31 are from the MIT-Green Bank Survey (Langston et al., 1990, MG), the Jodrell Bank-VLA Astrometric Survey (Patnaik et al., 1992, JVAS), the Cosmic Lens All-Sky Survey (Myers et al., 2003; Browne et al., 2003, CLASS), the Parkes-NRAO-MIT survey (Griffith & Wright, 1993, PMN) and other radio surveys, all of which are dominated by radio-luminous AGN due to their respective flux-density limits. The remaining three sources are Q0957+561 (Garrett et al., 1994), H1413+117 (Stacey et al. in prep) and HS 0810+2554 (Hartley et al., 2019).

At low radio luminosities, composite AGN and star formation emission are likely,

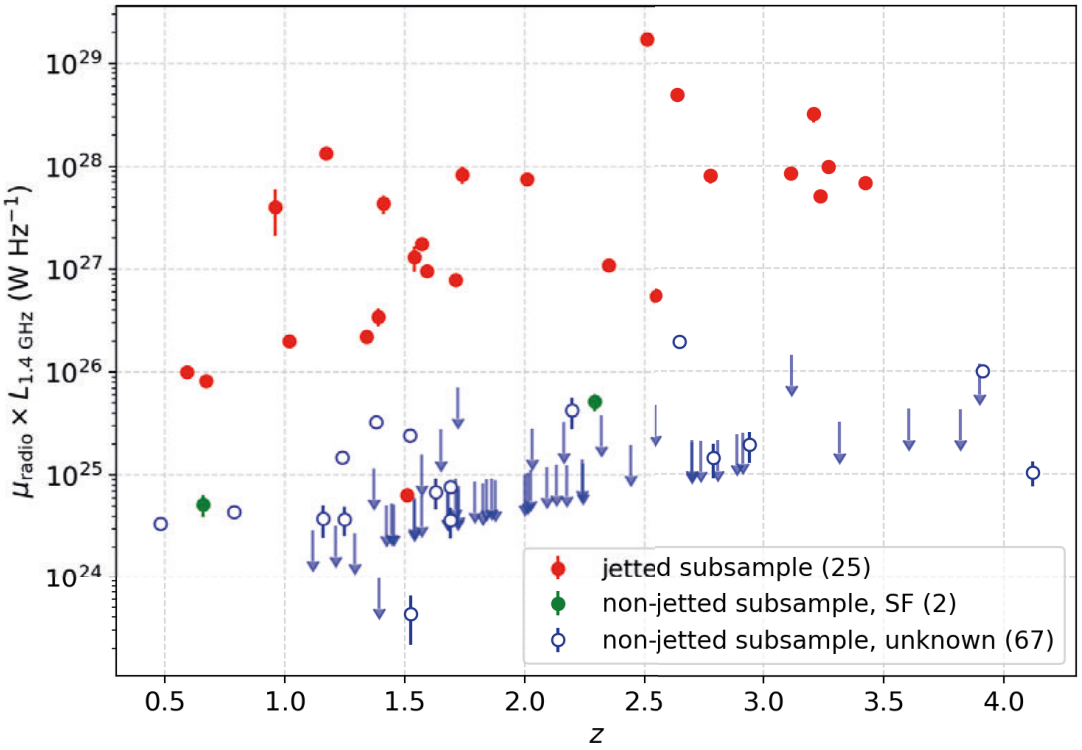

Figure 2.2 | The rest-frame 1.4 GHz radio luminosity-density (interpolated or extrapolated from existing data) as a function of redshift for 92 objects in our quasar sample with radio measurements and a known redshift. Most of the upper limits are taken from FIRST or NVSS. The jetted subsample, with known jet-dominated radio emission, are shown in red. The non-jetted subsample includes two quasars with star-formation-dominated radio emission (shown in green) and 67 with unknown radio emission mechanism (shown in blue).

Table 2.1 | Number of detections in each *Herschel*/SPIRE band for the jetted and non-jetted subsamples.

	N	250 μm	350 μm	500 μm
Jets	34	24 (71 percent)	23 (68 percent)	16 (47 percent)
No jets	70	47 (67 percent)	41 (59 percent)	23 (33 percent)
Total	104	71 (68 percent)	64 (62 percent)	39 (38 percent)

and differentiating between these possibilities is difficult. We define only two sources in our sample with established star-formation-dominated radio emission, RX J1131−1231 and IRAS F10214+5255. VLBI experiments to detect the radio core of these quasars suggest the radio emission is primarily due to star formation (Wucknitz & Volino, 2008; Deane et al., 2013). In all other cases, the emission mechanism is undetermined, either because they are not detected at radio wavelengths or the detections are at too low an angular resolution to discriminate between compact (AGN) or extended (star formation) emission. We obtain the majority of these measurements from the National Radio Astronomy Observatory (NRAO) Very Large Array (VLA) Sky Survey (Condon et al., 1998, NVSS) and the Faint Images of the Radio Sky at Twenty-Centimeters (Becker et al., 1995, FIRST), both at 1.4 GHz and with beam sizes of 45 and 5 arcsec, respectively.

We show the rest-frame 1.4 GHz radio luminosities for the sample in Fig. 2.2. We include all quasars without evidence of jet-dominated radio emission in the non-jetted subsample for the time being, but refine these classifications using the radio–infrared correlation in Section 2.4.3.

2.2.3. Photometry

The sources have been observed with the *Herschel*/SPIRE instrument in three bands centred on 250, 350 and 500 μm, which effectively cover the rest-frame spectrum from 40 to 394 μm for the redshift range of our sample. The calibrated data were obtained from the *Herschel* Science Archive using the *Herschel* Interactive Processing Environment (HIPE) (Ott, 2010) version 14.0.0.

The photometry was performed using the SUSSEXtractor and Timeline Fitter algorithms within HIPE (Savage & Oliver, 2007; Bendo et al., 2013) using recommendations in the SPIRE Data Reduction Guide[‡]. The Timeline Fitter performs point source photometry by fitting Gaussians to the baseline subtracted timeline samples, given

[‡]`http://herschel.esac.esa.int/hcss-doc-14.0/print/spire_drg/spire_drg.pdf`

source locations on the sky. The SUSSEXtractor method extracts point sources from the beam-smoothed, calibrated maps. We set a threshold of 3σ, where σ is the RMS noise of the background around the source. While the Timeline Fitter gives more precise measurements and was the preferred method, SUSSEXtractor was occasionally more successful at extracting lower flux-density sources ($S_\nu \lesssim 30$ mJy). We place a detection limit of 3σ on the photometric measurements, where σ is the RMS noise of the map, including confusion, given that we know the positions of the gravitational lens systems.

We explored the possibility of fixing the positions of source extraction with SUSSEXtractor to the 'true' sky positions in order to avoid an upward bias due to fitting to random noise spikes. While the effect of this is reduced as SUSSEXtractor fits to beam-smoothed maps, it has been noted to cause a bias in submillimetre measurements where the signal-to-noise ratio is low (Ivison et al., 2002; Coppin et al., 2005, for example). As we would expect, there is a systematic upward shift in the flux densities measured when the position is left free. However, the change is generally not more than 10 percent and within the photometric errors. We choose not to employ this method as we find there are often significant uncertainties on both the *Herschel* astrometry and the 'true' source position from the literature. We compared the extracted source positions of the five FIR-bright objects from our sample detected in ALMA to their ALMA positions (which have accurate and precise astrometry due to phase-referencing) and find offsets up to several arcsec. This is consistent with other findings in the literature (Melbourne et al., 2012, for example). We also find differences as much as several arcsec in the positions from optical or X-ray positions in the literature relative to the ALMA positions. There is an additional positional uncertainty as the targets are gravitationally-lensed with a range of image separations (Fig. 2.1). Thus, the result of fixing the position for source extraction would be a systematic down-shift of the extracted source flux densities. This bias can be more significant than the bias due to noise spikes and, as many sources are close to the detection limit, this would have a negative effect on the analysis. In any case, these uncertainties in the photometry are far lower than the uncertainties in the FIR luminosity and SFR due to SED fitting and the unknown magnification factor of the lensed systems (see Sections 2.3.4 and 2.3.3).

2.2.4. Source matching and confusion

Due to the sizes of the *Herschel*/SPIRE beams, we must also consider the contribution to the measured flux densities from field galaxies, including sources not associated with the target quasars or their lensing galaxies. For example, this could be due to dust-obscured star formation or AGN activity within the lensing galaxy at mm-wavelengths

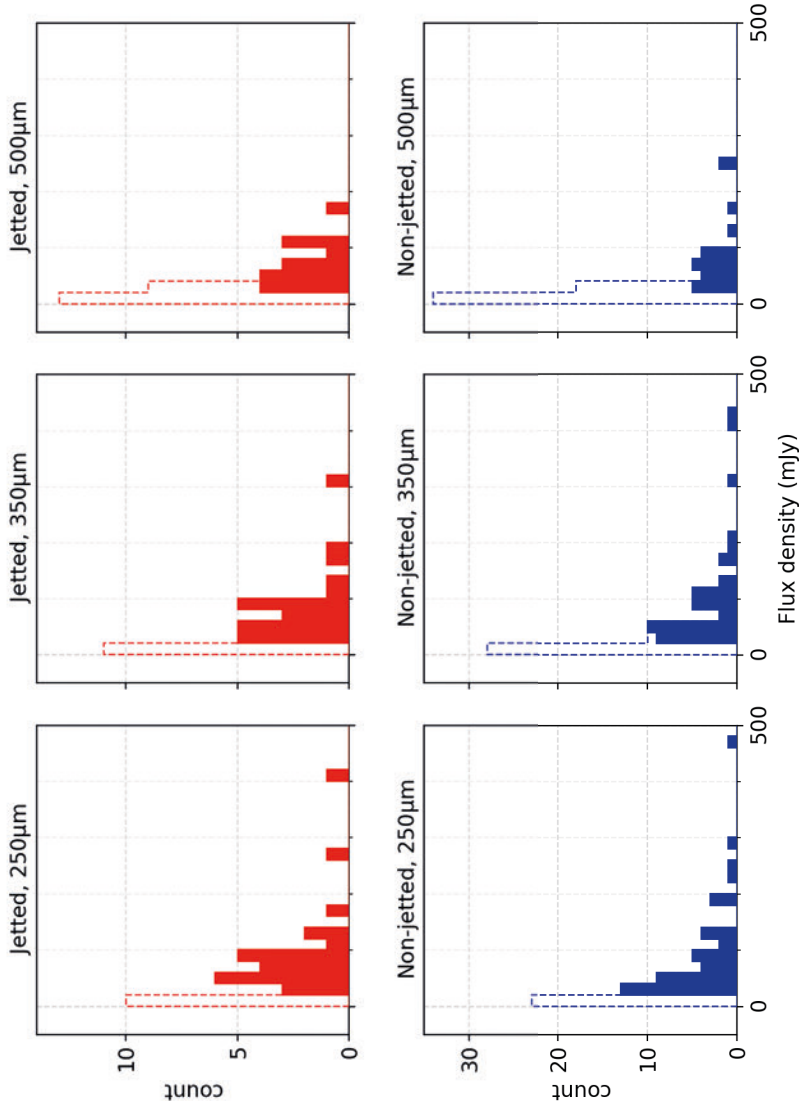

Figure 2.3 | Number of sources binned by measured flux-density for the three *Herschel*/SPIRE bands, divided into jetted (blue) and non-jetted (red) sub-samples. 1.5 σ limits of non-detections are stacked on top of the measured values and outlined with a dashed line. Note that PKS 1830−211 is excluded, for clarity, due to its high flux-density ($S_{250\ \mu m}$ = 537 mJy, $S_{350\ \mu m}$ = 670 mJy, $S_{500\ \mu m}$ = 806 mJy).

as has been seen in three gravitational lenses observed at high angular resolution with ALMA (ALMA Partnership et al., 2015; Paraficz et al., 2018, McKean et al. in prep). We also note that at radio wavelengths, about 10 percent of lensing galaxies have detected synchrotron emission from an AGN (McKean et al., 2005, 2007).

We take a series of steps to match the photometric data with our target quasars. We compare the extracted source position from SUSSEXtractor or the Timeline Fitter algorithm with the 'true' position of the lensing galaxy (where there is good astrometry, else the brightest lensed image) taken from the NASA Extragalactic Database (NED). We rejected extracted sources whose positional offsets are larger than half the FWHM of the SPIRE beam. We allow for some freedom in source fitting to allow for the combined uncertainties on the *Herschel* pointing, the 'true' source position, and source fitting. The extracted source positions are then cross-checked with nearby sources listed on NED to minimise the possibility of mis-matching. In addition to this, we use detection in the 250 μm band (which has the highest resolution and lowest confusion noise) as a prior to confirm a match at 350 μm and 500 μm[§]. This strategy reduces the likelihood of contamination from field sources, but does not exclude the possibility of emission from the lensing galaxy or a nearby unknown FIR-bright field source being included in our photometric measurements.

While most of the targets appear uncontaminated, in some cases, blending is evident in the level 2 (fully calibrated) maps by visual inspection. For example, individual sources may be resolved in the higher resolution 250 μm maps, but become blended in the 500 μm band where the beam is largest. The blending results in over-fitting by the source extractor and returns incorrect flux densities. We attempt to overcome this by simultaneously fitting to both the known target position and the blended source using the Timeline Fitter, where possible, then applying the same source matching criteria. Where this fails, we use SUSSEXtractor and fix the extracted position to the 'true' target position and blended source position (if known).

We can further identify confusion or mismatching by comparison of the *Herschel*/SPIRE data with the source SED. It is likely, based on inspection of their spectra, that we are unable to remove blended emission completely for 8 sources, including CLASS B0712+472, CLASS B0850+054, SDSS J0903+5028, CLASS B1152+200, Q 1208+101, CLASS B1359+154, SBS 1520+530 and Q 2237+030 (SEDs for all but CLASS B0712+472 are given in Fig. 2.16 of the Appendix). For CLASS B0712+472 and Q 2237+030, there is too much blended emission to confidently measure the quasars, so we assume upper limits for all three bands by measuring the off-source RMS noise of the maps. For CLASS B1152+200 this is the case at 350 μm and 500 μm. The remaining sources appear to have an additional contribution to their 500 μm measurement that is

[§]We make an exception for PMN J1632−0033 because of the completeness of the SED (see Fig. 2.17).

inconsistent with thermal dust emission or with synchrotron emission, based on their radio measurements. This may be due to errors in fitting to the blended source or further blending with nearby field sources. We identify known sources within a few arcsec of SDSS J0903+5028, Q 1208+101, Q 2237+030 that could be responsible and do not find evidence of confusion from the lensing galaxy for these objects. While SBS 1520+530 does have a star-forming lensing galaxy, the measured 500 μm flux-density implies a flat spectrum that is inconsistent with the upper limits in the sub-mm/mm. In these cases, we assume upper limits for the 500 μm measurements that include confusion.

Almost all of the ancillary data that is used to derive the source SEDs is taken from literature, which typically consists of high resolution, targeted observations at mm-to-radio wavelengths, and lower resolution surveys at radio wavelengths. Where sources are detected and unresolved, we cannot be certain that they relate to a single source (the target, as opposed to a nearby companion or the lensing galaxy) without higher resolution observations on about arcsec-scales. The detections at 250 μm are matched to unique radio detections using the same matching criteria described previously, and these are assumed to relate solely to the quasar based on the assumptions that i) the spatial density of quasars is lower than DSFGs, and so we are likely observing a single source rather than multiple sources, and ii) as these quasars are intrinsically bright and gravitationally-magnified, any companion would have to be similarly bright to contaminate our measurements, which is unlikely. Of course, further observations at higher angular resolution with mm-wavelengths interferometers will better match the FIR emission detected here with the optical-to-radio counterparts of the quasars. However, throughout this chapter we assume that the quasar is the sole source of the position-matched FIR emission detected with *Herschel*/SPIRE.

2.3. Results and analysis

In this section, we present the photometric results and describe the SED fitting analysis used to determine the physical properties for each gravitationally-lensed quasars within our sample.

2.3.1. *Herschel*/SPIRE measurements

The *Herschel*/SPIRE photometry for all of the sources observed in our sample is detailed in Table 2.6 of the Appendix, and their SEDs, using all available data points, are shown in Fig. 2.16 in the Appendix. Of the 104 sources observed, 72 are detected in at least one

band down to a detection threshold of 3σ. Upper limits are given for those sources not detected at this confidence level. Of the sample, 10 targets suffer from contamination from the lensing galaxy or nearby field sources, which is apparent from their spectral properties and known properties of the lensing galaxies or nearby sources. This mostly affects the 500 μm band, due to the larger FWHM of the point spread function and their rising synchrotron spectra at longer wavelengths (see Section 2.2.4).

The measured flux-density distribution for each of the bands, separated by their radio properties, is shown in Fig. 2.3 and the number of detections is given in Table 2.1. We use the two-sample Kolmogorov–Smirnov (K–S) test to compare whether the measured flux densities of the subsamples are consistent with the same underlying distribution. For all K–S tests in this work we employ a Peto–Prentice Generalized Wilcoxon method[¶] for censored data using the *twosampt* task in the STSDAS statistics package within IRAF. The test returns a probability (p) for the null hypothesis, for which $p < 0.05$ we take as statistically-significant. For our subsamples, the test returns probabilities of 0.44, 0.57 and 0.75 for the distributions of measured flux densities at 250 μm, 350 μm and 500 μm, respectively. While the detection rates are slightly higher for the jetted quasars, the differences between the subsamples are not statistically-significant.

2.3.2. Spectral slopes

In Figs. 2.4 and 2.5, we show the spectral index between 850 and 500 μm ($\alpha_{500\ \mu\mathrm{m}}^{850\ \mu\mathrm{m}}$) and 500 and 250 μm ($\alpha_{250\ \mu\mathrm{m}}^{500\ \mu\mathrm{m}}$)[‖]. 74 objects in our sample have detections in the FIR to sub-mm, including the 72 *Herschel*/SPIRE detected sources and a further 2 which have only sub-mm detections. In most cases, we find evidence for heated dust emission: of these 74 objects, we ascribe the emission in 69 cases (66 percent of the sample) as being due to thermal dust emission from their rising or peaking spectra in FIR with frequency, relative to their sub-mm/mm/radio emission.

Of the five remaining sources that are detected in at least one band, there is no clear evidence for heated dust emission in the current data (see Fig. 2.17 for their SEDs). These sources are CLASS B1030+074, JVAS B0218+357, PKS 1830−211, PMN J1838−3427 and PMN J1632−0033. These sources do not have rising spectra in the FIR and have strong flat-spectrum synchrotron emission in the radio. Unfortunately, these sources were not observed by the SCUBA and MAMBO surveys or were discovered too late to

[¶]We employ this method as it is usually the most reliable and least affected by differences in the censoring patterns.

[‖]The spectral index is defined as a power-law, $S_\nu \propto \nu^\alpha$, where S_ν is flux-density and ν is frequency.

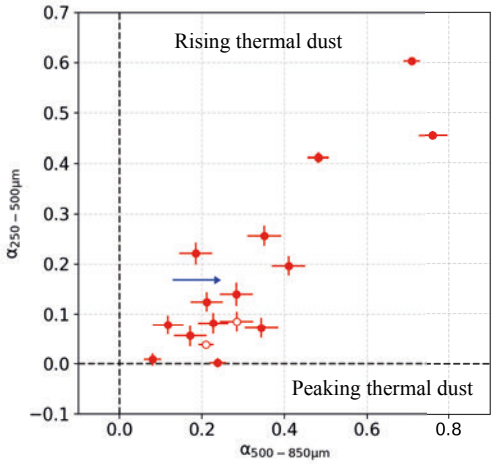

Figure 2.4 | Spectral index with frequency of the high and low *Herschel*/SPIRE bands relative to 850 μm, for the 17 sources in the sample with previous sub-mm detections and three SPIRE detections. Open circles are measurements at the same wavelength, but not from SCUBA. Limits due to non-detections at 850 μm are shown in blue. The plot excludes PKS 1830−211, for clarity, due to its large negative spectral index ($\alpha = -0.5$).

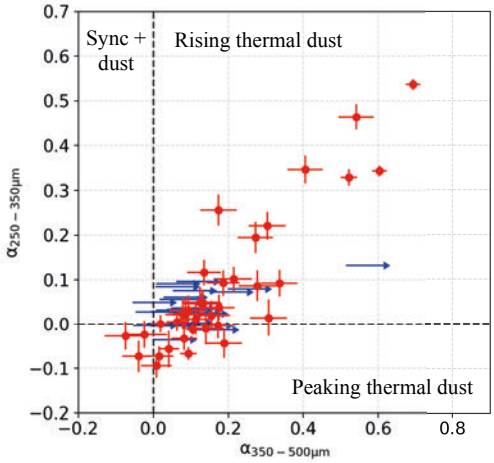

Figure 2.5 | Spectral index of high-to-mid against mid-to-low *Herschel*/SPIRE for 63 sources with 250 μm and 350 μm detections. The positive quadrants contain rising spectra associated with dust. 3 sources with falling spectra from 350 to 500 μm may have contamination from synchrotron emission, as discussed in Section 2.3.2. Lower limits due to non-detections at 500 μm are shown in blue. The plot excludes PKS 1830−211 due to its steep negative spectral index ($\alpha = -0.5$).

be part of the Barvainis & Ivison (2002) sample. Without measurements in the sub-mm regime, it is not clear how the synchrotron component falls off towards the FIR. In the cases of CLASS B1030+074, JVAS B0218+357 and PKS 1830−211, the flat-spectrum component continues into the mm-regime, so it is likely there will be a significant contribution from optically-thin synchrotron emission in the *Herschel*/SPIRE measurements (SED fitting of PKS 1830−211 is discussed further in 2.C.4 of the Appendix). PMN J1838−3427 and PMN J1632−0033 do not have enough high-frequency data to extrapolate their spectra into the FIR. It is possible these sources have spectra comparable to CLASS B1127+385 or CLASS B1152+200, where sub-mm measurements or upper-limits dictate that synchrotron emission does not have a significant contribution in the FIR (see Fig. 2.17 of the Appendix for their SEDs). JVAS B0218+357 and PMN J1838−3427 have measurements that appear characteristic of peaking dust emission, but this could also be explained by variability or a self-absorbed synchrotron component. We fit thermal SEDs to the *Herschel*/SPIRE measurements for these five quasars to place upper limits on a possible contribution of heated dust to the FIR emission.

2.3.3. Magnifications

To derive the *intrinsic* properties of the quasars in the sample, the measurements must be corrected for their lensing magnification. Generally, these are obtained from the literature and are typically derived from an analysis of optical or radio gravitational lensing data. However, optical and radio components of quasars tend to be compact (size scales of ≤ pc to a few 10s of pc), and can result in very high magnification factors if the source is close to a lensing caustic. For example, JVAS B1938+666 has a radio magnification factor of 173 (Barvainis & Ivison, 2002), whereas the 2.2 μm infrared emission from the AGN host galaxy has a magnification of about 13 (Lagattuta et al., 2012). This presents a problem for accurately estimating the properties of this sample of gravitationally-lensed quasars at FIR to sub-mm wavelengths, as the size scales of AGN emitting regions may be anywhere from ~pc (in the case of the AGN core) to ~kpc (radio jets or a star-forming disc). Where the radio or optical magnifications are high, it is likely that the dust emission (assuming it is coincident with the quasar) will be differentially magnified as only a small region will be close to the caustic and the overall magnification will be lower. Magnifications derived from optical or radio data are therefore unlikely to be accurate indicators of the actual dust magnification.

Only a few quasars in our sample have high-resolution observations in the FIR to sub-mm regime, thus we list the source properties given in Tables 2.6 and 2.7 uncorrected for lensing magnification. Known magnifications ($\mu_{\rm SF}$) in the FIR to sub-

mm, based on dust or molecular gas tracers relating to star-forming regions, are given in Table 2.2. We assume that cold molecular gas has a similar extent, thus similar average magnification, as the star formation heated dust emission. Only two of the sources in the sample have resolved dust emission related to star formation. These are the Cloverleaf quasar and RX J0911+0551, which have magnifications of 11 and 19, respectively**. For the intrinsic properties discussed below, we conservatively assume a magnification of $\mu_{\rm est.} = 10^{+10}_{-5}$ for the sources without known magnifications. This is consistent with lens modelling of dust emission in *Herschel*-selected strongly-lensed star-forming galaxies: Bussmann et al. (2013) find total magnification factors 2–15 ($\bar{\mu} = 8$) for a sample of 20 observed with the Submillimeter Array (SMA), and Dye et al. (2018b) find magnifications factors 4–24 ($\bar{\mu} = 12.5$) in a sample of six observed with ALMA.

Magnifications of more than 20 are unlikely if the sources are extended more than ~ 200 pc, as discussed in the Barvainis & Ivison study. The two sources in our sample with reconstructed dust emission, RX J0911+0551 and the Cloverleaf quasar, both have dust emitting regions of ~ 1 kpc in size (Tuan-Anh et al. 2017; Chapter 4). Assuming these sizes are characteristic, our assumption of $\mu_{\rm est.} = 10^{+10}_{-5}$ is likely representative of the magnifications of the sample, including a conservative uncertainty to account for outliers, and will provide an indication of the unlensed properties of the sample as a whole. The median values of the intrinsic properties we derive in the following analyses do not account for the factor of 2 error in the magnification because the assumption is taken for all but seven objects.

**M. Rybak and P. Tuan-Anh, private communication.

Table 2.2 | Magnification values from the literature, with errors where given, and the data with which the lens modelling is performed (line or continuum). CO line emission is assumed to have a similar location and extent as star-formation-heated dust emission, thus a similar magnification.

Source	μ_{SF}	Method	Reference
APM 08279+5255	4.2	CO (1–0)	Riechers et al. (2009)
RX J0911+0551	18.7 ± 1.3	360 GHz continuum	P. Tuan-Anh, private communication
Q 0957+561	7 ± 1	CO (2–1)	Krips et al. (2005)
IRAS F10214+4724	6 ± 1.5	CO (1–0)	Deane et al. (2013)
RX J1131-1231	7.3	CO (2–1)	Paraficz et al. (2018)
H1413+117	11.0	690 GHz continuum	M. Rybak, private communication††
PSS J2322+1944	2.5	CO (2–1)	Carilli et al. (2003)

†† Venturini & Solomon (2003) also find a factor of 11 based on CO (7–6) line observations.

2.3.4. SED modelling

To constrain the physical properties of the FIR emission in each quasar host galaxy, we fit a combined non-thermal and thermal SED model to the *Herschel*/SPIRE data, along with any available data in the literature, excluding our measurements that are affected by confusion, as noted in Table 2.6. This model will account for any synchrotron component, in the case of the jetted targets, and any heated dust component of the SED. We use a power-law with spectral index α,

$$S_\nu \propto \nu^\alpha, \tag{2.1}$$

to describe the flux-density (S_ν) as a function of frequency (ν) in the case of synchrotron emission. We do this only to estimate the contribution of synchrotron to the FIR spectrum, so do not attempt more complex fitting describing spectral turn-overs (for example CLASS B1422+231 shown in Fig. 2.16 of the Appendix). The SEDs of flat spectrum radio sources will likely turn down at higher frequencies and have a negligible synchrotron contribution in the FIR (for example, CLASS B1127+385 in Fig. 2.16). In some cases, there is a suggestion that the synchrotron emission turns down towards the sub-mm (for example, Q0957+561, suggested by an upper limit at 230 GHz) so we assume this does not contribute substantially to the FIR emission. We choose not to fit a synchrotron component where there is a single radio detection as we have no knowledge of the spectral behaviour, and, as these single measurements typically correspond to lower luminosities, the FIR contribution will be small.

We use a characteristic modified black-body,

$$S_\nu \propto \frac{\nu^{3+\beta}}{e^{h\nu/kT_\mathrm{d}} - 1}, \tag{2.2}$$

to describe the heated dust component, where h is the Planck constant, k is the Boltzmann constant, T_d is effective dust temperature, and β is the emissivity index, which determines the steepness of the Rayleigh-Jeans slope of the spectrum.

The Python implementation EMCEE (Foreman-Mackey et al., 2013) was used to build a Markov Chain Monte Carlo (MCMC) analysis of the fitted SED for each data set, allowing the dust temperature and normalization as free parameters to sample the posterior probability distribution of the model. Where possible, we also leave β as a free parameter in the model, allowing for a test of the range of dust emissivities that are consistent with the data. However, fitting for β requires at least four data points to constrain the peak and Rayleigh-Jeans slope of the modified black-body function. For many sources, our *Herschel*/SPIRE data are the only measurement in the FIR–sub-mm regime. Thus, we assume a value of $\beta = 1.5$ for these sources, as is frequently applied

in the literature (Magnelli et al., 2012, for example). Various combinations of T_d and β have been found for samples of high-redshift quasars. For example, Priddey & McMahon (2001) find an average of $T_d = 41 \pm 5$ K and $\beta = 1.95 \pm 0.3$, whereas Beelen et al. (2006) find an average of $T_d = 47 \pm 3$ K and $\beta = 1.6 \pm 0.1$ for their sample. For the sources that were not detected, or had only one detection to constrain the fit, we assume the median fitted dust temperature of the sample (38 K, see Fig. 2.6) and $\beta = 1.5$, and fit only for the normalization. For these sources with only one detection, we fit the 16th and 84th percentile values of the median fitted temperatures to estimate our errors on the FIR luminosity. As β is highly correlated with T_d, errors on the derived properties of sources without β-fitting may be underestimated. However, the FIR luminosity is not strongly affected by our assumptions due to the joint dependency of T_d, β and normalization, so this will not have a significant effect on the inferred values of L_{FIR} or SFR. This is unsurprising, as the luminosity is derived by the integral of the fit defined by the data points.

For the purpose of spectral fitting, the ten sources without a known redshift are assumed to have $z = 1.8$, equivalent to the median redshift of the sample. The choice of redshift significantly affects the luminosity-distance, thus these objects are not included in the overall statistics.

For three sources (APM 08279+5255, H1413+117 and IRAS F10214+4724) there is sufficient data in the mid-IR (MIR) to motivate fitting a two-temperature dust model. Table 2.3 shows the number of sources fitted with each combination of spectral parameters.

We have included posterior probability distributions of the MCMC output of the SED fit for three sources, to show the correlation between the various fitting parameters and highlight the effect of sparse sampling of the SED. Fig. 2.7 shows the result for APM 08279+5255, where there is sufficient data to fit seven spectral parameters. In Fig. 2.8, we compare the results for two sources: PSS J2322+1944, where the peak of the dust emission and the Rayleigh-Jeans slope are both well constrained, and Q 1208+101, where the peak is poorly constrained.

2.3.5. Physical properties

The dust temperature, FIR luminosity and SFR of 69 gravitationally-lensed AGN in our sample are listed in Table 2.7. We give both the results from the MCMC analysis and those from least-squares fitting. The values from the MCMC analysis are the median, 16th and 84th percentile of the posterior probability distributions. We give upper limits for the remaining 30 sources of the sample with insufficient detections, and the further 5 that appear to be synchrotron dominated. For clarification, a summary of median

Table 2.3 | Number of sources fitted with each set of spectral parameters. The number of upper limits are given in brackets. Five synchrotron-dominated sources (JVAS B0218+357, CLASS B1030+074, PMN J1632−0033, PKS 1830−211 and PMN J1838−3427) are fitted with single temperature modified black bodies to compute upper limits on contributions from any dust emission to their FIR spectra (for PKS 1830−211 this includes a synchrotron component). Of the sources with no temperature fitting, 30 sources have no detections and 10 have only one detection.

Spectral fit	Number of sources
Two $T_{\rm dust}$ + β + synchrotron	3
Single $T_{\rm dust}$ + β + synchrotron	8
Single $T_{\rm dust}$ + β	10
Single $T_{\rm dust}$ + synchrotron	5
Single $T_{\rm dust}$	33(5)
Fixed $T_{\rm dust}$	10(30)
Total	69(35)

values of various properties we derive and an explanation of the objects included in these statistics are given in Table 2.5.

A histogram of the dust temperatures derived directly from the modified black-body fits is shown in Fig. 2.6. Where a model with two dust components are fit, we include only the colder component here. We find a median of $T_{\rm d} = 38^{+12}_{-5}$ K for the 53 sources with fitted dust temperatures and known redshifts, 51 of which have dust temperatures < 60 K that, as we discuss in Section 2.4, can be reasonably attributed to be due to heating by star formation.

The FIR luminosity ($L_{\rm FIR}$) is derived for all sources with fitted modified black-body spectra by integrating the fitted modified black-body spectra between the rest-frame wavelengths 40 and 120 μm, using the definition of the FIR regime given by Helou et al. (1988), that is,

$$L_{\rm FIR} = \frac{4\pi D_L^2}{(1+z)} \int_{40\ \mu{\rm m}}^{120\ \mu{\rm m}} S_{\nu,{\rm rest}}\, d\nu, \tag{2.3}$$

where z is the redshift and D_L is the luminosity distance. We then extrapolate to the total infrared luminosity (8 to 1000 μm; rest-frame) using the colour correction factor of 1.91 given by Dale et al. (2001) (i.e. $L_{\rm IR} = 1.91\, L_{\rm FIR}$) to correct for the contribution from MIR spectral features. 8The methodology used to calculate the star formation

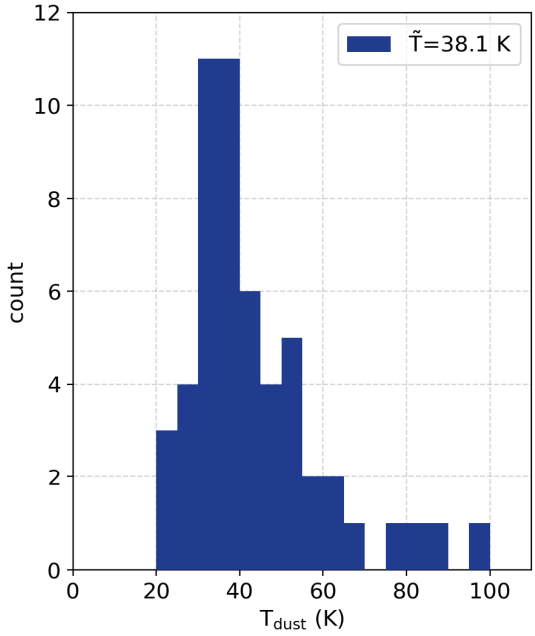

Figure 2.6 | Histogram of effective dust temperatures for 53 quasars in the sample with temperature fitting, excluding those without a known redshift and synchrotron-dominated sources. The median dust temperature is 38^{+12}_{-5} K. Where two dust temperatures are fit, only the colder component is included here.

rate (SFR) is that given by Kennicutt (1998), assuming a Salpeter initial mass function,

$$\mathrm{SFR}\,(\mathrm{M}_\odot\ \mathrm{yr}^{-1}) = \frac{L_{\mathrm{IR}}}{5.8 \times 10^9}, \tag{2.4}$$

where L_{IR} is in units of $\mathrm{L}_\odot$.

In Figs. 2.9 and 2.10, we show the FIR luminosity uncorrected for lensing magnification based on the fitted SED models as a function of redshift and dust temperature, respectively. Note that the dust temperature is invariant to the lensing magnification in the absence of strong differential magnification. The uncorrected luminosity as a function of redshift (Fig. 2.9) shows a clear trend in the data, from $\sim 10^{12}$ $\mathrm{L}_\odot$ at redshift 0.5–1 to $\sim 10^{13}$–10^{14} $\mathrm{L}_\odot$ at redshift 3–4.

We use the *bhkmethod* task in the STSDAS statistics package to compute the Kendall correlation test, taking into account the luminosity upper limits. The Kendall statistic τ quantifies the degree of correlation (from -1 for a strong anti-correlation, 0 for no correlation, to 1 for a strong positive correlation) and the significance of this is

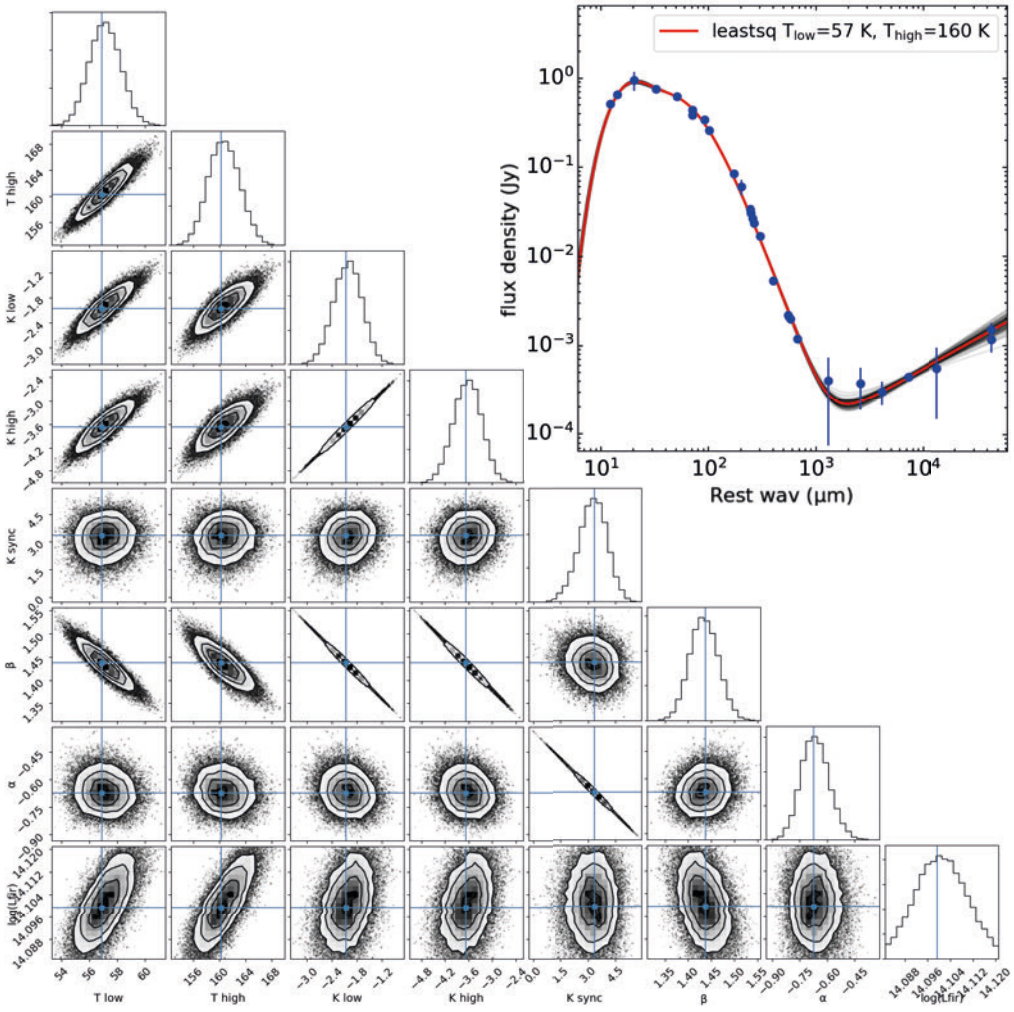

Figure 2.7 | Two-dimensional probability densities of the MCMC output for the SED fitting of APM 08279+5255, fit with all parameters: T1, low dust temperature (observed); T2, high dust temperature (observed); K1, K2, K3, log normalizations of the dust and synchrotron fits; β, the emissivity index; α, the synchrotron power-law index. Also shown is L_{FIR}. The blue points on the corner plot show the least-squares parameters. The SED is shown above, with 100 random samples of the MCMC in black and the least-squares model in red.

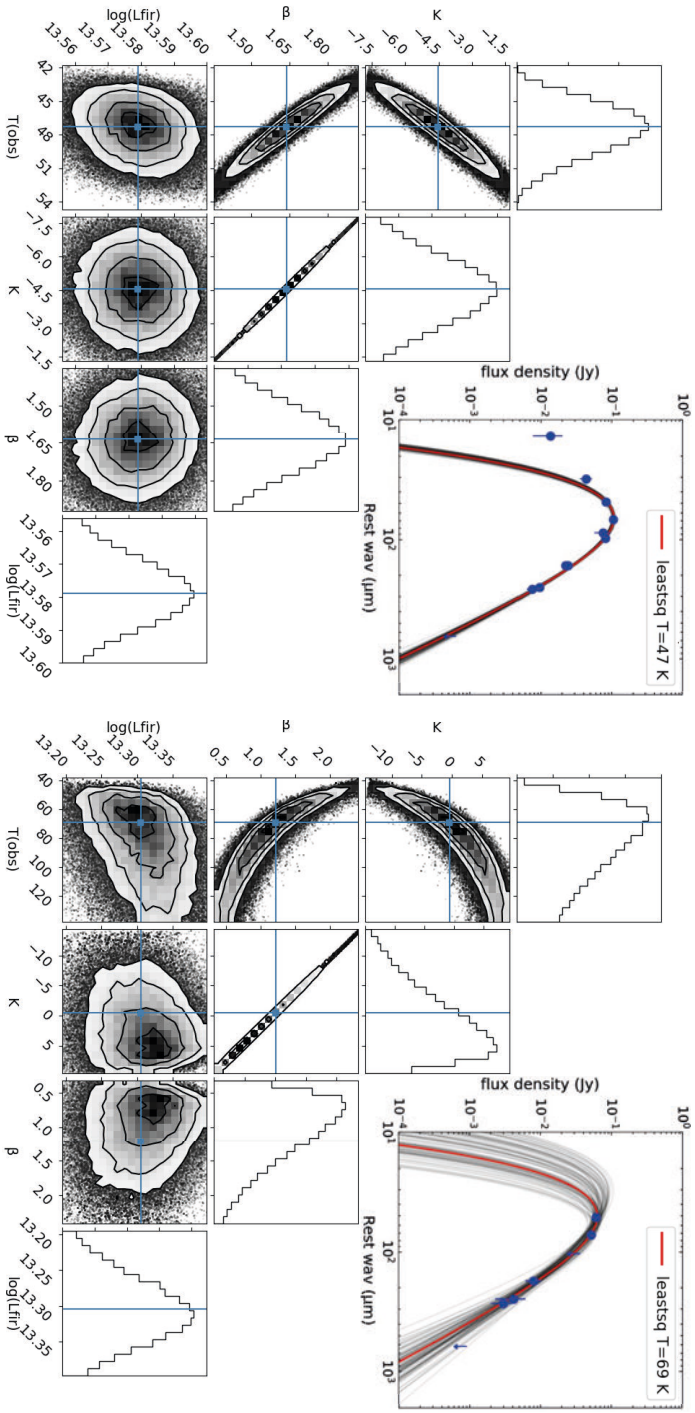

Figure 2.8 | Two-dimensional probability densities of the MCMC results of SED fitting for PSS J2322+1944 (left) and Q 1208+101 (right), showing the correlations between the spectral parameters: T, observed dust temperature; K, normalization; β, the emissivity index. Also shown is L_{FIR}. The blue points on the corner plots show the least-squares parameters. The SEDs are shown above the corner plots, with 100 random samples of the MCMC in black and the least-squares model in red.

given by the probability (p), for which < 0.05 we take as statistically-significant. Our data shows a correlation in temperature with redshift ($\tau = 0.64$, $p = 4 \times 10^{-4}$) and in temperature with $L_{\rm FIR}$ ($\tau = 0.77$, $p < 1 \times 10^{-4}$).

We find a large spread of $L_{\rm FIR}$, as is clear from Fig 2.10: the low luminosities are associated with low temperatures and low redshifts, and the high luminosities with high redshifts and generally higher dust temperatures. The 6 sources with measured luminosities $< 1.5 \times 10^{12}$ $L_\odot$ (corresponding to magnification-corrected SFRs < 50 $M_\odot$ yr^{-1}) are associated with dust temperatures < 25 K and/or redshifts $z < 1.5$. These trends can be explained by observational bias given the wavelength limits of the *Herschel*/SPIRE bands and the flux-limits of our observations, which approximately correspond to the luminosity detection limit shown in Fig. 2.9.

In Fig. 2.11, we present the dust emissivity as a function of dust temperature. We find a strong anti-correlation ($\tau = -1.30$, $p < 1 \times 10^{-4}$) between the parameters. This effect is expected for internally-heated dust clouds (Juvela & Ysard, 2012b). However, it is not clear to what extent this correlation is a reflection of the 'true' β–$T_{\rm d}$ relation, as the effect of source blending or observational noise may cause an artificial steepening of the anti-correlation, as noted by Juvela & Ysard (2012a). The shallow β values may be a result of fitting a composite of dust emission from star formation and AGN-heating with a single greybody, when multiple components are required (see HS 0810+2554, Section 2.C.1 in the Appendix). These problems further highlight the need for more multi-frequency data to better sample the SED and to reduce fitting errors due to observational noise.

2.4. Discussion

In this section, we investigate the global properties of the sample of gravitationally-lensed quasars and compare them with samples of unlensed FIR bright quasars and star-forming galaxies.

2.4.1. Comparison to DSFGs

We select the unlensed DSFGs observed with *Herschel*/SPIRE by Magnelli et al. (2012) (hereafter, M12) for comparison with our lensed quasar sample, after correcting for the magnifications (see Section 2.3.3). The M12 objects are canonical DSFGs selected in ground-based submillimetre surveys with no evidence of a strong AGN component. We select the 46 unlensed objects with known redshifts from the M12 sample, which

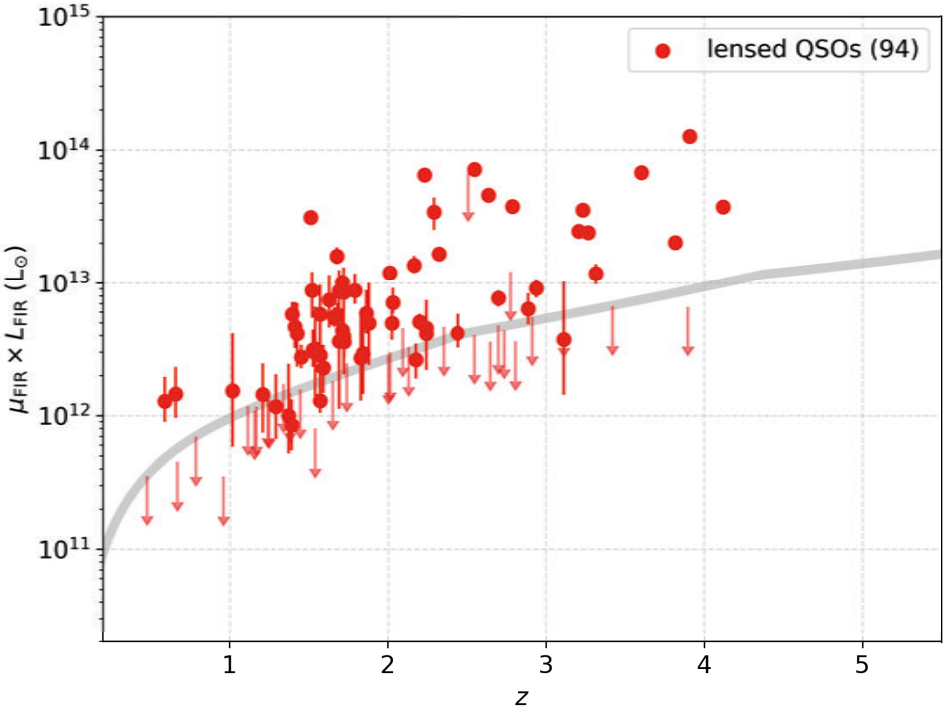

Figure 2.9 | FIR luminosity (40–120 μm) against redshift for the 94 objects in our sample with known redshift. This includes 53 with fitted dust temperatures, 10 with fixed dust temperatures, and 31 upper limits. The measured luminosities are shown in red, with no magnification correction. The grey line shows the estimated luminosity detection limit for a source with $T_d = 38$ K and $\beta = 1.5$, assuming a 3σ detection limit based on the mean RMS noise in each *Herschel*/SPIRE band. This is an overestimate at low redshift, as sources with lower dust temperatures will be preferentially detected, likewise, this is an overestimate at high-redshift where there will be bias towards higher temperature sources.

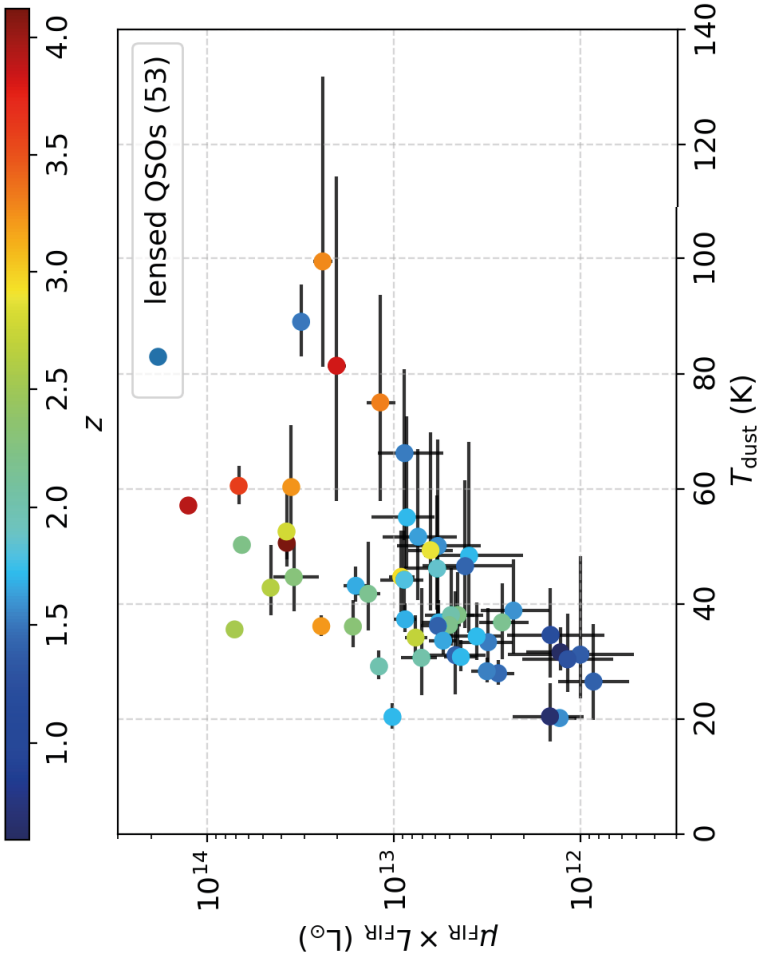

Figure 2.10 | FIR luminosity against fitted dust temperature for the 53 objects in our sample with fitted dust temperature and known redshift. The colour scale indicates source redshift. The luminosities are not corrected for lensing magnification.

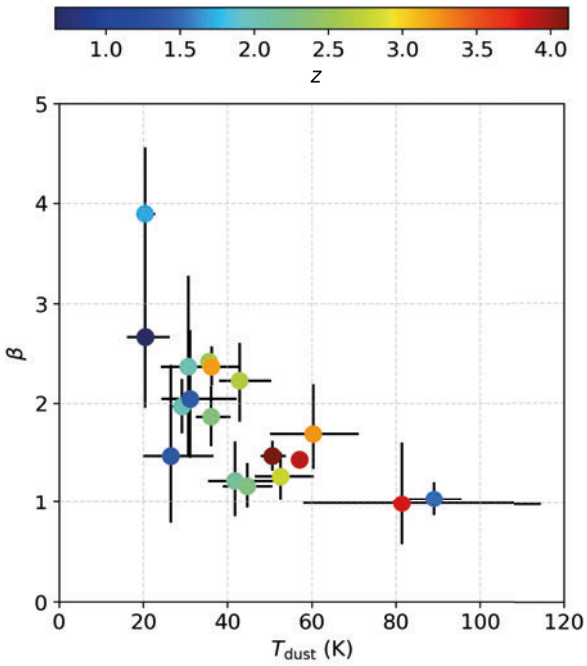

Figure 2.11 | β against effective dust temperature for 18 objects in our sample with fitted β and known redshift. The colour scale indicates source redshift.

have redshifts $2.2^{+0.5}_{-0.7}$, FIR luminosities of $5.4^{+3.1}_{-3.7} \times 10^{12}$ $L_\odot$ and star formation rates of 1800^{+1000}_{-1200} $M_\odot$ yr^{-1} (median, 25th and 75th percentiles). If the dust emission we detect is related to dust-obscured star formation, we expect dust temperatures comparable to DSFGs. Further to this, if DSFGs are antecedent to quasars, we would expect some fraction of our quasar sample to be FIR-luminous with star formation rates that are comparable to DSFGs.

We show in Figs. 2.12 and 2.13 the FIR luminosity against redshift and against dust temperature, respectively, for our sample and the M12 DSFGs. The median fitted dust temperature of our sample is 38^{+12}_{-5} K (ranges are the 25th and 75th percentiles) for 53 objects with sufficiently constrained SEDs and redshifts. This is consistent with the M12 DSFGs, which have a median temperature of 36^{+4}_{-9} K, typical of star-forming galaxies at $z \sim 2$.

We apply the Kaplan–Meier (K–M) method to estimate the underlying distribution of FIR luminosities, taking into account the upper limits, using the task *kmestimate* in the STSDAS statistics package. This method assumes a randomly censored distribution: while this seems counter-intuitive as we have a fixed flux-density limit, our redshift

range spans several orders of magnitude in luminosity distance so the sample is effectively randomly censored. We find a K–M estimated median, 25th and 75th percentiles of $3.6^{+4.8}_{-2.4} \times 10^{11}$ $L_\odot$ for the intrinsic luminosities for 94 objects with redshifts, including 63 detections and 31 upper limits, compared to $5.8^{+7.1}_{-2.7} \times 10^{11}$ $L_\odot$ for just the 63 objects with detected dust emission and known redshifts. The K–M estimated median of SFRs in our sample is 120^{+160}_{-80} $M_\odot$ yr^{-1}, with 190^{+230}_{-90} $M_\odot$ yr^{-1} for just the objects with detected dust emission.

The SEDs determined here clearly demonstrate that 69 objects (66 percent) of our sample show evidence for heated dust emission at FIR to sub-mm wavelengths (these SEDs are shown in Fig. 2.16 of the Appendix). Also, given the similar dust temperatures of our lensed quasar sample and the DSFGs studied by M12, there is at least circumstantial evidence that this dust heating is due to star formation activity. Approximately 10 percent of the sample have extreme star-formation rates > 1000 $M_\odot$ yr^{-1} comparable to typical, unlensed DSFGs at $z \sim 2$–4 detected in *Herschel*/SPIRE. The SFRs of these lensed quasars are consistent with sources that are transitioning from DSFGs to UV-bright quasars according to the Sanders et al. evolutionary model. The rest of the detected sample have still extreme SFRs similar to the lower luminosity DSFGs selected at $z < 1.5$, but there is no clear cut-off at low SFR. The range of SFRs we find (< 20–10000 $M_\odot$ yr^{-1}) is consistent with sources at different stages of evolution, and is not too surprising given the heterogeneous nature of our sample. Nevertheless, the high detection rate in the *Herschel*/SPIRE bands implies that most quasars are FIR-luminous sources with a strong coexistence of extreme dust-obscured star formation and AGN activity. This result implies a transition time from quasar-starburst to unobscured, gas-poor system of the order of the lifetime of the quasar (i.e. $\lesssim 100$ Myr), rather than much shorter timescales of ~ 1 Myr, as has been suggested (Simpson et al., 2012). Further studies, including spectral line data of the molecular gas in these systems, are required to understand anything of the gas reservoirs and depletion times, or make any conclusions regarding possible implications for AGN and stellar feedback.

2.4.2. Comparison by radio properties

Using the two-sample K–S test (described in Section 2.3.1) we compare the derived $L_{\rm FIR}$ distributions of the jetted subsample with the remaining quasars in the sample. We do not correct for the lensing magnification here to prevent any bias due to our assumptions about the magnification factor of the heated dust. Including all measured luminosities and upper limits (excluding those without redshifts), the test returns a probability of 0.23 that these subsamples are drawn from the same underlying distribution. The K–M estimated median, 25th and 75th percentiles of the FIR luminosity is

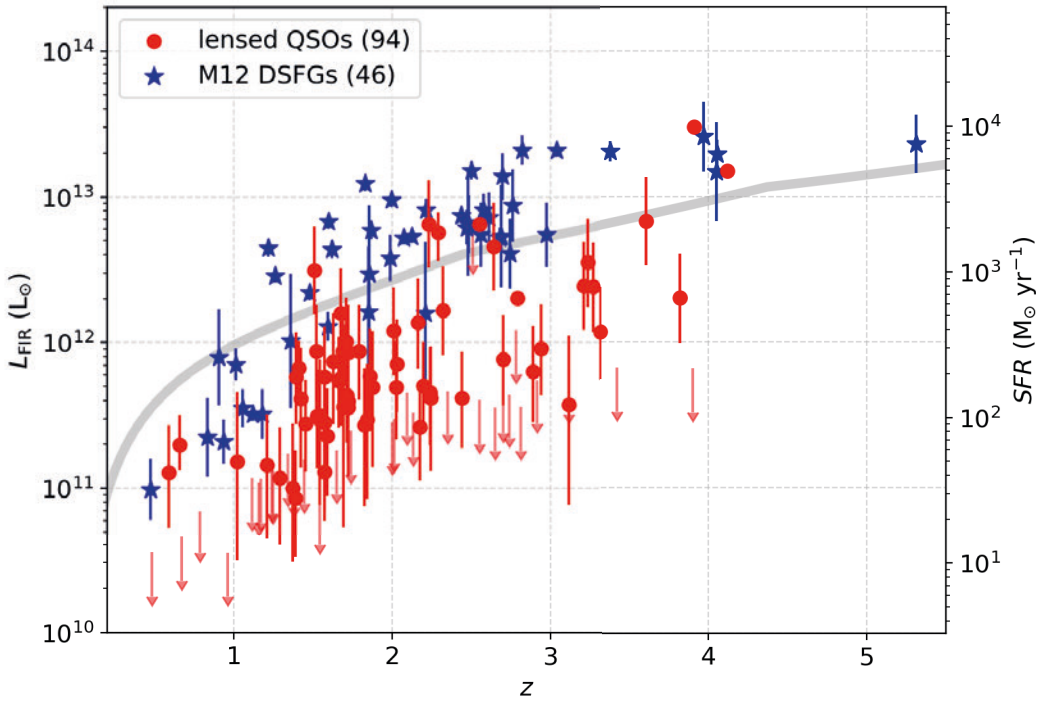

Figure 2.12 | FIR luminosity (40–120 μm) and equivalent SFR against redshift for lensed quasars in this sample (94 objects, excluding those without known redshifts) and for the M12 DSFGs (46 objects). The quasar luminosities are magnification-corrected (see Section 2.3.3). Magnification factors for seven sources are given in Table 2.2. Where the magnification factor is unknown, a we assume a value of 10^{+10}_{-5}. The grey line shows the luminosity detection limit for a source with $T_{\rm d} = 38$ K and $\beta = 1.5$, assuming a 3σ detection limit.

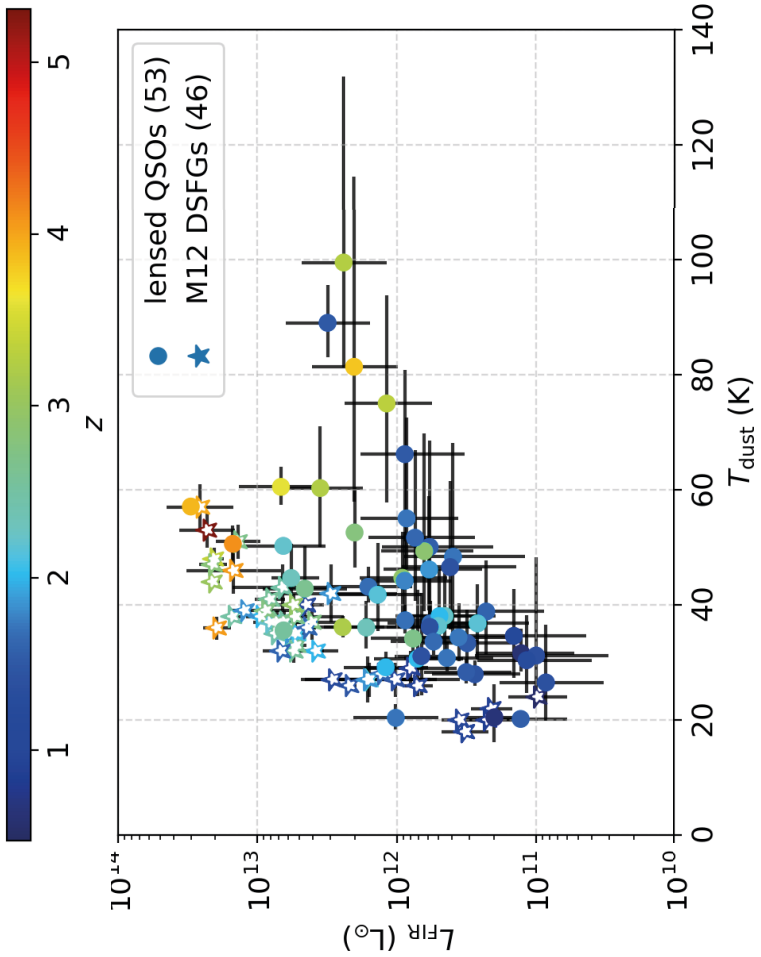

Figure 2.13 | FIR luminosity against dust temperature for our lensed quasar sample (53 objects, with fitted dust temperature and known redshift) and for the M12 DSFGs (46 objects). Quasar luminosities are magnification-corrected (see Section 2.3.3). The colour scale indicates source redshift.

Table 2.4 | Kaplan–Meier (K–M) estimated 50th, 25th and 75th percentile ranges of the FIR luminosity distributions of the jetted and non-jetted subsamples. This includes the 92 objects in our sample with radio measurements and known redshifts. We give the number of values, N, and in brackets the number of upper limits. We also give the results when the subsamples are selected by $q_{\rm IR}$ value, and the K–S test probability that these samples are drawn from the same underlying distribution.

		N(lims)	K–M $L_{\rm FIR}$ (10^{12} $L_\odot$)	K–S test
uncorrected	jetted	15(10)	$1.6^{+10}_{-1.5}$	0.23
	non-jetted	48(19)	$3.7^{+3.5}_{-2.4}$	
corrected	jetted	19(17)	$1.3^{+7.8}_{-1.3}$	0.06
	non-jetted	43(13)	$4.1^{+3.3}_{-1.4}$	

$1.6^{+10}_{-1.5}\times10^{12}$ $L_\odot$ for the jetted subsample and $3.7^{+3.5}_{-2.4}\times10^{12}$ $L_\odot$ for the remaining quasars. While the jetted subsample has a larger distribution of luminosities, the test suggests that the difference in the luminosity distributions is not statistically-significant.

A combination of systematic biases and the smaller size of the jetted subsample may affect our findings. We note that quasars with radio jets tend to be hosted in more massive galaxies (Mandelbaum et al., 2009), thus our jetted subsample may be biased towards larger FIR luminosities and hence larger SFRs. At present, we do not have data to account for the stellar mass of the galaxies in our sample.

The median, 25th and 75th percentiles of the redshifts are $1.7^{+0.9}_{-0.3}$ for the jetted subsample and $1.8^{+0.6}_{-0.3}$ for the non-jetted. Despite the fact that the sample selection between these groups is different, with the jetted quasars generally selected in the radio by source properties and the non-jetted objects typically selected by lens population, the redshift distributions of the two groups are similar and therefore not a substantial source of systematic bias.

Our result is consistent with the conclusions of Barvainis & Ivison (2002) who found no statistically-significant difference in 850 μm luminosity between their samples of quasars and radio galaxies. Other studies have found no significant differences in the star-forming properties of quasars by radio mode. Harris et al. (2016) analysed a sample of optically-luminous quasars at redshifts between 2 and 3 through stacking, of which 95 percent are undetected individually with *Herschel*/SPIRE. They find a mean SFR of 300 ± 100 $M_\odot$ yr^{-1}, consistent with our overall result, but find no correlation with black hole accretion. A recent study by Pitchford et al. (2016) of higher luminosity quasars with *Herschel*/SPIRE also find no relation between AGN accretion/outflows and the FIR properties of their host galaxies. Alternatively, Kalfountzou et al. (2014)

studied a stacked sample of quasars and do find a positive correlation between jet activity and FIR luminosity for jetted quasars, defined by a 5 GHz/4000 Å ratio >10. However, they find average SFRs to be comparable for jetted and non-jetted quasars, except at low optical luminosities.

Overall, our results do not point towards there being an enhancement in the FIR luminosity of jetted quasars and radio galaxies, relative to the non-jetted quasars in our sample. However, a more complete understanding of this result, particularly given the contradictory studies discussed above, will require detailed observations of individual objects. In this respect, our investigation of lensed quasars from within our sample will again be important since it will allow the radio-jets, (stellar) host galaxy and the heated dust to be mapped on small angular-scales.

2.4.3. Radio–infrared correlation

The radio–infrared luminosity correlation for star-forming galaxies has been well established for several decades. The relation is described by the parameter $q_{\rm IR}$, the ratio between the total infrared luminosity (8 to 1000 μm; rest-frame) and the 1.4 GHz rest-frame luminosity, defined by Condon et al. (1991) as,

$$q_{\rm IR} = \log_{10}\left(\frac{L_{\rm IR}}{3.75\times10^{12}\ L_{1.4\ \rm GHz}}\right). \tag{2.5}$$

We explore the radio–infrared correlation for our sample to evaluate the contributions from star formation to the radio and FIR emission; for example, those sources above the correlation would have an excess of non-thermal synchrotron emission and those below the correlation would have an excess of thermal dust emission in the FIR, both of which could be related to the presence of a significant AGN contribution to the respective wavelength regimes (Sopp & Alexander, 1991). Ivison et al. (2010) find $q_{\rm IR} = 2.40 \pm 0.24$ for a flux-limited sample of sources selected from *Herschel*/SPIRE at 250 μm with VLA flux-densities at 1.4 GHz. We plot the rest-frame radio and IR-luminosity for the sample in Fig. 2.14 and the median $q_{\rm IR}$ from Ivison et al. for reference. We interpolate or extrapolate to the rest-frame 1.4 GHz (depending on the low-frequency data available) by fitting the radio SEDs with a power-law, as given by equation (2.1). A spectral index of $\alpha = -0.70 \pm 0.14$ is assumed for those objects with a single radio measurement, which is typically at 1.4 GHz from NVSS or FIRST. As above, we do not account for magnification to prevent bias due to our assumptions about the magnification factor of the dust emission. The $q_{\rm IR}$ values for the radio-detected quasars are shown in Fig. 2.15.

We find that almost all of the jetted quasars lie significantly above the radio–infrared correlation for star-forming galaxies, by up to 3 to 4 orders of magnitude in rest-frame 1.4 GHz luminosity, and thus have $q_{\rm IR}$ values below that obtained by Ivison et al. (2010). This is to be expected as these are all powerful radio sources that are known to be dominated by synchrotron emission associated with AGN activity; the core and jet components of many sources are well studied as part of the CLASS, MG and PMN gravitational lens surveys. We note that the average magnification factors of jetted radio sources will likely be higher than that of the dust, as the radio emission comes from a more compact region, although how much higher will be dependent on where the radio source lies relative to the lens and the lensing caustics. In such cases, the inferred $q_{\rm IR}$ values may be lower if the radio component is boosted relative to the dust heated by star formation. However, we do not expect this to alter our conclusions as the effect will only be significant for sources with extremely compact radio emission associated with jets and, in almost all cases, this will not produce the several orders of magnitude difference needed to account for the offset from the correlation seen in Fig. 2.15.

Quasars whose radio emission is associated with star formation are not expected to have significantly different magnifications between the radio and FIR, and so should remain close to the radio–infrared correlation for star-forming galaxies. Only 19 quasars in our sample classified as non-jetted have radio detections, of which only 2 are confirmed to have radio emission that is dominated by star formation (IRAS F10214+5255 and RX J1131−1231), the rest are currently undetermined. We observe a scatter around the radio–infrared relation for the non-jetted quasars. The scatter above the Ivison et al. relation may be due to contributions to their radio emission from low-power radio jets, or possibly additional radio emission from the foreground lensing galaxy. As the radio components of these sources have not yet been observed at a high enough angular resolution, it is not clear whether the apparent radio power dichotomy represents a true bi-modality in emission mechanism.

Recent studies point towards synchrotron emission from star formation as the dominant source of radio emission in non-jetted quasars (Padovani, 2016, for review). However, evidence of a milliarcsecond-scale jet in the classically radio-'quiet' lensed quasar HS 0810+2554 (part of our sample) suggests that it is not correct to assume that star formation is the primary radio emission mechanism in all cases (Hartley et al. in prep). There may be a composite of emission processes, or a further sub-population of quasars with low-power radio jets. Most of the detected radio-'quiet' quasars in our sample have $q_{\rm IR}$ values around the Ivison et al. relation, within the expected scatter. Deeper, higher spatial resolution observations of these sources are required to determine whether they hold to the relation, indicating whether the radio and FIR emission are indeed dominated by star formation. The radio upper limits in Fig. 2.14,

due to non-detections in FIRST and NVSS, indicate that this population of quasars would be found in the ~ μJy regime as proposed by White et al. (2007), if star formation dominates.

We add eleven of the non-jetted quasars with radio detections more than 2σ above the radio–infrared correlation to our jetted subsample to refine our subsamples[‡‡], under the assumption that the radio excess is due to AGN activity within the background object and not from the foreground lensing galaxy.

We again perform the K–S test on the FIR luminosity distribution of the samples with measured $L_{\rm FIR}$ and radio emission, as before, and find the probability that they are drawn from the same sample decreases from 0.23 to 0.06, but is still not statistically-significant. The K–M-estimated median is higher for the objects which do not have a radio excess: $1.3^{+7.8}_{-1.2} \times 10^{12}$ L$_\odot$ for the new jetted subsample and $4.1^{+3.3}_{-1.4} \times 10^{12}$ L$_\odot$ for the remaining sources (as above, the uncertainties are at the 25th and 75th percentiles). It is possible that different FIR properties are simply caused by the small number of detections in the jetted subsample.

Notably, HS 0810+2554 lies below the radio–infrared relation with a $q_{\rm IR}$ value of 2.90 despite having radio jets that dominate its radio emission. In Section 2.C.1 of the Appendix we explore the possibility that this is caused by fitting a single temperature dust model to a composite of AGN and star-formation-heated dust. It is possible this is also the case for another 7 sources with larger fitted dust temperatures ($T_{\rm d} > 60$ K) that appear to be outliers from the bulk of the sample (see Fig. 2.13) and would explain some of the observed anti-correlation between β and $T_{\rm d}$ (as shown in Fig. 2.11). Interestingly, when we apply a two-temperature model to HS 0810+2554 (described in Section 2.C.1), the corrected $q_{\rm IR}$ lies within the 2σ range of the radio–infrared correlation amidst the non-jetted sources. This suggests that the correlation may not be a reliable method of isolating jet-dominated quasars in the case of radio-weak AGN. If indeed quasars with radio jets are misidentified as non-jetted, this may cause or mask differences in the FIR properties between the subsamples.

The fact that no sources lie below the expected $q_{\rm IR}$ range in Fig. 2.14 implies that we do not significantly overestimate the FIR luminosity due to an additional un-modelled AGN component in the dust emission, with the exception of HS 0810+2554. We note that APM 08279+5255, which has the most well defined SED and is fitted here with a two-temperature dust model, falls exactly on the radio–infrared correlation with a $q_{\rm IR}$ value of 2.40. Therefore, with sufficient data in the MIR and sub-mm it will be possible to better isolate the star-forming contribution to the SEDs. However, the radio and FIR luminosities derived for our current *Herschel*/SPIRE dataset, like in the case

[‡‡]We exclude WFI 2026−4536 and WFI 2033−4723 in our radio–infrared correlation analysis as there are no radio data for these sources.

of the fitted dust temperatures, appear to be consistent with star formation being the dominant mechanism for heating the dust.

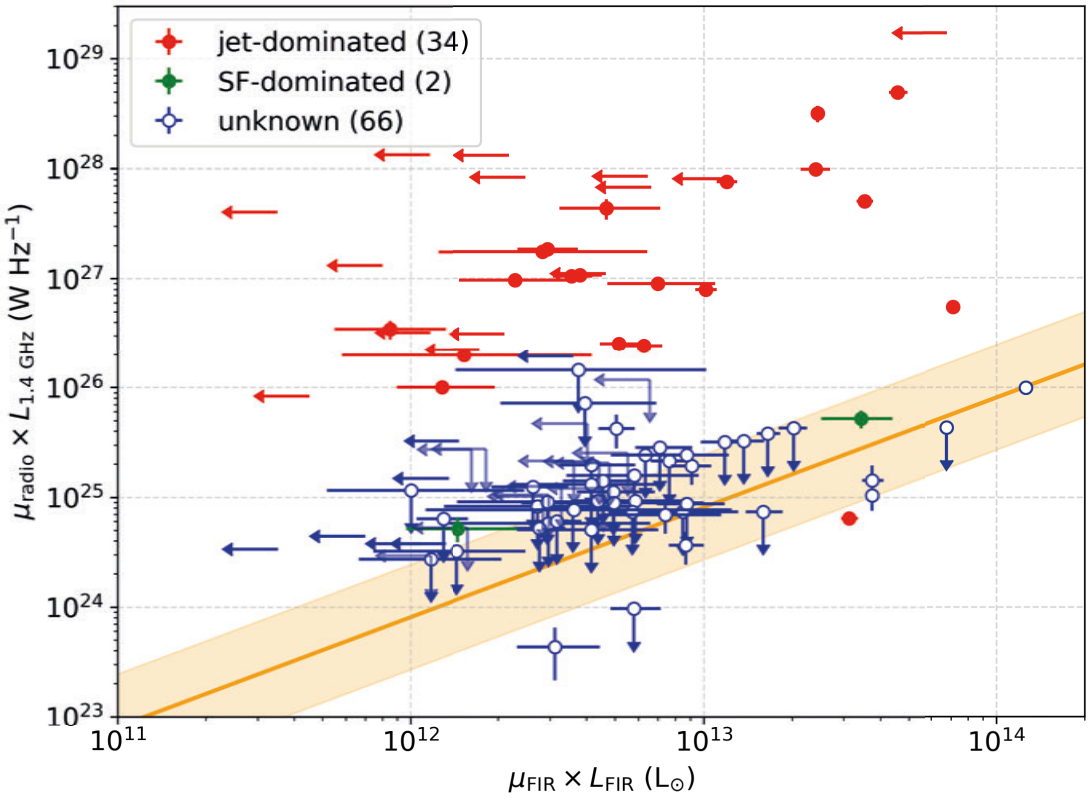

Figure 2.14 | The radio–infrared correlation for 102 quasars in our sample, excluding WFI J2026−4536 and WFI J2033−4723 for which there are no radio data available. The median $q_{\rm IR}$ for star-forming galaxies from Ivison et al. (2010) is shown in yellow; the shaded region is $2\sigma_{\rm qIR}$.

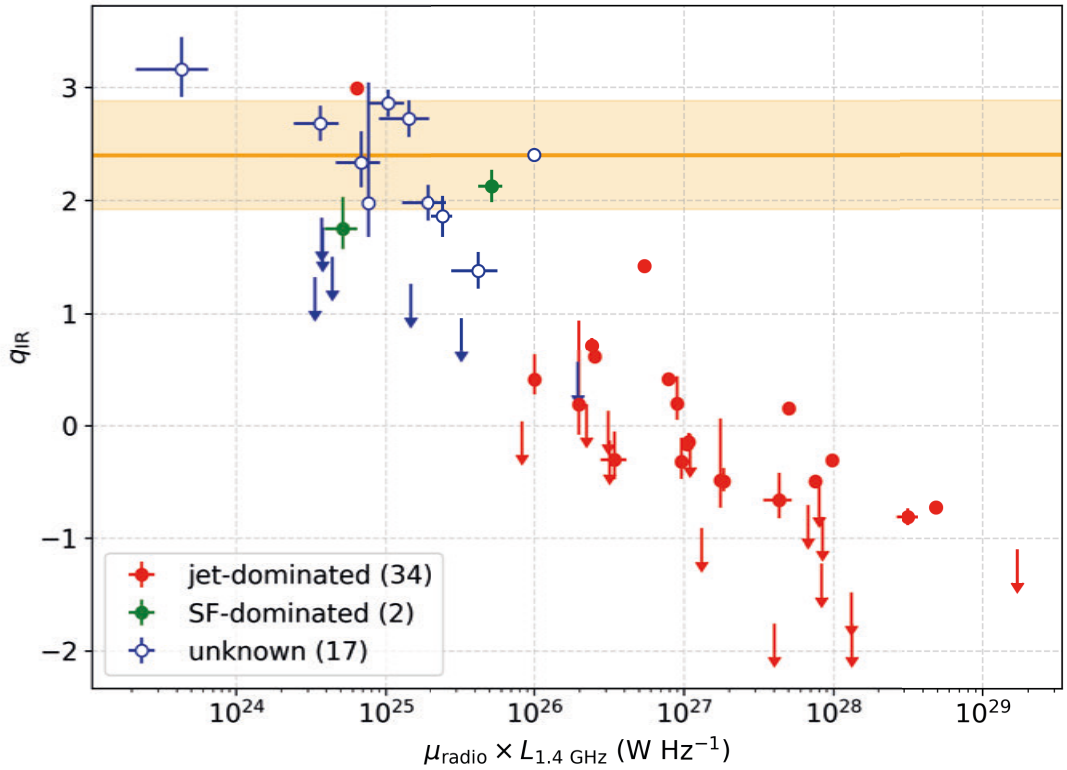

Figure 2.15 | The radio–infrared factor, q_{IR}, for 53 quasars in the sample with radio detections. The median q_{IR} for star-forming galaxies from Ivison et al. (2010) is shown in yellow; the shaded region is $2\sigma_{qIR}$.

Table 2.5 | A summary of the objects used for our statistics. We give the median, 25th and 75th percentiles of certain properties, the number of measurements (N) this includes (number of limits, in brackets, where included), relevant figures within the chapter, and an explanation of which objects are included in the selection. We give magnification-corrected luminosities here, but the selection is the same for the uncorrected luminosities and SFRs.

Property	Median	N(lims)	Fig.	Comment
z	$1.8^{+0.7}_{-0.3}$	94	2.1	Objects with known redshift.
$T_{\rm dust}$	38^{+12}_{-5} K	53	2.6,2.10	Objects with known redshift, and dust temperature fitted as a free parameter in the SED.
β	$2.0^{+0.4}_{-0.5}$	21	2.11	Objects with β fitted as a free parameter in the SED. 18 of these have known redshift.
$L_{\rm FIR}$	$3.6^{+4.8}_{-2.4} \times 10^{11}$ L$_\odot$	63(31)	2.9,2.12	Objects with known redshifts, of which 63 have measured dust emission and 31 have upper limits.

2.5. Conclusions

According to the current paradigm of galaxy evolution, some fraction of the quasar population is expected to be transitional sources from DSFGs to UV-luminous quasars. These transition sources will be FIR-luminous, with clear evidence of ongoing star formation. However, only a handful of extremely FIR-luminous sources have been studied thus far due to the limitations in observational sensitivity, and then at wavelengths relatively insensitive to $T_{\rm d}$ and $L_{\rm FIR}$. In order to study the link between DSFGs and quasars, we observed 104 gravitationally-lensed quasars with the *Herschel*/SPIRE instrument at 250, 350 and 500 μm to determine the fraction that are FIR-luminous. Due to the magnification effects of gravitational lensing, we are able to measure the star-forming properties of individual quasars at lower intrinsic luminosities than those previously studied and thus more representative of the quasar population. We find most sources in our sample have magnification-corrected FIR luminosities below the estimated detection limit, a factor of 10 lower on average.

From our study, we detected 72 (69 percent) of the gravitationally-lensed quasars in at least one band with *Herschel*/SPIRE, and find evidence for heated dust emission in 69 (66 percent) of the objects given the shape of their SEDs. By fitting modified black bodies to our new measurements and to data in the literature, we derive a median $\mu_{\rm FIR} \times L_{\rm FIR}$ of $3.6^{+4.7}_{-2.4} \times 10^{12}$ $L_\odot$ and an implied magnification-corrected $L_{\rm FIR}$ of $3.6^{+4.8}_{-2.4} \times 10^{11}$ $L_\odot$ and SFR of 120^{+160}_{-80} $M_\odot$ yr^{-1} for 94 objects with redshifts, under the assumption that for the vast majority of the targets the FIR magnification is $\mu_{\rm FIR} = 10^{+10}_{-5}$. The range of fitted dust temperatures of the sample is 38^{+12}_{-5} K for 53 objects with redshifts and sufficiently constrained SEDs to fit for the dust temperature, which is characteristic of ongoing dust obscured star formation. We compare our sample of gravitationally-lensed quasars to a sample of DSFGs observed with *Herschel*/SPIRE at similar redshifts and find similar dust temperatures, which gives circumstantial evidence of star formation being the dominant mechanism for heating the dust. We find ∼ 10 percent have similar SFRs to DSFGs, suggestive of sources transitioning from DSFGs to UV-luminous quasar, and a large range of SFRs < 20–10000 $M_\odot$ yr^{-1}.

Finally, using the radio–infrared correlation for star-forming galaxies, we find that the jetted quasars, selected by measured jet emission based on high resolution radio data, show an excess of radio luminosity by of up to 4 orders of magnitude. Non-jetted quasars lie close to the correlation expected for star-forming galaxies, however, the scatter above the correlation suggests at least some of these sources have contributions to their radio emission from AGN activity. We do not find evidence for an excess of FIR emission in the sample, given their radio luminosities, which again supports the view that the dust heating is dominated by star formation.

We find no significant difference in the $L_{\rm FIR}$ distribution of our jetted and non-jetted

subsamples. Non-jetted quasars are three times as luminous on average when we select jetted sources by their radio excess relative to the radio–infrared correlation, however the difference is not statistically-significant. We caution that further data are required to eliminate the possibility of a systematic bias due to stellar mass or small sample sizes. Radio investigations are also required to identify the radio emission mechanism (and hence AGN feedback mechanisms) associated with non-jetted quasars, as our results suggest that the radio–infrared correlation may not be sufficient to identify sources with jet-dominated radio emission.

Our results reveal a strong co-existence of AGN activity and host galaxy star formation in quasars, as proposed in the Sanders et al. model. We find that this is true for the majority of quasars, suggesting that the FIR-luminous quasar phase is not distinct from the unobscured quasar phase and there is no sharp transition between them. However, our analysis is limited by the available observational data, which prevents us from making definitive statements about the implications for AGN and stellar feedback models. More photometric data points in the mm and sub-mm are needed to reduce the errors and assumptions in SED fitting, and thus the derived host galaxy properties. With additional MIR data, we can fit the AGN contribution to the dust heating and derive better constraints on the SFR for these sources. Much progress can also be made with the advent of ALMA, where the extent of the heated dust emission can be mapped on 50–500 mas-scales, which given the magnifications provided by the gravitational lenses, will also allow structures < 50 pc in size to be resolved. In addition, through high resolution imaging of the mm-emission from these sources, it will also be possible to determine robust wavelength-dependent magnifications from lens modelling, which will further reduce the uncertainties in our analysis for individual objects.

Acknowledgements

We thank the anonymous referee who helped improve the clarity of the paper on which this chapter is based. HRS would like to thank Kristen Coppin, Alison Kirkpatrick, Leon Koopmans and Simona Vegetti for helpful discussions. NCR acknowledges support from the ASTRON/JIVE Summer Student Programme. RJI acknowledges support from ERC in the form of the Advanced Investigator Programme, 321302, COSMICISM. DRGS thanks for funding through Fondecyt regular (project code 1161247), through the 'Concurso Proyectos Internacionales de Investigación, Convocatoria 2015' (project code PII20150171), through ALMA-Conicyt (project code 31160001) and the BASAL Centro de Astrofísica y Tecnologías Afines (CATA) PFB-06/2007.

Herschel is an ESA space observatory with science instruments provided by European-led Principal Investigator consortia and with important participation from NASA. *Herschel* /SPIRE has been developed by a consortium of institutes led by Cardiff University (UK) and including Univ. Lethbridge (Canada); NAOC (China); CEA, LAM (France); IFSI, Univ. Padua (Italy); IAC (Spain); Stockholm Observatory (Sweden); Imperial College London, RAL, UCL-MSSL, UKATC, Univ. Sussex (UK); and Caltech, JPL, NHSC, Univ. Colorado (USA). This development has been supported by national funding agencies: CSA (Canada); NAOC (China); CEA, CNES, CNRS (France); ASI (Italy); MCINN (Spain); SNSB (Sweden); STFC, UKSA (UK); and NASA (USA). HIPE is a joint development (are joint developments) by the Herschel Science Ground Segment Consortium, consisting of ESA, the NASA Herschel Science Center, and the HIFI, PACS and SPIRE consortia.

This research has made use of the NASA/ IPAC Infrared Science Archive, which is operated by the Jet Propulsion Laboratory, California Institute of Technology, under contract with the National Aeronautics and Space Administration.

IRAF is distributed by the National Optical Astronomy Observatory, which is operated by the Association of Universities for Research in Astronomy (AURA) under co-operative agreement with the National Science Foundation. STSDAS is a product of the Space Telescope Science Institute, which is operated by AURA for NASA.

2.A. Source tables

Table 2.6 | *Herschel*/SPIRE measurements of the lensed quasar sample. We give the lens name, whether the object is jetted (J) or non-jetted (N), the maximum separation of the lensed images ($\Delta\theta$), the source redshift (z_s), the measured flux-densities at 250, 350, and 500 μm (in mJy), and in brackets, the uncertainty from the source extraction. We comment on notable features of the lens system or with a † denote any issues with the flux-density measurements not discussed in Section 2.2.4. Redshifts and image separations are from the CASTLES catalogue (Kochanek et al., 1999), unless another reference is given.

Lens Name	Type	$\Delta\theta$ (")	z_s	$S_{250\ \mu m}$	$S_{350\ \mu m}$	$S_{500\ \mu m}$	Comments	References
HE 0047−1756	N	1.44	1.676	197(9)	130(8)	60(9)		
CLASS B0128+437	J	0.55	3.114	< 33	< 33	< 36		
Q J0158−4325	N	1.22	1.29	39(9)	38(8)	< 27		
JVAS B0218+357	J	0.34	0.96	89(7)	122(7)	120(8)		
HE 0230−2130	N	2.05	2.162	126(9)	109(8)	77(9)		
SDSS J0246−0825	N	1.19	1.68	88(7)	75(7)	30(8)		
CFRS 03.1077	N	2.1	2.941	43(7)	44(7)	< 37		
MG J0414+0534	J	2.4	2.64	266(7)	190(8)	112(10)		
HE 0435−1223	N	2.42	1.689	133(7)	101(7)	53(9)		
CLASS B0445+123	J	1.35	–	< 38	< 50	< 42		
HE 0512−3329	N	0.65	1.57	60(7)	39(9)	< 32		
CLASS B0631+519	J	1.16	–	63(12)	82(7)	71(12)		
CLASS B0712+472	J	1.46	1.34	< 33	< 28	< 36		
CLASS B0739+366	J	0.53	–	69(6)	61(10)	< 40		
SDSS J0746+4403	N	1.11	2.0	< 30	< 27	< 27		Inada et al. (2007)
MG J0751+2716	J	0.7	3.21	102(4)	105(3)	78(4)		
SDSS J0806+2006	N	1.4	1.54	40(9)	< 21	< 26		Inada et al. (2006)
HS 0810+2554	N	0.96	1.5	186(9)	98(8)	53(10)†	†Possible blending	
HS 0818+1227	N	2.83	3.115	< 30	< 28	< 30		
SDSS J0819+5356	N	4.04	2.239	40(9)	40(8)	< 40		Inada et al. (2009)
SDSS J0820+0812	N	2.2	2.024	49(9)	54(8)	< 32		Jackson et al. (2009)
APM 08279+5255	N	0.38	3.91	621(3)	437(3)	259(4)		Downes et al. (1999)

Table 2.6 | (continued)

Lens Name	Type	$\Delta\theta$ (")	z_s	$S_{250\ \mu m}$	$S_{350\ \mu m}$	$S_{500\ \mu m}$	Comments	References
SDSS J0832+0404	N	1.98	1.116	< 30	< 30	< 32		Oguri et al. (2008a)
CLASS B0850+054	J	0.68	–	57(9)	45(7)	< 32		
SDSS J0903+5028	N	2.99	3.605	227(11)	182(8)	< 50		Johnston et al. (2003)
SDSS J0904+1512	N	1.13	1.826	27(7)	< 30	< 47		Kayo et al. (2010)
SBS J0909+523	J	1.17	1.38	< 27	< 30	< 47		
RX J0911+0551	N	2.47	2.79	181(11)	176(9)	97(9)		
RX J0921+4529	N	6.97	1.65	< 26	< 30	< 30		
SDSS J0924+0219	N	1.75	1.524	67(8)	56(8)	32(10)		Inada et al. (2003)
FBQS J0951+2635	J	1.11	1.24	< 30	< 30	< 41		
Q 0957+561	J	6.26	1.41	108(10)	81(7)	< 30		
SDSS J1001+5027	N	2.82	1.84	30(9)	< 27	< 30		
SDSS J1004+1229	J	1.54	2.65	< 26	< 26	< 41		
LBQS J1009−0252	N	1.54	2.74	< 25	< 27	< 27		
SDSS J1011+0143	N	3.67	2.701	< 28	< 30	< 40		
Q 1017−207	N	0.85	2.55	< 27	< 30	< 40		
SDSS J1021+4913	N	1.14	1.72	38(9)	28(8)	< 30		
IRAS F10214+4724	J	1.59	2.29	416(5)	303(4)	169(4)		
SDSS J1029+2623	N	22.5	2.197	49(5)	47(6)	30(5)		
JVAS B1030+074	J	1.65	1.54	35(6)	44(9)	63(11)		
SDSS J1054+2733	N	1.27	1.452	88(9)	84(8)	55(9)		Kayo et al. (2010)
SDSS J1055+4628	N	1.15	1.249	< 28	< 30	< 33		Kayo et al. (2010)
HE 1104−1805	N	3.19	2.32	139(7)	122(7)	88(10)		
PG 1115+080	N	2.32	1.72	69(17)	40(7)	< 39		
CLASS B1127+385	J	0.74	–	90(9)	105(7)	56(10)		
RX J1131−1231	N	3.8	0.658	285(7)	166(8)	62(9)		
MG J1131+0456	J	2.1	–	< 25	< 32	< 32		
SDSS J1131+1915	N	1.46	2.915	< 28	< 30	< 30		Kayo et al. (2010)
SDSS J1138+0314	N	1.34	2.44	33(7)	< 27	< 38		
SDSS J1155+6346	N	1.95	2.89	29(7)	30(6)	< 30		

Table 2.6 | (continued)

Lens Name	Type	$\Delta\theta$ (")	z_s	$S_{250\ \mu m}$	$S_{350\ \mu m}$	$S_{500\ \mu m}$	Comments	References
CLASS B1152+200	J	1.59	1.019	37(10)	< 30	< 32		
SDSS J1206+4332	N	2.9	1.79	95(7)	70(8)	< 31		
Q 1208+101	N	0.48	3.82	61(9)	52(7)	< 36		
SDSS J1216+3529	N	1.49	2.013	< 32	< 32	< 30		Oguri et al. (2008a)
HST 12531−2914	N	1.23	–	< 28	< 26	< 32		
SDSS J1258+1657	N	1.28	2.702	46(7)	54(8)	60(13)		Inada et al. (2009)
SDSS J1304+2001	N	1.87	2.175	27(6)	26(7)	< 30		Kayo et al. (2010)
SDSS J1313+5151	N	1.24	1.877	49(6)	< 30	< 36		Ofek et al. (2007)
SDSS J1322+1052	N	2.0	1.711	87(10)	79(7)	57(9)		Oguri et al. (2008a)
SDSS J1330+1810	N	1.76	1.393	126(7)	91(7)	36(11)		Oguri et al. (2008b)
SDSS J1332+0347	N	1.14	1.445	< 27	< 30	< 32		
LBQS J1333+0113	N	1.63	1.57	90(9)	80(7)	55(10)		
SDSS J1339+1310	N	1.69	2.241	27(8)	< 30	< 32		Inada et al. (2009)
SDSS J1349+1227	N	3.0	1.722	59(8)	52(8)	32(9)		Kayo et al. (2010)
SDSS J1353+1138	N	1.41	1.629	69(9)	43(7)	< 30		
Q 1355−2257	N	1.23	1.37	28(7)	30(8)	< 32		
CLASS B1359+154	J	1.71	3.235	139(7)	99(7)	64(9)†	†Possible blending	
SDSS J1400+3134	N	1.74	3.317	45(7)	28(9)	< 42		Inada et al. (2009)
SDSS J1402+6321	J	1.35	0.48	< 27	< 25	< 30		
SDSS J1406+6126	N	1.98	2.13	< 35	< 36	< 41		
HST 14113+5211	N	1.8	2.81	< 28	< 30	< 34		
H 1413+117	J	1.35	2.55	521(3)	403(3)	247(4)		
JVAS B1422+231	J	1.68	3.62	36(11)	< 30	< 45		
SDSS J1455+1447	N	1.73	1.424	54(7)	34(7)	< 30		Kayo et al. (2010)
SBS J1520+530	N	1.59	1.86	54(9)	43(8)	< 33		
MG J1549+3047	J	1.7	1.17	< 28	< 32	< 36	Lensed radio lobe	
CLASS B1555+375	J	0.42	–	< 29	< 30	< 30		
CLASS B1600+434	J	1.4	1.59	36(6)	27(6)	< 39	Star-forming lens galaxy	
CLASS B1608+656	J	2.27	1.39	33(6)	33(4)	28(5)		

Table 2.6 | (continued)

Lens Name	Type	$\Delta\theta$ (")	z_s	$S_{250\ \mu m}$	$S_{350\ \mu m}$	$S_{500\ \mu m}$	Comments	References
SDSS J1620+1203	N	2.77	1.158	< 26	< 28	< 40		Kayo et al. (2010)
PMN J1632−0033	J	1.47	3.424	< 24	35(6)	56(9)		
FBQS J1633+3134	J	0.75	1.52	62(9)	30(8)	< 30		
SDSS J1650+4251	N	1.23	1.54	86(9)	89(8)	53(9)		
MG J1654+1346	J	2.1	1.74	< 34	< 30	< 43	Lensed radio lobe	
PKS J1830−211	J	0.99	2.51	537(9)	670(9)	806(11)		
PMN J1838−3427	J	0.99	2.78	65(5)	90(6)	86(8)		
CLASS B1933+503	J	1.0	1.71	243(7)	212(8)	125(10)		
JVAS B1938+666	J	1.0	2.01	163(7)	164(7)	120(10)		
PMN J2004−1349	J	1.18	–	38(7)†	49(6)†	28(7)†	†Diffuse galactic emission	
MG J2016+112	J	3.52	3.27	81(7)	48(6)	< 32		
WFI J2026−4536	N	1.34	2.23	460(7)	301(7)	162(10)		
WFI J2033−4723	N	2.33	1.66	100(7)	84(7)	50(11)		
CLASS B2045+265	J	2.74	2.35⋆	< 36	< 33	< 43		⋆C. Fassenacht, priv. comm.
CLASS B2108+213	J	4.57	0.67	< 32	< 32	< 36		
JVAS B2114+022	J	1.31	0.59	137(7)	108(9)	36(9)	Star-forming lens galaxy	
HE 2149−2745	N	1.7	2.03	84(7)	77(9)	37(9)		
CY 2201−3201	N	0.83	3.9	< 37	< 30	< 44		
Q 2237+030	N	1.78	1.69	< 30	< 28	< 40		
CLASS B2319+052	J	1.36	–	56(6)	57(7)	< 33		
PSS J2322+1944	N	1.49	4.12	83(4)	105(3)	81(5)		
SDSS J2343−0050	N	1.51	0.787	< 26	< 30	< 34		Jackson et al. (2008)

Table 2.7 | We give the FIR luminosities (40–120 μm) and star formation rates of the quasar sample, derived from both the least squares SED fit and the median, 16th and 84th percentiles from the MCMC analysis. The values are not corrected for lensing magnification ($\mu_{\rm FIR}$). Where objects are fit with two-temperature dust models, both temperatures are reported but the lower temperature is used for estimation of $L_{\rm FIR}$ (i.e. luminosity due to star formation) and SFR. Square brackets denote temperature fits where the source is synchrotron-dominated (noted in the comments), which are used only to derive upper limits on the dust emission.

	Least squared				MCMC			
Lens Name	$T_{\rm dust}$ (K)	β	log μ $L_{\rm FIR}$ ($L_\odot$)	log μ SFR ($M_\odot$ yr^{-1})	$T_{\rm dust}$ (K)	β	log μ $L_{\rm FIR}$ ($L_\odot$)	log μ SFR ($M_\odot$ yr^{-1})
HE 0047−1756	42.6	-	13.2	3.7	$43.2^{+3.4}_{-2.8}$	-	$13.2^{+0.1}_{-0.1}$	$3.7^{+0.1}_{-0.1}$
CLASS B0128+437	-	-	< 12.8	< 3.3	-	-	-	-
Q J0158−4325	27.7	-	12.0	2.5	$30.4^{+7.9}_{-5.7}$	-	$12.1^{+0.3}_{-0.2}$	$2.6^{+0.3}_{-0.2}$
JVAS B0218+357	[16.8]	-	< 11.5	< 2.1	-	-	-	-
HE 0230−2130	39.4	1.3	13.1	3.6	$41.8^{+9.0}_{-6.3}$	$1.2^{+0.4}_{-0.4}$	$13.1^{+0.1}_{-0.1}$	$3.65^{+0.08}_{-0.06}$
SDSS J0246−0825	36.0	-	12.7	3.3	$36.8^{+3.9}_{-3.1}$	-	$12.8^{+0.1}_{-0.1}$	$3.3^{+0.1}_{-0.1}$
CFRS03.1077	42.7	-	13.0	3.5	$44.7^{+8.0}_{-6.1}$	-	$13.0^{+0.1}_{-0.1}$	$3.48^{+0.07}_{-0.07}$
MG J0414+0534	41.2	2.3	13.7	4.2	$42.8^{+7.4}_{-4.8}$	$2.2^{+0.4}_{-0.4}$	$13.66^{+0.04}_{-0.03}$	$4.18^{+0.04}_{-0.03}$
HE 0435−1223	37.0	-	12.9	3.4	$37.3^{+2.7}_{-2.3}$	-	$12.9^{+0.1}_{-0.1}$	$3.5^{+0.1}_{-0.1}$
CLASS B0445+123	-	-	< 12.1	< 2.6	-	-	-	-
HE 0512−3329	41.8	-	12.6	3.1	$50.1^{+18.4}_{-12.2}$	-	$12.8^{+0.3}_{-0.2}$	$3.3^{+0.3}_{-0.2}$
CLASS B0631+519	26.3	-	12.6	3.1	$26.7^{+1.4}_{-1.3}$	-	$12.6^{+0.1}_{-0.1}$	$3.1^{+0.1}_{-0.1}$
CLASS B0712+472	-	-	< 12.2	< 2.8	-	-	-	-
CLASS B0739+366	25.7	2.9	12.7	3.2	$27.0^{+6.2}_{-4.2}$	$2.7^{+0.7}_{-0.7}$	$12.7^{+0.1}_{-0.1}$	$3.2^{+0.1}_{-0.1}$
SDSS J0746+4403	-	-	< 12.5	< 3.0	-	-	-	-
MG J0751+2716	36.2	2.4	13.4	3.9	$36.2^{+1.9}_{-1.7}$	$2.4^{+0.2}_{-0.2}$	$13.39^{+0.01}_{-0.01}$	$3.91^{+0.01}_{-0.01}$
SDSS J0806+2006	-	-	$12.4^{+0.4}_{-0.2}$	$2.9^{+0.4}_{-0.2}$	-	-	-	-
HS 0810+2554	89.1	1.0	13.5	4.0	$89.0^{+6.5}_{-6.0}$	$1.0^{+0.2}_{-0.2}$	$13.50^{+0.03}_{-0.03}$	$4.01^{+0.03}_{-0.03}$
SDSS J0819+5356	36.2	-	12.6	3.2	$38.1^{+7.5}_{-6.3}$	-	$12.7^{+0.1}_{-0.1}$	$3.2^{+0.1}_{-0.1}$
SDSS J0820+0812	35.8	-	12.7	3.2	$38.1^{+8.1}_{-5.2}$	-	$12.7^{+0.2}_{-0.1}$	$3.2^{+0.2}_{-0.1}$
HS 0818+1227	-	-	$12.6^{+0.4}_{-0.4}$	$3.1^{+0.4}_{-0.4}$	-	-	-	-
APM 08279+5255	56.9, 160.3	1.4	14.1	4.6	$57.1^{+1.2}_{-1.2}$, $160.7^{+2.5}_{-2.5}$	$1.43^{+0.03}_{-0.03}$	$14.10^{+0.01}_{-0.01}$	$4.62^{+0.01}_{-0.01}$
SDSS J0832+0404	-	-	< 12.1	< 2.6	-	-	-	-
CLASS B0850+054	42.4	-	12.8	3.3	$48.8^{+17.6}_{-10.0}$	-	$12.8^{+0.3}_{-0.1}$	$3.4^{+0.3}_{-0.1}$
SDSS J0903+5028	60.2	-	13.8	4.3	$60.5^{+3.5}_{-3.1}$	-	$13.83^{+0.02}_{-0.02}$	$4.35^{+0.02}_{-0.02}$

Table 2.7 | (continued)

	Least squared				MCMC			
Lens Name	$T_{\rm dust}$ (K)	β	log μ $L_{\rm FIR}$ ($L_\odot$)	log μ SFR ($M_\odot$ yr^{-1})	$T_{\rm dust}$ (K)	β	log μ $L_{\rm FIR}$ ($L_\odot$)	log μ SFR ($M_\odot$ yr^{-1})
SDSS J0904+1512	-	-	$12.4^{+0.2}_{-0.2}$	$3.0^{+0.2}_{-0.2}$	-	-	-	-
SBS 0909+523	-	-	< 12.2	< 2.7	-	-	-	-
RX J0911+0551	51.0	1.3	13.6	4.1	$52.6^{+7.8}_{-6.1}$	$1.3^{+0.2}_{-0.2}$	$13.58^{+0.04}_{-0.03}$	$4.09^{+0.04}_{-0.03}$
RX J0921+4529	-	-	< 12.3	< 2.8	-	-	-	-
SDSS J0924+0219	31.8	-	12.5	3.0	$33.4^{+5.9}_{-4.0}$	-	$12.5^{+0.2}_{-0.1}$	$3.0^{+0.2}_{-0.1}$
FBQS 0951+2635	-	-	< 12.1	< 2.6	-	-	-	-
Q 0957+561	27.9	2.3	12.6	3.1	$31.1^{+11.1}_{-6.8}$	$2.0^{+0.7}_{-0.6}$	$12.7^{+0.2}_{-0.1}$	$3.2^{+0.2}_{-0.1}$
SDSS J1001+5027	-	-	$12.5^{+0.3}_{-0.1}$	$3.0^{+0.3}_{-0.1}$	-	-	-	-
SDSS J1004+1229	-	-	< 12.6	< 3.1	-	-	-	-
LBQS 1009−0252	-	-	< 12.6	< 3.2	-	-	-	-
SDSS J1011+0143	-	-	< 12.7	< 3.2	-	-	-	-
Q 1017−207	-	-	< 12.6	< 3.1	-	-	-	-
SDSS J1021+4913	38.8	-	12.4	3.0	$48.4^{+19.8}_{-13.4}$	-	$12.6^{+0.3}_{-0.2}$	$3.1^{+0.3}_{-0.2}$
IRAS F10214+4724	40.6, 104.3	1.3	13.5	4.0	$44.7^{+5.9}_{-5.9}$, $90.2^{+7.8}_{-6.0}$	$1.2^{+0.2}_{-0.2}$	$13.5^{+0.1}_{-0.1}$	$4.1^{+0.1}_{-0.1}$
SDSS J1029+2623	35.9	-	12.7	3.2	$36.4^{+3.1}_{-2.5}$	-	$12.7^{+0.1}_{-0.1}$	$3.2^{+0.1}_{-0.1}$
JVAS B1030+074	[20.2]	-	<11.9	<2.4	-	-	-	-
SDSS J1054+2733	27.6	-	12.4	2.9	$28.0^{+2.3}_{-2.0}$	-	$12.4^{+0.1}_{-0.1}$	$3.0^{+0.1}_{-0.1}$
SDSS J1055+4628	-	-	< 12.1	< 2.6	-	-	-	-
HE 1104−1805	35.5	1.9	13.2	3.7	$36.1^{+4.6}_{-3.6}$	$1.9^{+0.3}_{-0.3}$	$13.22^{+0.04}_{-0.04}$	$3.74^{+0.04}_{-0.04}$
PG 1115+080	51.7	-	13.2	3.7	$55.1^{+17.5}_{-8.9}$	-	$12.9^{+0.2}_{-0.1}$	$3.4^{+0.2}_{-0.1}$
CLASS B1127+385	23.7	2.9	12.8	3.3	$24.2^{+4.3}_{-3.1}$	$2.8^{+0.6}_{-0.6}$	$12.8^{+0.1}_{-0.1}$	$3.3^{+0.1}_{-0.1}$
RX J1131−1231	19.4	2.9	12.1	2.6	$20.5^{+5.7}_{-4.3}$	$2.7^{+1.0}_{-0.7}$	$12.2^{+0.3}_{-0.1}$	$2.7^{+0.3}_{-0.2}$
MG J1131+0456	-	-	< 12.3	< 2.9	-	-	-	-
SDSS J1131+1915	-	-	< 12.7	< 3.2	-	-	-	-
SDSS J1138+0314	-	-	$12.6^{+0.2}_{-0.1}$	$3.1^{+0.2}_{-0.1}$	-	-	-	-
SDSS J1155+6346	43.0	-	12.8	3.3	$49.4^{+20.5}_{-10.5}$	-	$12.8^{+0.1}_{-0.1}$	$3.3^{+0.1}_{-0.1}$
CLASS B1152+200	-	-	$12.2^{+0.8}_{-0.3}$	$2.7^{+0.8}_{-0.3}$	-	-	-	-
SDSS J1206+4332	42.0	-	12.9	3.4	$44.2^{+8.5}_{-5.5}$	-	$12.9^{+0.2}_{-0.1}$	$3.5^{+0.2}_{-0.1}$
Q 1208+101	68.9	1.2	13.3	3.8	$81.4^{+33.1}_{-23.5}$	$1.0^{+0.6}_{-0.4}$	$13.3^{+0.1}_{-0.1}$	$3.8^{+0.1}_{-0.1}$
SDSS J1216+3529	-	-	< 12.5	< 3.0	-	-	-	-

Table 2.7 | (continued)

	Least squared				MCMC			
Lens Name	$T_{\rm dust}$ (K)	β	$\log \mu\, L_{\rm FIR}$ ($L_\odot$)	$\log \mu$ SFR ($M_\odot$ yr^{-1})	$T_{\rm dust}$ (K)	β	$\log \mu\, L_{\rm FIR}$ ($L_\odot$)	$\log \mu$ SFR ($M_\odot$ yr^{-1})
HST 12531−2914	-	-	< 12.2	< 2.7	-	-	-	-
SDSS J1258+1657	33.3	-	12.9	3.4	$34.2^{+3.9}_{-3.2}$	-	$12.9^{+0.1}_{-0.1}$	$3.4^{+0.1}_{-0.1}$
SDSS J1304+2001	35.5	-	12.4	2.9	$31.0^{+7.3}_{-4.6}$	-	$12.4^{+0.2}_{-0.1}$	$2.9^{+0.2}_{-0.1}$
SDSS J1313+5151	-	-	$12.7^{+0.4}_{-0.2}$	$3.2^{+0.4}_{-0.2}$	-	-	-	-
SDSS J1322+1052	30.4	-	12.6	3.2	$30.8^{+2.9}_{-2.4}$	-	$12.6^{+0.1}_{-0.1}$	$3.2^{+0.1}_{-0.1}$
SDSS J1330+1810	35.6	-	12.7	3.3	$36.2^{+3.5}_{-2.7}$	-	$12.8^{+0.1}_{-0.1}$	$3.3^{+0.1}_{-0.1}$
SDSS J1332+0347	-	-	< 12.2	< 2.7	-	-	-	-
LBQS 1333+0133	20.1	-	12.1	2.6	$20.2^{+1.4}_{-1.3}$	-	$12.1^{+0.1}_{-0.1}$	$2.6^{+0.1}_{-0.1}$
SDSS J1339+1310	-	-	$12.6^{+0.3}_{-0.2}$	$3.1^{+0.3}_{-0.2}$	-	-	-	-
SDSS J1349+1227	32.9	-	12.5	3.0	$34.4^{+5.9}_{-4.1}$	-	$12.6^{+0.2}_{-0.1}$	$3.1^{+0.2}_{-0.1}$
SDSS J1353+1138	45.7	-	12.8	3.3	$51.7^{+15.2}_{-11.0}$	-	$12.9^{+0.2}_{-0.2}$	$3.4^{+0.2}_{-0.2}$
Q 1355−2257	25.7	-	11.8	2.3	$31.2^{+17.1}_{-7.6}$	-	$12.0^{+0.6}_{-0.2}$	$2.5^{+0.6}_{-0.2}$
CLASS B1359+154	58.8	1.7	13.5	4.1	$60.3^{+10.8}_{-10.2}$	$1.7^{+0.5}_{-0.4}$	$13.55^{+0.03}_{-0.03}$	$4.06^{+0.03}_{-0.03}$
SDSS J1400+3134	69.6	-	13.4	3.9	$75.0^{+18.7}_{-17.2}$	-	$13.1^{+0.1}_{-0.1}$	$3.6^{+0.1}_{-0.1}$
SDSS J1402+6321	-	-	< 11.5	< 2.0	-	-	-	-
SDSS J1406+6126	-	-	< 12.5	< 3.0	-	-	-	-
HST 14113+52116	-	-	< 12.6	< 3.1	-	-	-	-
H 1413+117	35.5, 124.1	2.4	13.85	4.37	$35.6^{+0.6}_{-0.6}$, $125.6^{+10.6}_{-8.9}$	$2.4^{+0.1}_{-0.1}$	$13.85^{+0.01}_{-0.01}$	$4.37^{+0.01}_{-0.01}$
JVAS B1422+231	-	-	12.4	2.9	-	-	$12.36^{+0.40}_{-0.18}$	$2.87^{+0.40}_{-0.18}$
SDSS J1455+1447	39.7	-	12.5	3.0	$46.6^{+14.9}_{-10.8}$	-	$12.6^{+0.3}_{-0.2}$	$3.1^{+0.3}_{-0.2}$
SBS 1520+530	42.1	-	12.7	3.2	$46.2^{+12.7}_{-7.2}$	-	$12.8^{+0.2}_{-0.1}$	$3.3^{+0.2}_{-0.1}$
SDSS J1524+4409	32.0	-	12.4	2.9	$34.6^{+8.1}_{-7.4}$	-	$12.2^{+0.3}_{-0.2}$	$2.7^{+0.3}_{-0.2}$
HST 15433+5352	-	-	< 12.7	< 3.2	-	-	-	-
MG J1549+3047	-	-	< 12.1	< 2.6	-	-	-	-
CLASS B1555+375	-	-	< 12.3	< 2.8	-	-	-	-
CLASS B1600+434	35.8	-	12.3	2.8	$38.9^{+8.9}_{-7.5}$	-	$12.4^{+0.2}_{-0.2}$	$2.9^{+0.2}_{-0.2}$
CLASS B1608+656	31.9	1.8	11.9	2.4	$36.3^{+13.7}_{-9.2}$	$1.5^{+0.9}_{-0.7}$	$11.9^{+0.2}_{-0.1}$	$2.4^{+0.2}_{-0.1}$
SDSS J1620+1203	-	-	< 12.0	< 2.6	-	-	-	-
PMN J1632−0033	[26.8]	-	< 12.8	< 3.3	-	-	-	-
FBQS 1633+3134	65.1	-	12.9	3.5	$66.2^{+14.6}_{-15.1}$	-	$12.9^{+0.2}_{-0.2}$	$3.5^{+0.2}_{-0.2}$

Table 2.7 | (continued)

	Least squared				MCMC			
Lens Name	$T_{\rm dust}$ (K)	β	$\log \mu\, L_{\rm FIR}$ ($L_\odot$)	$\log \mu$ SFR ($M_\odot$ yr^{-1})	$T_{\rm dust}$ (K)	β	$\log \mu\, L_{\rm FIR}$ ($L_\odot$)	$\log \mu$ SFR ($M_\odot$ yr^{-1})
SDSS J1650+4251	28.1	-	12.5	3.0	$28.3^{+2.3}_{-1.9}$	-	$12.5^{+0.1}_{-0.1}$	$3.0^{+0.1}_{-0.1}$
MG J1654+1346	-	-	<12.4	<2.9	-	-	-	-
PKS J1830−211	[29.7]	-	<13.8	<4.3	-	-	-	-
PMN J1838−3427	[32.8]	-	<13.1	<3.6	-	-	-	-
CLASS B1933+503	20.4	3.9	13.0	3.5	$20.4^{+2.3}_{-2.1}$	$3.9^{+0.7}_{-0.6}$	$13.01^{+0.04}_{-0.03}$	$3.52^{+0.04}_{-0.03}$
JVAS B1938+666	28.9	2.0	13.1	3.6	$29.2^{+2.7}_{-2.3}$	$2.0^{+0.3}_{-0.3}$	$13.08^{+0.04}_{-0.03}$	$3.59^{+0.04}_{-0.03}$
PMN J2004−1349	30.7	-	12.5	3.0	$31.8^{+4.0}_{-3.1}$	-	$12.5^{+0.1}_{-0.1}$	$3.0^{+0.1}_{-0.1}$
MG J2016+112	88.6	-	13.4	3.9	$99.5^{+32.4}_{-18.3}$	-	$13.38^{+0.05}_{-0.05}$	$3.90^{+0.05}_{-0.05}$
WFI J2026−4536	50.1	-	13.8	4.3	$50.3^{+1.3}_{-1.2}$	-	$13.81^{+0.02}_{-0.02}$	$4.33^{+0.02}_{-0.02}$
WFI J2033−4723	33.2	-	12.7	3.2	$33.7^{+3.0}_{-2.4}$	-	$12.7^{+0.1}_{-0.1}$	$3.3^{+0.1}_{-0.1}$
CLASS B2045+265	-	-	<12.7	<3.2	-	-	-	-
CLASS B2108+213	-	-	<11.7	<2.2	-	-	-	-
JVAS B2114+022	30.4	-	12.1	2.6	$31.6^{+4.3}_{-3.1}$	-	$12.1^{+0.2}_{-0.1}$	$2.6^{+0.2}_{-0.1}$
HE 2149−2745	26.9	2.8	12.8	3.3	$30.7^{+12.0}_{-6.5}$	$2.4^{+0.9}_{-0.9}$	$12.9^{+0.1}_{-0.2}$	$3.4^{+0.1}_{-0.2}$
CY 2201−3201	-	-	<12.8	<3.3	-	-	-	-
Q 2237+030	-	-	$12.5^{+0.3}_{-0.4}$	$3.1^{+0.3}_{-0.4}$	-	-	-	-
CLASS B2319+052	19.1	4.5	12.6	3.1	$19.0^{+4.1}_{-3.0}$	$4.6^{+1.2}_{-1.1}$	$12.6^{+0.1}_{-0.1}$	$3.1^{+0.1}_{-0.1}$
PSS J2322+1944	47.2	1.65	13.6	4.1	$47.4^{+2.5}_{-2.3}$	$1.6^{+0.1}_{-0.1}$	$13.58^{+0.01}_{-0.01}$	$4.10^{+0.01}_{-0.01}$
SDSS J2343−0050	-	-	<11.8	<2.4	-	-	-	-

2.B. SEDs and ancillary data

Figure 2.16 | Included here are 69 SEDs for the quasars in our sample with fitted SEDs, excluding synchrotron-dominated sources (see Fig. 2.17). The legend details the free parameters of the model and their least squared values, excluding the normalization (FIR luminosities are given in Table 2.7). Where β is not given, it is fixed to 1.5. For objects with T fixed, the dust temperature is set to 38 K, the median of the sample. For composite spectra, modified black-body fits are in red, synchrotron in cyan, and the total spectrum in green. The *Herschel*/SPIRE bandwidth is in grey. As we discuss in Section 2.3.4, we do not attempt to fit complex synchrotron components in cases where there is a suggestion that the synchrotron emission is falling off towards the sub-mm or if there is only one detection.

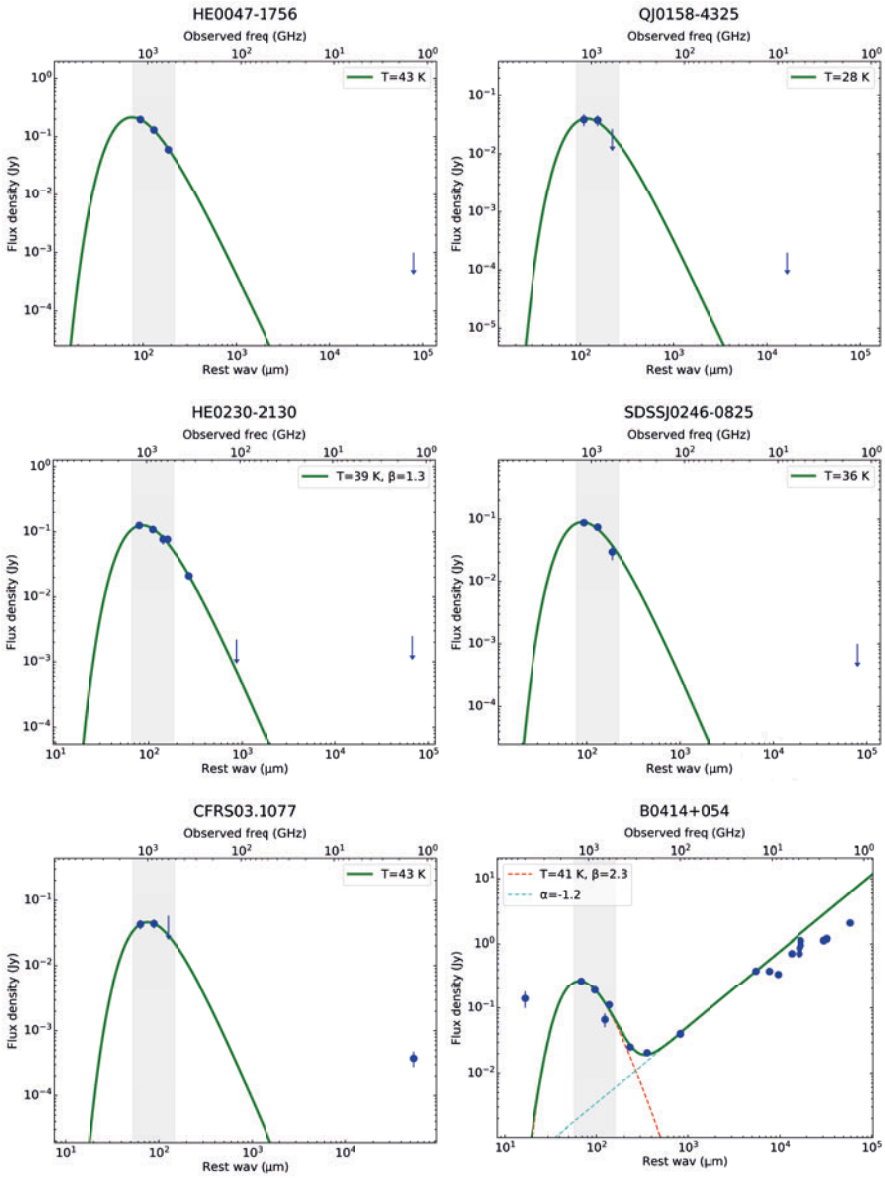

Figure 2.16 | (continued)

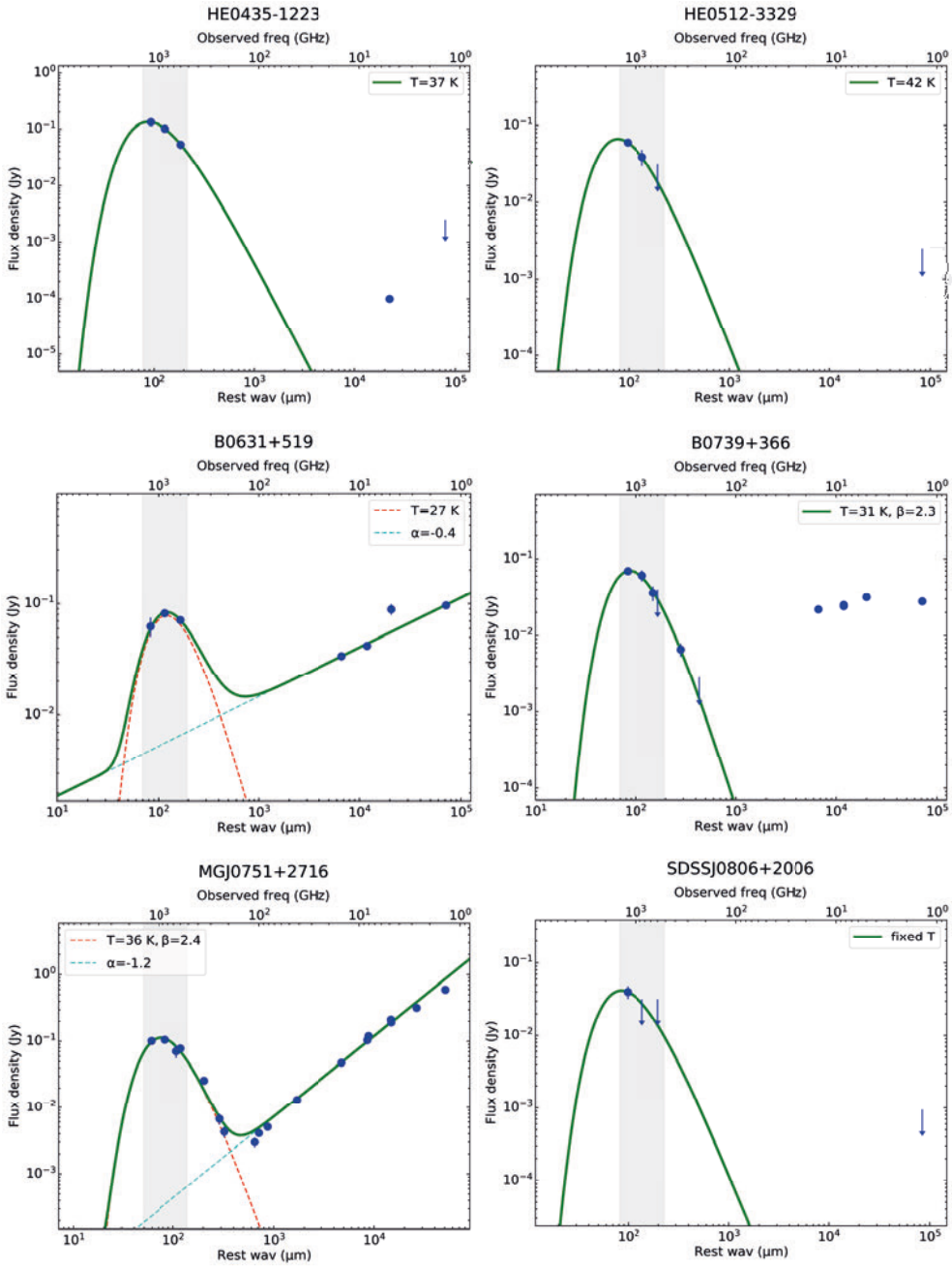

Figure 2.16 | (continued)

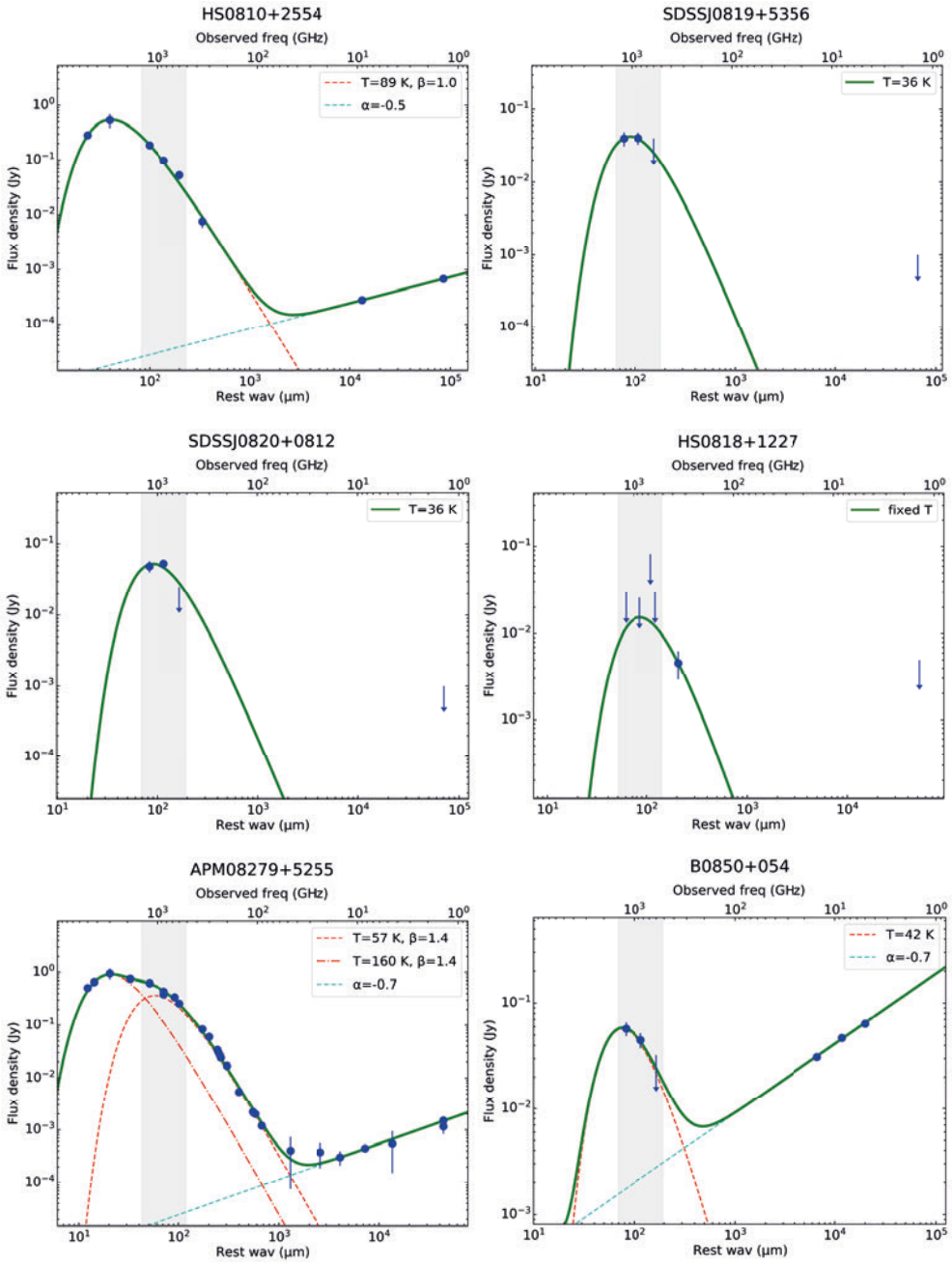

Figure 2.16 | (continued)

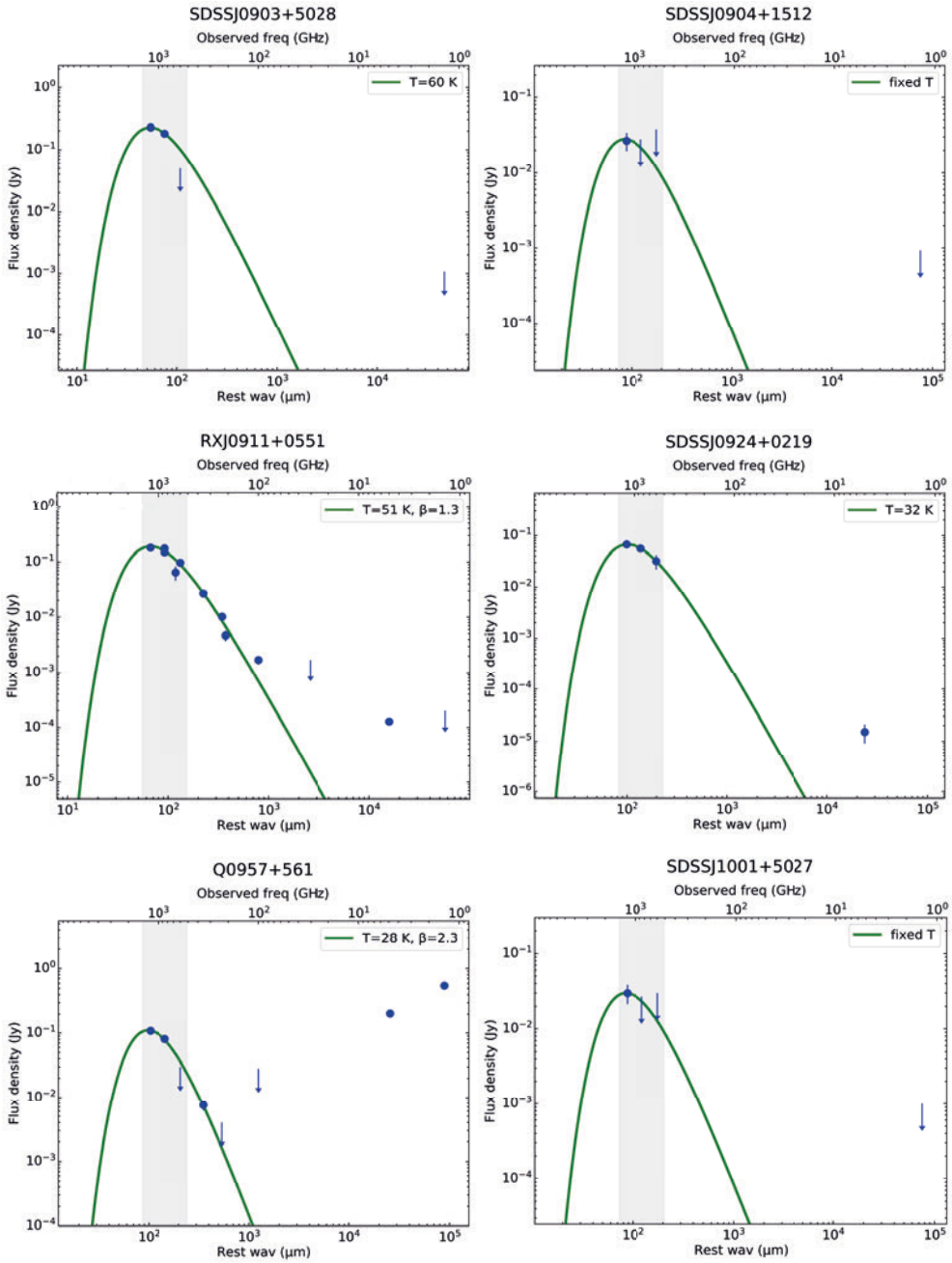

Figure 2.16 | (continued)

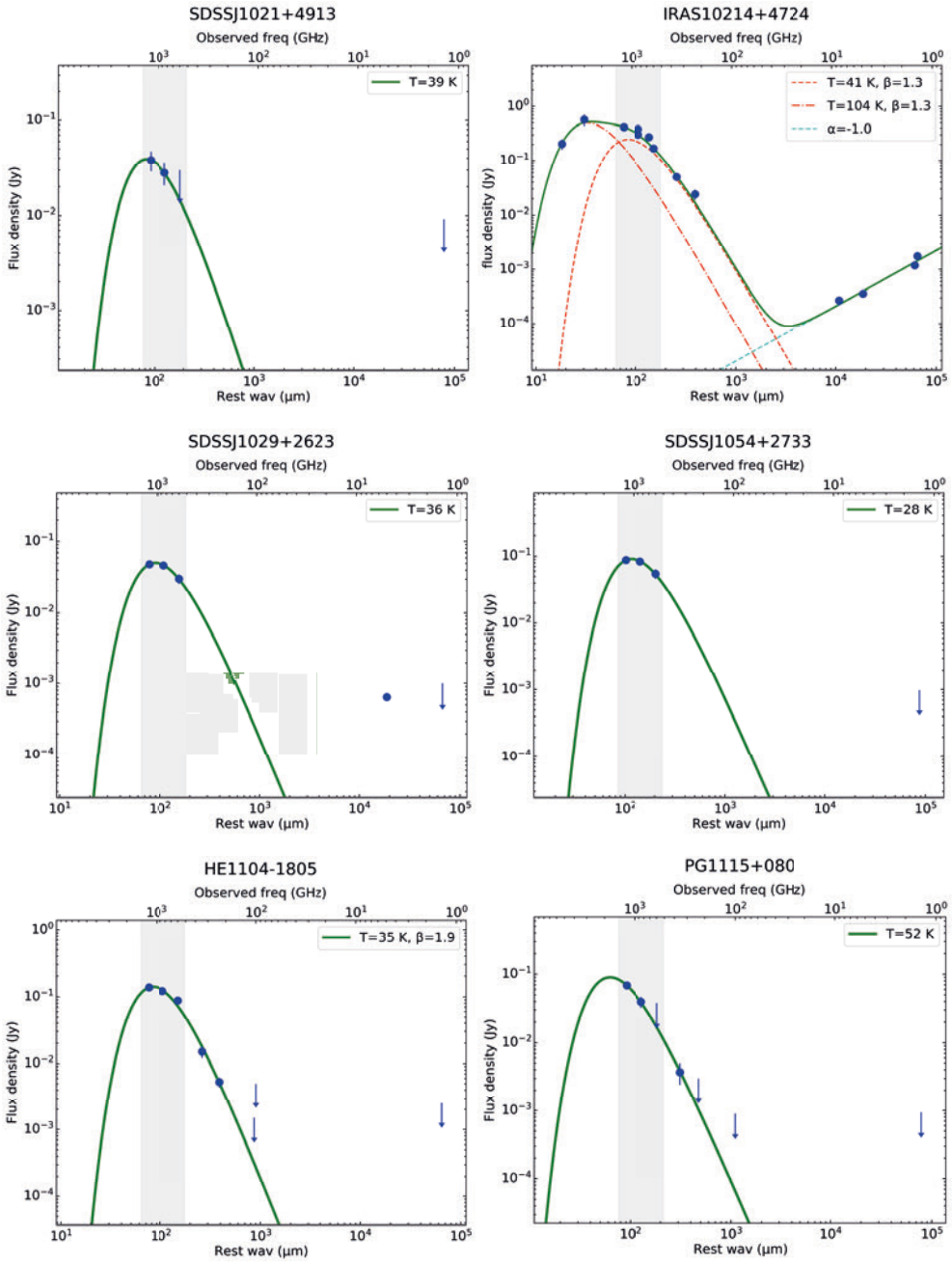

Figure 2.16 | (continued)

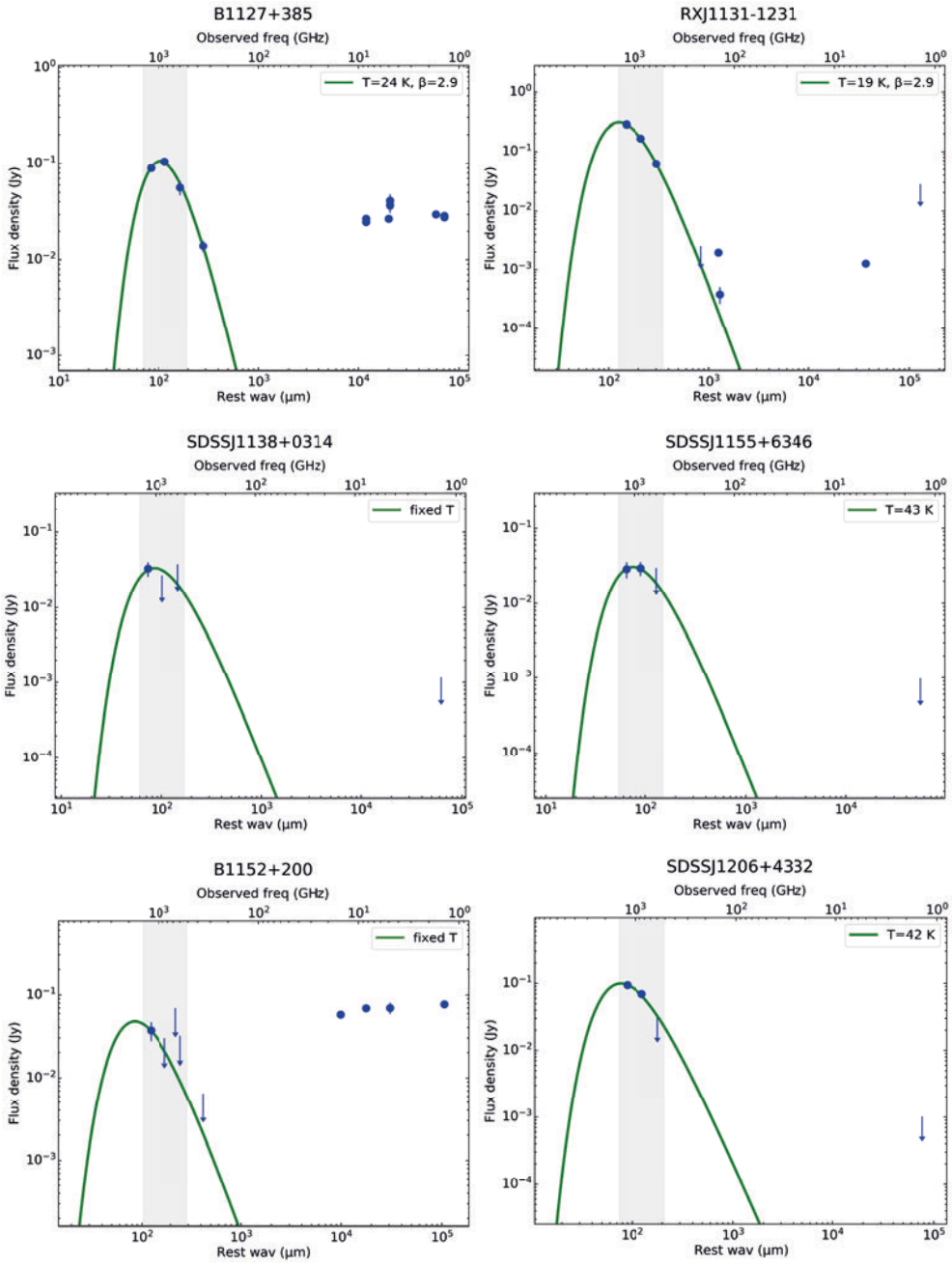

Figure 2.16 | (continued)

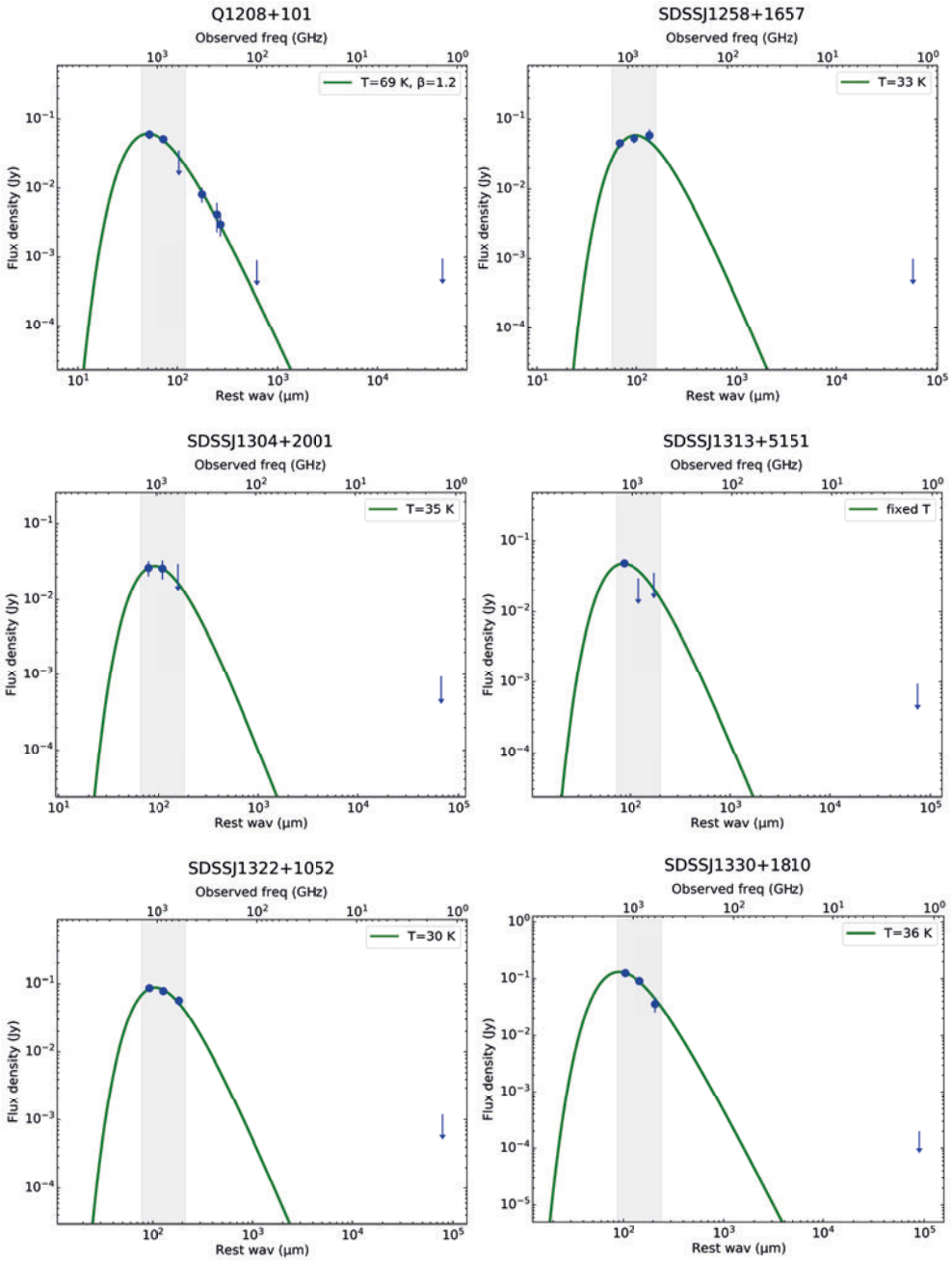

Figure 2.16 | (continued)

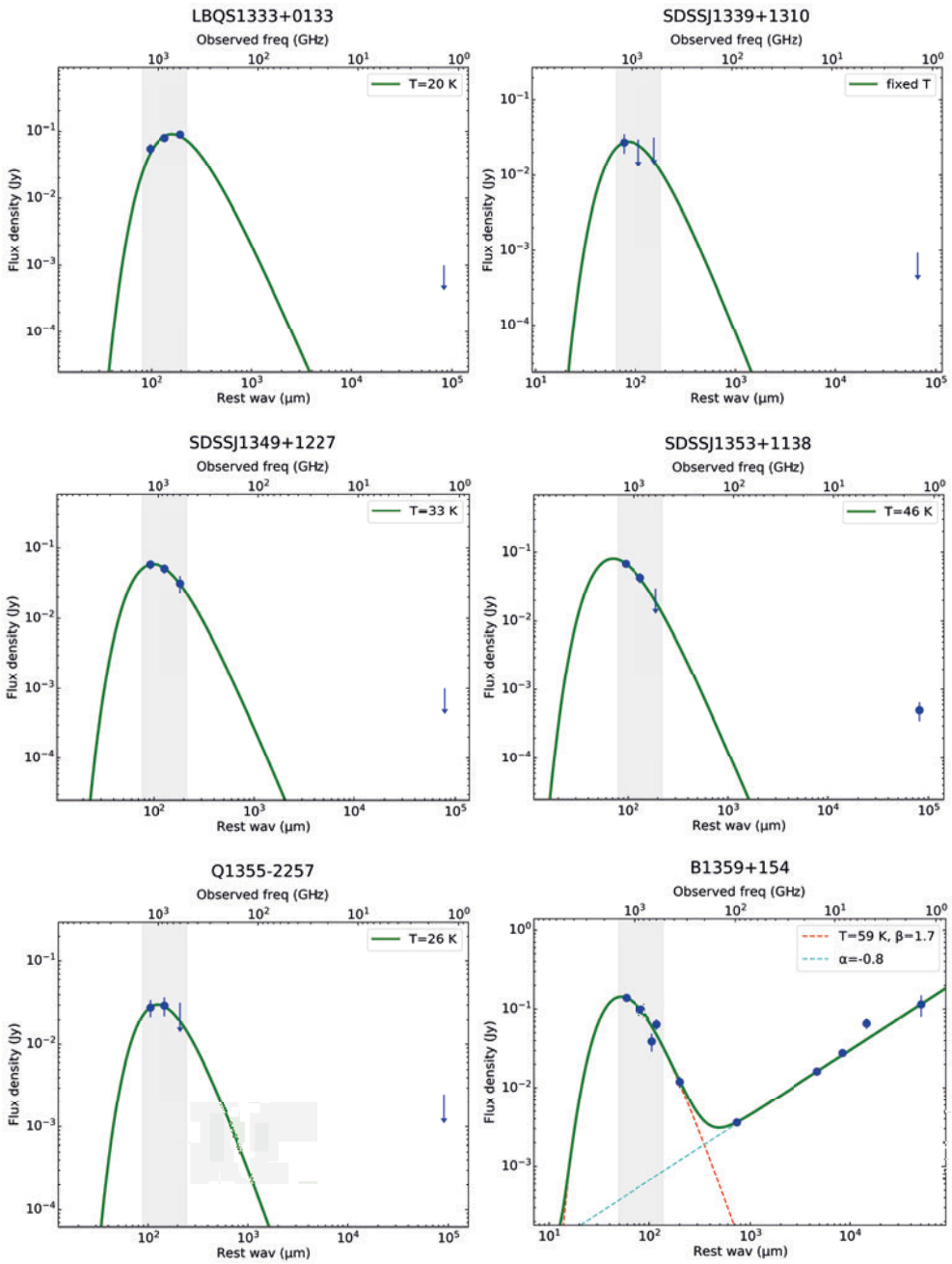

Figure 2.16 | (continued)

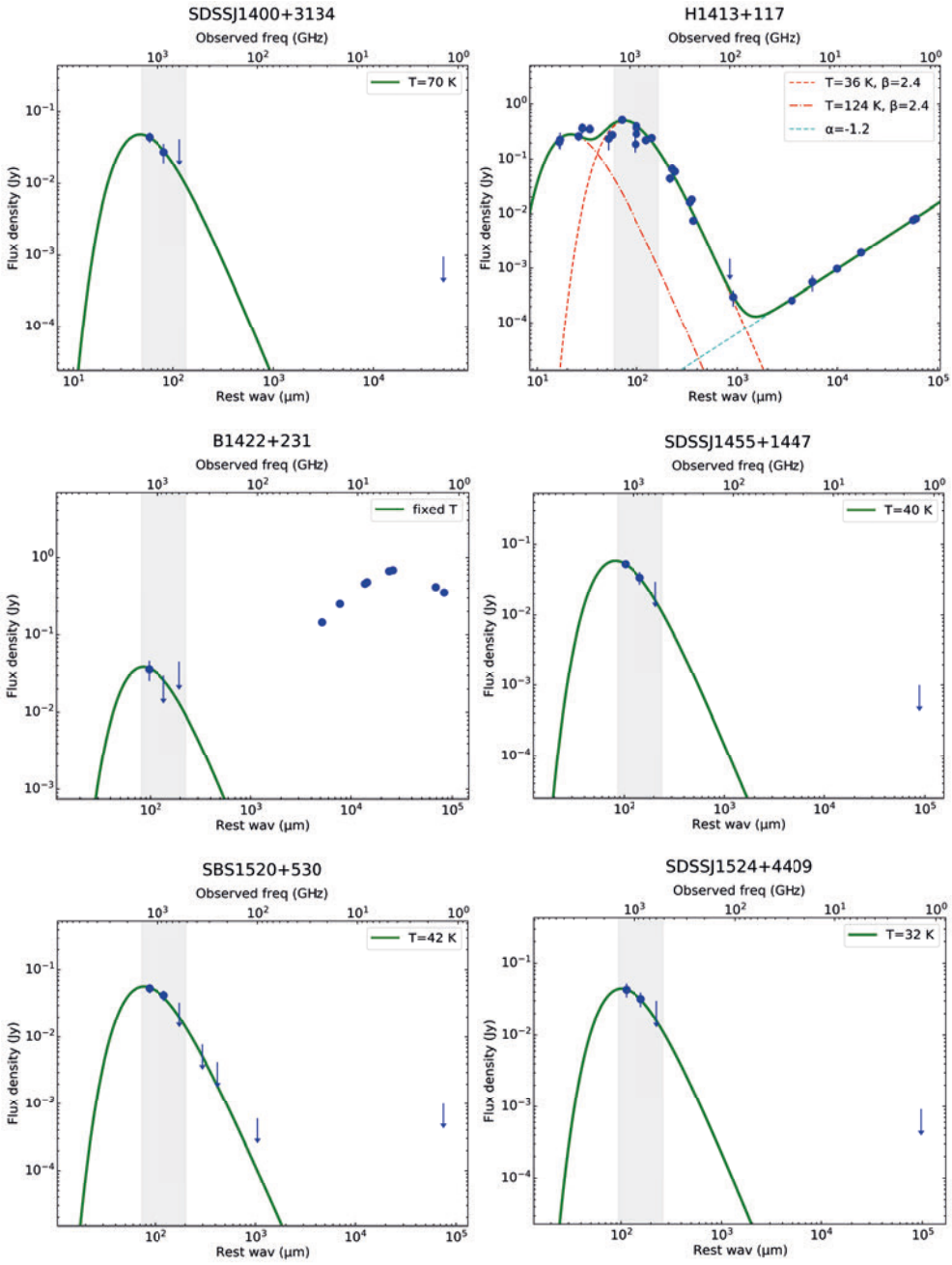

Figure 2.16 | (continued)

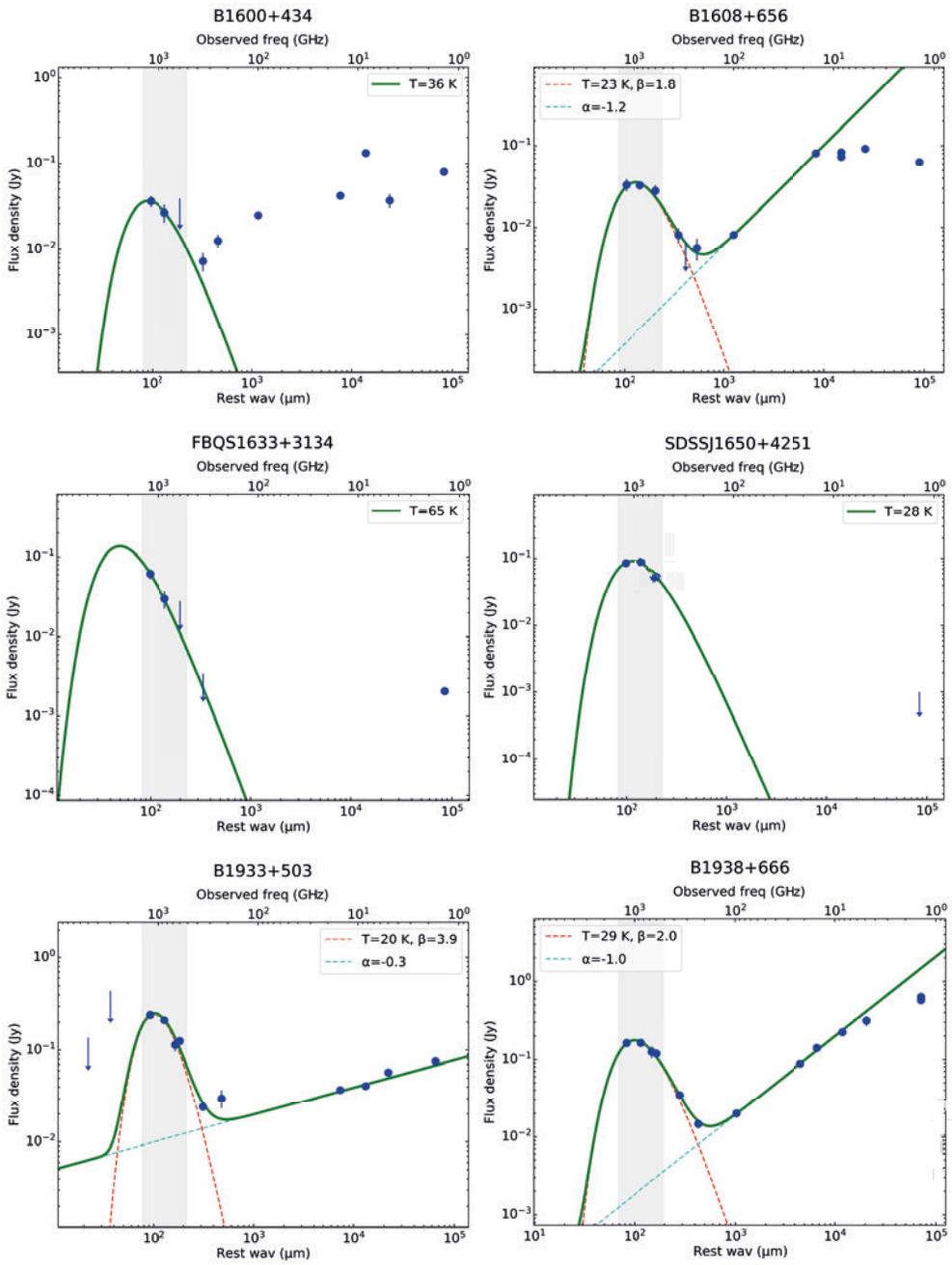

Figure 2.16 | (continued)

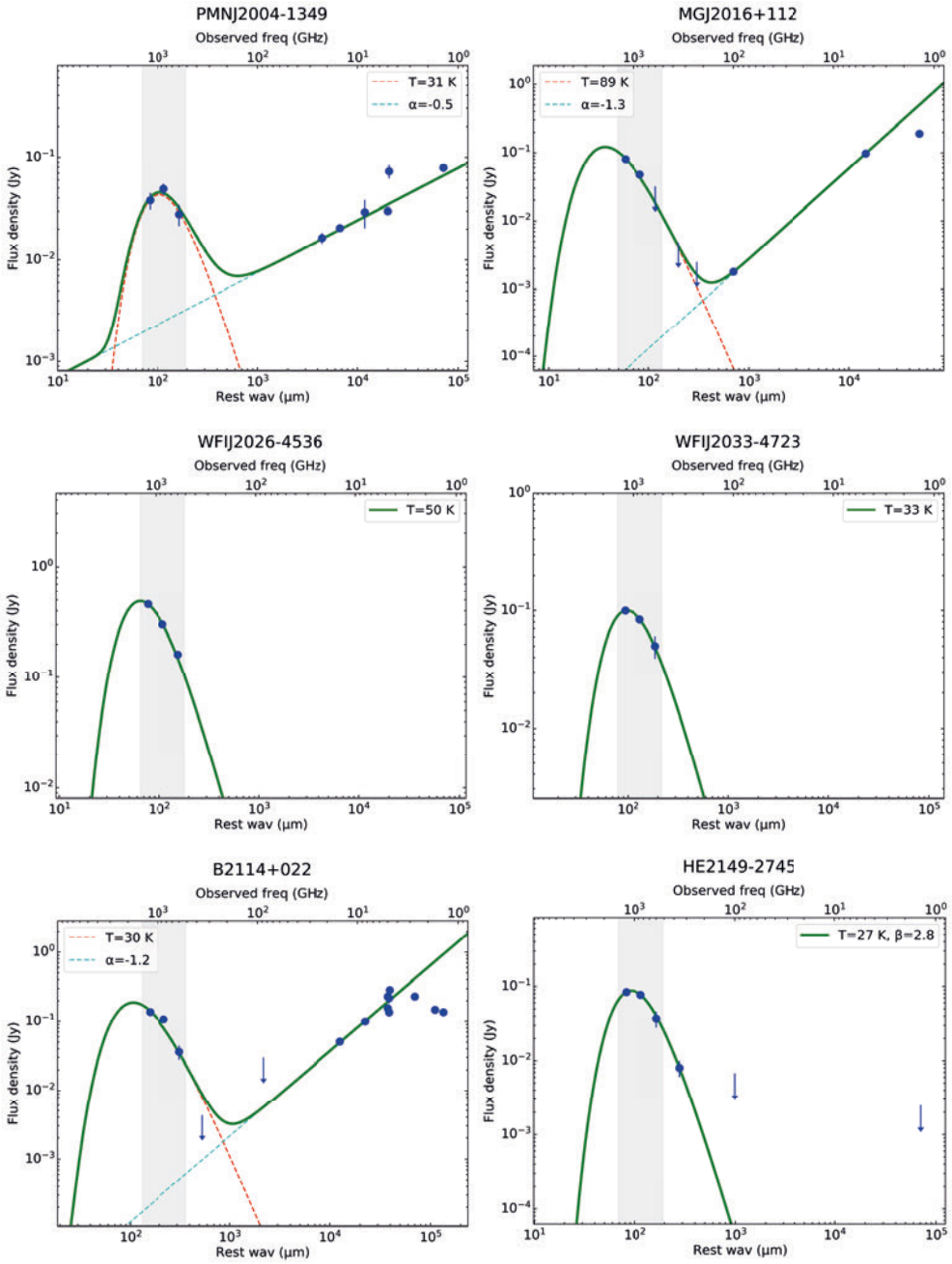

Figure 2.16 | (continued)

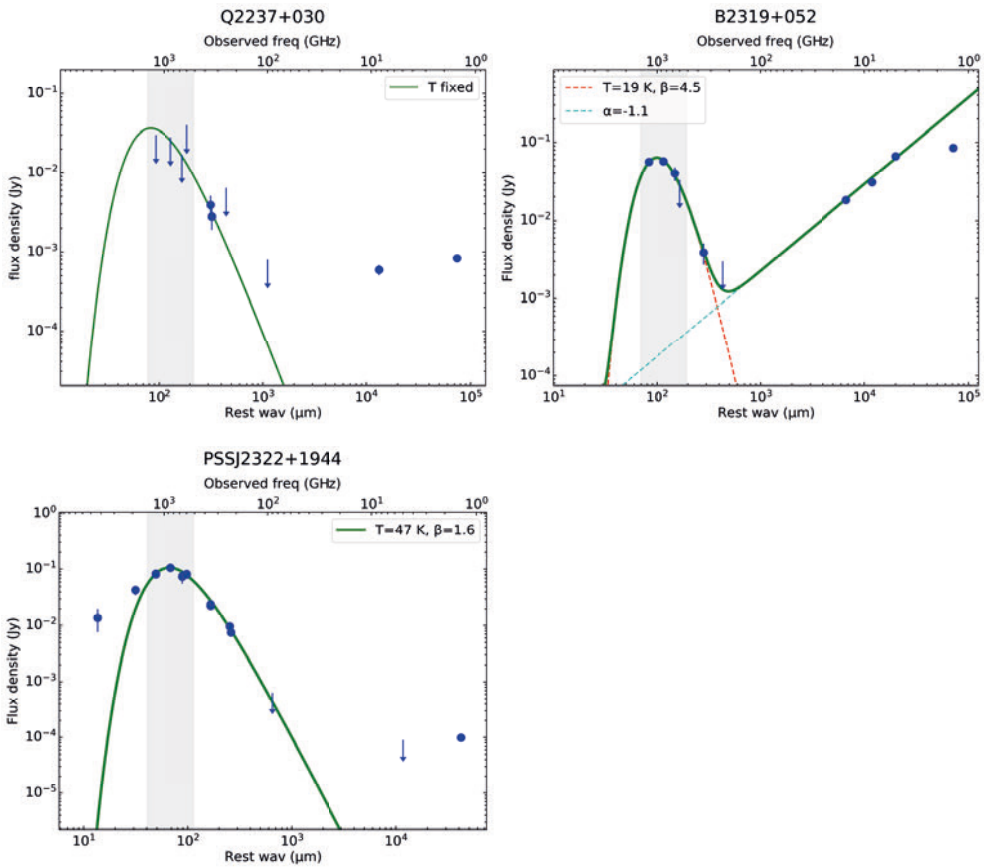

Figure 2.17 | Included here are SEDs for 5 quasars which appear to have synchrotron-dominated emission in the FIR.

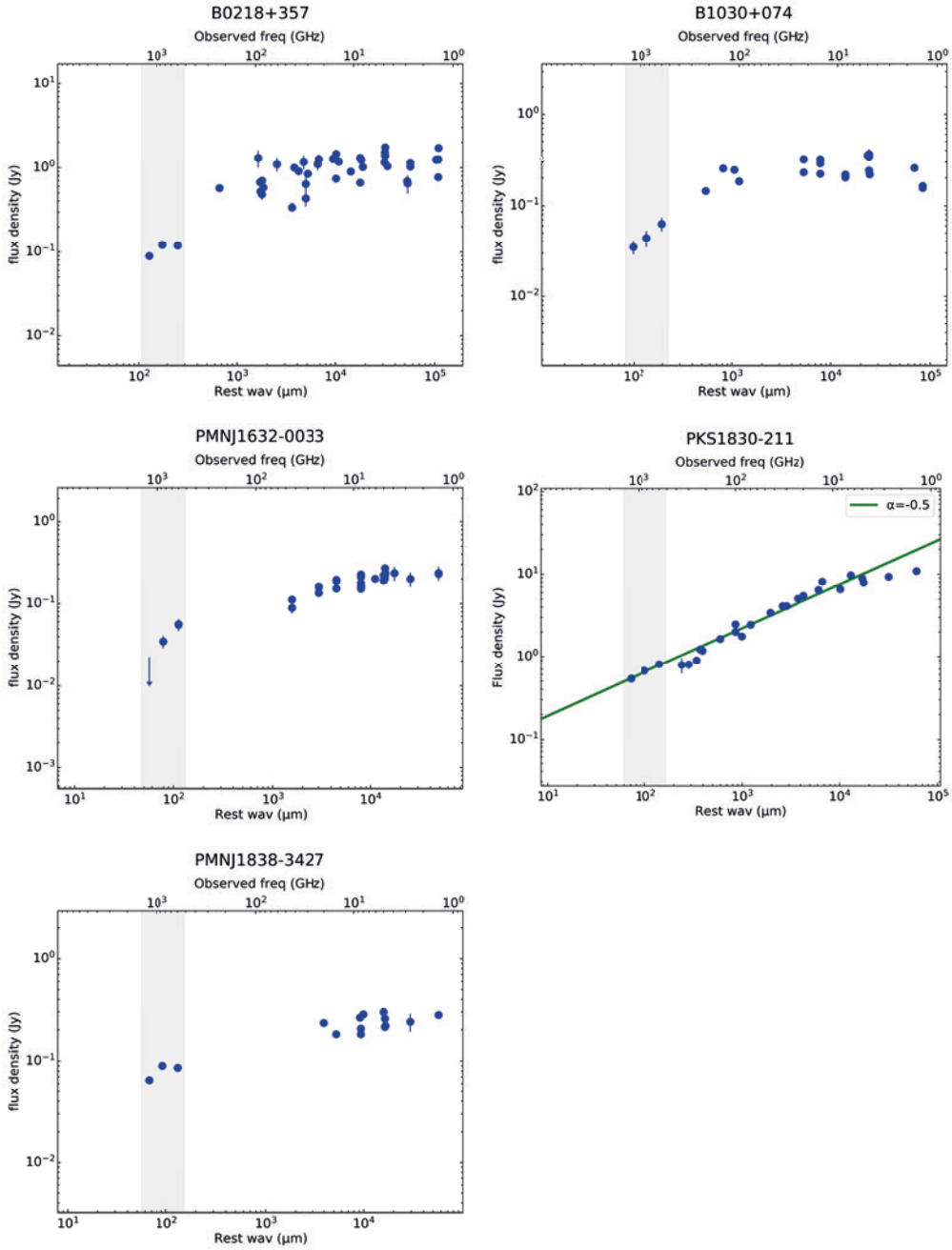

Table 2.8 | Data from the literature shown in our SEDs in Fig. 2.16. Data points in the FIR–sub-mm frequency range that have been excluded from our SED fitting are denoted by †. Any radio data not given here are upper limits from FIRST (Becker et al., 1995, < 1 mJy) or NVSS (Condon et al., 1998, < 2.5 mJy) at 1.4 GHz. BI02 refers to Barvainis & Ivison (2002). If errors are not given in the literature, we assume a flux calibration error of 10 percent.

ν (GHz)	S_ν (Jy)	Reference
	QJ0158-4325	
8.46	< 0.0002	Morgan et al. (1999)
	B0218+357	
229	0.57 ± 0.03	Agudo et al. (2014)
94	1.3 ± 0.3	Wright et al. (2009)
90	0.67 ± 0.07	Kühr et al. (1981)
89.3	0.52 ± 0.08	Jethava et al. (2007)
86.4	0.48 ± 0.07	Jethava et al. (2007)
86.2	0.70 ± 0.03	Agudo et al. (2014)
83.6	0.58 ± 0.09	Jethava et al. (2007)
61.1	1.0 ± 0.2	Wright et al. (2009)
43.2	0.34 ± 0.03	Jethava et al. (2007)
41	1.0 ± 0.1	Wright et al. (2009)
37	0.91 ± 0.09	Nieppola et al. (2011)
33	1.170 ± 0.216	Wright et al. (2009)
31.4	0.64 ± 0.18	Kühr et al. (1981)
31.4	0.43 ± 0.08	Kühr et al. (1981)
30	0.846 ± 0.043	Lowe et al. (2007)
23	1.104 ± 0.175	Wright et al. (2009)
22.4	1.253 ± 0.172	Patnaik et al. (1992)
16.1	1.27 ± 0.13	Davies et al. (2009)
15.064	0.74 ± 07	Kühr et al. (1981)
15.0	1.445 ± 0.145	Richards et al. (2011)
14.1	1.18 ± 0.12	Jethava et al. (2007)
10.695	0.90 ± 0.04	Kühr et al. (1981)
8.6	1.30 ± 0.13	Jethava et al. (2007)
8.6	0.663 ± 0.022	Zeiger & Darling (2010)
8.4	1.236 ± 0.046	Patnaik et al. (1992)
8.085	1.02 ± 0.050	Kühr et al. (1981)
4.9	1.16 ± 0.01	Kühr et al. (1981)
4.85	1.498 ± 0.188	Gregory & Condon (1991)
4.83	1.74 ± 0.17	Griffith et al. (1990)

Table 2.8 | (continued)

ν (GHz)	S_ν (Jy)	Reference
	B0218+357 (cont)	
4.585	1.04 ± 0.05	Kühr et al. (1981)
4.84	1.383 ± 0.083	Patnaik et al. (1992)
2.9	0.69 ± 0.06	Jethava et al. (2007)
2.867	0.650 ± 0.16	Zeiger & Darling (2010)
2.695	1.03 ± 0.02	Kühr et al. (1981)
2.695	1.14 ± 0.06	Kühr et al. (1981)
1.415	0.770 ± 0.077	Patnaik et al. (1992)
1.41	1.25 ± 0.01	Kühr et al. (1981)
1.41	1.24 ± 0.06	Kühr et al. (1981)
	HE0230-2130	
667.0	0.077 ± 0.013	BI02
353.0	0.0210 ± 0.0017	BI02
109.0	< 0.0022	Riechers et al. (2011c)
1.4	< 0.0025	NVSS
	CFRS03.1077	
1.4	0.00038 ± 0.00012	FIRST
	B0414+054	
5000	0.18 ± 0.04	Lawrence et al. (1995)
3000	< 0.786	Lawrence et al. (1995)
667	$0.066 \pm 0.016^\dagger$	BI02
353	0.0253 ± 0.0018	BI02
231	0.0207 ± 0.0013	BI02
100	0.040 ± 0.002	BI02
15.0	0.381 ± 0.006	Hewitt et al. (1992)
10.7	0.38 ± 0.02	Kellermann & Pauliny-Toth (1973)
8.6	0.340 ± 0.034	Tingay et al. (2003)
6.1	0.71 ± 0.02	Castangia et al. (2011)
5.0	0.864 ± 0.015	Hewitt et al. (1992)
5.0	0.710 ± 0.071	Wright et al. (1990)
4.8	1.110 ± 0.154	Gregory & Condon (1991)
4.8	0.959 ± 0.051	Griffith et al. (1995)
2.7	1.130 ± 0.113	Wright et al. (1990)
2.5	1.200 ± 0.012	Tingay et al. (2003)
1.4	2.087 ± 0.074	NVSS

Table 2.8 | (continued)

ν (GHz)	S_ν (Jy)	Reference
	HE0435-1223	
5.0	$1.13 \pm 0.04 \times 10^{-4}$	Jackson et al. (2015)
	B0631+519	
15.0	0.034 ± 0.003	York et al. (2005)
8.4	0.042 ± 0.002	York et al. (2005)
4.8	0.089 ± 0.010	Gregory & Condon (1991)
1.4	0.0966 ± 0.0029	NVSS
	B0739+366	
667	0.036 ± 0.008	BI02
353	0.0066 ± 0.0013	BI02
231	< 0.0028	BI02
15	0.0219 ± 0.0019	Marlow et al. (2001)
8.4	0.0251 ± 0.0022	"
8.4	0.0241 ± 0.0021	"
5.0	0.0317 ± 0.0027	"
1.4	0.0279 ± 0.0010	NVSS
	MGJ0751+2716	
667	0.071 ± 0.015	BI02
353	0.0258 ± 0.0030	BI02
246	0.0067 ± 0.0013	Barvainis et al. (2002)
220	0.0043 ± 0.0008	Alloin et al. (2007)
110	0.0030 ± 0.0005	Alloin et al. (2007)
100	0.0041 ± 0.0005	BI02
82	0.0051 ± 0.0004	Alloin et al. (2007)
42	0.0132 ± 0.0010	Carilli et al. (2005)
15	0.048 ± 0.004	Lehar et al. (1997)
8.1	0.12 ± 0.01	Condon et al. (1983)
8.3	0.104 ± 0.001	Lehar et al. (1997)
4.8	0.191 ± 0.001	Lehar et al. (1997)
4.8	0.214 ± 0.028	Gregory & Condon (1991)
2.7	0.32 ± 0.02	Condon et al. (1983)
1.4	0.595 ± 0.018	NVSS

Table 2.8 | (continued)

ν (GHz)	S_ν (Jy)	Reference
	HS0810+2554	
5000.0	0.284 ± 0.040	Moshir et al. (1990)
3000.0	0.538 ± 0.156	Moshir et al. (1990)
353.0	0.0076 ± 0.0018	Priddey et al. (2003)
9.0	0.000278 ± 0.000007	Jackson et al. (2015)
1.4	0.000679 ± 0.000058	Jackson et al. (2015)
	HS0818+1227	
667.0	< 0.083	BI02
353.0	0.0046 ± 0.0017	BI02
1.4	< 0.001	FIRST
	APM08279+5255	
5000	0.511 ± 0.051	Irwin et al. (1998)
4300	0.654 ± 0.009	PACS catalog
3000	0.951 ± 0.228	Irwin et al. (1998)
1875	0.759 ± 0.010	PACS catalog
857	0.386 ± 0.032	Beelen et al. (2006)
667	0.342 ± 0.026	Beelen et al. (2006)
353	0.084 ± 0.003	Lewis et al. (1998)
302	0.060 ± 0.012	Krips et al. (2007)
250	0.034 ± 0.001	Lis et al. (2011)
246	0.031 ± 0.002	van der Werf et al. (2011)
237	0.027 ± 0.001	van der Werf et al. (2011)
231	0.024 ± 0.002	Lewis et al. (1998)
201	0.017 ± 0.001	van der Werf et al. (2011)
153	0.0054 ± 0.0003	van der Werf et al. (2011)
111	0.0022 ± 0.0002	Riechers et al. (2010)
109	0.0021 ± 0.0002	"
105	0.0020 ± 0.0001	"
90.8	0.00120 ± 0.00013	García-Burillo et al. (2006)
46.9	0.000405 ± 0.000330	Riechers et al. (2009)
23.5	0.000376 ± 0.000190	"
14.9	0.000303 ± 0.000093	"
8.4	0.000446 ± 0.000020	"
4.5	0.000551 ± 0.000400	"
1.4	0.00116 ± 0.00033	"
1.4	0.0015 ± 0.0003	NVSS

Table 2.8 | (continued)

ν (GHz)	S_ν (Jy)	Reference
	B0850+054	
15.0	0.031 ± 0.001	Biggs et al. (2003)
8.5	0.047 ± 0.001	"
5.0	0.064 ± 0.002	"
	RXJ0911+0551	
857	0.150 ± 0.021	Wu et al. (2009)
667	0.065 ± 0.019	BI02
353	0.027 ± 0.004	Hainline et al. (2004)
353	0.0267 ± 0.0014	BI02
230	0.0102 ± 0.0018	BI02
212.5	0.0047 ± 0.0010	Tuan-Anh et al. (2013)
100.0	0.0017 ± 0.0003	BI02
30.4	< 0.0017	Riechers et al. (2011b)
5.0	$1.28(\pm 0.05) \times 10^{-4}$	Jackson et al. (2015)
1.4	< 0.0002	Jackson et al. (2015)
	SDSSJ0924+0219	
5.0	$1.5(\pm 0.4) \times 10^{-5}$	Jackson et al. (2015)
	Q0957+561	
353	0.0075 ± 0.0014	BI02
231	< 0.004	BI02
100	< 0.0284	Planesas et al. (1999)
4.8	0.205 ± 0.022	Gregory & Condon (1991)
1.4	0.552 ± 0.017	NVSS
	IRAS F10214+4724	
5000	0.2 ± 0.045	Moshir et al. (1990)
3000	0.57 ± 0.14	Moshir et al. (1990)
857	0.38 ± 0.05	Benford et al. (1999)
667	0.27 ± 0.05	Rowan-Robinson et al. (1993)
375	0.050 ± 0.005	"
272	0.024 ± 0.005	"
8.4	0.00027 ± 0.00005	Lawrence et al. (1993)
4.86	0.00036 ± 0.00006	"
1.49	0.00118 ± 0.0001	"
1.4	0.0018 ± 0.0001	FIRST

Table 2.8 | (continued)

ν (GHz)	S_ν (Jy)	Reference
	SDSSJ1029+2623	
5.0	$6.43(\pm 0.23) \times 10^{-4}$	Kratzer et al. (2011)
	CLASS B1030+074	
216	0.114 ± 0.010	Xanthopoulos et al. (2001)
144	0.225 ± 0.012	"
112	0.246 ± 0.012	"
100	0.184 ± 0.002	Barvainis et al. (2002)
22	0.320 ± 0.030	Lee et al. (2017)
22	0.231 ± 0.012	Xanthopoulos et al. (1998)
15	0.319 ± 0.016	"
15	0.223 ± 0.015	"
15	0.290 ± 0.004	Richards et al. (2011)
8.4	0.210 ± 0.011	Xanthopoulos et al. (1998)
8.4	0.218 ± 0.011	Xanthopoulos et al. (1998)
8.4	0.203 ± 0.0003	Xanthopoulos et al. (2001)
5.0	0.353 ± 0.018	Xanthopoulos et al. (1998)
4.85	0.364 ± 0.051	Gregory & Condon (1991)
4.85	0.356 ± 0.052	Becker et al. (1991)
4.85	0.242 ± 0.016	Griffith et al. (1995)
4.85	0.341 ± 0.005	Xanthopoulos et al. (2001)
4.775	0.219 ± 0.20	Bennett et al. (1986)
1.7	0.258 ± 0.013	Xanthopoulos et al. (1998)
1.4	0.163 ± 0.004	White & Becker (1992)
1.4	0.155 ± 0.004	NVSS
1.4	0.156 ± 0.005	Xanthopoulos et al. (2001)
	HE1104-1805	
353	0.015 ± 0.003	BI02
231	0.0053 ± 0.0009	BI02
100	< 0.0022	BI02
1.4	< 0.0025	NVSS

Table 2.8 | (continued)

ν (GHz)	S_ν (Jy)	Reference
	PG1115+080	
353	0.0037 ± 0.0013	BI02
231	< 0.003	BI02
104	< 0.0015	Riechers et al. (2011c)
100	< 0.005	BI02
1.4	< 0.00094	FIRST
	B1127+385	
667	< 0.065	BI02
353.0	0.014 ± 0.002	BI02
231	< 0.0028	BI02
8.4	0.027 ± 0.002	Koopmans et al. (1999)
5.0	0.027 ± 0.002	Koopmans et al. (1999)
4.85	0.041 ± 0.007	Gregory & Condon (1991)
4.85	0.037 ± 0.006	Becker et al. (1991)
1.7	0.030 ± 0.002	Koopmans et al. (1999)
1.4	0.029 ± 0.001	Becker et al. (1995)
	RX J1131-1231	
216.0	< 0.0025	Leung et al. (2017)
144.1	0.00195 ± 0.00020†	Paraficz et al. (2018)
139.3	0.00039 ± 0.00012†	Leung et al. (2017)
4.9	0.00127 ± 0.00004	Leung et al. (2017)
1.4	< 0.028	FIRST
	B1152+200	
667	< 0.07	BI02
353	< 0.0065	BI02
14.94	0.0581 ± 0.0004	Myers et al. (1999)
8.46	0.0695 ± 0.0005	Myers et al. (1999)
4.85	0.070 ± 0.0011	Gregory & Condon (1991)
1.4	0.0774 ± 0.008	NVSS

Table 2.8 | (continued)

ν (GHz)	S_ν (Jy)	Reference
	Q1208+101	
353	0.0081 ± 0.0020	BI02
250	0.0042 ± 0.0019	Andreani et al. (1999)
231	0.003 ± 0.001	BI02
100	< 0.0009	BI02
1.4	< 0.00095	FIRST
	SDSSJ1330+1810	
1.4	< 0.0002	Stacey (2015)
	SDSSJ1353+1138	
1.4	0.0005 ± 0.00015	FIRST
	B1359+154	
667	$0.039 \pm 0.010^{\dagger}$	BI02
353	0.012 ± 0.002	BI02
96.4	0.00360 ± 0.00018	Riechers et al. (2011c)
14.94	0.01625 ± 0.0009	Myers et al. (1999)
8.46	0.0279 ± 0.0014	Myers et al. (1999)
4.8	0.066 ± 0.010	Becker et al. (1991)
1.4	0.115 ± 0.035	NVSS
	B1422+231	
22.5	0.145 ± 0.015	Tinti et al. (2005)
15.0	0.251 ± 0.013	"
8.5	0.460 ± 0.016	"
8.1	0.479 ± 0.016	"
4.9	0.669 ± 0.020	"
4.5	0.686 ± 0.021	"
1.7	0.414 ± 0.012	"
1.4	0.352 ± 0.011	"

Table 2.8 | (continued)

ν (GHz)	S_ν (Jy)	Reference
	H1413+117	
5080	0.207 ± 0.051	Weiß et al. (2003)
5000	0.230 ± 0.078	Barvainis et al. (1995)
3261	0.266 ± 0.050	Weiß et al. (2003)
3000	0.370 ± 0.078	Barvainis et al. (1995)
2520	0.356 ± 0.048	Weiß et al. (2003)
1630	0.240 ± 0.095	Weiß et al. (2003)
1500	0.280 ± 0.014	Rowan-Robinson (2000)
870	0.189 ± 0.056	Barvainis et al. (1992)
857	0.376 ± 0.015	Weiß et al. (2003)
857	0.293 ± 0.014	Benford et al. (1999)
685	0.224 ± 0.038	Barvainis et al. (1992)
394	0.044 ± 0.008	Barvainis et al. (1992)
375	0.066 ± 0.007	Hughes et al. (1997)
353	0.059 ± 0.008	BI02
250	0.016 ± 0.002	Weiß et al. (2003)
240	0.018 ± 0.002	Barvainis et al. (1995)
230	0.0075 ± 0.0006	Weiß et al. (2003)
100	< 0.0015	Weiß et al. (2003)
92.9	0.0003 ± 0.0001	Stacey et al. in prep
24.0	0.00026 ± 0.00003	Solomon et al. (2003)
14.9	0.00056 ± 0.00018	Barvainis et al. (1997)
8.5	0.00098 ± 0.00008	"
4.9	0.00195 ± 0.00013	"
1.5	0.00768 ± 0.00050	"
1.4	0.0082 ± 0.0006	NVSS
	SBS1520+530	
353	< 0.0078	BI02
250	< 0.0042	BI02
100	< 0.0006	BI02
1.4	< 0.001	FIRST

Table 2.8 | (continued)

ν (GHz)	S_ν (Jy)	Reference
	B1600+434	
353	0.0073 ± 0.0018	BI02
300	0.0126 ± 0.0023	BI02
100	0.0250 ± 0.0003†	BI02
15	0.042 ± 0.002	Waldram et al. (2003)
8.4	0.132 ± 0.013	Jackson et al. (1995)
4.8	0.037 ± 0.007	Gregory & Condon (1991)
1.4	0.079920 ± 0.000145	FIRST
	B1608+656	
353.0	0.0081 ± 0.0017	BI02
300.0	< 0.0066	Xanthopoulos et al. (2001)
231.0	0.0056 ± 0.0017	BI02
100.0	0.0081 ± 0.0004	BI02
15	0.081 ± 0.004	Snellen et al. (1995)
8.4	0.083 ± 0.004	Snellen et al. (1995)
8.4	0.0732 ± 0.0020	Myers et al. (1995)
4.8	0.0920 ± 0.0090	Gregory & Condon (1991)
1.4	0.063 ± 0.003	Snellen et al. (1995)
	FBQS1633+3134	
353.0	< 0.0035	BI02
1.4	0.00177 ± 0.00014	FIRST

Table 2.8 | (continued)

ν (GHz)	S_ν (Jy)	Reference
	PMN J1632-0033	
43.34	0.089 ± 0.014	Winn et al. (2002)
43.34	0.112 ± 0.006	Winn et al. (2004)
22.46	0.135 ± 0.014	Winn et al. (2002)
22.46	0.161 ± 0.008	Winn et al. (2004)
22.46	0.158 ± 0.008	Winn et al. (2004)
14.94	0.153 ± 0.007	Winn et al. (2002)
14.94	0.187 ± 0.009	Winn et al. (2004)
14.94	0.195 ± 0.010	Winn et al. (2004)
8.64	0.177 ± 0.005	Winn et al. (2002)
8.46	0.220 ± 0.011	Winn et al. (2004)
8.46	0.227 ± 0.011	"
8.46	0.211 ± 0.011	"
8.46	0.152 ± 0.008	McKean et al. (2007)
8.45	0.165 ± 0.030	Winn et al. (2002)
8.44	0.160 ± 0.040	"
6.1	0.201 ± 0.006	"
5.0	0.191 ± 0.020	"
5.0	0.222 ± 0.011	Winn et al. (2003)
4.8	0.233 ± 0.007	Winn et al. (2002)
4.86	0.223 ± 0.011	Winn et al. (2002)
4.86	0.204 ± 0.010	McKean et al. (2007)
4.85	0.270 ± 0.040	Becker et al. (1991)
3.9	0.235 ± 0.047	Larionov et al. (1994)
2.7	0.200 ± 0.040	Wright et al. (1990)
1.4	0.230 ± 0.012	Winn et al. (2002)
1.4	0.236 ± 0.047	White & Becker (1992)

Table 2.8 | (continued)

ν (GHz)	S_ν (Jy)	Reference
	PKS 1830−211	
353	0.79 ± 0.17	Giommi et al. (2012)
300	0.8 ± 0.1	Martí-Vidal et al. (2013)
250	0.9 ± 0.1	Martí-Vidal et al. (2013)
229	1.23 ± 0.06	Agudo et al. (2010)
217	1.18 ± 0.08	Giommi et al. (2012)
143	1.64 ± 0.07	Giommi et al. (2012)
100	2.0 ± 0.02	Muller et al. (2006)
100	2.47 ± 0.11	Giommi et al. (2012)
86	1.76 ± 0.09	Agudo et al. (2010)
70	2.44 ± 0.22	Giommi et al. (2012)
44	3.42 ± 0.36	Giommi et al. (2012)
33	4.12 ± 0.24	Massardi et al. (2009)
30	4.11 ± 0.33	Giommi et al. (2012)
23	5.08 ± 0.22	Massardi et al. (2009)
20	5.50 ± 0.36	Massardi et al. (2008)
14	6.45 ± 0.65	Henkel et al. (2008)
12.8	8.12 ± 0.81	Henkel et al. (2008)
8.4	6.59 ± 0.66	Wright et al. (1990)
6.55	9.74 ± 0.97	Ellingsen et al. (2012)
5	8.9 ± 0.9	Wright et al. (1990)
4.9	7.92 ± 0.10	Griffith et al. (1994)
2.7	9.3 ± 0.93	Wright et al. (1990)
1.4	10.90 ± 0.33	NVSS
	PMN J1838−3427	
20	0.234 ± 0.012	Murphy et al. (2010)
14.94	0.181 ± 0.009	Winn et al. (2000)
8.64	0.264 ± 0.009	"
8.46	0.206 ± 0.006	"
8.46	0.181 ± 0.005	"
8	0.284 ± 0.014	Murphy et al. (2010)
5	0.299 ± 0.015	Murphy et al. (2010)
4.86	0.214 ± 0.006	Winn et al. (2000)
4.85	0.258 ± 0.021	Wright et al. (1990)
4.80	0.219 ± 0.007	Winn et al. (2000)
2.7	0.240 ± 0.048	Wright et al. (1990)
1.4	0.280 ± 0.008	NVSS

Table 2.8 | (continued)

ν (GHz)	S_ν (Jy)	Reference
	B1933+503	
3000	< 0.443	Chapman et al. (1999)
667	0.114 ± 0.017	"
353	0.0240 ± 0.0026	"
231	0.030 ± 0.007	"
15	0.0371 ± 0.0011	Sykes et al. (1998)
8.4	0.0410 ± 0.0011	"
5.0	0.0575 ± 0.0057	"
1.7	0.0759 ± 0.0075	"
	B1938+666	
667	0.126 ± 0.022	BI02
353	0.0346 ± 0.0020	BI02
231	0.0147 ± 0.0020	BI02
97	0.0200 ± 0.0014	Riechers et al. (2011c)
22	0.088 ± 0.009	King et al. (1997)
15	0.141 ± 0.14	King et al. (1997)
8.4	0.224 ± 0.022	Patnaik et al. (1992)
4.8	0.314 ± 0.047	Becker et al. (1991)
4.8	0.316 ± 0.028	Gregory & Condon (1991)
1.4	0.5768 ± 0.0173	NVSS
1.4	0.634 ± 0.063	FIRST
ν (GHz)	S_ν (Jy)	Reference
	PMNJ2004-1349	
22.46	0.0164 ± 0.002	Winn et al. (2001)
14.96	0.0205 ± 0.0010	"
8.46	0.0294 ± 0.0090	"
5.0	0.030 ± 0.002	"
4.8	0.073 ± 0.011	Griffith et al. (1994)
1.4	0.079 ± 0.08	NVSS
	MGJ2016+112	
353.0	< 0.0048	Barvainis et al. (2002)
231.0	< 0.0025	"
100.0	0.0018 ± 0.0002	"
4.8	0.098 ± 0.010	Bennett et al. (1986)
1.4	0.1911 ± 0.0058	NVSS

Table 2.8 | (continued)

ν (GHz)	S_ν (Jy)	Reference
	B2114+022	
353.0	< 0.0043	BI02
87	< 0.030	Xanthopoulos et al. (2001)
15.0	0.051 ± 0.002	Augusto et al. (2001)
8.4	0.100 ± 0.002	"
5.0	0.156 ± 0.016	"
5.0	0.230 ± 0.023	Wright et al. (1990)
4.85		Griffith et al. (1990)
4.85	0.136 ± 0.003	Vollmer et al. (2008)
4.775		Bennett et al. (1986)
2.6		Wright et al. (1990)
1.7	0.148 ± 0.015	Augusto et al. (2001)
1.4	0.137 ± 0.004	NVSS
	HE2149-2745	
353.0	0.008 ± 0.002	BI02
100.0	< 0.0064	BI02
1.4	< 0.0025	NVSS
	Q2237+030	
667	< 0.017	BI02
353	0.0039 ± 0.0012	BI02
250	< 0.0064	BI02
100	< 0.0008	BI02
8.4	0.000593 ± 0.000088	Falco et al. (1996)
1.5	0.000832 ± 0.000087	Falco et al. (1996)
	B2319+052	
667.0	0.040 ± 0.008	BI02
353.0	0.0039 ± 0.0012	BI02
231.0	< 0.003	BI02
15.0	0.0182 ± 0.0006	Rusin et al. (2001)
8.4	0.0308 ± 0.0001	"
5.0	0.0666 ± 0.0001	"
1.4	0.0853 ± 0.0004	"

Table 2.8 | (continued)

ν (GHz)	S_ν (Jy)	Reference
	PSSJ2322+1944	
4300	$0.0137 \pm 0.0061^{\dagger}$	PACS catalog
1875	$0.0434 \pm 0.0084^{\dagger}$	PACS catalog
660	0.075 ± 0.019	Cox et al. (2002)
353	0.0225 ± 0.0025	Isaak et al. (2002)
353	0.024 ± 0.002	Cox et al. (2002)
231	0.0096 ± 0.0005	Omont et al. (2001)
225	0.0075 ± 0.0013	Cox et al. (2002)
90	< 0.00064	Cox et al. (2002)
5.0	$< 9 \times 10^{-5}$	Carilli et al. (2001)
1.4	$9.8(\pm 1.5) \times 10^{-5}$	Carilli et al. (2001)

2.C. Notes on individual sources

We discuss the results for a few individual sources of note.

2.C.1. HS 0810+2554

HS 0810+2554 is an outlier of our sample in several respects. It has a high effective dust temperature ($T_{\rm d} = 89.0^{+6.5}_{-6.0}$ K) and the lowest dust emissivity index ($\beta = 1.0 \pm 0.2$) of our sample. Such a high dust temperature is more consistent with dust heated by the AGN than star formation (e.g. APM 08279+5255; Weiß et al. 2007).

Despite its weak radio flux-density (~ μJy), this source has a mas-scale radio jet that is the major contributor to its radio emission (Hartley et al., 2019). Radio observations with the VLA and the Multi-Element Radio Linked Interferometer Network (e-MERLIN) also imply a compact radio-emitting region with a scale of 70 pc (Jackson et al., 2015). However, we find this source falls below the radio–infrared correlation, rather than above as would be expected for a source with a radio excess.

The emissivity index of 1.0 is lower than the typically observed values of $\beta = 1.5$–2 for star-forming galaxies. These properties could be a result of composite dust emission from both AGN and star formation heating, similar to that observed in APM 08279+5255, IRAS F10214+4724 and the Cloverleaf (Beelen et al., 2006). Differential magnification could be responsible for a boosting of the more compact AGN-heated component.

The measured $L_{\rm FIR}$ and star formation rate given in Table 2.7 of this Appendix are from a single-temperature model, and likely an overestimate the actual properties of this quasar. Additional data, taken at mm and sub-mm wavelengths will be needed to properly separate the two components of the true SED.

We try fitting a two-component dust model, one of fixed temperature 38 K (the median fitted dust temperature of the sample) and leave the second temperature as a free parameter, both with fixed $\beta = 1.5$. We find a fit for the warmer component of $84.4^{+6.5}_{-5.7}$ K and derive a FIR luminosity of $3.7^{+1.7}_{-2.3} \times 10^{12}$ $L_\odot$ for the cold component: almost an order of magnitude lower than that from the single-temperature model. The result is consistent within 2σ with the radio–infrared correlation and falls amid non-jetted sources.

2.C.2. RX J1131-1231

RX J1131−1231 is one of the lower redshift quasars in our sample, at $z = 0.67$. The quasar is known to have a radio jet based on JVLA observations (Wucknitz & Volino, 2008). Leung et al. (2017) observed RX J1131−1231 with the Plateau de Bure Interferometer (PdBI) and Combined Array for Research in Millimeter-wave Astronomy (CARMA) at 2.2 and 3 mm, respectively. They derive star-forming properties of this source by fitting an SED, assuming both the PdBI measurement and CARMA upper-limit describe the Rayleigh-Jeans slope of the modified black-body. We consider these data and also include a recent ALMA observation at 2.1 mm (Paraficz et al., 2018), however, we find significant differences between the ALMA 2.1 mm and PdBI 2.2 mm measurements. Paraficz et al. propose the difference is due to a contribution from synchrotron emission at the base of the jet associated with the AGN, which could be either highly variable, or so compact ($\sim 10^{-4}$ pc) that micro-lensing may be changing the flux-density over time-scales of months (the observations were performed 5–7 months apart: PdBI between December 2014 and February 2015; ALMA in July 2015). We include only the *Herschel*/SPIRE measurements and the CARMA upper limit to constrain the thermal dust emission, finding a relatively low dust temperature of $T_{\rm d} = 21^{+6}_{-4}$ K and a high emissivity index of $\beta = 2.7^{+1.0}_{-0.7}$, however, this is not robust as the peak is poorly constrained. We do not attempt to fit a synchrotron component due to the uncertainties discussed here and by Paraficz et al. (2018). Further high and low wavelength data are needed to better constrain the dust temperature and $L_{\rm FIR}$, and characterise the millimetre emission for this object.

2.C.3. H 1413+117

The *Cloverleaf* quasar (H 1413+117) has been studied extensively over the past ∼20 years as it is one of the most FIR-luminous gravitationally-lensed quasars known, and so there are many measurements in the literature that cover the full infrared SED. The SED can be resolved into two dust peaks that are presumably due to heating by both star formation ($T_d = 35.6 \pm 0.6$ K) and AGN activity ($T_d = 125.6^{+10.6}_{-8.9}$ K). We find this quasar falls above the radio–infrared correlation with a $q_{\rm IR}$ value of 1.42 ± 0.01, consistent with jet emission known to exist in this source based on radio observations with e-MERLIN (Stacey et al. in prep).

With the addition of the *Herschel*/SPIRE data, we see clear differences in the measurements around the lower-temperature peak over a period of ∼20 years. This is most obvious with the four measurements around 350 μm, which have increased intermittently to a factor of 2 relative to the first measurement by Barvainis et al. (1992).

This is likely the effect of calibration errors in previous measurements rather than intrinsic variability.

The spread of the data causes uncertainty in the SED fitting as the AGN contribution and Rayleigh-Jeans slope are not well constrained. However, the new *Herschel*/SPIRE data constrain the peak of the SF-heated dust component accurately, thus, assuming the contribution from the AGN component is small at those wavelengths, the effect of the uncertainty on the derived FIR luminosity due to star formation is not significant.

2.C.4. PKS 1830-211

PKS 1830−211 is a radio-powerful gravitationally-lensed blazar; a radio source that is being viewed directly down the line-of-sight of the relativistic jet (Martí-Vidal et al., 2013). The SED appears to be dominated by synchrotron emission from the radio through to the FIR measured with *Herschel*/SPIRE. While there appears to be a tentative suggestion that the synchrotron component begins to fall off towards the FIR, this is far from clear because this source is highly variable. We fit the data > 10 GHz with both a simple power-law, typical of optically-thin synchrotron emission, and a function that includes a modified black-body (leaving the temperature as a free parameter) to account for the possibility of a contribution from thermal dust. We assume this grey-body represents an upper limit on the star-forming properties, meaning there could be underlying dust-obscured star formation in the host galaxy at a rate as high as $\sim 1000\ \mathrm{M_\odot\ yr^{-1}}$. The data are also consistent with a simple power law of $\alpha = -0.5$ that begins to flatten ~ 10 GHz.

Interferometry

Tequila and Tabasco, as a ski shot.

3

Surveying quasar host galaxies with gravitational lensing

I. Disentangling star formation and AGN activity in radio-quiet quasars at low radio frequencies

H. R. Stacey, J. P. McKean, N. J. Jackson, P. N. Best, G. Calistro Rivera, J. R. Callingham, K. J. Duncan, G. Gürkan, M. J. Hardcastle, M. Iacobelli, A. P. Mechev, L. K. Morabito, I. Prandoni, H. J. A. Röttgering, J. Sabater, T. W. Shimwell, C. Tasse and W. L. Williams

Based on "LoTSS/HETDEX: Disentangling star formation and AGN activity in gravitationally lensed radio-quiet quasars"
Stacey et al. 2019, Astronomy & Astrophysics, Volume 622, A18

Abstract

Determining the star-forming properties of radio-quiet quasars is important for understanding the co-evolution of star formation and black hole accretion. Here, we present the detection of the gravitationally lensed radio-quiet quasars SDSS J1055+4628, SDSS J1313+5151 and SBS 1520+530 at 144 MHz that fall in the HETDEX Spring Field targeted in the LOFAR Two-metre Sky Survey (LoTSS) first full data release. We compare their radio and far-infrared luminosities relative to the radio–infrared correlation and find that their radio luminosities can be explained by star formation. The implied star formation rates derived from their radio and infrared luminosities are between 20 and 300 $M_\odot$ yr^{-1}. These detections represent the first study of gravitationally lensed sources with LOFAR, opening a new frequency window for investigating the star-forming properties of high redshift quasars at radio wavelengths. We consider the implications for future data releases and estimate that many of the objects in our parent sample will be detected during LoTSS, significantly increasing the fraction of gravitationally lensed radio-quiet quasars with radio detections.

3.1. Introduction

The star formation history of galaxies is thought to be strongly linked with black hole accretion, as evidenced through the peak in the activity of these two processes at $z \sim 2$ (Madau & Dickinson, 2014), and through the correlation between bulge luminosity and black hole mass (Magorrian et al., 1998; Ferrarese & Merritt, 2000; Gebhardt et al., 2000). Hydrodynamical simulations suggest that feedback from active galactic nuclei (AGN) is required to regulate star formation in the most massive galaxies in the Universe (Di Matteo et al., 2005; Springel et al., 2005; Bower et al., 2006). The mechanism of AGN feedback may take the form of jets or winds, which mechanically eject gas from the host galaxy and deplete the reservoir of cold gas, or through radiative heating, which ionises the cold gas to quench star formation (see Fabian, 2012, for review). A key test of this evolutionary scenario, therefore, is the star-forming properties of quasar host galaxies, most of which are expected to be dusty and gas-rich (Hopkins et al., 2005).

Investigations of star formation in the high redshift Universe often focus on the far-infrared (FIR), which probes the cold dust of the interstellar medium (ISM) in the star-forming disc, or on radio wavelengths, which provide a view of star formation that is unobscured by dust. A major challenge in characterising star formation in quasar host galaxies has been sensitivity limitations. For the case of FIR–sub-mm instruments, these have historically detected the most extreme star-forming–quasar composites at high redshifts (Isaak et al., 2002; Priddey et al., 2003; Pitchford et al., 2016, for example). Similarly, radio synchrotron emission from all but the most extreme star-forming regions is faint and hard to detect. While progress in the FIR–sub-mm is being made with the Atacama Large (sub-)Millimetre Array (ALMA; e.g. Stanley et al. 2018), and in the radio with deep, wide-field surveys such as with the Karl G. Jansky Very Large Array (VLA; e.g. Smolčić et al. 2017) and the Low Frequency Array (LOFAR; Rottgering et al. 2006), in both of these wavelength regimes there may also be a contribution due to black hole accretion, that is, from radio core/jet emission or AGN-heated dust emission, which is difficult to disentangle (e.g. Zakamska et al., 2016).

Understanding the relative contributions of star formation and black hole accretion is evidently important, not only to infer star formation rates (SFRs), but to understand the AGN feedback mechanisms involved. The well-established radio–infrared correlation for star-forming galaxies has been employed to determine if there is a radio excess due to radio jet emission (Sopp & Alexander, 1991). For radio-bright, jetted radio sources, we expect an excess of radio emission, however the majority of quasars are radio-'quiet' (i.e. have faint or undetected radio counterparts). Previous studies of optically-selected AGN have had conflicting results on their primary radio emission mechanism; some find this emission largely consistent with star formation (Barthel, 2006; de Vries et al., 2007; Condon et al., 2013), while others find that the

AGN dominates (White et al., 2015, 2017). Studies of radio-selected samples also point towards primarily star formation (Padovani et al., 2011; Bonzini et al., 2013, 2015) or AGN emission (Maini et al., 2016; Herrera Ruiz et al., 2016, 2017) or a composite of both (Delvecchio et al., 2017). These studies have typically focused on low redshift AGN or brighter-selected sources, or have detected fainter sources through stacking the optical positions of many undetected sources.

By taking advantage of the magnification effect of gravitational lensing, we can probe the FIR and radio properties of individual sources at high redshifts that otherwise would not be detectable. Chapter 2 reported the results from a survey of 104 gravitationally lensed quasars ($z \sim 1$–4) that were observed with the SPIRE instrument aboard the *Herschel Space Observatory* at 250, 350 and 500 μm, with which intrinsic flux densities below the confusion limit of the telescope could be probed. Under the assumption that the cold dust heating was due to star formation, they derived SFRs for the majority of the sample and upper-limits for the remaining sources. In general, high levels of dust-obscured star formation were found with a median of 120^{+160}_{-80} $M_\odot$ yr^{-1}. While largely consistent with evolutionary models (e.g. Mancuso et al., 2016), the SFRs in the sample reach up to 10^4 $M_\odot$ yr^{-1} in the most extreme case. The radio-quiet quasars in the sample were found to be scattered close to the radio–infrared correlation with no general infrared excess that would suggest there is a significant contribution to the FIR luminosity from AGN heating. In addition, the median cold dust temperature of the sample was 38^{+12}_{-5} K, which is consistent with the population of starburst galaxies at similar redshifts, and only a handful of the lensed quasars in the sample had dust temperatures larger than 50 K, which would suggest additional heating of the dust by the AGN. These high SFRs are difficult to reconcile with the expected luminosity functions of starburst galaxies (Symeonidis & Page, 2018) and are in tension with current cosmological simulations (e.g. Davé et al., 2010). Thus, independent measurements of the star formation and AGN activity are needed.

However, such investigations are limited by the fact that the majority of the sample are currently undetected at radio wavelengths; almost all of the radio data for the radio-quiet sub-sample, as for most studies of large samples of quasars, come from the Faint Images of the Radio Sky at Twenty Centimeters (FIRST) survey (Becker et al., 1995) or the NRAO VLA Sky Survey (NVSS) (Condon et al., 1998), which have detection limits of $S_{1.4\ \mathrm{GHz}} > 1$ mJy and $S_{1.4\ \mathrm{GHz}} > 2.5$ mJy, respectively. As optically-thin synchrotron emission from star-forming galaxies or AGN typically has a negative spectral index, observed radio luminosities are larger at lower frequencies. Therefore, using observations with the new low-frequency interferometric arrays, such as LOFAR (van Haarlem et al., 2013), we can increase our rate of detection at the same given sensitivity. As there are currently no survey instruments capable of observing at 40–100 μm, where AGN-heated dust at $z \sim 2$ dominates in the observed-frame, low-frequency

radio observations present an alternative method of identifying these extreme cases where the radiative output from the AGN is heating the cold dust at FIR wavelengths.

In this chapter, we report on the radio properties of three gravitationally lensed quasars from the Chapter 2 sample that are detected with the LOFAR Two-metre Sky Survey (LoTSS, Shimwell et al. 2017) of the HETDEX Spring Field. Our aim is to determine whether the radio emission from these quasars is consistent with what we would expect from the radio–infrared correlation, further adding to the case that these objects are also undergoing extreme bursts of star formation. Alternatively, we may find evidence for a radio or FIR excess, which would suggest that the AGN is contributing to the radio or heated dust emission, respectively. Either of these outcomes would also be interesting, as these quasars are thought to be radio-quiet, and detecting AGN-heated dust is difficult due to the thermal spectrum peaking at FIR wavelengths much shorter than the atmospheric cut-off. In Section 3.2, we review the quasars, and in Section 3.3, we summarise the radio data. In Section 3.4, we compare the radio and FIR properties relative to the radio–infrared correlation. The implications of our findings and future prospects are discussed in Section 3.5. Finally, we present our conclusions in Section 3.6.

Throughout, we assume the Planck Collaboration et al. (2016) instance of a flat ΛCDM cosmology with $H_0 = 67.8\ \mathrm{km\,s^{-1}\ Mpc^{-1}}$, $\Omega_\mathrm{M} = 0.31$ and $\Omega_\Lambda = 0.69$.

3.2. Sample

The targets of our pilot study are three lensed quasars from the *Herschel*/SPIRE parent sample introduced in Chapter 2 that fall in the LoTSS observations of the HETDEX Spring Field. All of these quasars were discovered at optical wavelengths, have two lensed images, and are undetected at 1.4 GHz in FIRST (Becker et al., 1995). Dust temperatures and FIR-derived luminosities and SFRs (uncorrected for lensing magnification) are summarised in Table 3.1. The lensing magnifications of the radio and FIR emission for these systems are unknown, but are typically a factor of ∼ 10 based on analyses of high-resolution data of other lensed AGN (see Chapter 2 for details).

3.2.1. SDSS J1055+4628

SDSS J1055+4628 (SDSS J105545.45+462839.4) was discovered in the Sloan Digital Sky Survey (SDSS) Quasar Lens Search (SQLS) by Kayo et al. (2010). The quasar is at $z_s = 1.25$ and is gravitationally lensed by a foreground galaxy at $z_l = 0.39$. The

separation between the two lensed images is 1.15″. This system was undetected in *Herschel*/SPIRE, implying a limit on the lensing-corrected SFR of < 44 $M_\odot$ yr^{-1}, assuming the median fitted dust temperature of the parent sample and a magnification factor of 10.

3.2.2. SDSS J1313+5151

SDSS J1313+5151 (SDSS J131339.98+515128.4) was discovered in the SQLS by Ofek et al. (2007). The background quasar is at $z_s = 1.88$ and is gravitationally lensed into two images with a separation of 1.24″ by a foreground galaxy at $z_l = 0.19$. Heated dust emission that is assumed to be from the quasar host galaxy was detected only in the 250 μm band, and is equivalent to a lensing-corrected SFR of 160^{+170}_{-80} $M_\odot$ yr^{-1}, based on the median and distribution of dust temperatures of the sample, and assuming a typical magnification of 10.

3.2.3. SBS 1520+530

SBS 1520+530 is a gravitationally lensed quasar at $z_s = 1.86$ that was discovered in the Second Byurakan Survey (Chavushyan et al., 1997). The primary lensing galaxy is at $z_l = 0.72$ (Burud et al., 2002). There is also evidence for a secondary lensing galaxy with a photometric redshift of $z_l \simeq 0.9$ (Faure et al., 2002). The two lensed images are separated by 1.59″. Chapter 2 reported dust emission, likely from the quasar host galaxy, at 250 μm and 350 μm, and blended emission at 500 μm that included flux from nearby stars. The fitted dust temperature is $46.2^{+12.7}_{-7.2}$ K and the derived lensing-corrected SFR is 190^{+100}_{-60} $M_\odot$ yr^{-1} assuming a typical magnification of 10. The peak of the dust emission is not well constrained, hence there are large uncertainties in the derived dust temperature and FIR luminosity for this object.

3.3. Data

3.3.1. LOFAR LoTSS-DR1 data

The LoTSS-DR1 data set is described in detail by Shimwell et al. (2017). To summarise, the first public data release of high quality survey images from LOFAR encompassed

424 square degrees that are coincident with the HETDEX Spring Field. In total, 325 694 radio sources were detected at the 5σ-level with an angular resolution of $6''$. The median rms noise is ~ 71 μJy beam^{-1}, which is equivalent to a factor of about 10 times improvement in sensitivity when compared to the FIRST survey, accounting for the typical spectral index of synchrotron emission ($\alpha_{144}^{1400} \sim -0.7$) between 144 MHz and 1.4 GHz.

We first carried out a search of the LoTSS-DR1 sky coverage for known gravitationally lensed quasars, finding that the positions of the three targets described in Section 3.2 were within the survey footprint. The properties of the radio-counterparts of these objects were then extracted from the LOFAR data using the software PyBDSF (Mohan & Rafferty, 2015), which fits 2-dimensional Gaussian models to the image-plane maps, as described by Shimwell et al. (2017). The fitted positions of these sources in the LOFAR data are within the errors of the optical positions given by SDSS for SDSS J1055+4628 and SDSS J1313+5151, and from observations with the *Hubble Space Telescope* (*HST*) for SBS 1520+530 (Faure et al., 2002).

The best quality optical imaging available for the three targets, with the contours from the LOFAR imaging overlaid, are presented in Figure 3.1, and the properties of the 144 MHz radio emission derived from the Gaussian fits are given in Table 3.2.

3.3.2. Archival VLA data

Previous investigations with the VLA have targeted SBS 1520+530; it was observed on 1997 August 28 at 1.4 GHz, with 20 minutes on source, under programme AH632. These data were extracted from the NRAO archive* and calibrated using the Common Astronomy Software Applications (CASA) package in a standard way, using 3C286 to set the absolute flux scale and nearby phase calibrators to trace and remove phase and amplitude variations. A $2'$ error in the pointing position of the phase calibrator was corrected for during this process.

The rms noise level in the map is 65 μJy beam^{-1}, although there are artefacts at the 200–300 μJy beam^{-1} level due to a combination of residual phase errors and incomplete u-v coverage. There is a positive spike of 280 μJy beam^{-1} around the position of the source, but due to the quality of the map it is not clear whether this is a noise artefact. Therefore, we assume 280 μJy as an upper limit for the flux density of SBS 1520+530 at 1.4 GHz.

In addition, only SBS 1520+530 is currently covered in the 3 GHz VLA Sky Survey (VLASS) preliminary data release (Myers & VLASS Survey Team, 2018). The object is

*https://archive.nrao.edu

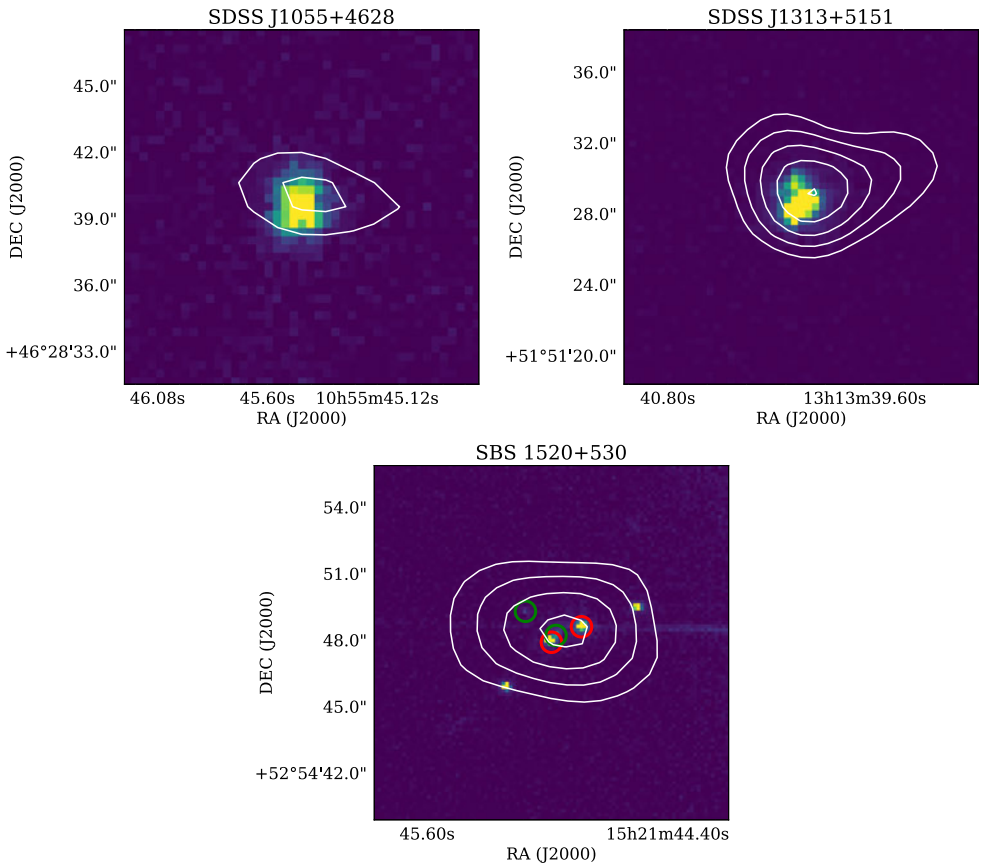

Figure 3.1 | The optical counterparts of the three gravitationally lensed quasars, with the 144 MHz LoTSS contours overlaid. The contours shown are at the 3σ, 4σ, 5σ, 6σ and 7σ level, where σ is the off-source rms noise (given in Table 3.2). For SDSS J1055+4826 and SDSS J1313+5151, we show the SDSS g-band images. For SBS 1520+350, we show the *HST* V-band (F555W filter). For SBS 1520+350, the quasar images are indicated with the red circles, and the primary and secondary lensing galaxies are marked with the green circles; the unlabelled objects are foreground stars.

not detected with an rms noise level of 110 μJy beam^{-1}.

3.4. Results

3.4.1. LOFAR detections

All three gravitationally lensed quasars in the HETDEX footprint are detected in the LoTSS imaging between 6 to 9σ, based on the total flux-density, with peak surface brightness at the 4 to 7σ-level (see Figure 3.1). The quality of the data for SBS 1520+530 is lower than for the other two targets, as it is located at the edge of the field where the primary beam response is lower and is also affected by the residual side-lobes from a bright source nearby. While the emission from all three gravitational lens systems appears to be marginally resolved, unresolved sources are artificially broadened in these data, perhaps due to a combination of ionospheric effects, astrometric errors or calibration quality, as discussed by Shimwell et al. (2017). Criteria established by Shimwell et al. (2017) classify these sources as unresolved, which is consistent with the 6″ beam-size of the observations and the 1.2″ to 1.6″ separations of the lensed images. We use the integrated flux density for the rest of our analysis, as the peak surface brightness of a point source is likely to be underestimated.

With the 144 MHz flux densities provided by LoTSS, we are now able to estimate the rest-frame 1.4 GHz luminosities for these three sources. We use a simple power-law with spectral index α,

$$S_\nu \propto \nu^\alpha, \tag{3.1}$$

to describe the flux density (S_ν) as a function of frequency (ν) for optically-thin synchrotron emission. We assume a spectral index between 144 MHz and 1.4 GHz of $\alpha_{144}^{1400} = -0.7$ to extrapolate to the observed-frame 1.4 GHz flux density. This assumption is consistent with the typical 150 MHz to 1.4 GHz spectral index found for both AGN and star-forming galaxies by Calistro Rivera et al. (2017) and Gürkan et al. (2019). It is also consistent, in the case of SBS 1520+530, with the archival data from the VLA at GHz frequencies: the possible detection at 280 μJy derived from the 1.4 GHz VLA map would suggest a spectral index of $\alpha_{144}^{1440} = -0.78$ for this object. This is also consistent with the non-detection in VLASS, which implies a limit on the spectral index of $\alpha_{144}^{3000} < -0.6$ assuming an object could be detected at the 3σ-level.

Finally, we determine the rest-frame 1.4 GHz luminosity using,

$$L_{1.4\ \mathrm{GHz,rest}} = 4\pi\, D_L^2\, S_{1.4\ \mathrm{GHz,obs}}\, (1+z_s)^{-(1+\alpha)}, \tag{3.2}$$

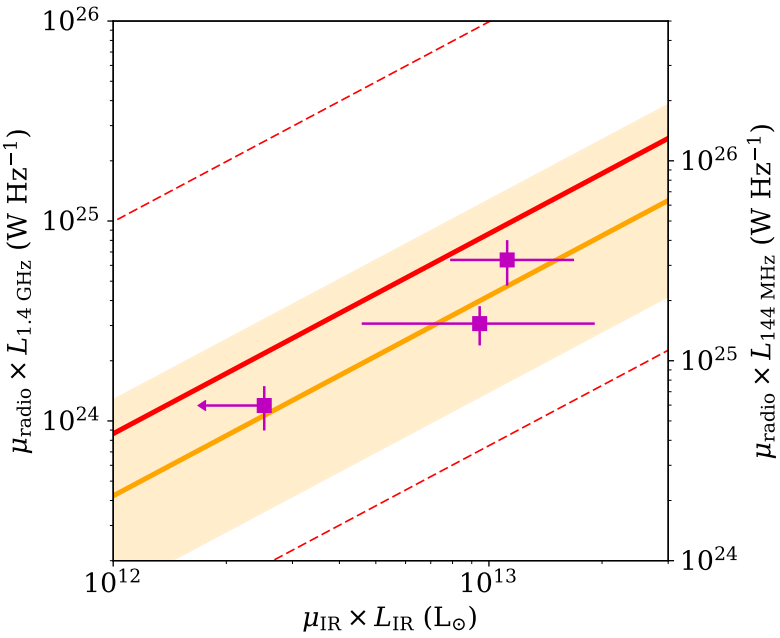

Figure 3.2 | The rest-frame infrared and 1.4 GHz luminosities of the three lensed quasars detected with LOFAR, uncorrected for the lensing magnification. The corresponding rest-frame 144 MHz luminosities are shown on the opposing axis, scaled by spectral index $\alpha_{144}^{1400} = -0.7$. The median $q_{\rm IR}$ for star-forming galaxies from Ivison et al. (2010) is shown in yellow; the shaded region is $2 \times \sigma_{q_{\rm IR}}$, where $\sigma_{q_{\rm IR}}$ is the intrinsic scatter. The solid red line shows the radio–infrared correlation at 150 MHz from Calistro Rivera et al. (2017) at $z \sim 1.5$ scaled to 1.4 GHz, with the dashed line showing $2 \times \sigma_{q_{\rm IR}}$.

where D_L is the luminosity distance.

We also check for any uncertainties in the absolute flux scaling of LoTSS by comparing the relative flux ratios between common sources in our target fields and the TIFR GMRT Sky Survey (TGSS; Intema et al. 2017) catalogue (see Shimwell et al. 2017 for details). We find that, for the fields of SDSS J1055+4628 and SBS 1520+350, the LoTSS and TGSS flux-densities of bright objects agree to within a few percent. But for the field of SDSS J1313+5151, the median difference may be as much as 20%. This will have a limited impact on our analysis as the uncertainty in the radio–SFR relation is typically a factor of 2.

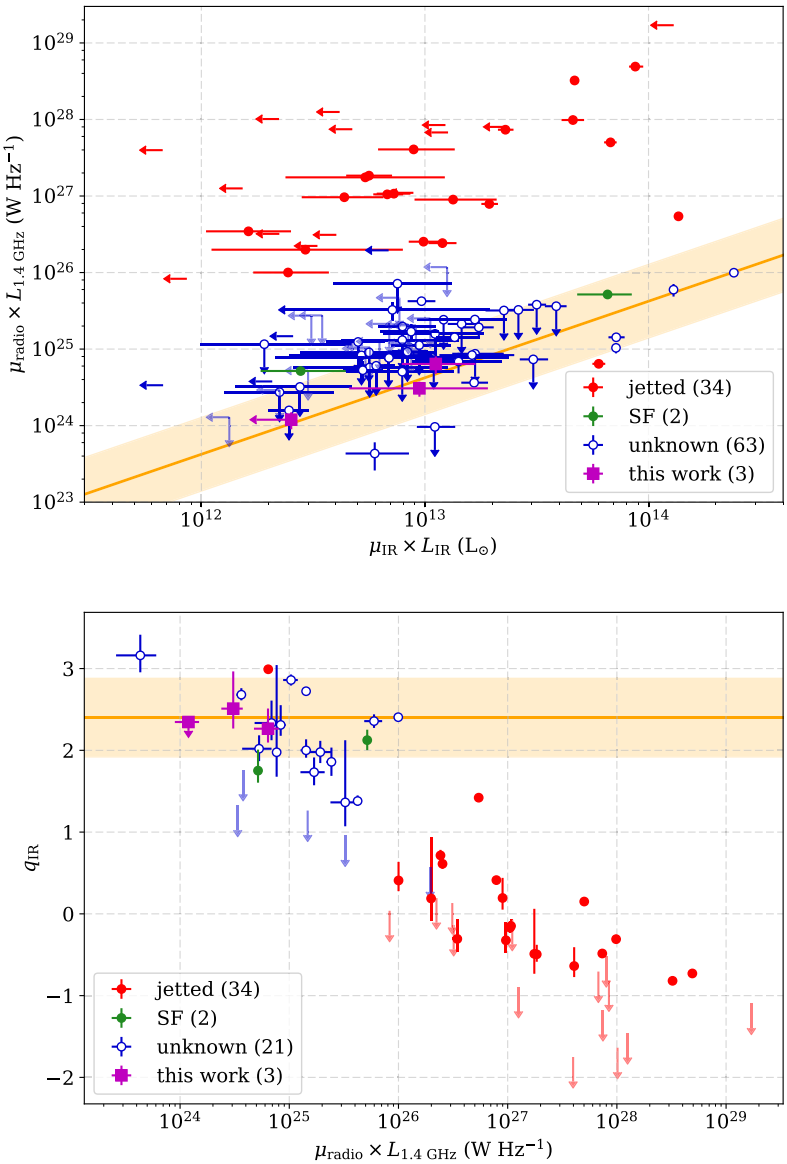

Figure 3.3 | The top panel shows the rest-frame infrared and extrapolated 1.4 GHz luminosities of the parent sample from Chapter 2, uncorrected for the lensing magnification. The bottom panel shows the $q_{\rm IR}$ values and extrapolated 1.4 GHz luminosities of those lensed quasars in the parent sample with a known radio detection. Quasars with jet-dominated radio emission are shown in red; quasars with radio emission known to be star-formation-dominated are shown in green; those with an undetermined radio emission mechanism are shown in blue. The three objects in this work are shown in purple. The median $q_{\rm IR}$ for star-forming galaxies from Ivison et al. (2010) is shown in yellow; the shaded region is $2 \times \sigma_{q_{\rm IR}}$.

3.4.2. Radio–infrared correlation at 1.4 GHz

The radio–infrared correlation is described by the parameter $q_{\rm IR}$, the ratio between the total infrared luminosity (8 to 1000 μm; rest-frame) and the 1.4 GHz rest-frame luminosity, defined by Condon et al. (1991) as,

$$q_{\rm IR} = \log_{10}\left(\frac{L_{\rm IR}}{3.75\times10^{12}\ L_{1.4\ \rm GHz}}\right). \tag{3.3}$$

This relation falls naturally from the dust and radio emission being associated with star formation that is produced by the same stellar population (Schober et al., 2017). We extrapolate from $L_{\rm FIR}$ (40 to 120 μm; rest-frame) given in Chapter 2 to the total infrared luminosity (8 to 1000 μm; rest-frame) using the colour correction factor of 1.91 of Dale et al. (2001) (i.e. $L_{\rm IR} = 1.91\,L_{\rm FIR}$), calibrated for star-forming galaxies, to allow for the contribution from mid-infrared spectral features. Ideally, we would use a spectral energy distributions (SED) model or template which would also account for an AGN component (e.g. Siebenmorgen et al. 2015; Calistro Rivera et al. 2016). However, our targets have no data beyond 22 μm (e.g. from *Spitzer*/MIPS, *Herschel*/PACS) that would enable us to constrain contributions from the AGN torus emission to the FIR. We adopt the Dale et al. colour correction under the assumption that the FIR luminosity is associated with star formation, without a significant contribution from black hole accretion (an assumption that we will test here by comparison with the radio properties). For consistency with other analyses, we use $q_{\rm IR} = 2.40\pm0.24$ (Ivison et al., 2010), which was derived from 1.4 GHz radio and *Herschel*/SPIRE observations for luminous infrared galaxies at a similar redshift to our targets, and assume a Salpeter (1955) initial mass function (IMF) for conversion from luminosity to SFR.

We also consider the evolution of the radio–infrared correlation with redshift, for which there are conflicting reports in the literature. Ivison et al. (2010) find a suggestion of evolution with redshift, which may be due to selection bias. Delhaize et al. (2017) and Magnelli et al. (2015) find statistically-significant evidence of evolution with redshift, however for the redshifts of our targets ($z\sim1.5$) the inferred $q_{\rm IR}\simeq2.3$–2.4 are consistent with Ivison et al. (2010).

As there is no high-resolution imaging for our targets, we do not have information on the lensing magnification of the radio ($\mu_{\rm radio}$) or dust emission ($\mu_{\rm IR}$). If the radio and FIR emission both originate from the star-forming disc and are co-spatial, their total magnifications will be similar. In this case, the ratio of the observed luminosities (and, hence, $q_{\rm IR}$) will be the same as the lensing-corrected (intrinsic) ratio. However, the relative magnification of any radio emission associated with the AGN will depend on the morphology and location of this relative to the FIR emission and the lensing caustics: while the radio emission in radio-quiet quasars associated with accretion is assumed

to be compact, these can also exhibit diffuse radio structures (e.g. Harrison et al. 2015; Alexandroff et al. 2016; Baldi et al. 2018). Here, we assume that the star formation is not preferentially magnified relative to any AGN emission. While high-resolution data will be needed to fully account for such a scenario through lens modelling, simulations by Serjeant (2012) suggest that the effect of differential magnification is not likely to be significant enough to alter our interpretation.

The rest-frame radio and infrared luminosities of our targets, relative to the expectations from the radio–infrared correlation, are shown in Figure 3.2. We find that for the gravitationally lensed quasars detected with LoTSS, their infrared luminosities are consistent with the radio–infrared correlation derived at 1.4 GHz by Ivison et al. (2010) and at 150 MHz by Calistro Rivera et al. (2017). This suggests that the radio emission is mostly or entirely driven by star formation.

In Figure 3.3, we show the same data for the targets studied here, but also include the other 99 lensed quasars in the *Herschel*/SPIRE sample (the remaining 2 objects of the *Herschel*/SPIRE sample have no radio measurements; see Chapter 2). Also in Figure 3.3, the $q_{\rm IR}$ values of the radio-detected quasars relative to their radio luminosities are shown. We have defined sub-samples of the sources to indicate those that are jetted (34 objects that show evidence for radio-jets in high-angular-resolution imaging) and those that are non-jetted (2 objects with confirmed diffuse radio emission that is expected to be due to star formation). Due to the lack of very long baseline interferometric imaging for the whole sample, the nature of the radio emission from most of the quasars, including the three sources detected by LoTSS, is unconfirmed.

3.4.3. Radio-derived star formation rates

Under the assumption that the radio continuum is attributed to only star formation, the radio luminosity can be used to estimate the SFR by inferring the IR luminosity from the radio–infrared correlation. For consistency with Chapter 2, we derive SFRs using the methodology of Kennicutt (1998), assuming a Salpeter initial mass function,

$$SFR\ (\mathrm{M_\odot\ yr^{-1}}) = \frac{L_{\rm IR}}{5.8 \times 10^9}, \tag{3.4}$$

where $L_{\rm IR}$ is in units of $\mathrm{L_\odot}$.

From the radio–infrared correlation of Ivison et al., we expect SFRs (uncorrected for lensing magnification) of 500±130, 1300±290 and 2700±700 $\mathrm{M_\odot\ yr^{-1}}$ for SDSS J1055+4628, SDSS J1313+5151 and SBS 1520+530, respectively. In the case of SDSS J1055+4628, this is the first estimate of the SFR for this radio-quiet quasar.

We also derive SFRs from the 144 MHz continuum using the radio–infrared correlation at $z \sim 1.5$ from Calistro Rivera et al. (2017), for which we also use the relation in Equation 3.4 for consistency with 1.4 GHz. In this case we find apparent SFRs of 250 ± 60, 650 ± 140 and 1300 ± 340 $M_\odot$ yr^{-1} for SDSS J1055+4628, SDSS J1313+5151 and SBS 1520+530, respectively. These are also within the errors of the SFRs we derive from the FIR luminosity for SDSS J1313+5151 and SBS 1520+530, however a they are factor of 2 lower than the SFR derived from the Ivison et al. correlation at 1.4 GHz. This is perhaps unsurprising given the large scatter of the correlation at 150 MHz, but could relate to thermal contributions in either band. Gürkan et al. (2018) find a significant difference in the radio-derived SFRs between 1.4 GHz and 150 MHz, which they attribute to a contribution from thermal (free-free) emission at GHz frequencies. However, it is not clear that the 150 MHz luminosities are free from thermal processes either. Indeed, Calistro Rivera et al. (2017) found evidence for flattening spectra at lower radio frequencies, a feature that has been also observed in low-redshift star-forming galaxies (e.g. Marvil et al. 2015; Galvin et al. 2018). Such a scenario could also account for differences in the radio-derived SFRs calibrated at low and high frequencies.

Given the redshifts of our targets, the 144 MHz LoTSS data from LOFAR are probing the rest-frame ~ 400 MHz emission, where the suppression due to free-free absorption is expected to be less, and any systematic error due to extrapolating the radio spectrum to 1.4 GHz should be limited. Therefore, we use the SFRs derived from the 1.4 GHz luminosity for the remainder of our analysis.

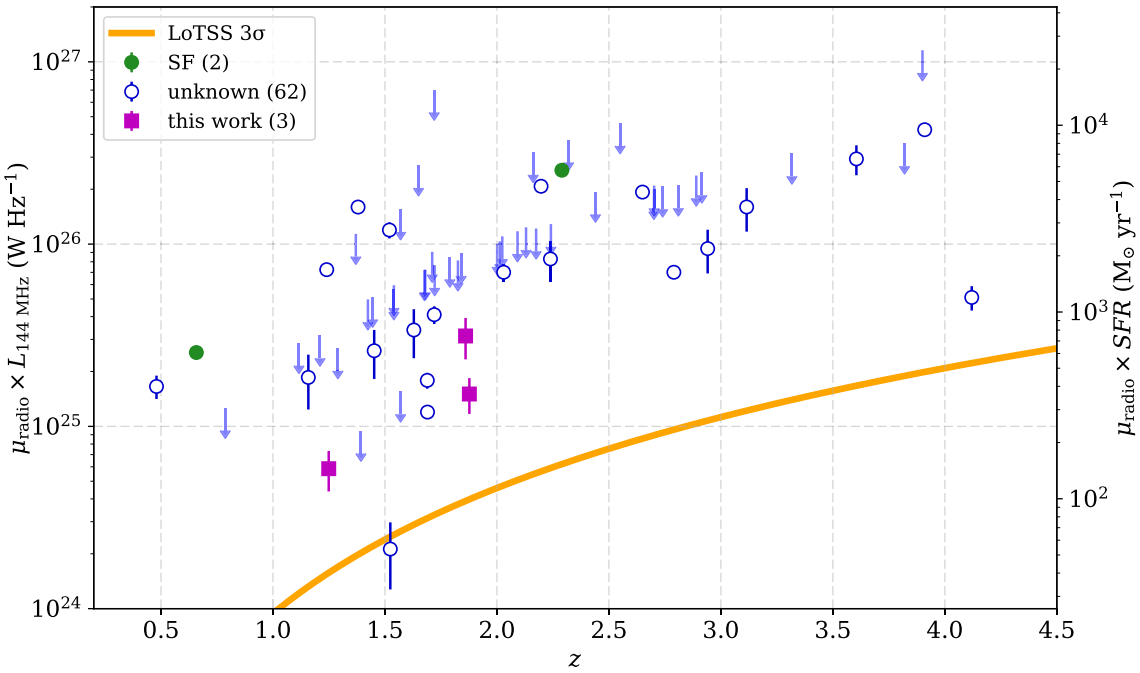

Figure 3.4 | The extrapolated rest-frame 144 MHz luminosities of 67 quasars in the parent sample with known redshifts and radio measurements that have not been confirmed as jetted from high angular-resolution radio imaging at mas-scales. Quasars with star-formation-dominated radio emission are shown in green; those with an undetermined radio emission mechanism are shown in blue. The quasars in this work are shown in purple. The orange line shows a 3σ surface brightness threshold in luminosity for an unresolved point source detected in LoTSS, assuming a median rms noise of 0.07 mJy beam^{-1}. The SFR implied from the 1.4 GHz luminosity is shown on the right-hand y-axis using the radio–infrared correlation of Ivison et al. (2010). Most of the upper limits are from FIRST at the 5σ-level, thus the LoTSS threshold shows a clear advantage in sensitivity.

Table 3.1 | The rest-frame dust temperature ($T_{\rm dust}$) and FIR luminosity ($\mu L_{\rm FIR}$), radio-infrared factor ($q_{\rm IR}$), IR-derived apparent SFR ($SFR_{\rm IR}$) for the three gravitationally lensed quasars in this work. We also give the radio-derived apparent SFRs using the Calistro Rivera et al. (2017) radio–infrared correlation at 150 MHz (SFR_{150}) and the Ivison et al. (2010) correlation at 1.4 GHz (SFR_{1400}). $T_{\rm dust}$, log $\mu SFR_{\rm IR}$ and $\mu L_{\rm FIR}$ are as given in Chapter 2. As the lensing magnification of the radio and FIR is not known for these objects, luminosities and SFRs given here are uncorrected for magnification (μ).

Source	$T_{\rm dust}$ (K)	log $\mu L_{\rm FIR}$ ($L_\odot$)	$q_{\rm IR}$	log $\mu SFR_{\rm IR}$ ($M_\odot$ yr^{-1})	log μSFR_{150} ($M_\odot$ yr^{-1})	log μSFR_{1400} ($M_\odot$ yr^{-1})
SDSS J1055+4628	-	< 12.1	< 2.3	< 2.6	2.4 ± 0.1	2.7 ± 0.1
SDSS J1313+5151	-	$12.7^{+0.4}_{-0.2}$	$2.5^{+0.5}_{-0.2}$	$3.2^{+0.4}_{-0.2}$	2.8 ± 0.1	3.1 ± 0.1
SBS 1520+350	46^{+13}_{-7}	$12.8^{+0.2}_{-0.1}$	$2.3^{+0.2}_{-0.2}$	$3.3^{+0.2}_{-0.1}$	3.1 ± 0.1	3.4 ± 0.1

Table 3.2 | Parameters of the 2-dimensional Gaussian models fitted to the 144 MHz LoTSS image-plane data using PyBDSF. We give the peak surface brightness ($I_{\rm peak}$) and the integrated flux density ($S_{\rm int}$), the size of the fitted Gaussians (not de-convolved from the LOFAR beam-size; $6'' \times 6''$), and the off-source rms noise in the region of the targets. We also show the ratio of the flux-densities from LoTSS and TGSS for nearby radio sources in each field ($S_{\rm LoTSS}/S_{\rm TGSS}$).

Source	$I_{\rm peak}$ (mJy beam^{-1})	$S_{\rm int}$ (mJy)	Major axis (arcsec)	Minor axis (arcsec)	PA (° E of N)	rms noise (mJy beam^{-1})	$S_{\rm LoTSS}/S_{\rm TGSS}$
SDSS J1055+4628	0.40 ± 0.08	0.76 ± 0.12	10.1 ± 2.3	6.7 ± 1.2	55 ± 25	0.07	1.02 ± 0.24
SDSS J1313+5151	0.41 ± 0.06	0.81 ± 0.09	9.4 ± 1.5	7.6 ± 1.0	79 ± 32	0.07	0.80 ± 0.18
SBS 1520+350	1.07 ± 0.17	1.64 ± 0.26	9.2 ± 1.7	6.0 ± 0.8	84 ± 21	0.16	0.97 ± 0.26

3.5. Discussion

3.5.1. Radio emission mechanism of radio-quiet quasars

For the two lensed quasars detected with *Herschel*/SPIRE, we find that these objects lie on the radio–infrared correlation, therefore the radio emission at 144 MHz can be explained by star formation. This implies that there is no significant AGN-heating of the cold dust, under the assumption that the radio emission is also dominated by star formation. While we cannot determine this for the lensed quasar that was not detected with *Herschel*/SPIRE, which could still have a radio excess, we do not find evidence of a FIR excess here. The SFRs implied from their projected radio luminosities are consistent within the errors and upper limit of the SFRs that were derived from the FIR emission, and they are in the range 20 to 300 $M_\odot$ yr^{-1}, assuming a typical lensing magnification of 10.

A study of unlensed quasars in the LoTSS first data release by Gürkan et al. (2019) find that optically-selected quasars at $z < 1.0$, with a comparable radio luminosity to our sample, are scattered close to the radio–infrared correlation, consistent with our findings. They do not detect any distinct bi-modality in the radio properties of the quasar population, the lack of which may imply that this population has a composite of emission related to both black hole accretion and star formation, where star formation begins to dominate at low radio luminosities. This scenario is consistent with other studies focusing on deep observations of single fields, such as Delvecchio et al. (2017), who find that star formation accounts for most of the radio emission in the majority of AGN based on a large sample in the VLA-COSMOS 3 GHz survey. These findings may also be reconciled with studies such as by White et al. (2017), where half of the sample of 70 radio-quiet quasars are detected, which in general were found to have a radio excess. The differing conclusions may relate to how the studies are designed; if there is composite emission in most quasars, deep observations with very long baseline interferometry at cm-wavelengths will detect the compact emission associated with low-luminosity AGN activity in many cases (e.g. Herrera Ruiz et al., 2017; Radcliffe et al., 2018), and observations to test this for our sample of lensed quasars are under way.

High levels of star formation in quasar host galaxies are expected according to the paradigm of galaxy evolution in which star formation and AGN co-evolve. A lack of radio activity related to black hole accretion has implications on the AGN feedback mechanisms by which these quasars interact with their host galaxies; in the small sample studied here it seems that jets do not play a dominant role. However, radiative

feedback from the AGN may have an effect, which is not traced by these data. We do note that for the sample of quasars studied here, we find both on-going AGN activity in the form of optical emission and evidence for on-going star formation, based on the radio and FIR emission. This suggests that star formation has not been halted in these objects. Additional radio imaging for the larger sample of lensed quasars from Chapter 2, which includes those objects with predicted SFRs $> 10^3$ $M_\odot$ yr^{-1} based on their FIR emission, will give a more complete view on the level of star formation activity and AGN heating of the dust within quasar host galaxies. In this way, we can confirm or discount the extreme rates of star formation inferred from the FIR. In general, such studies would be complementary to those of field quasars, such as by Gürkan et al. (2019), and can provide a more complete picture of the evolutionary role of AGN within galaxy formation.

3.5.2. Implications for future radio surveys

Recently, significant progress has been made in characterising the faint radio population with deep surveys of single fields, such as the VLA-COSMOS 3 GHz survey (Smolčić et al., 2017). However, most lensed quasars still lie below the detection limits of all-sky surveys such as FIRST, and even forthcoming surveys such as VLASS. The steep negative spectrum of synchrotron radiation provides an efficient way to detect the faint emission from star formation at high redshifts with LOFAR. The detection in this work of all three lensed quasars in the HETDEX field implies that future LoTSS data releases will enable a large sample of radio-quiet lensed quasars to be detected. If these sources do not have a significant excess from AGN-heated dust, we can expect these lensed quasars to be consistent with star-formation-dominated radio emission in the absence of radio jet emission. If we do not detect these sources, we can conclude that the AGN are heating dust on large-scales in their host galaxies. Further studies of the cold dust at high angular resolution with ALMA and the NOrthern Extended Millimetre Array (NOEMA) would help us to better understand the effect AGN have on the ISM of galaxies. The LoTSS survey being carried out with LOFAR could provide a novel method for selecting such targets.

We extrapolate our 144 MHz detections to ~GHz frequencies, in the same way as described in Section 3.4, and find that the three quasars in our sample have implied flux densities at observed-frame 1.4 GHz of 0.1–0.2 mJy. This implies that we would require sensitivities 5–10 times better than FIRST to detect these sources. In Figure 3.4, we show the extrapolated 144 MHz radio luminosities (including current upper limits) of the *Herschel*/SPIRE sample, including the three detections reported here, and a 3σ surface brightness threshold given the typical rms noise of LoTSS. We also show the

inferred SFR from the 1.4 GHz luminosity (uncorrected for the lensing magnification). Where there are no detections or detections in only one radio band, we assume a spectral index of $\alpha_{144}^{1400} = -0.7$, as before, otherwise we extrapolate or interpolate from existing radio measurements to the rest-frame frequencies. Only one quasar that was previously detected at GHz frequencies from targeted observations is projected to be a non-detection at the 3σ-level in LoTSS images. The significant detection of the three lensed quasars in this work suggests that many of the lensed quasars currently undetected in FIRST could be detected in future LoTSS data releases. The typical magnifications of the star formation in these systems is a factor of 10, suggesting that we will probe SFRs an order of magnitude lower than accessible in large surveys of unlensed systems at similar redshifts in LoTSS (Gürkan et al., 2018, 2019).

Finally, we note that without the capability to resolve the gravitational lens systems, we cannot be sure that there is no contribution to the measured radio emission from the foreground lensing galaxy. This has been found to be the case for ~ 10% of gravitational lens systems with resolved radio emission at cm-wavelengths (McKean et al., 2005, 2007; Wucknitz & Volino, 2008; Jackson et al., 2015). With the forthcoming long baseline capabilities of the International LOFAR Telescope as part of LoTSS, we will be able to achieve $\sim 0.2''$ angular-resolution and potentiality identify these relative contributions. Alternatively, high resolution, high sensitivity observations at cm-wavelengths could also detect if there is any radio emission from the lensing galaxies (e.g. Jackson et al., 2015).

3.6. Conclusions

We have detected three gravitationally lensed radio-quiet quasars in the HETDEX Spring Field with LOFAR at 144 MHz that were undetected at ~GHz radio frequencies. These quasars were previously observed with *Herschel*/SPIRE, with which SFRs could be derived for two and an upper limit placed on the third, based on their FIR SEDs. In this chapter, we derived rest-frame luminosities from our radio measurements and, by comparing with the radio–infrared correlation, find that the radio luminosities can be produced by star formation. The SFRs inferred from their projected 1.4 GHz luminosities are consistent with the rates derived from their total infrared luminosities. Overall, the radio luminosities, infrared luminosities, low dust temperatures and steep dust emissivities are all consistent with extreme levels of on-going star formation within our parent sample of lensed quasars. However, we find a factor of 2 lower SFRs when using luminosity relations calibrated at 150 MHz for low redshift star-forming galaxies relative to the relation calibrated at 1.4 GHz. The reasons for this are not clear,

but may be due to thermal contributions in one or both radio bands, which would have the effect of increasing the flux measurements due to free-free emission at 1.4 GHz and decreasing them due to free-free absorption at 150 MHz.

The nature of the radio emission from radio-quiet quasars has been the subject of controversy, with studies yielding different conclusions on the primary emission mechanism and whether the physical difference between the radio-loud and radio-quiet quasars reflects a true dichotomy in the quasar population. Our results point towards star-formation-dominated radio emission for the sources in our pilot sample, which is consistent with a similar study of unlensed radio-quiet quasars at low redshifts in this LoTSS data release by Gürkan et al. (2019). A larger sample will be required to understand how robust these conclusions are for the quasar population in general. By extrapolating the 1.4 GHz luminosities of the parent sample to 144 MHz, we predict that many of the lensed quasars currently undetected at 1.4 GHz will be detected in future LoTSS data releases. As most of the radio-quiet lensed quasars in our parent sample are currently undetected, we expect to significantly increase the fraction with radio detections. Due to the magnification effect of gravitational lensing, we will be able to probe lower luminosities than otherwise accessible at $z \sim 2$ and create a more complete picture of the radio-quiet quasar population at this epoch, when both the star formation and AGN activity peaked.

Acknowledgements

PNB and JS are grateful for support from the UK STFC via grant ST/M001229/1. KJD acknowledges support from the ERC Advanced Investigator programme NewClusters 321271. GG acknowledges the CSIRO OCE Postdoctoral Fellowship. MJH and WLW acknowledge support from the UK Science and Technology Facilities Council (STFC) [ST/M001008/1]. APM would like to acknowledge the support from the NWO/DOME/IBM programme "Big Bang Big Data: Innovating ICT as a Driver For Astronomy", project #628.002.001. LKM acknowledges support from Oxford Hintze Centre for Astrophysical Surveys which is funded through generous support from the Hintze Family Charitable Foundation. This publication arises from research partly funded by the John Fell Oxford University Press (OUP) Research Fund. IP acknowledges support from INAF under PRIN SKA/CTA 'FORECaST'. The LOFAR group in Leiden is supported by the ERC Advanced Investigator programme New-Clusters 321271. LOFAR, the Low Frequency Array designed and constructed by ASTRON, has facilities in several countries, that are owned by various parties (each with their own funding sources), and that are collectively operated by the International LOFAR Telescope (ILT) foundation under a joint scientific policy. The ILT resources have benefited from the following recent major funding sources: CNRS-INSU, Observatoire de Paris and Université d'Orléans, France; BMBF, MIWF-NRW, MPG, Germany; Department of Business, Enterprise and Innovation (DBEI), Ireland; NWO, The Netherlands; The Science and Technology Facilities Council (STFC), UK. Part of this work was carried out on the Dutch national e-infrastructure with the support of the SURF Cooperative through grant e-infra 160022 & 160152. The LOFAR software and dedicated reduction packages on `https://github.com/apmechev/GRID_LRT` were deployed on the e-infrastructure by the LOFAR e-infragroup, consisting of J. B. R. Oonk (ASTRON & Leiden Observatory), A. P. Mechev (Leiden Observatory) and T. Shimwell (ASTRON) with support from N. Danezi (SURFsara) and C. Schrijvers (SURFsara). This research has made use of the University of Hertfordshire high-performance computing facility (`http://uhhpc.herts.ac.uk/`) and the LOFAR-UK computing facility located at the University of Hertfordshire and supported by STFC [ST/P000096/1]. The National Radio Astronomy Observatory is a facility of the National Science Foundation operated under cooperative agreement by Associated Universities, Inc. This research made use of Astropy, a community-developed core Python package for Astronomy (The Astropy Collaboration et al., 2018).

The rocky road to quiescence

60 ml aged jenever
15 ml dark crème de cacao liqueur
20 ml smoked porter syrup
25 ml lemon juice

Shake together with ice. Strain into an old fashioned glass over fresh ice and top with a white chocolate shavings.

4

Resolving quasar lens systems at sub-mm wavelengths

I. The rocky road to quiescence: witnessing the formation of massive galaxies at $z \sim 2$

H. R. Stacey, J. P. McKean, D. M. Powell, S. Vegetti, F. Rizzo, C. Spingola, M. W. Auger, R. J. Ivison and P. P. van der Werf

Based on "The rocky road to quiescence: witnessing the compaction and quenching of quasar hosts at z~2"
Stacey et al.; in review with Monthly Notices of the Royal Astronomical Society

Abstract

We investigate the host galaxies of six gravitationally lensed quasars at redshift 1.5 to 2.8 observed with the Atacama Large (sub-)Millimetre Array (ALMA), selected on the basis of their sub-mm luminosity. Using a visibility-plane lens modelling technique, we create pixellated reconstructions of the dust continuum, molecular gas distribution and kinematics with an equivalent spatial resolution of 100 to 300 pc. We find that the quasar hosts can be distinguished into two types: 1) galaxies characterised by clumpy, extended dust distributions and star formation rate surface densities comparable to dusty star-forming galaxies (DSFGs); 2) galaxies that have compact sizes in dust emission similar to coeval passive galaxies, with Eddington-limited star formation that could exhaust their gas reservoirs within 20 Myr. The size, morphology and star-forming properties of the quasar hosts suggests that we observe them at a stage in their transformation into compact spheroids, where a high density of dynamically unstable gas leads to efficient star formation and black hole accretion. We find that the level of star formation is sufficient to quench compact galaxies, without help from active galactic nuclei feedback.

4.1. Introduction

In the last two decades, large-area sub-millimetre surveys have revealed a population of high-redshift galaxies with extreme levels star formation, which were largely undetected in optical surveys as their ultraviolet (UV) emission is obscured by dust (Blain et al. 2002; Casey et al. 2014, for review). These dusty star-forming galaxies (DSFGs) are expected to be precursors to locally observed massive elliptical galaxies, which are characterised by dense, old stellar populations with dispersion-dominated dynamics (Hopkins et al., 2008). A key aspect of the study of galaxy evolution is understanding how these galaxies formed such high stellar densities and grew concurrently with their central supermassive black holes (Magorrian et al., 1998). Recent near-infrared surveys have revealed that the population of compact quiescent galaxies start to appear at $z \sim 2$ and rapidly increase in number density before apparently declining at $z \sim 1$ (Trujillo et al., 2006; van Dokkum et al., 2008, 2015). These galaxies are around four times smaller in size than $z \sim 0$ massive ellipticals and are thought to form the centre of these galaxies, which later grow in size (but little in mass) due to a series of gas-poor, minor mergers (Naab et al., 2007, 2009).

The characteristics and rapid formation of compact quiescent galaxies can be reproduced if a very high density of gas is concentrated within a region of ~ 1 kpc to generate a brief, intense starburst (Valentino et al., 2019). However, the mechanisms that cause such rapid morphological change and quenching of star formation are currently unclear. Compaction may be due to a net loss of angular momentum that results from dynamical instabilities induced by gas-rich mergers or tidal interactions (Mihos & Hernquist, 1996; Hopkins et al., 2008), or by non-axisymmetric structures caused by rapid accretion and clumpy star formation (Dekel et al., 2009; Zolotov et al., 2015). Alternatively, these galaxies could have formed secularly, in-situ at earlier epochs without the need for mergers or rapid evolution (Damjanov et al., 2011; Carollo et al., 2013; Williams et al., 2014; Wellons et al., 2015).

Star formation terminates as a result of depletion or cessation of the supply of molecular gas. In compact quiescent galaxies, this may happen as a result of compaction, where star formation is self-quenched by radiation pressure from massive stars and supernovae-driven winds (Murray et al., 2005; Andrews & Thompson, 2011; Diamond-Stanic et al., 2012). Eddington-limited 'maximum' starbursts have been discovered in DSFGs at high redshift (Riechers et al., 2013; Oteo et al., 2016; Cañameras et al., 2017; Spilker et al., 2019) as well as in nearby ultra-luminous infrared galaxies (ULIRGs; Barcos-Muñoz et al. 2017). These can be sufficiently vigorous to drive large-scale outflows and quench their hosts (Cañameras et al., 2017; Spilker et al., 2018), from the inside-out, on timescales of 10s Myr (Spilker et al., 2019).

Hydro-dynamical simulations and semi-analytic models of galaxy formation find

that feedback from active galactic nuclei (AGN) is necessary, in addition to stellar feedback, to reproduce observed galaxy stellar populations and luminosity functions (Di Matteo et al., 2005; Sijacki et al., 2007; Somerville et al., 2008; Schaye et al., 2015). AGN feedback occurs in the form of jets or radiative winds, which can suppress star formation by mechanically coupling to the molecular gas and/or by preventing (re-)accretion from the circumgalactic medium (Fabian 2012, for review).

Due to computational limitations, current cosmological simulations involve only phenomenological implementations of feedback, which are calibrated to match observational data (see Somerville & Davé 2015). Observations find circumstantial evidence that AGN could play a role in the evolution of their hosts, in that the compaction phase seems to coincide with the appearance of an AGN (Barro et al., 2013; Kocevski et al., 2017). However, studies have found conflicting results as to whether AGN have any effect on their host galaxies. While some earlier studies found evidence of suppressed star formation in AGN hosts (e.g. Page et al. 2012), more recent studies of statistical samples have found no correlation between star formation and black hole accretion (Harrison et al., 2012; Rosario et al., 2013; Harris et al., 2016; Stanley et al., 2017; Pitchford et al., 2016; Kirkpatrick et al., 2019; Schulze et al., 2019). This could be because the effects of AGN feedback can only be detected later, or because black hole accretion is stochastic (Gabor & Bournaud, 2014; Hickox et al., 2014). Even in simulations, star formation rates averaged over ~ 100 Myr can show no clear correlation with black hole accretion (Harrison, 2017), suggesting the effect of AGN may not be obvious in studies of the global properties of quasar hosts.

These key tests of the evolutionary sequence demand investigations of the size, structure and dynamical properties of individual quasar hosts during the cosmic peak of galaxy growth ($z \sim 2$). This requires high spatial resolution (~ 100 pc), which is most efficiently achieved by observing objects that are gravitationally lensed (e.g. Swinbank et al. 2010; ALMA Partnership et al. 2015). Chapter 2 introduced a survey of gravitationally lensed quasars systems with the *Herschel Space Observatory* to measure the level of obscured star formation in the quasar host galaxies. This chapter presents observations with the Atacama Large (sub-)Millimetre Array (ALMA) of a sub-sample of six optically luminous quasars from the parent sample in Chapter 2 to resolve their host galaxy emission. Using a pixellated lens modelling technique applied to the interferometric data, we reconstruct dust and gas in the host galaxies on 100 to 300 pc scales. In Section 4.2 we describe the targets, observations and data reduction process. In Section 4.3 we describe our lens modelling and source reconstruction technique. Section 4.4 reports the results of the structure of dust and gas, gas dynamics and star formation properties of the individual objects. We compare the morphological and star formation properties of the quasar host galaxies with a sample of DSFGs. In Section 4.5, we discuss the implications of our results in the context of evolutionary

models and possible avenues to test our conjectures. Section 4.6 presents a summary of our findings and avenues for future work.

Throughout, we assume the Planck Collaboration et al. (2016) instance of a flat ΛCDM cosmology with $H_0 = 67.8\ \mathrm{km\,s^{-1}\ Mpc^{-1}}$, $\Omega_\mathrm{M} = 0.31$ and $\Omega_\Lambda = 0.69$.

4.2. Sample and observations

Table 4.1 | Summary of the targets and ALMA observations. We give the phase centre right ascension and declination (in degrees, J2000), lens and source redshift, central frequency of the observation, total on-source integration, and project code for the six targets in this work. The redshift of the lens is not known for HS 0810+2554 or H 1413+117, but this has no bearing on our results as we are only interested in the source plane structure for our targets.

	RA (deg)	Dec (deg)	z_l	z_s	ν_obs (GHz)	t_s (min)	Project code
HS 0810+2254	123.38053	+25.75068	–	1.51	145 GHz	32	2017.1.01368.S
RX J0911+0551	137.86458	+05.84833	0.70	2.79	145 GHz	123	2017.1.01081.S
SDSS J0924+0219	141.23258	+02.32347	0.39	1.52	358 GHz	44	2018.1.01591.S
PG 1115+080	169.57083	+07.76603	0.31	1.74	346 GHz	27	2018.1.01591.S
H 1413+117	213.94271	+11.49539	–	2.56	285 GHz	10	2012.1.00175.S
WFI J2033−4723	308.42533	−47.39528	0.66	1.66	341 GHz	28	2018.1.01591.S

In this section, we first summarise the sample, the observations with ALMA and the data reduction processes, before giving a detailed description of the properties of each target studied here.

4.2.1. Summary of the sample, observations and data reduction

The targets in this work are six four-image gravitationally lensed quasar (Type 1 AGN) systems. Three targets, SDSS J0924+0219, PG 1115+080 and WFI J2033−4723 are from our own programme, which were selected for this study because they are luminous at sub-mm wavelengths (Chapter 2). We also include here archival data of HS 0810+2554, RX J0911+0551 and H 1413+117, which are known to have bright sub-mm emission (Barvainis & Ivison, 2002). From previous modelling of their spectral energy distributions (SEDs; Chapter 2; see Fig. 4.19– 4.21) we expect the sub-mm emission to be entirely dominated by thermal dust. As these systems were primarily

selected in optical imaging and subsequently selected on the basis of their sub-mm luminosity, their selection is not strongly influenced by dust temperature. We compile all accessible data with sufficiently high angular resolution to resolve the size and structure of the emission from cold dust at sub-mm/mm wavelengths. As a result, this sample is very heterogeneous, and the observations probe different CO line transitions (see Table 4.1).

The raw data were calibrated using the ALMA pipeline in the Common Astronomy Software Applications package (CASA; McMullin et al. 2007) to produce calibrated visibilities. The data were inspected to confirm the quality of the pipeline calibration and determine whether further flagging was required. RX J0911+0551, PG 1115+080 and H 1413+117 were self-calibrated using solution intervals of each scan length. Self-calibration was attempted for SDSS J0924+0219 and WFI J2033−4723, but was not successful, probably because of the lower signal-to-noise ratio of the surface brightness. We did not attempt to self-calibrate the data for HS 0810+2554 as the continuum emission is extremely weak (see below).

The targets were imaged with natural weighting of the visibilities and deconvolved using CLEAN (Högbom, 1974). The deconvolved images are shown in Figs. 4.1 to 4.6. The continuum emission is consistent with the level of thermal dust emission expected from SED-fitting (Chapter 2). Despite detecting the host galaxies of the quasars in the form of extended Einstein rings and gravitational arcs, we also find compact emission that, in all cases except for HS 0810+2554, is coincident with the optical quasar emission. No emission is detected from any of the lensing galaxies.

All data sets, except in the case of PG 1115+080, included observations of an emission line of CO. The spectral line data were prepared by fitting a linear model for the continuum to the line-free spectral windows and subtracting this from the visibilities. This produced a visibility data set that included only the line emission. The resulting line profiles, fit with simple Gaussians, are shown in Fig. 4.7. In some cases, the line peaks are offset from the systemic velocity (the rest-frame of the galaxy), which is possibly due to an uncertainty in the inferred redshift from optical spectroscopy: redshifts of quasars determined from optical spectroscopy can trace outflows of ionised gas, leading to incorrect inference on the systemic velocity. A summary of the spectral line observations is presented in Table 4.2.

The spectral line moment maps (velocity-integrated flux density, velocity field, velocity dispersion) are shown in Figs. 4.1 to 4.5. The velocity field and velocity dispersion are made by masking channel pixels below a signal-to-noise ratio threshold (stated within the figure captions).

4.2.2. HS 0810+2554

HS 0810+2554 is a quasar at $z_s = 1.51$ that is lensed into a characteristic fold configuration (Reimers et al., 2002; Hewett & Wild, 2010). The redshift of the foreground galaxy is unknown, but is estimated to be 0.9 based on the lens population distribution (Mosquera & Kochanek, 2011). This quasar is faint at radio wavelengths, but VLBI investigations find evidence of compact, low-luminosity radio-jet structure that dominates the radio emission (Hartley et al., 2019). HS 0810+2554 was observed with ALMA at 145 GHz, which also targeted the CO (3–2) emission line.

We resolve thermal dust emission from this system with ALMA at 145 GHz that has a peak surface brightness of 6σ (where σ is the rms noise per beam). The emission is detected around the close images, where the magnification is high. There is a hint of emission in the counter images, but not at a significant level. The achieved rms noise level is 13 μJy beam^{-1} with natural weighting. The total flux density of 0.3 mJy is consistent with the level of thermal dust emission expected at the observing frequency, based on SED fitting (see Fig. 4.19). This is also consistent with the weak synchrotron emission seen at cm wavelengths that is not expected to be detectable at the higher frequencies investigated here.

The CO (3–2) line profile for HS 0810+2554 is shown in Fig. 4.7, which has a FWHM of about 380 ± 10 km s^{-1}based on a single Gaussian fit. We find that the peak of the line emission is shifted -465 ± 6 km s^{-1}, which may be due to an uncertain redshift estimate from optical data. ALMA imaging of the line emission shows that the molecular gas is extended and lensed into an Einstein ring (see Fig. 4.1).

4.2.3. RX J0911+0551

RX J0911.4+0551 is a quasar at $z_s = 2.79$ that is lensed by a foreground galaxy at $z_l = 0.77$ (Burud et al., 1998; Kneib et al., 2000). The lens system has a characteristic cusp configuration with three close images. The environment of this lens system is quite complex: the primary lens has a satellite galaxy within the Einstein radius, and the lens galaxy is part of a cluster that contributes a high level of tidal shear (Kneib et al., 2000). Investigations at radio wavelengths have not been able to determine whether there is radio jet emission (Jackson et al., 2015). However, its radio luminosity is consistent with the expectations for star formation based on the radio–infrared correlation (Chapter 2). For our analysis, we use ALMA imaging at 145 GHz that also targeted the CO (5–4) emission line from RX J0911.4+0551.

We detect thermal dust continuum for this system with a total flux density at 145 GHz of 1.4 mJy, consistent with the expectations from SED fitting (see Fig. 4.19).

We achieve an rms noise of 7 μJy beam^{-1} with natural weighting of the visibilties. Imaging of the dust emission shows compact emission that is resolved around the triplet images (see Fig. 4.2). From the lens configuration, it is clear that the galaxy is crossing the cusp of the lens caustic.

The CO (5–4) line profile for RX J0911+0551, presented in Fig. 4.7, shows a strong peak at 220 km s^{-1} from the systemic velocity. This velocity offset is probably due to an inaccurate measurement of the systemic velocity obtained from optical spectroscopy. The line profile has a FWHM of 133 ± 3 km s^{-1} based on a single Gaussian fit, which is similar to the 120 ± 14 km s^{-1} reported for the CO (7–6) line by Tuan-Anh et al. (2017). Imaging of the CO (5–4) line emission shows compact structure that is similar to the dust continuum (see Fig. 4.2). The imaging is visually similar to the CO (11–10), CO (10–9), CO (7–6) and CO (1–0) emission reported by Tuan-Anh et al. (2017) and Sharon et al. (2016): none of which are extended into rings or arcs, suggesting the emission is similarly compact.

4.2.4. SDSS J0924+0219

SDSS J0924+0219 is a radio-quiet quasar at $z_s = 1.525$ that is lensed by a galaxy at $z_l = 0.39$ (Inada et al., 2003; Hewett & Wild, 2010). This lens system was discovered at optical wavelengths and has a characteristic fold-configuration. Observations with ALMA at 358 GHz, which also targeted the CO (8–7) line, were taken as part of our own observing programme.

The continuum emission from SDSS J0924+0219 is detected with a total flux density of 9.5 mJy at 358 GHz, consistent with the expectations for thermal dust emission from SED fitting (see Fig. 4.20). We achieve an rms noise of 28 μJy beam^{-1} with natural weighting of the visibilities. The continuum imaging shows an Einstein ring of clumpy dust with compact emission at the locations of the quasar images. The extent of the dust seems consistent with a 'red' ring seen in optical/infrared imaging (Eigenbrod et al., 2006). The same study also finds lensed arcs from a 'blue' component, of which there is a suggestion in the ALMA imaging where the Southern arc appears to split. These different optical components could be evidence of an ongoing merger or interaction (e.g. Rybak et al. 2015b).

The CO (8–7) line profile is presented in Fig. 4.7. The line profile is found from a Gaussian fit to have a FWHM of 176 ± 11 km s^{-1} that is shifted by 36 ± 5 km s^{-1} from the optical systemic velocity. Imaging of the CO (see Fig. 4.3) shows resolved emission at the position of the quasar images and evidence for a velocity gradient in the two close images.

4.2.5. PG 1115+080

PG 1115+080 is a quasar at $z_s = 1.74$ that is lensed by a galaxy at $z_l = 0.31$ (Weymann et al., 1980; Hewett & Wild, 2010). Investigations at radio wavelengths have not been able to determine whether the quasar has radio jet emission (Jackson et al., 2015), however its radio luminosity is consistent with the expectations for star formation based on the radio–infrared correlation (Chapter 2). PG 1115+080 was targeted as part of our own programme with ALMA at 346 GHz.

We detect continuum emission with a total flux density of 2.6 mJy, consistent with the expectations for thermal dust emission from SED fitting (see Fig. 4.20). The imaging of the dust emission for PG 1115+080 is presented in Fig. 4.6 and shows compact structure at the position of the quasar images, without any evidence of an extended Einstein ring. Given that the total flux density is close to what is expected from this system, we do not believe that significant emission from an extended component has been resolved out with these data. However, the emission is marginally radially resolved around the two close images. Unlike in the cases of the other quasar hosts in this sample, the unobscured star formation seen in the optical and near-infrared appears more extended than in the obscured star formation we observe here (Sluse et al., 2012; Chen et al., 2019).

4.2.6. H 1413+117

H 1413+117 (the Cloverleaf) is a quasar at $z_s = 2.56$ that is lensed by a galaxy at unknown redshift (Magain et al., 1988; Riechers et al., 2011c). Due to its extreme luminosity at far-infrared (FIR) wavelengths, the lens system is one of the best studied quasar-starbursts. While it is not extremely radio-luminous, this system does have a radio-excess relative to its infrared luminosity (Chapter 2) and has evidence of structure at radio wavelengths that may be from a low-luminosity radio jet. We use for our analysis archival data for H 1413+117 that was taken at 285 GHz with ALMA, which also targeted the CO (9–8) emission line.

Thermal dust emission is detected in the ALMA imaging with a total flux density of 26 mJy and an rms noise level of 93 μJy beam^{-1}, using a natural weighting of the visibilities. The CO (9–8) line emission is detected with a spatially integrated peak flux density of 83 mJy and a FWHM of 394 ± 8 km s^{-1}, from a Gaussian profile fit (see Fig. 4.7); this is the brightest line emission detected from our sample.

We resolve the four images of the quasar host galaxy in continuum and the CO (9–8) molecular line emission, with high surface brightness peaks at the position of the quasar images and an extended, almost complete Einstein ring that connects them (see

Fig. 4.4). The structure of the emission appears similar to previous observations of dust and gas in this system (Alloin et al., 1997; Ferkinhoff et al., 2015). We also identify an additional source with a flux density of ≃ 3.5 mJy within the field at a distance ∼ 6 arcsec North of the lens. This is a potential source of confusion for the SED fitting, where the photometric measurements are typically made at a low angular resolution (e.g. IRAS or *Herschel*/SPIRE). This additional source may also explain the scatter in the photometric measurements from H 1413+117 (e.g. see Chapter 2; Fig. 4.21). From a cursory inspection of the available ALMA archival data at a frequency of ∼ 100 GHz (project code 2015.1.01309.S), we find that the additional source is detected with a similar flux density ratio as at 290 GHz with respect to H 1413+117, suggesting that these galaxies have similar redshifts.

4.2.7. WFI J2033−4723

WFI J2033−4723 is a quasar at $z_s = 1.66$ that is lensed by a galaxy at $z_l = 0.66$ (Morgan et al., 2004) into four images in a typical fold configuration. There are no radio observations of this system to characterise its radio properties at 1.4 GHz, given the low declination. However, WFI J2033−4723 has a flux density of < 18 mJy at 843 MHz (< 12 mJy at 1.4 GHz, assuming a typical spectral index of −0.7) as it is not detected in the Sydney University Molonglo Sky Survey (SUMSS) Source Catalog (Mauch et al., 2003). The target was observed as part of our programme with ALMA at 341 GHz, which also observed the CO (8–7) emission line from the lensed quasar.

The ALMA observations detect thermal dust emission with a total flux density of 10.4 mJy and achieve an rms noise of 30 μJy beam^{-1} with natural weighting of the visibilities. Imaging of WFI J2033−4723 shows a ring of extended, clumpy dust emission and compact emission from the approximate location of the quasar images (see Fig. 4.5). Arcs of faint emission from the host galaxy have also been observed at optical wavelengths, similar to the extended dust emission observed here (Rusu et al., 2019). The observed flux-density at 341 GHz is in good agreement with the expectations of SED fitting to a thermal dust model (see Fig. 4.21).

We detect the CO (8–7) line emission with a spatially integrated peak flux density of 11 mJy. The FWHM of the line profile is quite narrow, at 83 ± 10 km s^{-1}, and is offset by 258 ± 4 km s^{-1} from the optical systemic velocity (see Fig. 4.7). The line profile shows a broad blue-shifted component to the main peak, but it is not clear whether this is a real feature or due to the low signal-to-noise ratio of the data. Imaging of the CO line shows resolved, compact emission that is coincident with the quasar positions (see Fig. 4.5).

Table 4.2 | Summary of the continuum and line measurements. $\nu_{\rm line}$ is the rest frequency of the CO line. No CO line was observed for PG 1115+080. We derive the FWHM and redshift of the CO line emission based on a single Gaussian fit to the observed line profile (see Fig. 4.7). Here, we give flux densities and luminosities *uncorrected* for the lensing magnification: values corrected for the lensing magnification are presented in Tables 4.4 and 4.5.

	$S_{\rm cont}$ (mJy)	line	$\nu_{\rm line}$ (GHz)	FWHM (km s^{-1})	$I_{\rm CO}$ (Jy km s^{-1})	$L_{\rm CO}$ (L$_\odot$)	$L'_{\rm CO}$ (K km s^{-1} pc^2)	$z_{\rm CO}$
HS 0810+2554	0.30 ± 0.04	CO (3–2)	345.796	370 ± 10	6.0 ± 0.2	$(4.9 \pm 0.2) \times 10^8$	$(3.0 \pm 0.1) \times 10^{11}$	1.50849 ± 0.00005
RX J0911+0551	1.35 ± 0.02	CO (5–4)	576.268	133 ± 3	4.9 ± 0.1	$(4.4 \pm 0.1) \times 10^8$	$(7.2 \pm 0.1) \times 10^{10}$	2.79607 ± 0.00002
SDSS J0924+0219	9.5 ± 0.2	CO (8–7)	921.800	180 ± 10	4.1 ± 0.3	$(8.9 \pm 0.6) \times 10^8$	$(3.5 \pm 0.3) \times 10^{10}$	1.52495 ± 0.00004
PG 1115+080	2.6 ± 0.1	–	–	–	–	–	–	–
H 1413+117	26.0 ± 0.6	CO (9–8)	1036.912	394 ± 8	32.0 ± 1.6	$(5.5 \pm 0.3) \times 10^9$	$(1.5 \pm 0.1) \times 10^{11}$	2.55784 ± 0.00004
WFI J2033−4723	10.4 ± 0.3	CO (8–7)	921.800	83 ± 10	1.0 ± 0.1	$(2.1 \pm 0.2) \times 10^8$	$(8.2 \pm 0.8) \times 10^9$	1.6629 ± 0.0002

4.3. Lens Modelling

The lens modelling analysis is adapted from the grid-based modelling technique of Vegetti & Koopmans (2009). The technique simultaneously optimises for the parameters of the lens galaxy mass distribution and the source surface brightness to produce a pixellated reconstruction of the source. This method is appropriate for optical or infrared images. However, interferometers do not measure the sky surface brightness distribution directly, but measure complex 'visibilities' in the Fourier (uv) plane. Imaging interferometric data is a non-linear process, and the resulting image fidelity can depend heavily on the sparsity of the uv-plane coverage and choice of deconvolution method (e.g. CLEAN Högbom 1974). These systematic uncertainties can be overcome by performing model fitting on the visibility data directly. This approach has been extended to lens modelling, with parametric source models (e.g. Hezaveh et al., 2013; Bussmann et al., 2013, 2015) and also pixellated sources (e.g. Rybak et al., 2015a,b; Hezaveh et al., 2016c; Dye et al., 2018a).

The lens modelling framework is adapted for use with interferometric data by optimising for the visibility-plane χ^2 and source-plane regularisation. This method was first introduced by Rybak et al. (2015a,b) and the full methodology will be presented by Powell et al. (in prep).

Under the assumption of a smooth mass distribution, we parameterise the primary lens potential as a singular isothermal ellipsoid with external shear (Kormann et al., 1994), that is, $\rho(r) \propto r^{-\zeta}$, where $\zeta = 2$. We find initial lens model parameters using the deconvolved images (shown in Figs. 4.1 to 4.6) to provide a good starting model with minimal computational effort. For all objects, with the exception of HS 0810+2554, we perform the model optimisation on the continuum data. For HS 0810+2554, we use the CO (3–2) spectral line channels, which provides more extended emission and a higher signal-to-noise ratio than the continuum, to better constrain the lens model.

For WFI J2033−4723, our lens model also includes a luminous satellite galaxy close to the Einstein radius of the primary lens, which we parameterise as a single isothermal sphere (SIS). The lensing galaxy of RX J0911+0551 also has a small satellite, however this is well within the Einstein radius and so does not have a significant effect on our lens modelling. For WFI J2033−4723, our mass model also includes a massive galaxy 4 arcsec from the primary lens that was required to produce an reasonable fit to the extended emission: the position of this galaxy was fixed based on its relative position from the primary lens in optical data measured by Vuissoz et al. (2008).

The lens redshifts are not known for HS 0810+2554 and H 1413+117, which we assume are at redshift 0.5. However, this choice of redshift only scales the angular size and mass of the perturber, so the inferred properties of the source are not affected by this assumption.

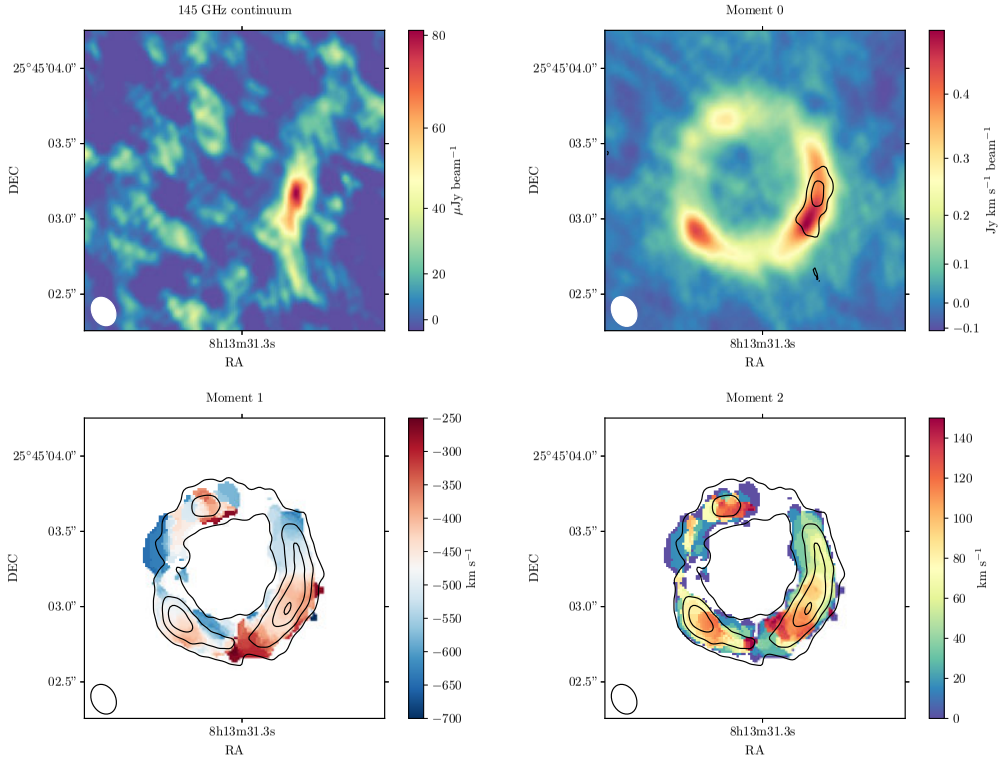

Figure 4.1 | ALMA continuum and CO (3–2) spectral line images of HS 0810+2554. The lensed images are defined A, B, C and D, clockwise from the brightest image. Top row: continuum image with natural weighting; moment 0 image of CO (3–2) image with contours of the continuum emission. Bottom row: moment 1 and moment 2 images, created by masking channel pixels below 4σ, overlaid with contours of the line intensity. The synthesised beam FWHM is shown in the bottom left-hand corner.

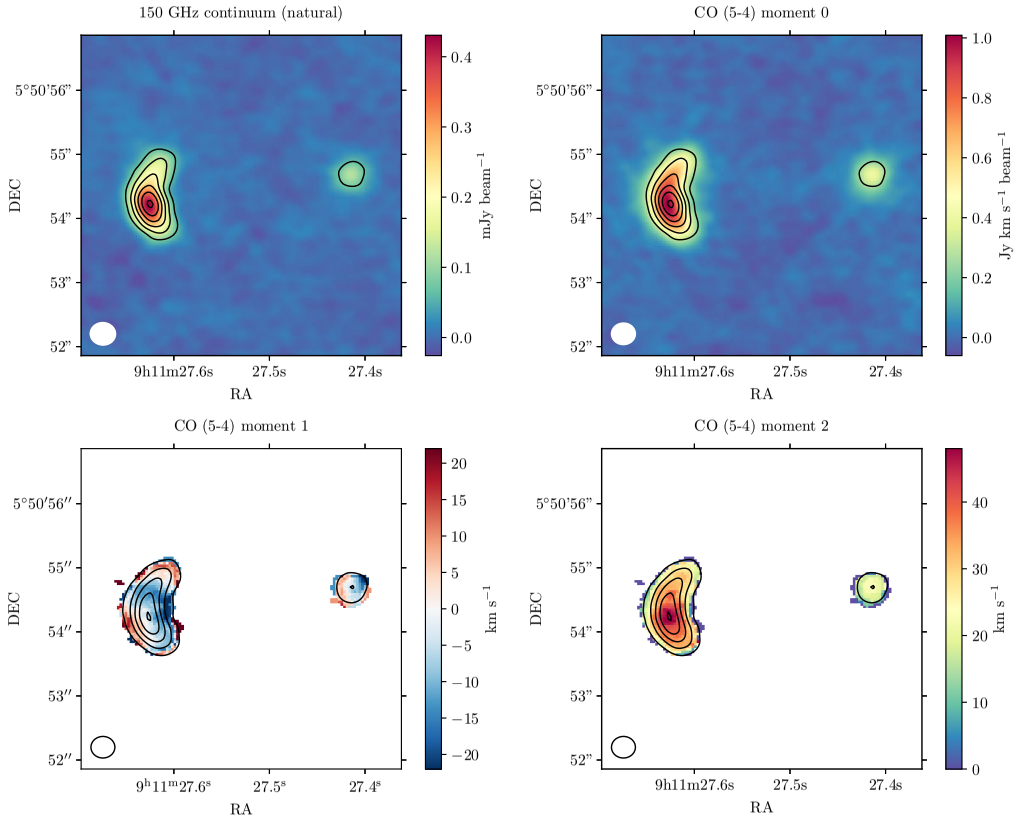

Figure 4.2 | ALMA continuum and CO (5–4) spectral line images of RX J0911+0551. The tripled images are defined A1, A2, A3 and the counter image as B. Top row: continuum image with natural weighting; moment 0 image of CO (5–4) overlaid with contours of the continuum emission. Bottom row: moment 1 and moment 2 images, made by masking channel pixels below 5σ, overlaid with contours of the line intensity. The synthesised beam FWHM is shown in the bottom left-hand corner.

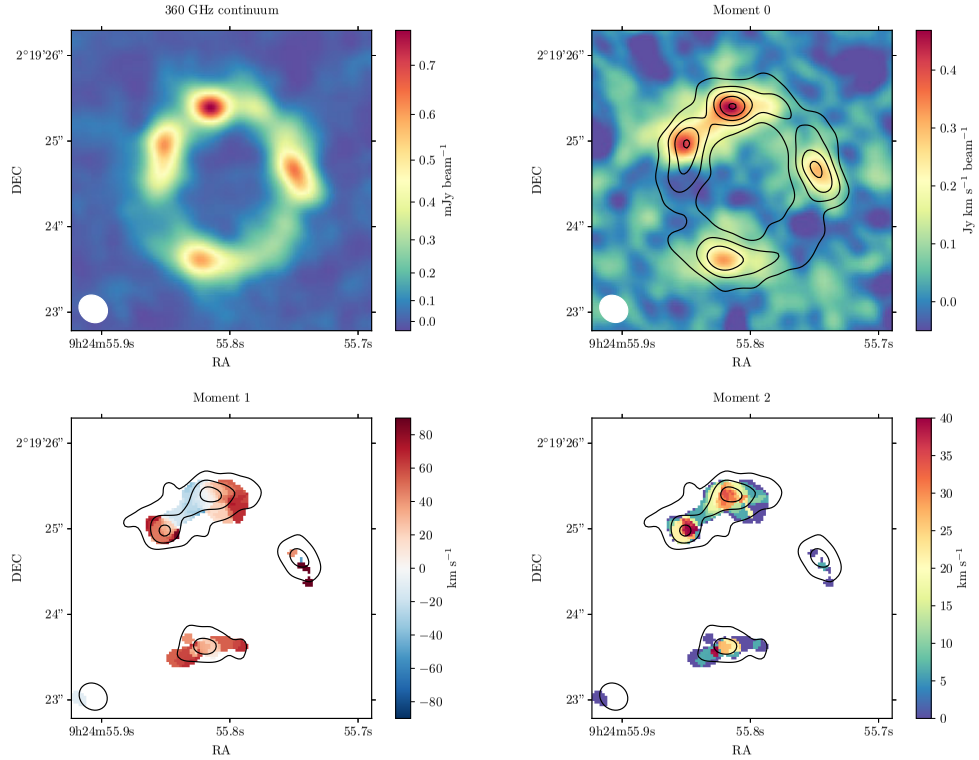

Figure 4.3 | ALMA continuum and CO (8–7) spectral line images of SDSS J0924+0219. The lensed images are defined A, B, C and D, clockwise from the brightest image. Top row: 358 GHz continuum image with natural weighting; moment 0 image of CO (8–7) made with a uv-taper equivalent to 0.3 arcsec, overlaid with contours of the continuum emission. Bottom row: moment 1 and moment 2 images, made by masking channel pixels below 4σ, overlaid with contours of the line intensity. The synthesised beam FWHM is shown in the bottom left-hand corner.

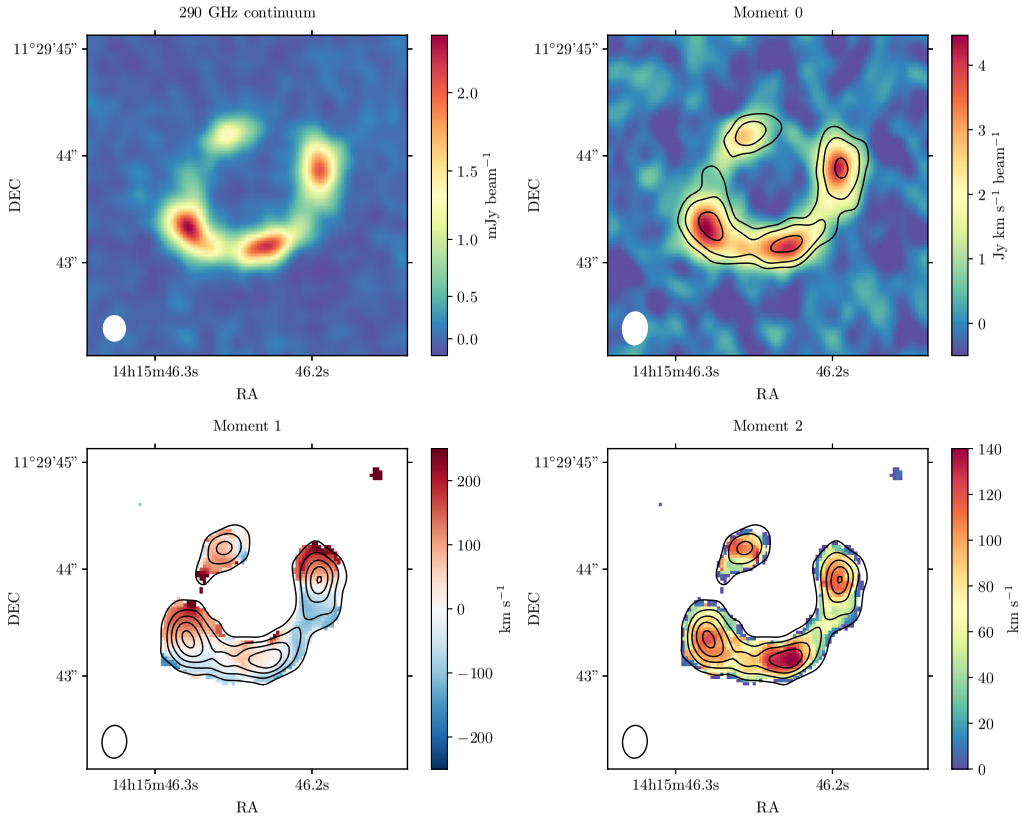

Figure 4.4 | ALMA continuum and CO (9–8) spectral line images of H 1413+117. Top row: 290 GHz continuum image with natural weighting of the visibilities; moment 0 image of CO (9–8) image with Briggs weighting, overlaid with contours of the continuum emission. Bottom row: moment 1 and moment 2 images, made by masking channel pixels below 4σ, overlaid with contours of the line intensity. The synthesised beam FWHM is shown in the bottom left-hand corner.

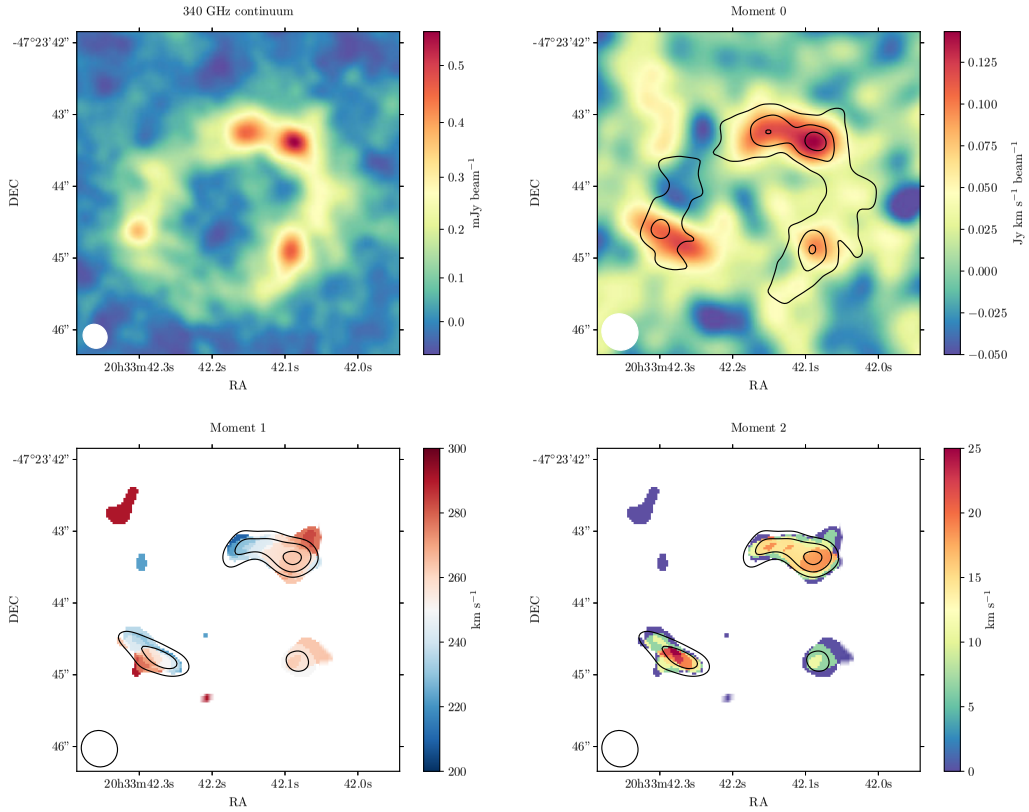

Figure 4.5 | ALMA continuum and CO (8–7) spectral line images of WFI J2033−4723. The lensed images are defined A1, A2, B and C, anti-clockwise from the brightest image. Top row: 345 GHz continuum image with natural weighting; moment 0 image of CO (8–7) made with a $u-v$-taper equivalent to 0.4 arcsec, overlaid with surface brightness contours of the continuum emission. Bottom row: moment 1 and moment 2 images, made by masking channel pixels below 3σ, overlaid with surface brightness contours of the line intensity. The synthesised beam FWHM is shown in the bottom left-hand corner.

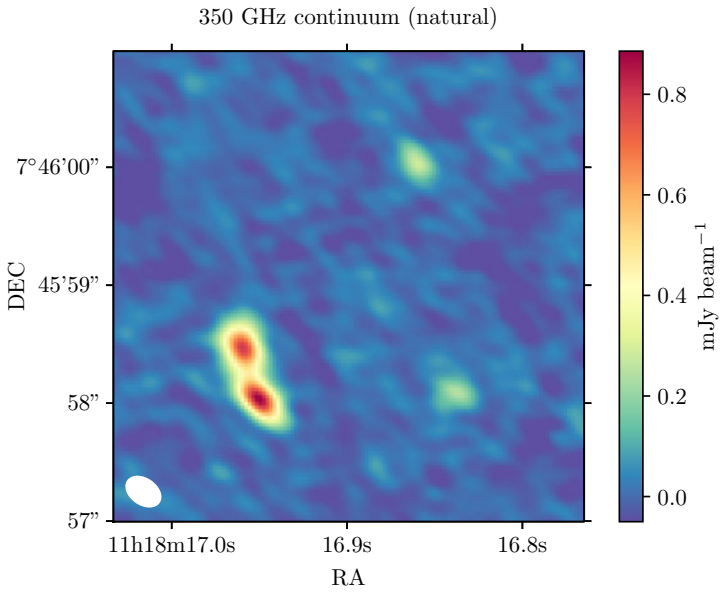

Figure 4.6 | ALMA 346 GHz continuum images of PG1115+080 with natural weighting of the visibility data. The lensed images are defined A1, A2, B and C, clockwise from the brightest image. The synthesised beam FWHM is shown in the bottom left-hand corner.

An initial set of lens parameters and source regularisation was obtained using a Bayesian optimisation of the posterior probability. The uncertainties on the lens model parameters were obtained from the posterior distributions derived using MultiNest (Feroz et al., 2013), with the source regularisation constant fixed to the optimised value. Flat prior ranges were assumed for each free parameter, typically ±20 percent of the optimised values.

Reconstructed velocity cubes were generated from the spectral line data by optimising for the source regularisation, keeping the lens parameters fixed to the maximum posterior values found with MultiNest. For WFI J2033−4723 and SDSS J0924+0219, we select uv data within a maximum baseline of 300 m to improve the surface brightness sensitivity.

4.4. Results

In this section, we present the results of the source reconstruction and an analysis of their physical properties.

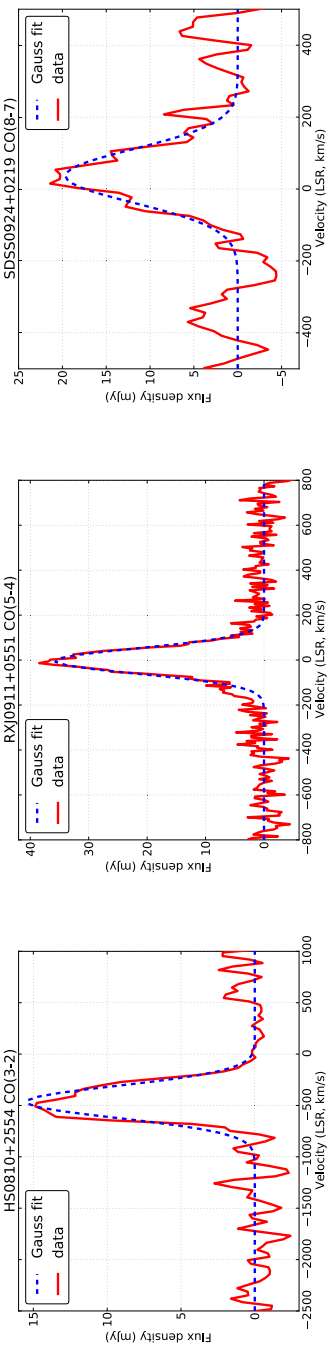

Figure 4.7 | Line profiles for the five objects with CO observations. The red line shows the data; the blue dotted line is a Gaussian fit to the data. The systemic velocity is relative to the best redshift from the literature, using the radio definition of velocity.

4.4.1. Source reconstructions

The lens models are shown in Figs. 4.22 to 4.24 of the Appendix. Although the models are able to fit the extended emission down to the noise level, in some cases, there remain significant residuals around the compact features up to the 6σ level. It is not clear to what extent this is a result of too high source regularisation, or to the failure of the smooth model to account for the surface brightness of the compact emission, which will be more sensitive to substructure in the lens or sub-haloes along the line-of-sight to the quasars (see Chapter 5). For example, H 1413+117 may be affected by a nearby galaxy, based on point-source modelling of mid-infrared observations (MacLeod et al., 2009), and RX J0911+0551 is affected by a large shear gradient from a nearby cluster (Kneib et al., 2000; Hjorth et al., 2002). As the model under-fitting does not contribute significantly to our interpretation of the source structure/size or the intrinsic properties, we consider only the results of smooth lens modelling here. The contribution from low-mass structure in these lens systems will be investigated in future work (see Chapter 7).

The reconstructed sources are shown in Figs. 4.8 to 4.13. The average FWHM of the synthesised beam, after correcting for magnification, is about 30 mas (200 pc) and all systems are resolved. The magnifications of the continuum and line emission for each source are given in Tables 4.4 and 4.5, respectively. Note that this is the mean magnification of the line emission, as the magnification changes across the source and with velocity. We note that the average magnifications are between 8.6 and 19.5 for the sample, which is within the range assumed in Chapter 2, when determining the intrinsic star formation rates of the 104 lensed quasars observed with *Herschel*/SPIRE.

For HS 0810+2554, RX J0911+0551, PG 1115+080 and H 1413+117, the reconstructed dust emission appears to be quite compact and smooth. The apparent smoothness may be due to angular resolution limitations, however, we note that other dusty galaxies at $z \sim 2$ are found to have smooth dust distributions (e.g. Falgarone et al. 2017). For SDSS J0924+0219 and WFI J2033−4723, the dust emission is more extended with clumpy features on kpc-scales, consistent with mergers or interactions. The radially averaged surface brightness distributions of the reconstructed continuum sources are shown in Fig. 4.14. Due to the regularisation parameter of the lens modelling, which limits the absorption of observational noise into the model, the reconstructed source may be smoother than suggested by the data (e.g. see SDSS J0924+0319; Fig. 4.22).

In most cases, the reconstructed line velocity structure shows evidence of rotation around the peak of the continuum emission. For HS 0810+2554, the peak of the line emission is slightly offset from the peak of the dust continuum and the resolved CO velocity structure exhibits an extended and disturbed morphology. However, no emission from the host galaxy is seen in optical or infrared imaging that relates to an

extended stellar disc (Falco et al., 1997; Nierenberg et al., 2019). We also find no other evidence of dust emission that could be from a companion, although this could be due to the signal-to-noise ratio of these data. We consider that the CO (3–2) velocity structure could relate to a bipolar outflow, rather than rotation. In Appendix 4.A we investigate the potential mass and mass loss rate, under the assumption that it is an outflow. Due to the low terminal velocity of the gas and the lack of a distinct resolved disc component, it is uncertain as to whether the velocity features are part of an outflow, or result from an unseen merger or interaction.

To estimate the uncertainties on the intrinsic source surface brightness distribution, we make reconstructions using 20 random samples of the posterior drawn by MultiNest. We do not include samples with relative statistical weights $\leq 1 \times 10^{-4}$ to avoid contributions from models with very low probability. We fit a Sérsic profile (Sérsic, 1963) to each realisation of continuum and line emission using a basin-hopping optimisation algorithm within the SciPy package (Wales & Doye, 1998; Jones et al., 2001). We fit a Gaussian function (weighted by the probability of each model) to the distribution of major and minor axes from the model fit, and source magnifications. We assume the weighted mean and standard deviation of the Gaussian as the parameter value and its uncertainty.

For HS 0810+2554, RX J0911+0551 and PG 1115+080, due to the lens configuration and angular resolution of the data, the lensed emission is not radially resolved. This results in a reconstructed source that appears flattened, as the size of the major axis is constrained only by the angular resolution. For these systems, we assume the minor axis as a more accurate estimate of the source size.

A further consequence of the lack of radial resolution is that there is a strong degeneracy between the source magnification and the slope of the lens mass density profile. The effect of this degeneracy is a geometric scaling of the reconstructed source. We assume an isothermal profile for our lens models (i.e. $\zeta \equiv 2$), however the empirical scatter in the total mass slope of early-type galaxies (0.16; Auger et al. 2010) is an additional source of uncertainty in the source size. We tested this by modelling PG 1115+080 with a profile fixed to a value $\pm 1\sigma$ from the median found by Auger et al. (2010). We find that the size and normalisation of a Sérsic fit to the reconstructed source changes by ≤ 10 percent. Therefore, we include an additional 10 percent error to our estimated sizes and magnifications to account for this uncertainty.

4.4.2. Dust properties

We use the new sub-mm data to improve SED models for our sample. The SED fitting follows the same procedure described in Chapter 2, using ancillary data listed therein.

Figure 4.8 | Reconstructed dust and CO (3–2) spectral line emission of HS 0810+2554. The dust emission is shown in units of star formation rate density. The moment 0 image is overlaid with the dust surface brightness contours. The moment 1 and 2 images are overlaid with contours of the line intensity. The line reconstructions are generated by masking pixels below 4 σ. The bar shows 1 kpc at the redshift of the source.

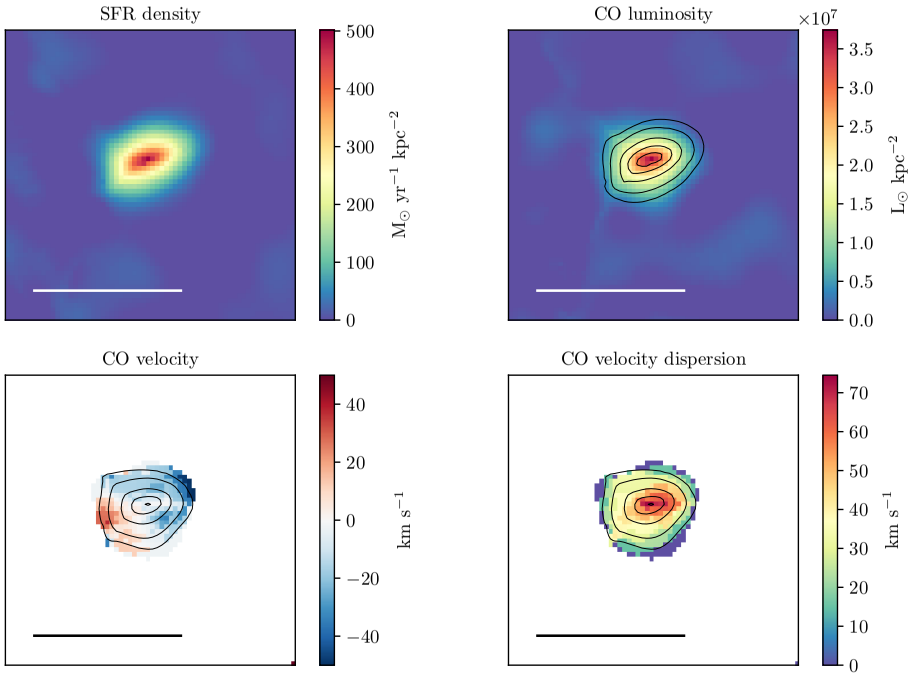

Figure 4.9 | Reconstructed dust and CO (5–4) spectral line emission of RX J0911+0551. The dust emission is shown in units of star formation rate density. The moment 0 image is overlaid with continuum surface brightness contours. The moment 1 and 2 images are overlaid with contours of the line intensity. The line reconstructions are generated by masking pixels below 3 σ. The bar shows 1 kpc at the redshift of the source.

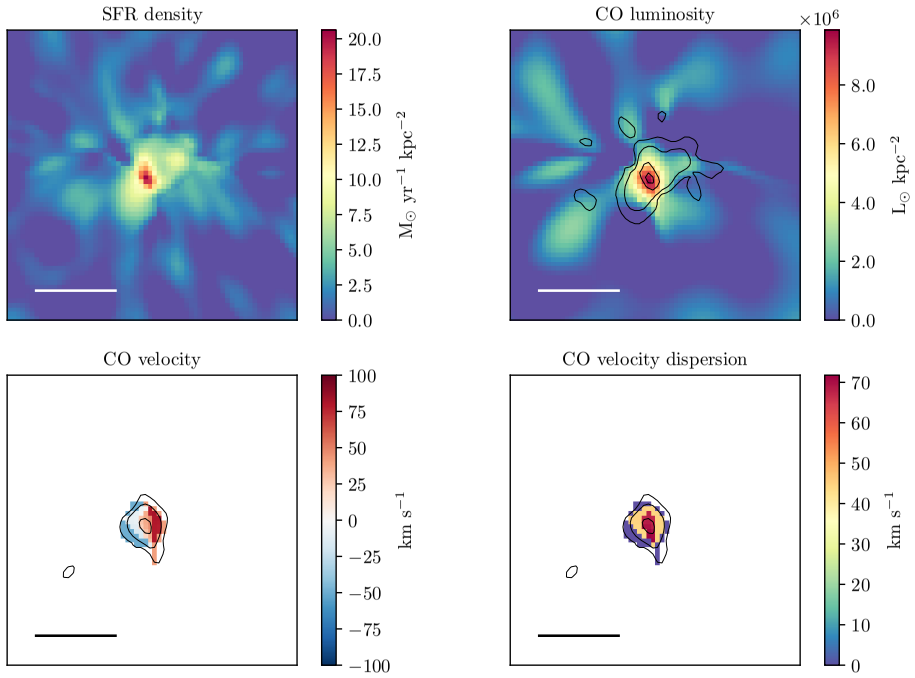

Figure 4.10 | Reconstructed dust and CO (8–7) spectral line emission of SDSS J0924+0219. The dust emission is shown in units of star formation rate density. The moment 0 image is overlaid with continuum surface brightness contours. The moment 1 and 2 images are overlaid with contours of the line intensity. The line reconstructions are generated by masking pixels below 4 σ. The bar shows 1 kpc at the redshift of the source.

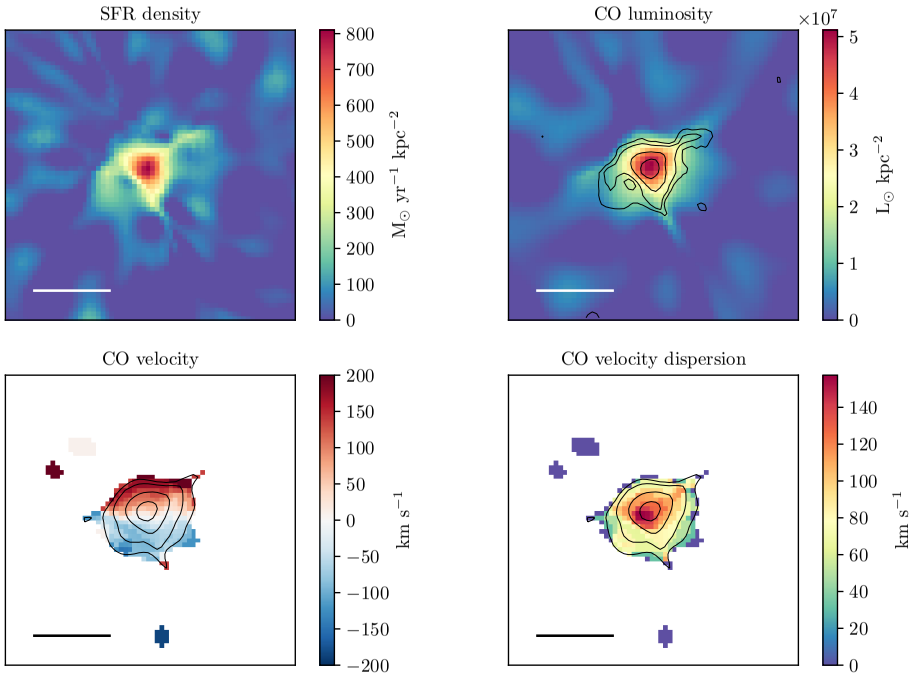

Figure 4.11 | Reconstructed dust and CO (9–8) spectral line emission of H 1413+117. The dust emission is shown in units of star formation rate density. The moment 0 image is overlaid with continuum surface brightness contours. The moment 1 and 2 images are overlaid with contours of the line intensity. The line reconstructions are generated by masking pixels below 3 σ. The bar shows 1 kpc at the redshift of the source.

Figure 4.12 | Reconstructed dust and CO (9–8) spectral line emission of WFI J2033+4723. The dust emission is shown in units of star formation rate density. The moment 0 image is overlaid with continuum surface brightness contours. The moment 1 and 2 images are overlaid with contours of the line intensity. The line reconstructions are generated by masking pixels below 3 σ. The bar shows 1 kpc at the redshift of the source.

The SED models consist of a characteristic modified black body component described by

$$S_\nu \propto \frac{\nu^{3+\beta}}{e^{h\nu/kT_\mathrm{d}} - 1}, \tag{4.1}$$

for optically thin thermal dust emission, where S_ν is the flux density, ν is the emission rest-frame frequency, h is the Planck constant, k is the Boltzmann constant, T_d is the dust temperature and β is the dust emissivity index. We leave the dust temperature and emissivity (which governs the steepness of the Rayleigh-Jeans slope of the spectrum) as free parameters. Depending on the available ancillary data, we also fit a power-law component described by

$$S_\nu \propto \nu^\alpha, \tag{4.2}$$

where α is the spectral index, to account for optically thin radio synchrotron emission.

We apply a Markov Chain Monte Carlo (MCMC) analysis using the Python implementation EMCEE (Foreman-Mackey et al., 2013) to infer the marginalised posterior distributions for each free parameter and the integrated FIR luminosity. The SED models are shown in Figs. 4.19–4.21 of the Appendix. The parameters from the SED modelling, corrected for the lensing magnification, are shown in Table 4.4.

The dust temperature we infer from our SED fitting is an *effective* dust temperature, which should not be considered a true measure of dust temperature but weighted by multiple components of dust emission. This may include a cold dust component from cirrus dust of the interstellar medium (~ 20 K) and a warmer dust component associated with star-forming regions (~ 50 K). Swinbank et al. (2014) find DSFGs require at least three dust components to account for the mid-infrared (MIR) to FIR SED. AGN host galaxies may also have contributions from AGN-heated dust emission. For HS 0810+2554 and H 1413+117, we account for a warm dust component, which we assume is associated with the AGN. For HS 0810+2554, β is kept fixed in the SED modelling as we do not have sufficient data points to fit both β and two dust components. We fix β to a value of 2, as 1.5 cannot produce a satisfactory fit to the data*. With the exception of H 1413+117 and HS 0810+2554, we do not have sufficient data at rest-frame wavelengths ~ 10 to 100 μm to consider multiple thermal dust components without over-fitting and, hence, over-interpreting our results. Note that, while we leave β as a free parameter, its value should not be considered physically significant as, for poorly sampled SEDs, the strong temperature–β degeneracy mostly absorbs the observational noise in the data (Juvela & Ysard, 2012c). We allow this as a free parameter to better estimate the true uncertainty on the fitted temperature and luminosity.

*For comparison, the median and distribution of the parent sample is $\beta = 2.0^{+0.4}_{-0.5}$, Chapter 2.

We follow the Helou et al. (1988) definition of FIR luminosity ($L_{\rm FIR}$), as the integrated spectra from 40 to 120 μm. We convert this to total infrared luminosity (8 to 1000 μm) using a colour correction factor of 1.91 (i.e. $L_{\rm IR} = 1.91 \times L_{\rm FIR}$) given by Dale et al. (2001) to account for spectral features in the MIR, assuming our fitted cold dust component is associated only with obscured star formation. We convert this to a star formation rate (SFR; $\mathrm{M_\odot\ yr^{-1}}$) assuming a Salpeter initial mass function with the conversion factor of Kennicutt (1998),

$$SFR = \frac{L_{\rm IR}}{5.8 \times 10^9}, \tag{4.3}$$

where $L_{\rm IR}$ is in units of $\mathrm{L_\odot}$[†].

We follow Dunne et al. (2000) to estimate the dust mass from our SED fits using

$$M_{\rm dust} = \frac{D_{\rm L}^2\ S_{850}^{\rm obs}}{(1+z)\ \kappa_{850}\ B_{850}(T_{\rm d})}, \tag{4.4}$$

where $S_{850}^{\rm obs}$ is the observed flux density at rest-frame wavelength 850 μm (350 GHz), $D_{\rm L}$ is the luminosity distance, κ_{850} is the dust mass opacity (0.077 $\mathrm{m^2\ kg^{-1}}$, from Dunne et al. 2000), and $B_{850}(T)$ is the value of a black body of temperature T at 850 μm.

It has long been established that a dust mass estimated from single temperature fitting can underestimate the total dust content, as most of the mass is in cold cirrus dust and not the dust that contributes most to the effective (luminosity-weighted) temperature. To minimise the effect of this bias, we fit two temperature models to our three sources with higher dust temperatures, where we fix the temperature of the cold component with constant temperature 25 K and $\beta = 2$, as recommended by previous studies (e.g. Dunne & Eales 2001). We do not find a benefit in fitting multiple components to the sources with temperatures < 40 K as the difference in the derived dust mass is not significantly different given our overall uncertainties. This cold component is appropriate for star-forming galaxies, but it has not been established to what extent a 25 K component is appropriate for quasar host galaxies. Note that, if the temperature of dust in the diffuse ISM is higher for quasar hosts, the dust masses of our sample could be underestimated. However, considering the gas-to-dust ratios computed in a subsequent section (Section 4.4.5), the dust masses are probably accurate within a factor of 2 as they correspond to an approximately solar metallicity, suggesting that super-solar metallicity values would be required to account for significantly higher

[†]Note that there is evidence that starbursts have top-heavy IMFs (Zhang et al., 2018). Our assumption of a Salpeter IMF may overestimate the star formation rate by overestimating the number of low-mass stars; thus, a different choice of IMF would result in an overall re-scaling of the star formation rates. However, as we are mostly concerned with *relative* star formation rates in this work, our choice of IMF does not significantly impact our results.

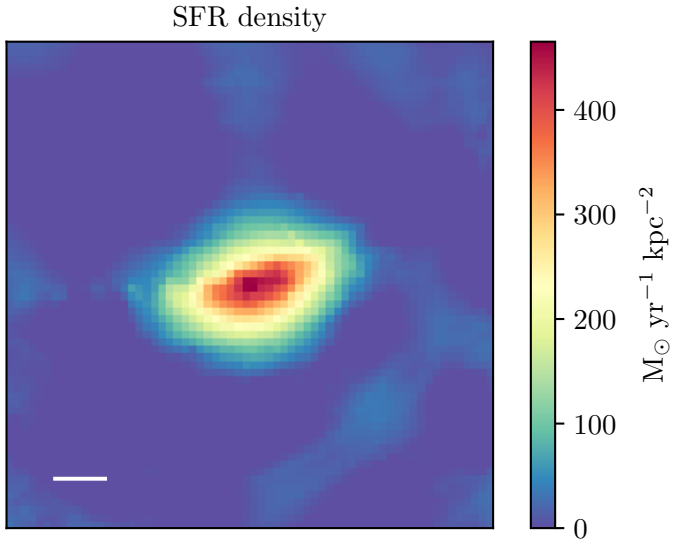

Figure 4.13 | Reconstructed dust emission of PG 1115+080, shown in units of star formation rate density.

dust masses.

The dust temperatures, emissivities, intrinsic luminosities, star formation rates and dust masses for the sample are given in Table 4.4. For H 1413+117, the nearby field source we identify in our ALMA imaging (Section 4.2.6) may cause modest confusion in SED fitting, which leads to overestimates of the inferred star formation properties of the source of interest. Photometric measurements at multiple frequencies will be required to accurately deblend this emission from the total infrared luminosity. Such an analysis is beyond the scope of this work, however, the consistent relative flux density of the objects at 100 and 290 GHz suggests that the neighbour contributes ~ 20 percent to the photometry of H 1413+117. Therefore, our measurements based on infrared luminosity are likely to be overestimated by a similar percentage. We estimate the effect of this by recomputing the SED after scaling all the photometric measurements above 300 GHz by 0.8. The physical properties based on the rescaled data are also shown in Table 4.4.

4.4.3. Molecular gas properties

Fig. 4.15 shows the intrinsic effective radius of the dust and CO emission against effective dust temperature and total infrared luminosity (8–1000 μm). The sample

in this work is quite heterogeneous and different rotational transitions of CO were observed. These CO lines correspond to different physical conditions in the ISM. At one extreme, CO (9–8) and CO (8–7) trace warm gas (150–200 K) in regions of intense star formation or that are associated with AGN. For the three objects where we observe one of these lines (SDSS J0924+0219, H 1413+117 and WFI J2033−4723), the molecular gas is more compact than the dust continuum. For RX J0911+0551, we observe CO (5–4), which has excitation conditions that are typical of star-formation: the gas has the same size and distribution as the dust continuum, consistent with this scenario. For HS 0810+2554, the one system in which we observe CO (3–2), which is a more accurate probe of the reservoir of cold gas (Sharon et al., 2016), we find the gas to be more extended than the dust. While little can be inferred about the relative contributions to the energy budget from observations of a single line transition, the observed morphologies are consistent with high levels of star formation, and with the expectations for a radially decreasing gas column density and temperature.

We convert our line flux densities to luminosities ($L_{\rm CO}$ and $L'_{\rm CO}$) with relations as given by Solomon & Vanden Bout (2005). We use the source-plane integrated line intensity to account for differential magnification of the line emission. The intrinsic line luminosities (corrected for lensing magnification) are given in Table 4.5. The reconstructed line emission in units of luminosity surface density, as well as the velocity field and velocity dispersion, are shown for each source in Figs. 4.8 to 4.12.

From the reconstructed line emission, we estimate the enclosed dynamical mass of the galaxies, assuming

$$M_{\rm dyn} = \frac{R_{\rm 2eff} V_{\rm max}^2}{G}, \tag{4.5}$$

where $R_{\rm 2eff}$ is twice the effective radius of the CO emission based on the Sérsic model fit described in Section 4.4.1. Here, σ is the maximum rotational velocity, assuming $V_{\rm max} = V_{\rm obs}/\sin i$, where i is the inclination angle. We derive $\sin i$ from the Sérsic model fit according to

$$\sin i = \sqrt{1 - \left(\frac{b}{a}\right)^2}, \tag{4.6}$$

where b is the minor axis and a is the major axis. Where we do not have a reliable constraint on the axis ratio due to a lack of radial resolution (i.e. RX J0911+0551, PG 1115+080 and WFI J2033−4723) we assume an inclination angle of 45 ± 15 deg, corresponding to axis ratios of 0.5 to 0.9. In this case, we do not consider axis ratios below 0.5 as they are smaller than the apparent axis ratio. This method assumes that the circular velocity accurately traces the gas rotation, ignoring the effect of a non-spherical gravitational potential and turbulent pressure. Simulations suggest that this assumption could result in an underestimate of the dynamical mass at very small

or large radii, but is accurate at the intermediate radii (~ 1 kpc) we probe here (Wellons et al., 2019). The dynamical masses for the quasar hosts are given in Table 4.5. Note that the dynamical mass inferred from the CO lines investigated here (particularly the high-excitation lines) may not probe the total mass of the galaxy.

In addition to the availability of gas, the level of star formation in a galaxy depends on the local balance between turbulent pressure and self-gravity. In dynamically unstable systems, self-gravity dominates over turbulent pressure allowing gas to fragment and efficiently form stars. As the systems in this work are known to have high star formation rates and, in some cases, have clumpy non-axisymmetric dust structures, we expect the gas discs to be globally dynamically unstable. As shown in Figs. 4.8 to 4.13, the reconstructed velocity maps appear to show radially increasing rotational velocity and high central dispersions. However, these 2-dimensional maps are likely to be strongly affected by beam-smearing, which can misguide interpretation of the dynamics of the systems (e.g. Lelli et al. 2010). We defer a 3D analysis to future work, combining lens and source kinematic modelling as introduced by Rizzo et al. (2018).

4.4.4. Comparison with dusty star-forming galaxies

We make a comparison between our lensed quasar hosts and high angular resolution ALMA observations of DSFGs from the LABOCA ECDFS Submm Survey (ALESS; Hodge et al. 2016). We select this sample as the redshift range ($z \sim 2$, including one at $z = 3.4$) and infrared luminosities are similar to our lensed quasar hosts. Note that none of the ALESS sample were unresolved when observed at high angular resolution (Hodge et al., 2016, 2019), so we do not explicitly introduce a bias to our comparison by selecting DSFGs with the largest sizes. We perform SED fitting for the ALESS sample with photometry from Swinbank et al. (2014) and Hodge et al. (2019). For consistency, we use the same methodology as for the quasar hosts to obtain effective dust temperatures and infrared luminosities. Following this methodology, we only include the 11 ALESS galaxies where there are sufficient detections at FIR–sub-mm wavelengths to constrain the dust temperature.

We note that sub-mm source selection may preferentially identify sources with lower dust temperatures at a given redshift, due to the effect of negative k-correction (Chapin et al., 2011). The quasar hosts are not strongly influenced by this selection effect, as they were selected in the FIR, which probes the peak of the dust rather than the Rayleigh-Jeans slope, but may influence the selection of the coeval DSFGs. Therefore, we further include DSFGs at $z > 4$ to try to mitigate this bias in our analysis. This sample includes one of the ALESS DSFGs (Hodge et al., 2019) and four other

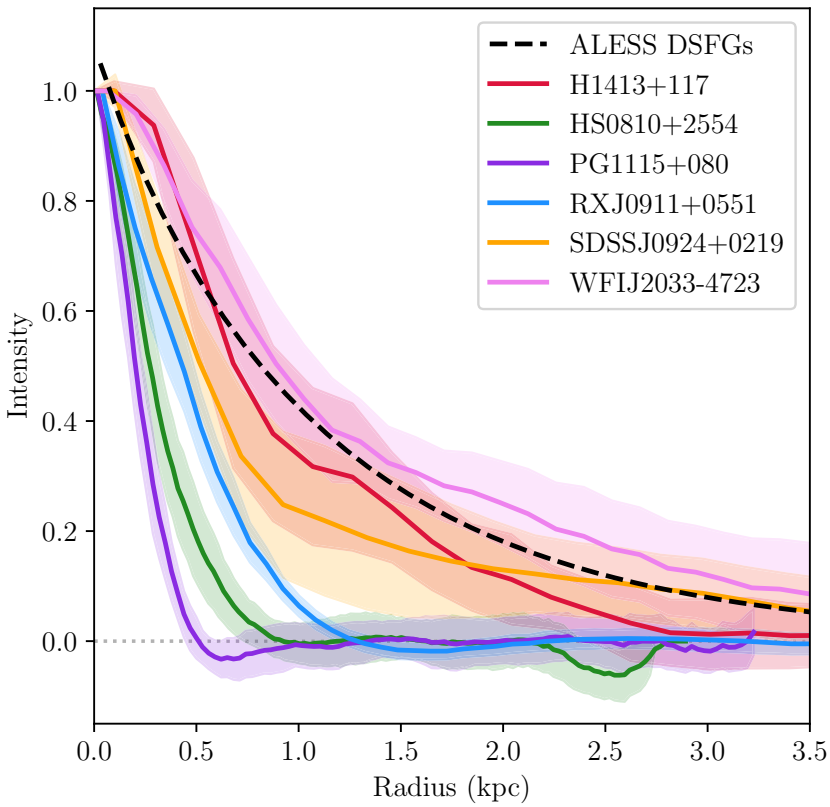

Figure 4.14 | Normalised, azimuthally averaged surface brightness profiles of the reconstructed dust emission from the quasar hosts. The shaded regions show the respective standard deviation of the dust emission. The radius of HS 0810+2554, RX J0911+0551 and PG 1115+080 are scaled to the size of the minor axis, based on the axis ratio from the Sérsic model fits (see Section 4.4.1). The black dotted line shows the mean profile of (unlensed) ALESS DSFGs from Sérsic fits (Hodge et al., 2016, 2019). The average magnification-corrected resolution is about 200 pc (100 pc radius).

objects that are spatially resolved, with spectroscopic redshifts and multiple detections at FIR–sub-mm wavelengths. These include GN20 (Hodge et al., 2015), HFLS3 (Riechers et al., 2013), AzTEC-3 (Riechers et al., 2014), the two components of SGP38326 (Oteo et al., 2016) and the two components of ADFS-27 (Riechers et al., 2017). At these high redshifts, the FIR–sub-mm photometry is dominated by optically-thick dust emission, so we assume the dust temperature and luminosity determined from previous SED fitting that accounts for this emission, with the exception of GN20 (which lacks the data). A summary of the DSFGs is given in Table 4.6 of the Appendix.

Fig. 4.16 (left) shows the continuum source size (effective radius) of the quasar hosts in this work and the $z \sim 2$ DSFGs. This shows that more compact dust emission is associated with higher effective dust temperatures. A Kendall rank test for correlation between size and temperature yields a coefficient of $\tau = -0.38$ with a significance of $p = 0.04$ (where $p = 0.05$ is often taken as significant). Such a relationship is expected as a natural consequence of the Stefan-Boltzmann law, which relates the luminosity of a black body to its temperature and physical size. If the luminosity and temperature of the thermal dust emission we observe from the quasar hosts is related only to star formation, they should follow this relation.

Fig. 4.17 shows the intrinsic infrared luminosity (and equivalent star formation rate) against effective dust temperature for our sample and the DSFGs. The relationship expected for the modified Stefan-Boltzmann law from Yan & Ma (2016) is also shown for different source sizes. The DSFGs and quasar hosts can be seen to broadly follow this relationship. Fig. 4.17 shows that the lensed quasars have sizes larger than implied by their dust temperature, which could indicate the sub-mm emission has a significant contribution from AGN-heating. However, we note that for these systems (SDSS J0924+0219 and WFI J2033−4723) the dust distribution is resolved into multiple clumps and a single Sérsic component is likely a poor descriptor of their surface brightness distribution (Figs. 4.10 and 4.12). This blending effect was also suggested by Yan & Ma (2016), who found some DSFGs have sizes larger than expected from the Stefan-Boltzmann relation.

Fig. 4.17 suggests that quasar hosts generally have smaller sizes and higher temperatures than DSFGs of similar infrared luminosity, and smaller sizes and higher luminosities than DSFGs of similar temperature. The $z \sim 2$ DSFGs are generally larger than quasar hosts, and the $z > 4$ DSFGs have intermediate sizes between the $z \sim 2$ DSFGs and quasar hosts. Based on the $L_{\rm IR}$–$T_{\rm d}$ distribution of the parent sample of lensed quasar systems, we can also expect the population to have a size distribution in the range probed by our sub-sample, i.e. they are generally characterised by sizes smaller than the samples of DSFGs.

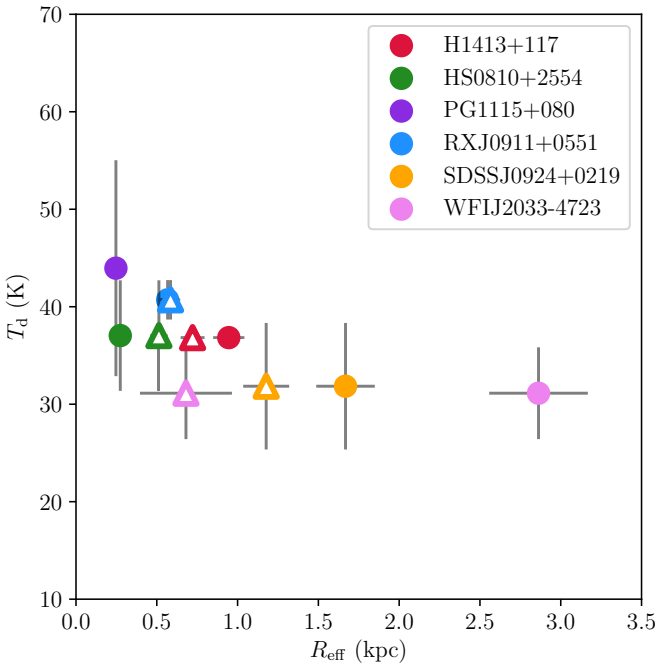

Figure 4.15 | The effective radius ($R_{\rm eff}$) of the dust continuum (solid circles) and CO line emission (open triangles) against effective dust temperature ($T_{\rm d}$) for the six lensed quasar hosts investigated here.

4.4.5. Intensity of star formation

We estimate the galaxy-averaged star formation rate surface density ($\Sigma_{\rm SFR}$; $M_\odot\ {\rm yr}^{-1}\ {\rm kpc}^{-2}$), for our sample and the DSFGs, assuming

$$\Sigma_{\rm SFR} = 0.5 \times \frac{SFR}{\pi R_{\rm eff}^2}, \tag{4.7}$$

where $R_{\rm eff}$ is the dust effective radius based on the Sérsic model fit. Fig. 4.16 (right) shows the galaxy-averaged star formation rate surface density against effective radius, where the dotted tracks show the analytic relationship for $\log L_{\rm IR}$ of 12, 12.5, 13 and 13.5, following Eq. 4.7.

While the CO lines we observe with ALMA are not reliable probes of cold gas, two of our sample have previous detections of CO (1–0), which is a common proxy for molecular hydrogen (H_2). From the gas surface density, we estimate the Eddington limit of star formation for these systems (adopting our magnifications and uncertainties) that we as-

sume are typical for the sample as a whole. We assume $\alpha_{CO} = 0.8\ M_\odot\ (K\ km\ s^{-1}\ pc^2)^{-1}$, as is often assumed for dusty starbursts, to convert L'_{CO} to total gas mass (M_{gas}). The gas surface density (Σ_{gas}) is derived in the same manner as Eq. 4.7, adopting the effective radius of the CO emission.

For RX J0911+0551, using CO (1–0) data from (Sharon et al., 2016), we find $M_{gas} = (5.7 \pm 1.1) \times 10^9\ M_\odot$ and $\Sigma_{gas} = (2.6 \pm 0.7) \times 10^9\ M_\odot\ kpc^{-2}$. This implies a dust-to-gas ratio of 0.010 ± 0.003 and a gas fraction of 0.6 ± 0.4 in comparison to our derived dynamical mass (see Table 4.5)[‡]. The high angular resolution observations reported by Sharon et al. (2016) are visually similar to our results for CO (5–4), suggesting that the CO (5–4) source size is not significantly larger for the CO (1–0) as it would be extended into an arc or Einstein ring.

For H 1413+117, using CO (1–0) data from Riechers et al. (2011c), we find $M_{gas} = (3.1 \pm 0.1) \times 10^{10}\ M_\odot$ and $\Sigma_{gas} = (1.0 \pm 0.2) \times 10^{10}\ M_\odot\ kpc^{-2}$, which implies a dust-to-gas ratio of 0.011 ± 0.001 and a gas fraction of 0.5 ± 0.1 in comparison to our derived dynamical mass (see Table 4.5). A gas fraction of ~ 0.5 is typical of DSFGs and main sequence galaxies at $z > 1$ (see Figure 4 of Spilker et al. 2016). A recent study of resolved CO (1–0) from two $z \sim 2$ DSFGs hosting radio-loud AGN found gas fractions of ~ 0.6 (Spingola et al., 2019). For H 1413+117, the CO (1–0) imaging reported by Riechers et al. (2011c) does not resolve the lensed emission, so it is not clear how reasonable our assumption is that the physical size of the CO (1–0) is similar to the CO (9–8) emission: we note that Riechers et al. (2011c) and Sharon et al. (2016) did not find evidence that CO (1–0) from AGN hosts is significantly more extended than higher J-level CO transitions. In this case, the inferred Eddington limit can be considered a lower limit.

We estimate the optically thick Eddington flux limit (F_{Edd}) assuming the relation from Andrews & Thompson (2011) for warm starbursts,

$$F_{Edd} \sim 10^{13}\ L_\odot\ kpc^{-2}\ f_{gas}^{-1/2}\ f_{dg,150}^{-1}, \tag{4.8}$$

where f_{gas} is the gas fraction and $f_{dg,150}$ is the dust-to-gas ratio multiplied by 150. Using the conversion in Eq. 4.3 for a Salpeter IMF, this implies an Eddington-limited star formation rate surface density of $1500 \pm 600\ M_\odot\ yr^{-1}\ kpc^{-2}$and $1500 \pm 200\ M_\odot\ yr^{-1}\ kpc^{-2}$for RX J0911+0551 and H 1413+117, respectively. As can be seen in Fig. 4.16, the mean star formation rate density of the four compact quasar hosts are within a factor of 2 to 3 of the estimated Eddington limit.

From the star formation rate and the molecular gas mass, we can predict the gas depletion timescale (i.e. $t_{dep} \equiv M_{gas}/SFR$). For RX J0911+0551 and H 1413+117, we

[‡]Incidentally, this gas fraction supports our assumption of a low α_{CO}, as Milky-Way-level factor of $4.6\ M_\odot\ (K\ km\ s^{-1}\ pc^2)^{-1}$ would significantly over-predict the gas mass.

predict that their molecular gas reservoirs will be consumed within a timescale of around 15 and 20 Myr, respectively.

4.5. Discussion

4.5.1. Evidence for extreme star formation in quasar host galaxies

The six objects investigated here were selected from a larger survey of 104 lensed quasars with *Herschel*/SPIRE that was reported in Chapter 2, who performed SED fitting to constrain the level of dust-obscured star formation in the sample. In all but three cases (including H 1413+117), a single dust component was used for the fitting due to the lack of data in the MIR to FIR. From this analysis, we found a median dust temperature of 38^{+12}_{-5} K and a median star formation rate of 120^{+160}_{-80} $M_\odot$ yr^{-1}, both of which are consistent with typical DSFGs. A concern from such a simple SED model is that AGN-heated dust emission could contribute to the FIR and result in a higher dust temperature and, hence, a higher effective dust temperature (e.g. Kirkpatrick et al. 2012). Indeed, in some cases, effective dust temperatures were found that are higher than typical for star formation. However, we find that the quasar hosts are generally consistent with the Stefan-Boltzmann relation between temperature and luminosity (see Fig. 4.15), suggesting that the dust is uniformly heated to higher temperatures by an extended starburst, as opposed to the central AGN. This does not exclude the possibility that the AGN contributes to the cold dust emission, but in such a scenario it cannot be a significant fraction without a conspiracy between the effective radius, temperature and luminosity. The higher dust temperatures found for some quasar hosts relative to DSFGs can be explained by their more compact physical sizes. The distribution of the parent sample of lensed quasars on the luminosity–temperature plane, as shown in Fig. 4.15, suggests that they are globally characterised by small physical sizes, with $R_{\rm eff} \sim 1$ kpc.

We estimate that the compact quasar hosts in our sample have Eddington-limited star formation rate surface densities. This finding is consistent with previous investigations of H 1413+117, which have independently verified an Eddington-limited starburst with radiative transfer modelling of spectral line ratios (Bradford et al., 2009; Riechers et al., 2011a; Uzgil et al., 2016). In general, while an X-ray radiation field may penetrate large column densities of molecular gas, it will not efficiently heat dust grains over large distances (Meijerink et al., 2007). These factors further suggest that the AGN are

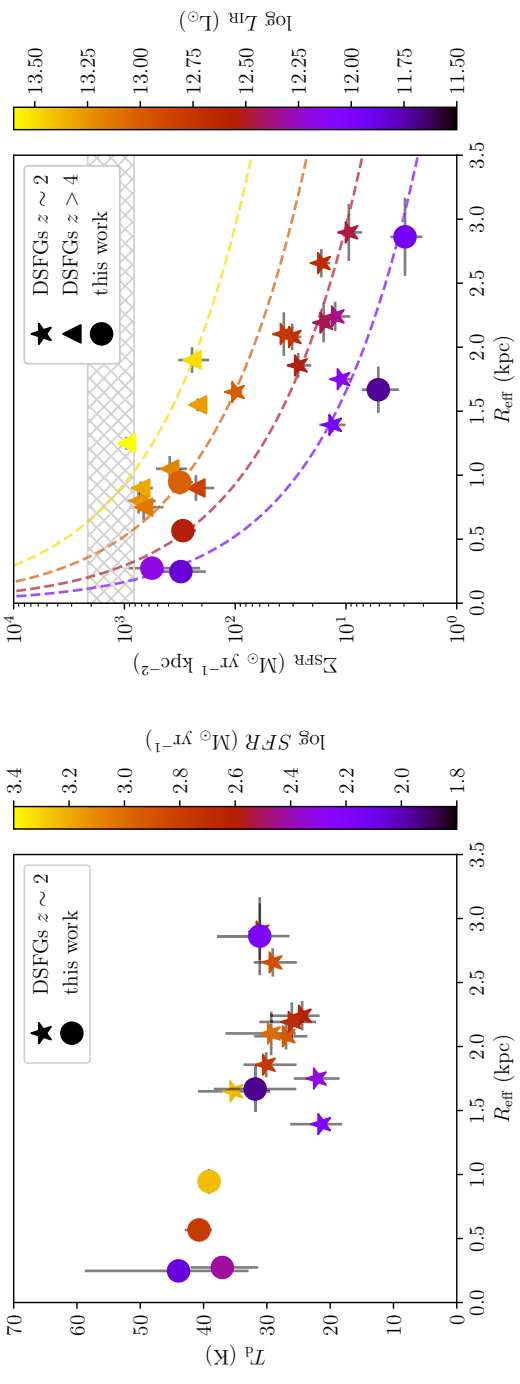

Figure 4.16 | (left) Effective radius ($R_{\rm eff}$) against dust temperature ($T_{\rm d}$), coloured by star formation rate. (right) Effective radius against mean star formation rate surface density ($\Sigma_{\rm SFR}$), where the grey region shows our estimated Eddington limit and its uncertainty. $\Sigma_{\rm SFR}$ and the dashed curves show the tracks for log$L_{\rm IR}$ values of 12, 12.5, 13, 13.5. Circles show the quasar hosts in this work (with H 1413+117 corrected for SED blending); stars show coeval DSFGs at $z \sim 2$ (Hodge et al., 2016, 2019); triangles show DSFGs at $z > 4$ (Hodge et al., 2015, 2016; Riechers et al., 2013, 2014, 2017). Four of the six quasar hosts have star formation rate surface densities close to the Eddington limit.

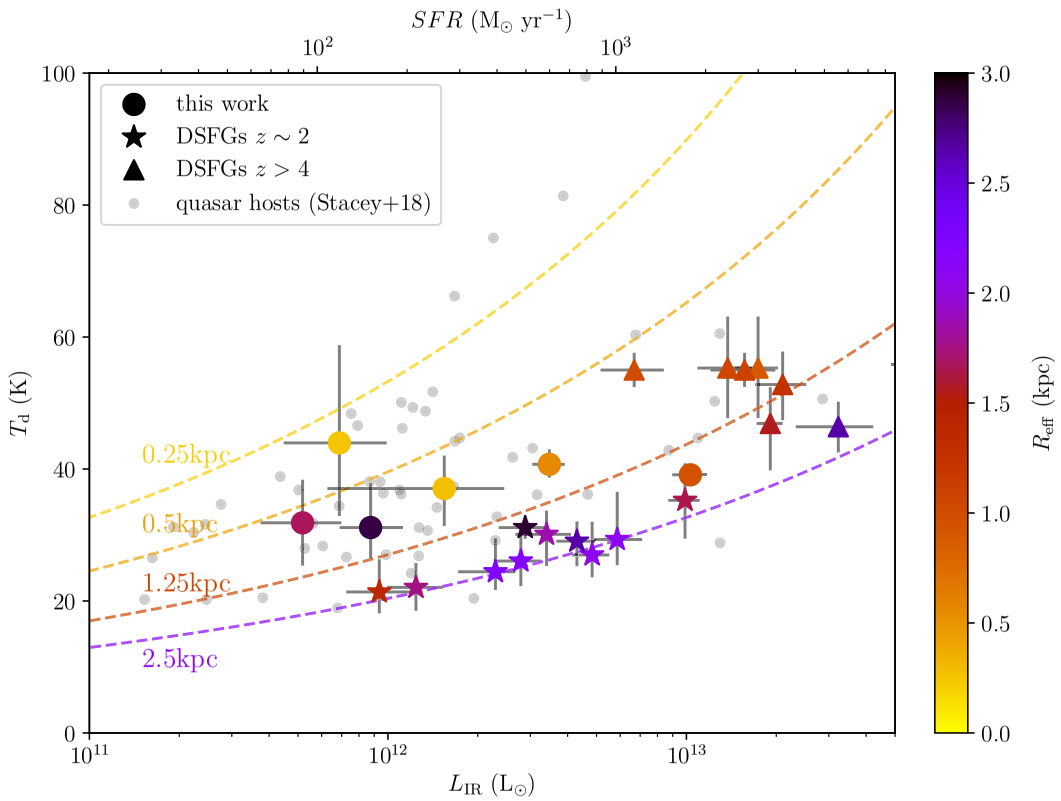

Figure 4.17 | Effective dust temperature against infrared luminosity, coloured by effective radius. The dashed lines show the modified Stefan-Boltzmann relation from Yan & Ma (2016) for sources of indicated physical sizes. Sources from this work are shown with circles (with H 1413+117 corrected for SED blending). DSFGs at $z \sim 2$ are shown with stars; DSFGs at $z > 4$ are shown with triangles; the parent sample of lensed quasar systems from Chapter 2 are shown with grey circles. The quasar hosts in this sample have higher effective dust temperature and are generally more compact than dusty star-forming galaxies of similar infrared luminosity.

unlikely to be responsible for a significant fraction of the sub-mm dust emission. We cannot determine the origin of the molecular gas heating from single CO lines, but a comparison between multiple transitions will help constrain the contribution from the AGN to the emission reported here. Radiative transfer models suggest that these are very likely to be enhanced by X-rays from the AGN (Vallini et al., 2019), so could probe the effect of radiative feedback on the host galaxy ISM.

Another potential source of uncertainty in the analysis in Chapter 2 was the assumption on the unknown lensing magnification of the FIR emission, which was set to be 10^{+10}_{-5}. If the lensing magnifications were significantly higher than was conservatively assumed, then the level of the inferred star formation would be much lower. However, from our analysis of the resolved sub-mm imaging that was obtained with ALMA at 100 to 300 pc angular resolution, we find source magnifications for the six sources investigated here that are consistent with this assumption. Also, we find that the star formation rates for our sample range from 70 to 3000 $M_\odot$ yr^{-1}.

4.5.2. Evidence for compact quasar hosts

The quasar hosts in our study can be divided into two types: galaxies characterised by clumpy dust distributions, with sizes and star formation rate densities similar to DSFGs (i.e. WFI J2033−4723 and SDSS J0924+0219), and galaxies characterised by compact ($R_{\rm eff} < 1$ kpc) sizes and Eddington-limited star formation densities of around 500 $M_\odot$ yr^{-1} kpc^{-2} (see Fig. 4.16). Our results are similar to those of Ikarashi et al. (2017), who find that $z \sim 1$–3 quasar-starburst composites have smaller sizes than both starburst-dominated DSFGs and quasars whose SEDs have a more dominant AGN fraction in the MIR.

While the extended quasar hosts seem similar to DSFGs, the sizes of the compact quasar hosts in this work are similar to the sub-mm sizes of compact star-forming galaxies (Ikarashi et al., 2015; Barro et al., 2016, 2017), suggesting that quasars are preferentially hosted in more compact systems. While it has been estimated that one in five DSFGs contains an X-ray luminous AGN (Wang et al., 2013), this is true for around half of compact star-forming galaxies (Barro et al., 2014). The small size of these compact systems requires that there has been a rapid infall of gas, such that the bulk of the star formation occurs within the central region of the galaxy, which could allow the AGN to accrete efficiently from the dense ISM. If the optical/infrared emission can be disentangled from the quasar light, SED modelling of our sample will help determine whether the host galaxy has a young stellar population, as their morphology suggests.

The sizes of both the compact galaxies and quasar hosts are similar to the opti-

cal/infrared sizes of compact quiescent galaxies at similar redshifts ($\tilde{R}_{\rm eff}$ = 0.9 kpc; van Dokkum et al. 2008), consistent with the hypothesis that compact starbursts are progenitors of compact quiescent galaxies (and ultimately massive ellipticals). The still-high star formation rates and molecular gas densities of these hosts could mean that we catch them at the moment of compaction, at the onset of gas depletion and quenching. This would require that at least some compact quiescent galaxies form rapidly, rather than through a slow evolution (Wellons et al., 2015).

Overall, the sizes of < 1 to 3 kpc we find for our sample are similar to those of Silverman et al. (2019), who found the optical/infrared sizes of quasar hosts at $z \sim 1.5$ are in the range < 1 to 6 kpc ($\bar{R}_{\rm eff}$ = 2.2 kpc), intermediate between main sequence and quiescent galaxies. Their results and ours are inconsistent with models that predict the size of quasar hosts to be larger than those of normal star-forming galaxies, due to adiabatic expansion that results from negative AGN feedback (Fan et al., 2008) or positive AGN feedback on kpc-scales (Ishibashi et al., 2013).

4.5.3. Mechanism of formation

In the context of the ongoing debate about how compact quiescent galaxies form their very high stellar densities, our finding that the host galaxies of quasars are compact is consistent with a model whereby they form rapidly in a period of dissipative contraction. Simulations suggest that star-forming galaxies are able to maintain high star formation rates in quasi-stable discs, fed by smooth accretion from the cosmic web (e.g. Kereš et al. 2005). For a galaxy to compactify, violent instabilities must to be induced by mergers or intense inflows that can drive gas into the centre of the galaxy on timescales shorter than the star formation rate (Zolotov et al., 2015). The high star formation rates and the existence of clumpy, non-axisymmetric dust features that we detect on 100 to 300 pc-scales strongly suggest that quasar hosts are globally unstable due to gravitational fragmentation, as has also been observed for DSFGs (Iono et al., 2016; Oteo et al., 2017; Hodge et al., 2019).

Optical imaging of DSFGs has confirmed that their molecular gas and obscured star formation is significantly more compact than pre-existing stellar distributions (Simpson et al., 2015; Ikarashi et al., 2015). The UV-luminous stellar emission observed for PG 1115+080 must also be more extended or offset from the dust, as it is lensed into an Einstein ring, whereas the dust is not. This could be another hint that these systems are in the process of compaction: the lack of dust or gas may suggest the unobscured stellar distribution is quenched as a result of gas compaction and stellar feedback (e.g. Maiolino et al. 2015). These unobscured stellar features may also exist for the quasar systems we observe here, but are too faint to be seen in optical imaging or cannot be

distinguished from the bright quasar emission.

We find no evidence for recent or ongoing mergers in the compact quasar hosts, nor in archival data of low-excitation gas tracers or optical imaging. This may be limited by the sensitivity of the observational data. However, one of the extended quasar hosts does have optical features that could be evidence of an ongoing merger or interaction (SDSS J0924+0219; Eigenbrod et al. 2006). This is consistent with models that predict mergers to play an important role in the formation of spheroids (Hopkins et al., 2008) and observational evidence that many DSFGs are ongoing mergers or interactions (Engel et al., 2010).

4.5.4. Mechanism of quenching

Simulations find that compaction can naturally lead to quenching, through rapid gas consumption and stellar feedback, coupled with increasing dynamical stability (Zolotov et al., 2015). Observations of dense starbursts suggest that radiation pressure from stars could be a feasible mechanism to suppress further star formation (Murray et al., 2005; Andrews & Thompson, 2011). If all the dust emission we observe here is associated with star formation, the four most compact sources in our work are in the regime of Eddington-limited maximum starbursts that will exhaust their gas reservoirs within ~ 20 Myr. This is consistent with observations of compact quiescent galaxies, whose star formation histories suggest a short starburst of ~ 50 Myr before quiescence (Valentino et al., 2019). In the absence of reliable stellar mass estimates, we cannot determine whether star formation in the compact quasar hosts has begun to quench by direct comparison with DSFGs. However, the higher implied star formation rate surface densities imply that stellar feedback could play a primary role.

For the one system where we observe a low-excitation transition of CO [CO (3–2) for HS 0810+2554], we find possible evidence of a large-scale outflow of low velocity (~ 150 km s^{-1}) that could deplete the gas reservoir in 1 to 3 Myr (see Appendix 4.A). In the canonical evolutionary scenario, AGN winds and jets are expected to actively inject energy into the ISM of their host galaxies during the quasar phase. HS 0810+2554 is known to have wide-angle, high-velocity outflows of ionised X-ray-emitting gas from the quasar (Chartas et al., 2016). High-velocity outflows of ionised gas are often observed from high-redshift quasars (e.g. Harrison et al. 2014), but molecular outflows are not frequently detected. HS 0810+2554 may present a rare case of a galaxy undergoing a period of rapid, AGN-induced quenching (e.g. Herrera-Camus et al. 2019). However, we estimate that the host galaxy starburst could be sufficient to drive this outflow, without help from the quasar. As the velocity is low, the gas will remain gravitationally bound to the galaxy, allowing the out-flowing gas to be re-accreted by

the host galaxy and fuel further star formation. Such a redistribution of gas is expected to be a mechanism by which star formation is regulated in galaxies (Muratov et al., 2015).

Our findings could suggest that AGN feedback is not necessary to quench or regulate star formation, contrary to simulations. However, long-term maintenance of quenching requires that the supply of fresh cold gas into the galaxy is halted. As the quasars in this work are likely hosted in massive haloes (Kormendy & Ho, 2013), virial shock-heating alone could help suppress accretion of cold gas from the cosmic web (Dekel & Birnboim, 2006). It is likely that AGN feedback becomes important at some point to prevent re-accretion of ejected gas (Croton et al., 2006), as the energy input from star formation falls far short of the level required to completely unbound the gas from the galaxy and maintain a quenched state. Indeed, we expect that compact galaxies quench abruptly (Valentino et al., 2019) and that 'maintenance mode' (or 'jet mode') AGN feedback tends to be observed after galaxies have already begun to quench (Hardcastle et al., 2007).

Observations of CO (1–0) in high-redshift lensed AGN-starbursts have revealed disturbed morphologies, suggesting feedback (AGN or stellar) or ongoing mergers (Thomson et al., 2012; Spingola et al., 2019), whilst others do not appear to show such features (Riechers et al., 2011c; Sharon et al., 2016). Additionally, in the former case, it is not clear that the outflows represent a significant fraction of the total gas reservoir. In this context, our findings for HS 0810+2554 are particularly significant as an outflow is not obvious from the shape of the line profile and its differential magnification, highlighting the importance of high spatial resolution to detect complex velocity features. Further observations of the molecular gas in this system will test the short depletion timescale we infer here and confirm the nature of the velocity structure of HS 0810+2554.

4.5.5. Selection effects and confusion

A source of caution in the interpretation of our findings is the combination of systematic biases that stem from the comparison of samples with different selection effects. Ideally, we would like to compare coeval samples of DSFGs and quasar hosts. However, the detection of DSFGs is strongly influenced by selection effects, such that systems with lower dust temperatures are preferentially detected at lower redshifts due to the shape modified black body spectrum. The quasar systems, on the other hand, were discovered in optical data and were observed with ALMA because they are bright in their FIR emission, which is less affected by negative k-correction as it probes the peak of the dust emission. Therefore, it is practically difficult to match samples of quasar hosts

and DSFGs because of the selection methods used to discover them. With comparable high-resolution imaging, FIR-selected DSFGs at $z \sim 2$ (e.g. Bussmann et al. 2015) may present a more unbiased sample for future investigations.

A further concern when comparing lensed and unlensed samples is that differential magnification effects will bias the selection of lensed galaxies by their FIR properties towards those that are more compact and, hence, likely to be more highly magnified (Serjeant, 2012; Hezaveh et al., 2012). This is less of a concern for our sample where the systems were primarily optically selected, based on the emission from their unobscured accretion discs, and subsequently selected for follow-up observations with ALMA on the basis of their FIR emission. Future analyses of fainter and less strongly magnified systems can potentially provide a better statistical comparison between galaxy populations and account for differential lensing bias.

Notably, we identify a companion source of one object (H 1413+117) that likely causes photometric confusion at shorter wavelengths. This has the important implication that source blending may contribute to the extreme infrared luminosities found for some quasar-starbursts. Observations with ALMA of (unlensed) optically selected quasars have revealed that 30 percent of FIR identifications can be resolved into secondary counterparts that contribute at least 25 percent to the measured infrared luminosity (Hatziminaoglou et al., 2018). This may be unsurprising as massive galaxies seem to be formed in over-dense regions (Zeballos et al., 2018). The sources investigated here are gravitationally lensed, so the relative contribution from companions will be lower on average than for field sources. However, our findings suggest care should be taken to account for field sources when compiling an SED with photometric measurements obtained with low spatial resolution (e.g. *Herschel*/SPIRE).

4.6. Conclusions

The properties of cold dust and molecular gas in quasar hosts at cosmologically important redshifts can give insights into the mechanism responsible for the transformation of these galaxies from gas-rich, dusty starbursts into passive, quiescent systems. We have presented high angular resolution imaging with ALMA of the host galaxies of six optically detected quasars at redshifts between 1.5 and 3. The gravitational magnification of these lens systems effectively boosts the 1 to 3 kpc (0.15 to 0.4 arcsec) spatial resolution of the observations to 100 to 300 pc with the aid of our pixellated lens modelling technique.

In comparison to unlensed DSFGs with similar redshifts and infrared luminosities, and DSFGs at higher redshifts with similar dust temperatures, the quasar hosts in this

work are generally more compact. The observed luminosities are broadly consistent with the expectations for more compact star formation, disputing the case for a significant contribution from black hole accretion to the global dust emission at sub-mm wavelengths.

We find that two of the quasar hosts are characterised by extended, clumpy dust distributions, but the rest are compact, Eddington-limited starbursts. These differences may represent quasar hosts at different stages of morphological change into compact galaxies. The more compact systems have sizes that are already similar to quiescent galaxies at $z \sim 2$, and whose extreme star formation rate densities will rapidly consume their gas reservoirs in a timescale of 15 to 20 Myr. This is consistent with a picture in which the inflow of gas resulting from mergers and/or dynamical instabilities triggers both the intense starburst and a period of efficient black hole accretion. These intense starbursts could be responsible for both the formation of the high stellar densities and rapid quenching of compact galaxies.

If quasar hosts are generally in the process of forming stellar bulges, we should find that these systems are globally characterised by violently unstable gas discs and rapidly depleting gas reservoirs. Matched, high angular resolution observations of low J-level CO emission would determine the size of the cold gas reservoir and determine whether the star formation rate efficiency and gas depletion timescales of quasar hosts are significantly different relative to those of DSFGs. Furthermore, cold gas diagnostics will be useful to determine whether outflows are prevalent and whether AGN or stellar feedback is ongoing, as expected from simulations and semi-analytic models.

Our conclusions here are based on the data for just six objects from the sample of lensed quasars that were selected with *Herschel*/SPIRE. In the next observing cycle of ALMA, we will obtain data for at least 28 lensed quasars in Band 6 and 7, which will further probe the size and structure of the heated dust emission from this class of objects, and probe the structure and kinematics of the molecular gas that is feeding both the star formation and AGN activity.

Acknowledgements

JPM acknowledges support from an NWO-CAS grant (project number 629.001.023). CS is grateful for support from the National Research Council of Science and Technology, Korea (EU-16-001).

This research made use of Astropy and Matplotlib packages for Python (The Astropy Collaboration et al., 2018; Hunter, 2007).

This chapter makes use of the following ALMA data:
ADS/JAO.ALMA#2012.1.00175.S, ADS/JAO.ALMA#2015.1.01309.S,
ADS/JAO.ALMA#2017.1.01368.S, ADS/JAO.ALMA#2017.1.01081.S,
ADS/JAO.ALMA#2018.1.01519.S. ALMA is a partnership of ESO (representing its member states), NSF (USA) and NINS (Japan), together with NRC (Canada), MOST and ASIAA (Taiwan), and KASI (Republic of Korea), in cooperation with the Republic of Chile. The Joint ALMA Observatory is operated by ESO, AUI/NRAO and NAOJ.

Table 4.3 | Parameters of the smooth lens models for the six lensed quasars. We give the median and percentile ranges of the likelihood-weighted posterior probability distribution found with MultiNest, where the maximum a posteriori model parameters are given in square brackets. For WFI 2033−4723, parameters for the secondary lenses are also given. Parameters denoted by † are fixed. δx and δy positions are relative to the phase centre positions given in Table 4.1. b is defined as the spherical-equivalent Einstein radius of the lens. e is the ellipticity of the lens, and γ is the reduced external shear. In all cases, position angles are measured East of North.

	δx (")	δy (")	b (")	e	θ_e (°)	γ	θ_γ (°)
HS 0810+2554	0.293 ± 0.007 [0.296]	0.865 ± 0.011 [0.865]	0.477 ± 0.005 [0.475]	0.26 ± 0.03 [0.26]	33.1 ± 2.1 [33.5]	$1.1(\pm 0.1) \times 10^{-4}$ [1.1×10^{-4}]	29.7 ± 5.6 [29.1]
RX J0911+0551	-0.943 ± 0.017 [−0.927]	2.441 ± 0.009 [2.441]	1.093 ± 0.013 [1.091]	0.29 ± 0.04 [0.35]	-73.5 ± 4.1 [−74.1]	0.369 ± 0.014 [0.382]	9.1 ± 0.8 [9.4]
SDSS 0924+0219	0.266 ± 0.011 [0.274]	0.044 ± 0.007 [0.046]	0.885 ± 0.005 [0.889]	0.30 ± 0.03 [0.33]	-90.6 ± 3.2 [−91.5]	0.022 ± 0.009 [0.021]	48.6 ± 14.7 [30.8]
PG 1115+080	1.738 ± 0.011 [1.741]	0.971 ± 0.009 [0.961]	1.135 ± 0.009 [1.146]	0.35 ± 0.03 [0.36]	-98.5 ± 2.5 [−102.0]	0.10 ± 0.01 [0.08]	40.0 ± 2.8 [39.9]
H 1413+117	0.138 ± 0.005 [0.135]	0.356 ± 0.007 [0.360]	0.627 ± 0.003 [0.631]	0.25 ± 0.03 [0.30]	1.3 ± 2.8 [3.9]	0.11 ± 0.01 [0.10]	38.2 ± 2.4 [41.5]
WFI 2033−4723	-0.799 ± 0.015 [−0.801]	-1.298 ± 0.018 [−0.129]	0.967 ± 0.016 [0.977]	0.12 ± 0.06 [0.12]	25.7 ± 9.2 [29.5]	0.20 ± 0.02 [0.19]	12.7 ± 1.9 [12.4]
	$3.301^\dagger$	$-1.243^\dagger$	0.952 ± 0.094 [0.918]		-	-	-
	-0.90 ± 0.03 [−0.87]	0.83 ± 0.03 [0.82]	0.04 ± 0.01 [0.03]	-	-	-	-

Table 4.4 | The properties of the reconstructed continuum emission, corrected for lensing magnification. For H 1413+117 we also give values after correcting the SED for photometric confusion (see Section 4.2.6).

	$\mu_{\rm dust}$	$R_{\rm dust}$ (kpc)	n	$T_{\rm d}^{\rm cold}$ (K)	$T_{\rm d}^{\rm warm}$ (K)	β	$L_{\rm FIR}$ (10^{12} L$_\odot$)	SFR (M$_\odot$ yr^{-1})	$\Sigma_{\rm SFR}$ (M$_\odot$ yr^{-1} kpc^{-2})	$M_{\rm d}$ (M$_\odot$)
HS 0810+2554	10.6 ± 1.0	0.27 ± 0.03	0.57 ± 0.05	37^{+5}_{-6}	82^{+16}_{-9}	–	$0.8^{+0.5}_{-0.5}$	270^{+160}_{-160}	560^{+350}_{-360}	$6.4^{+2.4}_{-2.0} \times 10^7$
RX J0911+0551	18.4 ± 0.7	0.56 ± 0.06	0.56 ± 0.01	41^{+2}_{-2}	–	$1.9^{+0.1}_{-0.1}$	$1.8^{+0.2}_{-0.2}$	600^{+80}_{-70}	300^{+70}_{-70}	$5.5^{+1.1}_{-1.3} \times 10^7$
SDSS J0924+0219	10.3 ± 0.1	1.7 ± 0.2	1.40 ± 0.07	32^{+7}_{-7}	–	$1.5^{+0.6}_{-0.4}$	$0.27^{+0.09}_{-0.07}$	90^{+30}_{-20}	5^{+2}_{-2}	$1.8^{+0.3}_{-0.3} \times 10^6$
PG 1115+080	19.5 ± 2.5	0.25 ± 0.03	0.47 ± 0.01	44^{+15}_{-11}	–	$2.0^{+0.6}_{-0.4}$	$0.36^{+0.16}_{-0.13}$	120^{+50}_{-40}	310^{+150}_{-125}	$2.7^{+1.7}_{-1.1} \times 10^6$
H 1413+117	8.6 ± 0.2	0.95 ± 0.10	1.05 ± 0.05	37^{+1}_{-1}	131^{+12}_{-10}	$2.3^{+0.1}_{-0.1}$	$8.4^{+0.9}_{-0.9}$	2800^{+300}_{-300}	490^{+110}_{-110}	$3.5^{+0.4}_{-0.4} \times 10^8$
				39^{+1}_{-1}	–	$2.0^{+0.1}_{-0.1}$	$6.8^{+0.9}_{-0.9}$	2250^{+300}_{-300}	400^{+110}_{-110}	$9.0^{+1.6}_{-1.3} \times 10^8$
WFI J2033−4723	11.5 ± 0.7	2.9 ± 0.3	1.40 ± 0.09	31^{+7}_{-5}	–	$1.8^{+0.4}_{-0.4}$	$0.46^{+0.13}_{-0.10}$	150^{+40}_{-30}	3^{+1}_{-1}	$1.6^{+0.3}_{-0.3} \times 10^8$

Table 4.5 | The properties of the reconstructed CO line emission, corrected for lensing magnification. For WFI J2033−4723, the source profile is fixed to a circular Gaussian. All parameters are derived from moment maps of the reconstructed source. Note that the magnification we report here is the *mean* magnification of the line emission, which may vary significantly across the source.

	$\bar{\mu}_{\rm CO}$	$R_{\rm CO}$ (kpc)	n	$I_{\rm CO}$ (Jy km s^{-1})	$L_{\rm CO}$ (L$_\odot$)	$L'_{\rm CO}$ (K km s^{-1} pc^2)	$M_{\rm dyn}$ (M$_\odot$)
HS 0810+2554	17.5 ± 1.1	0.51 ± 0.05	0.60 ± 0.04	0.20 ± 0.02	$(3.7 \pm 0.4) \times 10^6$	$(2.8 \pm 0.3) \times 10^9$	$(5.0 \pm 2.6) \times 10^{11}$
RX J0911+0551	11.6 ± 0.4	0.59 ± 0.06	0.56 ± 0.01	0.46 ± 0.05	$(4.2 \pm 0.4) \times 10^7$	$(6.8 \pm 0.7) \times 10^9$	$(9 \pm 5) \times 10^9$
SDSS J0924+0219	7.5 ± 0.2	1.2 ± 0.1	1.88 ± 0.06	0.34 ± 0.03	$(1.67 \pm 0.17) \times 10^7$	$(6.6 \pm 0.7) \times 10^8$	$(8 \pm 4) \times 10^9$
H 1413+117	11.3 ± 0.2	0.72 ± 0.07	0.71 ± 0.04	4.3 ± 0.4	$(6.0 \pm 0.6) \times 10^8$	$(1.7 \pm 0.2) \times 10^{10}$	$(6.7 \pm 1.6) \times 10^{10}$
WFI J2033−4723	9.1 ± 0.6	0.7 ± 0.3	[0.5]	0.09 ± 0.01	$(5.0 \pm 0.6) \times 10^6$	$(2.0 \pm 0.2) \times 10^8$	$(1.3 \pm 0.8) \times 10^{10}$

4.A. Possible outflow

The velocity structure for HS 0810+2554 has features that could represent a bipolar outflow of gas. In this section, we investigate the properties of this gas, under the assumption that it is an outflow.

The reconstructed velocity profile is shown in Fig. 4.18. We approximate the line structure with three Gaussian components centred on -310 ± 10 km s^{-1}, -480 ± 10 km s^{-1}and -600 ± 10 km s^{-1}relative to the systemic velocity, which have $L'_{\rm CO}$ of $(1.3 \pm 0.2) \times 10^9$, $(1.5 \pm 0.5) \times 10^9$ and $(3.7 \pm 2.0) \times 10^8$ Kkm s^{-1} pc^2, respectively. Assuming that the component centred on -500 km s^{-1}(velocity coincident with the dust emission) represents gas in the galaxy, and a CO-to-H_2 conversion factor of $\alpha_{\rm CO} = 0.8$ M$_\odot$ (K km s^{-1} pc^2)$^{-1}$, we estimate a gas mass in the galaxy of $(1.2 \pm 0.4) \times 10^9$ M$_\odot$ and a mass in the outflows of $(1.3 \pm 0.2) \times 10^9$ M$_\odot$.

As discussed in Harrison et al. (2018), for a conical or spherical volume of gas, the mass outflow rate can be described by

$$\dot{M}_{\rm out} = \frac{B\ M_{\rm gas}\ v_{\rm out}}{r_{\rm out}}, \tag{4.9}$$

where the factor B is usually 1 or 3, depending on the assumed geometry. We take the centroid of the fitted Gaussian component as the mean outflow velocity, relative to the assumed systemic velocity (i.e. the centroid of the galaxy component), and the radius as the effective radius of the line emission based on the Sérsic model fit. Considering the range of potential geometries, we infer an outflow rate in the range 400–1100 M$_\odot$ yr^{-1} and gas depletion time of just 1–3 Myr. We also consider a scenario in which the peaks at -300 and -500 km s^{-1}represent a rotating disc of gas in the host galaxy and only the feature at -600 km s^{-1}is an outflow: in this case, the implied mass outflow rate is only slightly higher and the depletion timescale similar to the previous case.

Momentum from supernovae explosions and radiation pressure from stars can be sufficient to drive outflows. From Murray et al. (2005), we can estimate the possible mass outflow rate from stars as

$$\dot{M}_{\rm max} = SFR\ \frac{\epsilon\ c}{v_{\rm max}}, \tag{4.10}$$

where ϵ is the efficiency with which star formation is converted into luminosity, which is $\sim 10^{-3}$ for a Salpeter IMF. Assuming $v_{\rm max} = 200 \pm 50$ km s^{-1}, the mass loss rate can be 420 ± 260 M$_\odot$ yr^{-1}. Therefore, given the star formation rate of 280 ± 160 M$_\odot$ yr^{-1}, the low outflow velocity and our overall uncertainties, it is possible that the outflow is

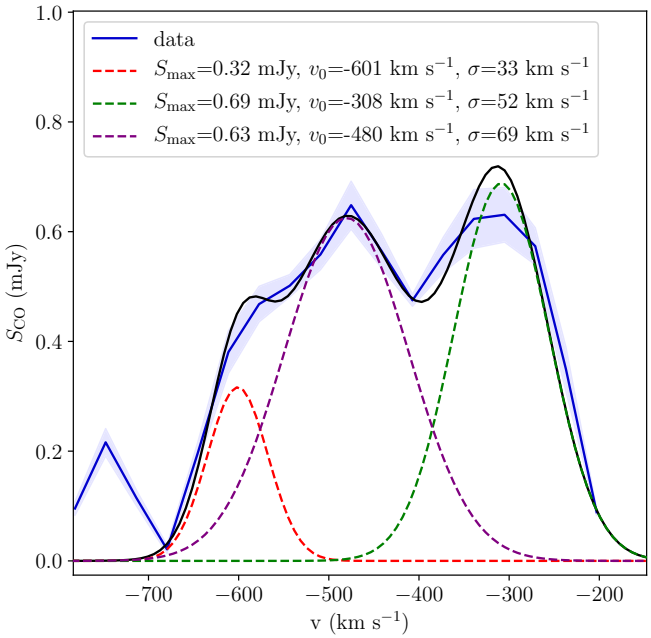

Figure 4.18 | The reconstructed line profile of HS 0810+2554. The data are fit with Gaussian components centred on −600 km s^{-1}, −500 km s^{-1}and −300 km s^{-1}.

driven by galactic winds.

We estimate the galaxy escape velocity with

$$v_{esc} = \sqrt{\frac{2GM_\star}{r}}, \tag{4.11}$$

where the radius (r) is the effective radius of the dust emission, and the stellar mass ($M_\star$) is assumed to be $0.5 \times M_{dyn}$ (based on the gas fractions found for RX J0911+0551 and H1413+117). This implies an escape velocity of ~ 3000 km s^{-1}. As the mean velocity of the outflowing gas is ~ 150 km s^{-1}, it likely does not have sufficient momentum to escape the galaxy.

4.B. Supplementary figures and tables

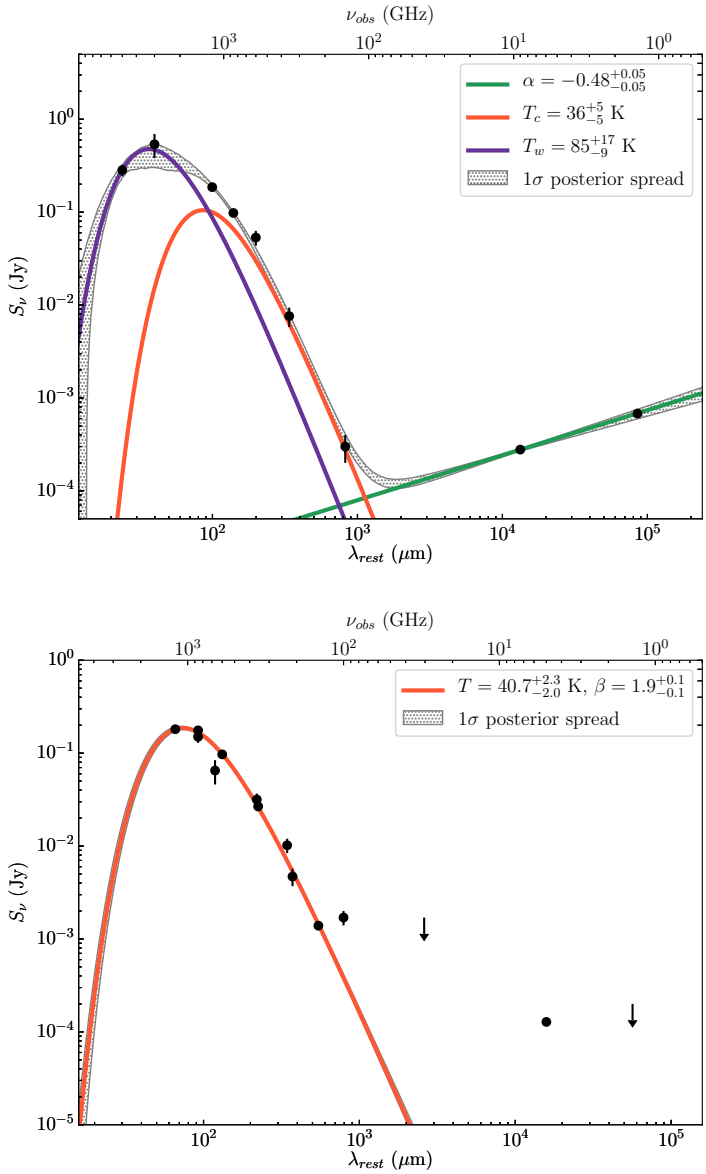

Figure 4.19 | SED from FIR to radio wavelengths for HS 0810+2554 (top) and RX J0911+0551 (bottom). The data are fit with one or two modified black body component for thermal dust emission (orange and purple) and, for HS 0810+2554, a power-law for radio synchrotron emission (green). The grey shaded region shows the 1σ distribution of the posterior from the MCMC sampling. The ancillary data points are listed and referenced in Chapter 2.

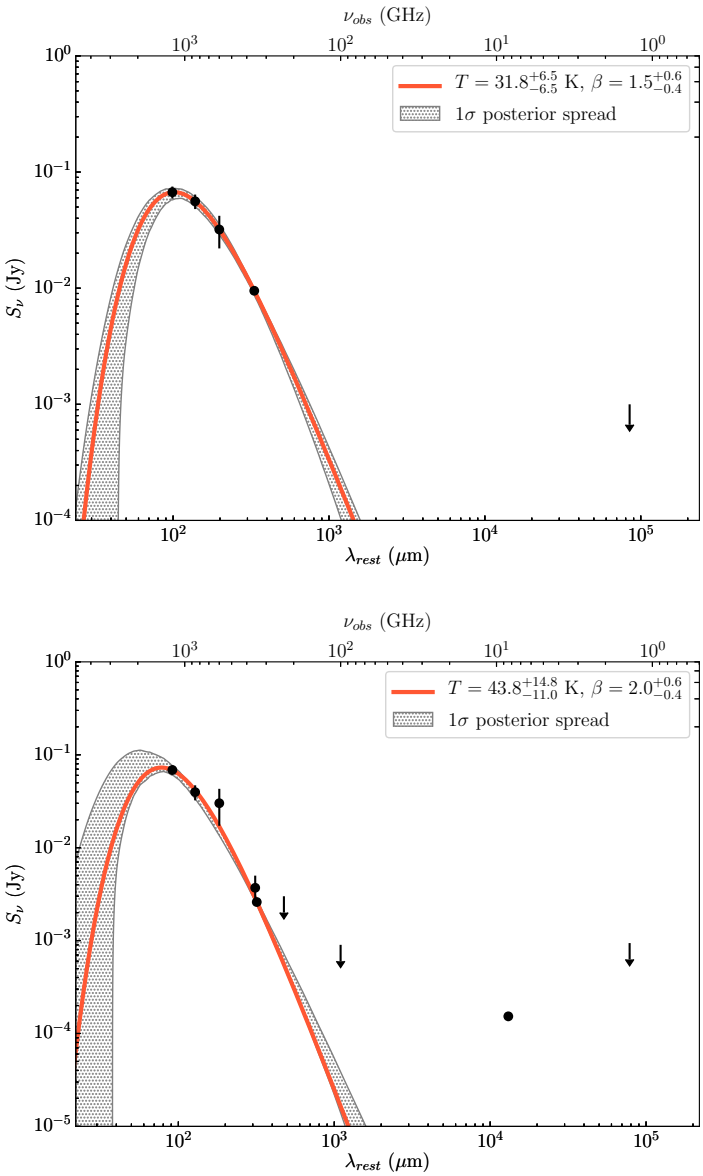

Figure 4.20 | SED from FIR to radio wavelengths for SDSS J0925+0219 (top) and PG 1115+080 (bottom). The data are fit with a modified black body component for thermal dust emission (orange). The grey shaded region shows the 1σ distribution of the posterior from the MCMC sampling. The ancillary data points are listed and referenced in Chapter 2.

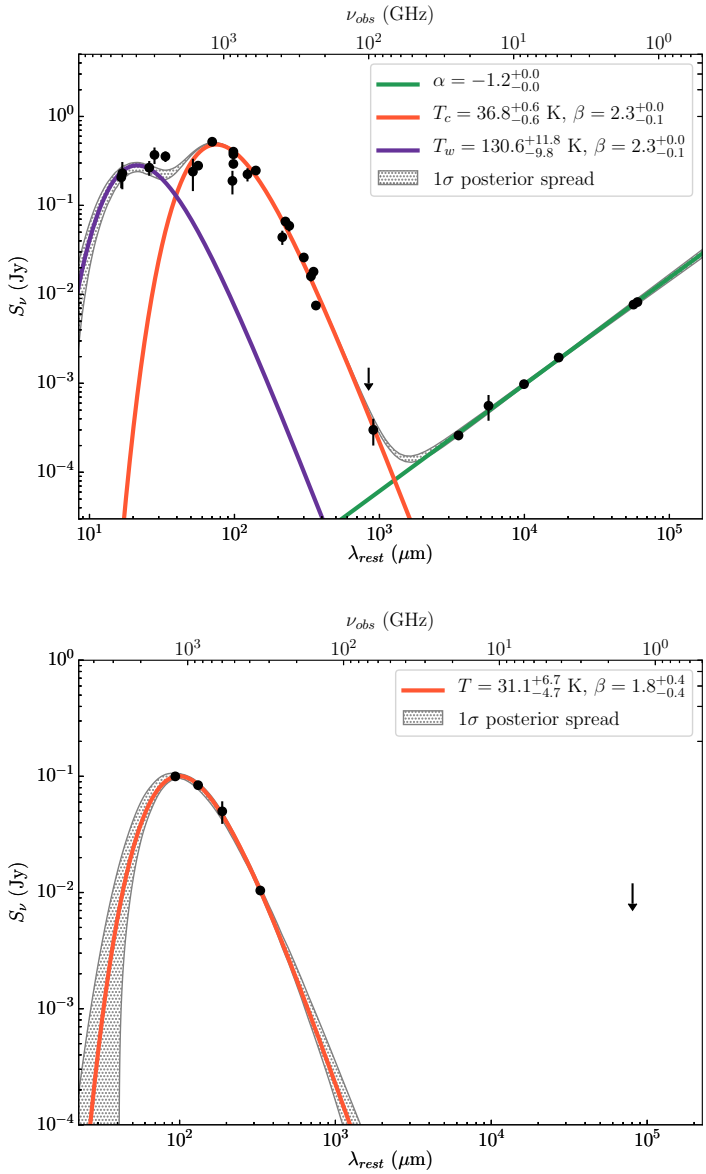

Figure 4.21 | SED from FIR to radio wavelengths for H 1413+117 (top) and WFI J2033−4723 (bottom). The data are fit with one or two modified black body component for thermal dust emission (orange and purple) and, for H 1413+117, a power-law for radio synchrotron emission (green). The grey shaded region shows the 1σ distribution of the posterior from the MCMC sampling. The ancillary data points are listed and referenced in Chapter 2.

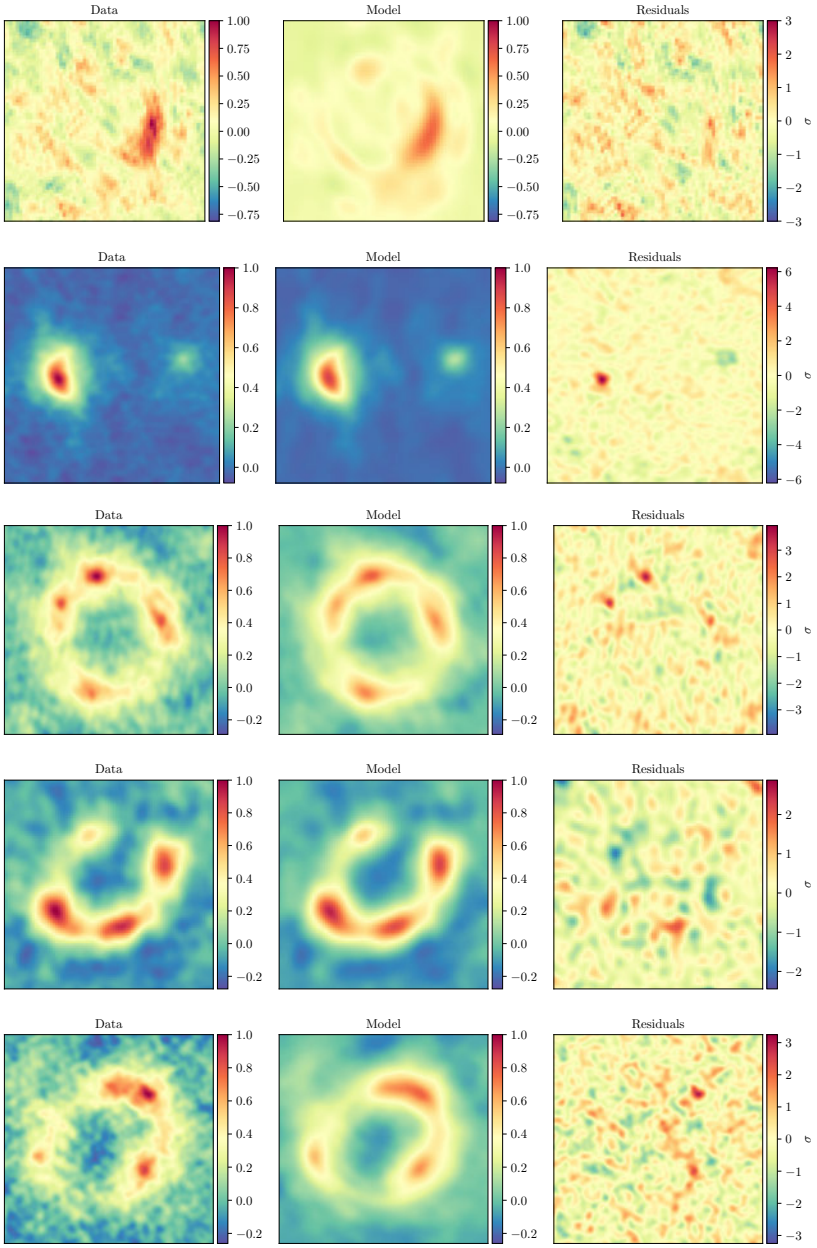

Figure 4.22 | Grid-based lens models of the continuum data. The rows, top to bottom, show HS 0810+2554, RX J0911+0551, SDSS J0924+0219 and WFI J2033−4723. Panels, left to right, show the dirty image of the data in arbitrary flux units, the dirty image of the model on the same scale as the data, and the residuals (data−model) in units of σ, where σ is the rms noise of the visibilities.

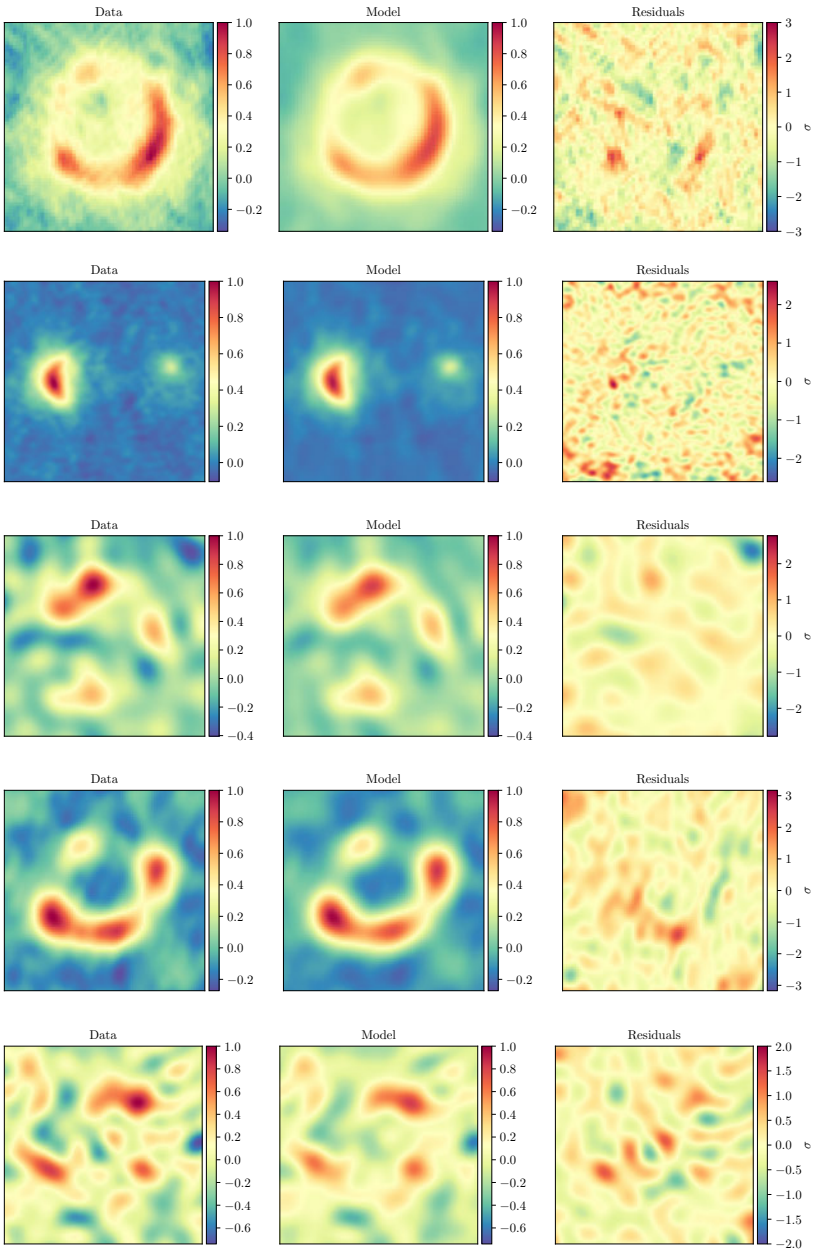

Figure 4.23 | Grid-based lens modelling of CO line data. Rows, top to bottom, show HS 0810+2554, RX J0911+0551, SDSS J0924+0219, H 1413+117 and WFI J2033−4723. Panels, left to right, show the dirty image of the data in arbitrary flux units, the dirty image of the model (on the same scale as the data), and the residuals (data−model) in units of σ, where σ is the rms noise of the visibilities.

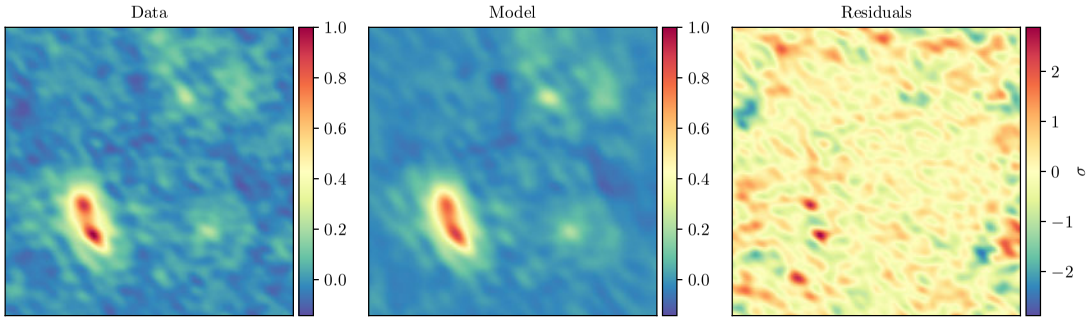

Figure 4.24 | Grid-based lens models of the continuum data for PG 1115+080. Panels, left to right, show the dirty image of the data in arbitrary flux units, the dirty image of the model on the same scale as the data, and the residuals (data−model) in units of σ, where σ is the rms noise of the visibilities.

Table 4.6 | List of DSFGs used in this study, with references for the photometry and size measurements. † notes where the dust temperature is obtained from an optically thick model, obtained from the literature; in all other cases, the SED fitting was performed in this work using the methodology described in Section 4.4.2

	z	$T_{\rm d}$ (K)	$L_{\rm FIR}$ (10^{12} L$_\odot$)	$R_{\rm eff}$ (kpc)	Ref
$z\sim2$					
ALESS 3.1	3.374	35^{+6}_{-6}	$5.2^{+0.6}_{-0.6}$	1.6 ± 0.1	[1,2]
ALESS 5.1	2.86	27^{+5}_{-3}	$2.5^{+0.4}_{-0.4}$	2.1 ± 0.1	[3,2]
ALESS 10.1	2.02	31^{+2}_{-2}	$1.5^{+0.3}_{-0.3}$	2.9 ± 0.4	[3,2]
ALESS 15.1	2.67	29^{+3}_{-4}	$2.3^{+0.3}_{-0.3}$	2.7 ± 0.2	[1,2]
ALESS 17.1	1.540	22^{+4}_{-4}	$0.65^{+0.15}_{-0.13}$	1.8 ± 0.1	[1,2]
ALESS 29.1	1.439	21^{+5}_{-3}	$0.49^{+0.15}_{-0.11}$	1.4 ± 0.1	[3,2]
ALESS 39.1	2.44	24^{+5}_{-3}	$1.2^{+0.2}_{-0.3}$	2.2 ± 0.1	[3,2]
ALESS 45.1	2.34	26^{+5}_{-4}	$1.5^{0.3}_{-0.3}$	2.2 ± 0.2	[3,2]
ALESS 67.1	2.123	29^{+7}_{-4}	$3.1^{+0.7}_{-0.5}$	2.1 ± 0.2	[3,2]
ALESS 112.1	2.315	30^{+4}_{-5}	$1.8^{+0.4}_{-0.4}$	1.9 ± 0.1	[1,2]
$z>4$					
ALESS 9.1	4.867	47^{+6}_{-7}	10^{+1}_{-1}	1.6 ± 0.1	[1,2]
ADFS-27(1)	5.655	55^{+8}_{-8} †	$9.1^{+1.5}_{-1.5}$	0.8 ± 0.1	[4]
ADFS-27(2)				0.8 ± 0.1	[4]
HFLS3	6.334	56^{+9}_{-12} †	29^{+3}_{-3}	1.3 ± 0.1	[5]
AzTEC-3	5.299	53^{+5}_{-5} †	11^{+2}_{-2}	0.9 ± 0.1	[6]
GN20	4.055	46^{+4}_{-4}	17^{+5}_{-5}	1.9 ± 0.1	[7]
SGP-196076(1)	4.425	55^{+3}_{-3} †	8^{+2}_{-2}	1.1 ± 0.1	[8]
SGP-196076(2)			4^{+1}_{-1}	0.9 ± 0.1	[8]

References: [1] Hodge et al. (2019); [2] Swinbank et al. (2010); [3] Hodge et al. (2016); [4] Riechers et al. (2017); [5] Riechers et al. (2013); [6] Riechers et al. (2014); [7] Hodge et al. (2015); [8] Oteo et al. (2016)

Dark matters

30 ml tawny port
30 ml aged rum
15 ml coffee liqueur
15 ml poached fig syrup

Shake all the ingredients with ice. Serve in an old-fashioned glass over fresh ice and garnish with a poached fig.

5

Resolving quasar lens systems at sub-mm wavelengths

II. A flux ratio anomaly in CO spectral line emission

H. R. Stacey and J. P. McKean

Based on "A flux-ratio anomaly in the CO spectral line emission from gravitationally lensed quasar MG J0414+0534"
Stacey & McKean 2018, Monthly Notices of the Royal Astronomical Society, Volume 481, L40

Abstract

We present an analysis of archival observations with the Atacama Large (sub-)Millimetre Array (ALMA) of the gravitationally lensed quasar MG J0414+0534, which show four compact images of the quasar and an Einstein ring from the dust associated with the quasar host galaxy. We confirm that the flux ratio anomalies observed in the mid-infrared and radio persists into the sub-mm for the continuum images of the quasar. We report the detection of CO (11–10) spectral line emission, which traces a region of compact gas around the quasar nucleus. This line emission also shows evidence of a flux ratio anomaly between the merging lensed images that is consistent with those observed at other wavelengths, suggesting high-excitation CO can also provide a useful probe of substructures that is unaffected by microlensing or dust extinction. However, we do not detect the candidate dusty dwarf galaxy that was previously reported with this dataset, which we conclude is due to a noise artefact. Thus, the cause of the flux ratio anomaly between the merging lensed images is still unknown. The composite compact and diffuse emission in this system suggest lensed quasar-starbursts will make excellent targets for detecting dark sub-haloes and testing models for dark matter.

5.1. Introduction

Almost all well-studied four-imaged gravitationally-lensed quasars have image flux ratios that are inconsistent with those expected from a smooth lensing mass distribution (e.g. Koopmans et al. 2003). These so-called *flux ratio anomalies* are primarily thought to be due to a local perturbation in the mass model that effects one or more of the image magnifications. These perturbations can be in the form of a population of low-mass sub-haloes either within the lensing galaxy or along the line-of-sight that are predicted by dark matter simulations (e.g. Mao & Schneider 1998; Dalal & Kochanek 2002; Xu et al. 2012), or due to massive companion satellite galaxies of the main lens (e.g. McKean et al. 2007; More et al. 2009), or from unaccounted for mass structure in the form of large-scale galactic discs (e.g. Gilman et al. 2017; Hsueh et al. 2018). In addition, disentangling these flux ratio anomalies from microlensing by stars within the lensing galaxy, or extrinsic effects such as scintillation or extinction, can be difficult due to the compactness of the lensed images (Sluse et al., 2013).

The confirmation of a persistent flux ratio anomaly has typically required high-resolution radio or mid-infrared observations, where the source is expected to be largely immune to microlensing and dust extinction (Minezaki et al., 2009; Jackson et al., 2015). Recently, the narrow-line emission from gravitationally-lensed quasars has provided an alternate strategy to measure reliable flux ratios, as this emission is expected to probe scales larger than is typically affected by microlensing and is not expected to be effected by intrinsic variability (Moustakas & Metcalf, 2003; Nierenberg et al., 2016, 2017).

However, the flux ratio anomaly method has thus far been limited by the very small statistical samples of around 7 quadruply-imaged lensed quasars that are suitable for constraining dark matter (Dalal & Kochanek, 2002; Xu et al., 2015). In the near and long-term, large-scale surveys at optical wavelengths through, for example, the Dark Energy Survey (DES; e.g. Agnello et al. 2017) and *Euclid* (e.g. Serjeant, 2014) will substantially increase the number of known gravitationally-lensed quasars with four images and provide a sample size that is large enough to rule out models for dark matter (Gilman et al., 2018). These systems will need to be followed-up with either radio/mid-infrared continuum or narrow-line flux measurements to establish robust flux ratios, which themselves may have unknown systematics (for example, on the assumed source size). Therefore, new methods for robustly measuring the flux ratios of the lensed images are required to test for such systematics, provide independent measurements for the same objects, or to increase sample sizes in general.

In this chapter, we present the detection of a flux ratio anomaly in the high-excitation CO (11–10) emission line from the gravitationally-lensed quasar MG J0414+0534, which reveals a new and independent channel for quantifying low-mass dark matter

haloes.

MG J0414+0534 is a radio-loud quasar at $z = 2.64$ that is gravitationally-lensed into four images by a foreground galaxy at $z = 0.96$. While the optical and near-infrared fluxes of this lensed quasar are effected by microlensing and extinction, the anomalous fluxes of images A2 and B, relative to image A1, persist at mid-infrared and radio wavelengths. The nature of the flux ratio anomalies are quite complex; image B is thought to be affected by an optically-luminous companion galaxy to the main lens (object X; Falco et al. 1997; Ros et al. 2000; Minezaki et al. 2009), whereas image A2 is thought to be perturbed by a dark sub-halo with a mass $\sim 10^7$ $M_\odot$ (within the Einstein radius; MacLeod et al. 2013).

A possible detection of mm-continuum emission from this optically dark sub-halo (object Y, located 0.6 arcsec East of image A2) was recently reported by Inoue et al. (2017) from deep Atacama Large (sub-)Millimetre Array (ALMA) observations. If genuine, this would confirm that the flux ratio anomaly between the two merging images is due to a single low mass sub-halo, as predicted from cold dark matter models.

Here, we re-analyse the ALMA observations of MG J0414+0534 to investigate the flux ratio anomaly in the continuum and, for the first time, also in the molecular gas emission from a lensed quasar at mm-wavelengths. We confirm that there is a flux ratio anomaly in the continuum emission from the quasar, but we do not find any evidence for the candidate dusty dwarf galaxy, object Y. We detect a flux ratio anomaly in the mm molecular gas emission, which is consistent with that seen at radio and mid-infrared continuum measurements for this object. In Sections 5.2 and 5.3 we report the observations and results, respectively, and in Section 5.4 we discuss our results in the context of substructure searches and consider future prospects for a direct detection of a dark sub-halo.

5.2. Observations and data reduction

MG J0414+0534 was observed with ALMA at a central frequency of 342 GHz (Band 7) on 2015 June 13 and 2015 August 14 (PI Inoue; project code 2013.1.01110.S). This frequency also provided an observation of the CO (11–10) emission line ($\nu_{\rm rest} = 1267.014$ GHz). The first set of observations were split into two blocks of about 80 mins duration each, with a combined on-source integration time of about 100 mins. In total, 35 antennas from the 12-m array were used, with baselines ranging from 21 to 687 m. The second observation (third observing block) was carried out over about 135 mins, with about 50 mins on-source. Here, 42 antennas from the 12 m array were used with baselines between 15 and 1575 m. The flux-density calibration was carried out using J0238+166,

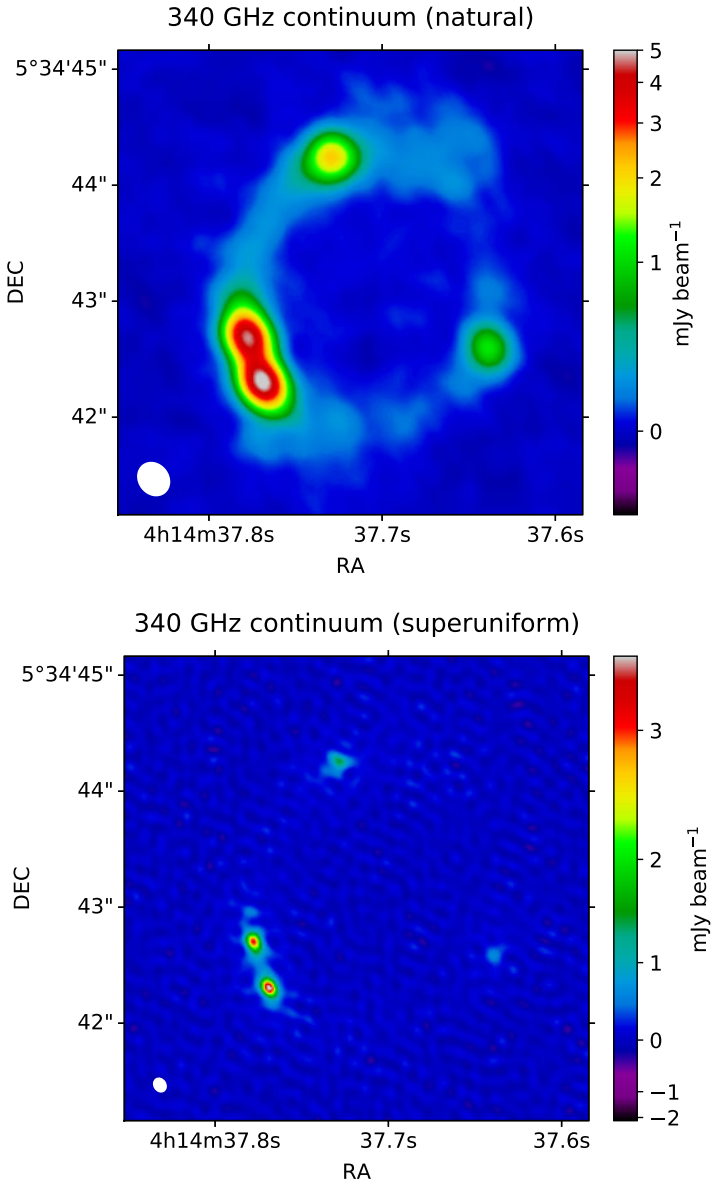

Figure 5.1 | ALMA 340 GHz continuum image of MG J0414+0534 using a natural (left) and a super-uniform (right) weighting of the visibilities. Clockwise from the brightest image A1 are images A2, B and C. The naturally weighted image has a beam-size of 0.30×0.25 arcsec at a positional angle of 37.6 deg East of North, and an rms map noise of 19 μJy beam^{-1}. The super-uniform weighted image has a beam-size of 0.12×0.10 arcsec at a positional angle of 32.3 deg East of North, and an rms map noise of 91 μJy beam^{-1}.

and the complex gains (amplitude and phase) as a function of frequency and time were solved for using J0423−013 and J0426+0518, with phase referencing carried out at 7 min intervals. For the second set of observations, which included longer baselines, an observation of J0406+0637 was used to correct for the residual delays over the large bandwidth. The data were recorded using both linear polarizations (XX and YY) over four spectral windows centred on 335.0, 336.9, 347.0 and 349 GHz with 2 GHz bandwidth each. The visibilities were correlated using an integration time of 2 s and 128 channels per spectral window.

The raw visibility dataset was processed using the ALMA pipeline within the Common Astronomy Software Applications (CASA) package to produce calibrated visibilities, which were inspected as a function of time, *uv*-distance and frequency to check the overall quality of the reduction. As the spectral line is spread across two spectral windows, we modified the pipeline to prevent flagging of the edge channels and allow a bandpass solution to be derived for the whole spectral window. After data inspection and flagging of a bad antenna, imaging and self-calibration of the continuum were carried out within CASA using a super-uniform to natural weighting to determine an accurate source model that accounted for both the small and large-scale structure of the target. Phase-only self-calibration over several time-scales, starting with each scan length, was used to progressively build the model for the source surface brightness distribution, down to a solution interval of 240 s. Note that this phase-only self-calibration was needed to both align the observations that were taken on different days and to correct for residual phase errors that remained after phase referencing. The self-calibrated phase corrections that were derived for the continuum as a function of time were then applied to the spectral line channels. The spectral line data was prepared by fitting a model to the line-free continuum and subtracting this model from the visibilities.

The flux densities of the compact components (continuum and spectral line) were measured by fitting models of delta functions to each image directly in the visibility plane using UVMULTIFIT (Martí-Vidal et al., 2014), which are presented in Table 5.1.

5.3. Results

5.3.1. Continuum

Using a natural weighting of the visibility data, we detect an Einstein ring of diffuse emission as well as four bright, compact components that we identify as composite

thermal dust and non-thermal synchrotron emission, respectively (see Fig. 5.1). This combination is consistent with the overall FIR–radio spectral energy distribution of MG J0414+0534 (Chapter 2). The total flux-density is $S_{340\ \mathrm{GHz}} = 24.3 \pm 1.2$ mJy, of which about 50 percent is contained in the compact images.

Contrary to the findings of Inoue et al. (2017), we do not detect a source near image A2 (object Y). We do find a 4σ surface brightness peak at this position in the pipeline-reduced data before self-calibration, in addition to a number of higher significance artefacts that are caused by residual phase errors; given that the noise is correlated in the sky-plane for interferometric data, the requirements for blind detections in the radio are typically $> 6.5\sigma$. These artefacts, including object Y, do not remain in the data after subsequent steps of self-calibration. The rms noise in our naturally-weighted image, after correcting for the residual antenna-based phase errors is 19 μJy beam^{-1}, in comparison to the 65 μJy beam^{-1} from the analysis by Inoue et al. (2017). To test that we did not bias the result with our choice of model during self-calibration, we also used an initial model that included object Y (as described in Section 5.2). However, the calibration does not converge to a solution were object Y remains after the process. Therefore, we conclude that object Y is a noise artefact resulting from residual phase errors rather than a genuine astronomical source.

With super-uniform weighting of the visibility data, we detect four compact components that are coincident with the optical and radio core of the AGN (see Fig. 5.1). The merging images are also marginally resolved and show evidence for an additional low surface brightness component, likely due to some contribution from compact dust emission. We fit a model of delta functions to the lensed images in the visibility plane (described in Section 5.2) for which we use only epoch 2 due to its higher angular resolution. We also attempted to fit Gaussian models, however, as the images are only marginally resolved and there is some evidence of extended dust emission also, the fitting did not produce stable results. We detect a flux ratio anomaly between images A1 and A2 (see Table 5.2), as seen at longer wavelengths, which have a ratio of $S_{\mathrm{A2}}/S_{\mathrm{A1}} = 0.86 \pm 0.01$ in the continuum. This ratio is more extreme than the flux ratio measured at ~GHz radio frequencies and in the mid-infrared, all of which are dominated by AGN emission. The flux ratios from the radio to near-infrared are shown in Fig. 5.2. A slight trend can be seen from 1.4 to 340 GHz towards a more extreme flux ratio anomaly between images A1 and A2. If genuine, this trend is likely the effect of a change in the source structure, where the lensed emission is more extended at lower frequencies due to an additional contribution from the steep-spectrum jet emission and the larger size of the synchrotron self-absorbed AGN core. Similarly, a less extreme flux ratio in the mid-infrared may be explained by the dusty torus being extended on scales larger than the sub-mm core.

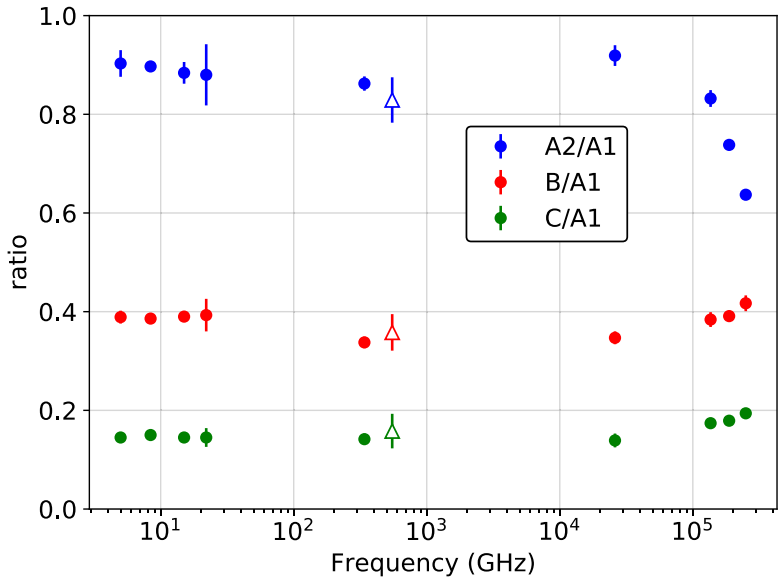

Figure 5.2 | The continuum flux ratio of images A2, B and C relative to image A1 from the radio to near-infrared. The CO (11–10) flux ratios are also shown, marked with open triangles at an arbitrary frequency. The flux ratios measured in the near-infrared are affected by extinction and microlensing. The radio, mid-infrared and near-infrared measurements are taken from Katz et al. (1997), MacLeod et al. (2013), and Kochanek et al. (1999), respectively.

5.3.2. CO (11–10)

The CO (11–10) molecular gas emission from MG J0414+0534 is clearly detected in the moment-zero map (see Fig. 5.3), which is found to be coincident with the four images of the lensed quasar. From extracting the one-dimensional spectral profile over the merging images A1 and A2 (see Fig. 5.4), we find that the line profile is broad and asymmetric, with a higher flux density in the blue-shifted component. The spatially resolved velocity structure for images A1 and A2 (see Fig. 5.5) shows that there is evidence of a rotating gas structure around the central black hole of the quasar; also, the blue-shifted component approaches the critical curve of the lens, and therefore subject to a higher magnification. Thus, the asymmetric line profile we observe is due to differential magnification across the velocity field, rather than an intrinsic property of the source, as has been seen in the molecular gas emission from other lensed galaxies (Rybak et al., 2015b; Paraficz et al., 2018). A single Gaussian fit to the line profile from images A1 and A2, gives a line FWHM of 1080 ± 20 km s^{-1}. The gas also has a high velocity dispersion of 300 km s^{-1} at the position of the black hole, as

seen in the moment-two map of images A1 and A2 (see Fig. 5.5).

We find that the line emission from the merging images is marginally spatially-resolved. The compact size, high velocity dispersion and broad profile of the line emission are consistent with warm, dense gas in the vicinity of the AGN. While large velocities are found in the broad line region of AGN, Lawrence et al. (1995) find Balmer lines with FWHM ~ 4000 km s^{-1} for this quasar, suggesting the gas is outside this region. There is no evidence of a change in the line profile between the two epochs (2015 June and August) that would suggest the gas is intrinsically variable or subject to microlensing.

We fit models to the lensed images in the visibility plane (described in Section 5.2), using the channels around the peak of the line in the velocity range -350 to 0 km s^{-1}. We select this range of the data as it has the highest signal-to-noise ratio and the emission is compact enough that it can be well approximated by delta functions. Furthermore, this corresponds to the blue-shifted component of the line emission that is close to the critical curve, and therefore should have a flux ratio that is close to unity for a smooth mass distribution in the absence of substructure. The measured flux ratios of the line emission are given in Table 5.2.

The flux ratios in the CO between images A1 and B, and between images C and B, are consistent with the anomalies detected in the radio and mid-infrared bands, which are attributed to the secondary lensing galaxy (object X). We detect a flux ratio anomaly between the merging images of $S_{\rm A2}/S_{\rm A1} = 0.83 \pm 0.05$. Image A2 is suppressed relative to A1, as observed at mid-infrared (Minezaki et al., 2009; MacLeod et al., 2013) and radio wavelengths (Katz et al., 1997, for example). The similarity of the flux ratios of images B and C in the CO and mid-infrared suggests that the gas is on a scale comparable to the AGN torus, as primarily observed in the mid-infrared. However, the flux ratio anomaly between images A1 and A2 is more extreme than observed in the mid-infrared or mm-continuum as the blue-shifted component of the line emission is likely offset from the position of the central black hole and, being close to the critical curve, is also preferentially magnified. This is the first detection of a flux ratio anomaly in the mm-line emission from a gravitationally lensed quasar.

5.4. Discussion and conclusions

Although the image flux ratios of gravitationally lensed quasars can be used to test models of galaxy formation and dark matter, the technique is currently limited by the small number of suitable objects that can be used in the analysis (e.g. Xu et al. 2015). Here, we have shown the detection of a flux ratio anomaly in the molecular gas from a

Table 5.1 | The flux densities of the 340 GHz continuum and CO (11–10) line emission (measured between −300 and 0 km s^{-1}).

Image	$S_{\rm cont}$ (mJy)	$S_{\rm line}$ (mJy)
A1	4.43 ± 0.05	2.54 ± 0.09
A2	3.82 ± 0.05	2.11 ± 0.09
B	1.50 ± 0.05	0.91 ± 0.09
C	0.63 ± 0.05	0.40 ± 0.09

Table 5.2 | The flux ratios of the lensed images at 340 GHz continuum and CO (11–10) line emission (measured between −300 and 0 km s^{-1}).

Images	$R_{\rm cont}$	$R_{\rm line}$
A2/A1	0.86 ± 0.01	0.83 ± 0.05
B/A1	0.34 ± 0.01	0.36 ± 0.04
C/A1	0.14 ± 0.01	0.16 ± 0.04

lensed quasar for the first time. By targeting the high excitation CO (11–10) emission, we are able to probe a compact region that is close to the central super-massive black hole, which gives an independent measurement to the flux ratios observed in the mm-continuum and other wavebands. In addition, we have shown that there is no evidence of variability in the line emission from either intrinsic or extrinsic effects and, as the dust is optically thin to the line emission, the CO (11-10) flux ratios are not affected by extinction. Thus, the study of molecular line emission appears to be a promising method to measure flux ratio anomalies.

As well as providing an independent measurement of the flux ratios, studies in the mm-regime have several advantages over other wavelengths. First, as shown here and in many other cases, the thermal dust emission in high redshift objects is sufficiently extended to produce an Einstein ring; such data can provide important constraints to the lensing macro-model, even at a low-angular resolution (e.g. Rybak et al. 2015a). Therefore, lenses that produce only two-images could also now be used in the analysis, increasing the sample size. Second, interferometric arrays such as ALMA can provide sufficiently high angular resolution (> 10 mas) such that any degeneracies between the inferred level of substructure and the source model (often assumed to be point-like) can be minimised. Finally, 70 percent of known gravitationally lensed quasars are FIR-bright (Chapter 2), and so are expected to have detectable high excitation gas associated with the quasar. This, coupled with the large-scale lens surveys being

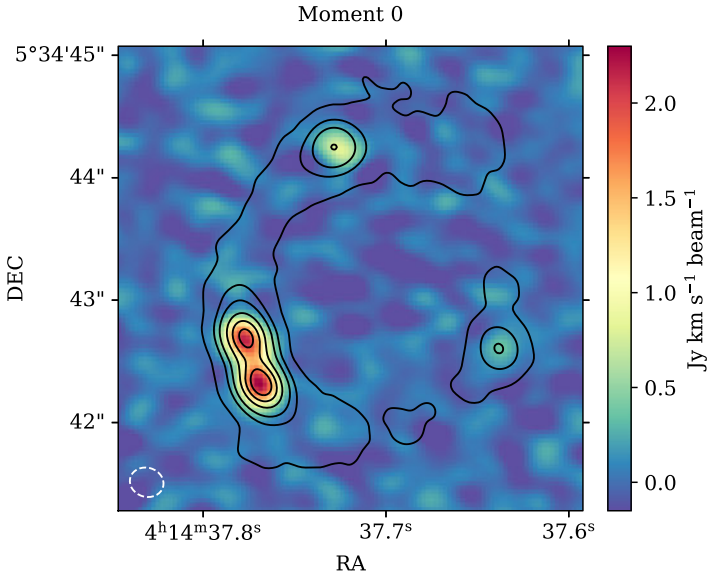

Figure 5.3 | The CO (11–10) integrated line intensity (moment zero) using a Briggs weighting scheme for the visibility data. Contours of the naturally weighted continuum are overlaid. The synthesised beam is shown in the lower left corner.

carried out with DES, for example, will provide a large population of potential targets for this work in the near-term. A pilot study of a well-selected sample of lensed quasars to investigate this is planned.

Our study of MG J0414+0534 has not revealed the cause of the flux ratio anomaly, although the similar flux ratios observed here and at other wavebands does suggest that it is due to some perturbation in the lensing potential. However, we have demonstrated that it is not due to a candidate dwarf satellite close to images A1 and A2 that was previously reported. As the magnitude of the anomaly is consistent with other studies, we have not tested the possible mass models that are consistent with the data, which we defer to a follow-up paper. This will include combining the continuum and line emission data (e.g. Hezaveh et al. 2013) to determine whether the perturbation is due to a sub-halo or a more massive structure that is currently unaccounted for in the lensing macro-model.

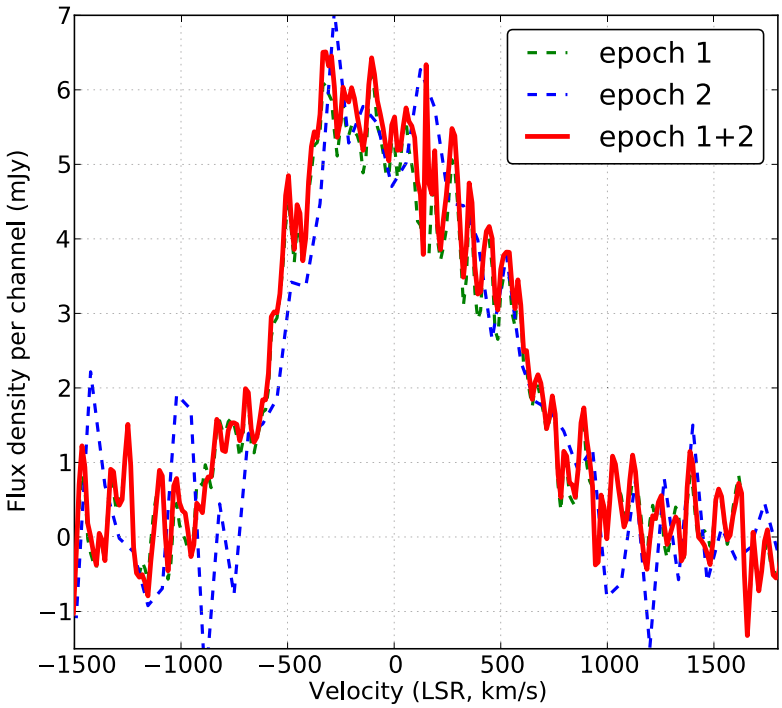

Figure 5.4 | The CO (11–10) line profile from MG J0414+0534 for images A1 and A2 (red). The dotted lines show the spectra from 2015 June 13 (green) and 2015 August 14 (blue), and demonstrate that there is no change in the line profile over this timescale. The data for epoch 2 has been smoothed with a boxcar kernel of width 5 channels. The systemic velocity is relative to $z = 2.639$, using the radio definition of the velocity.

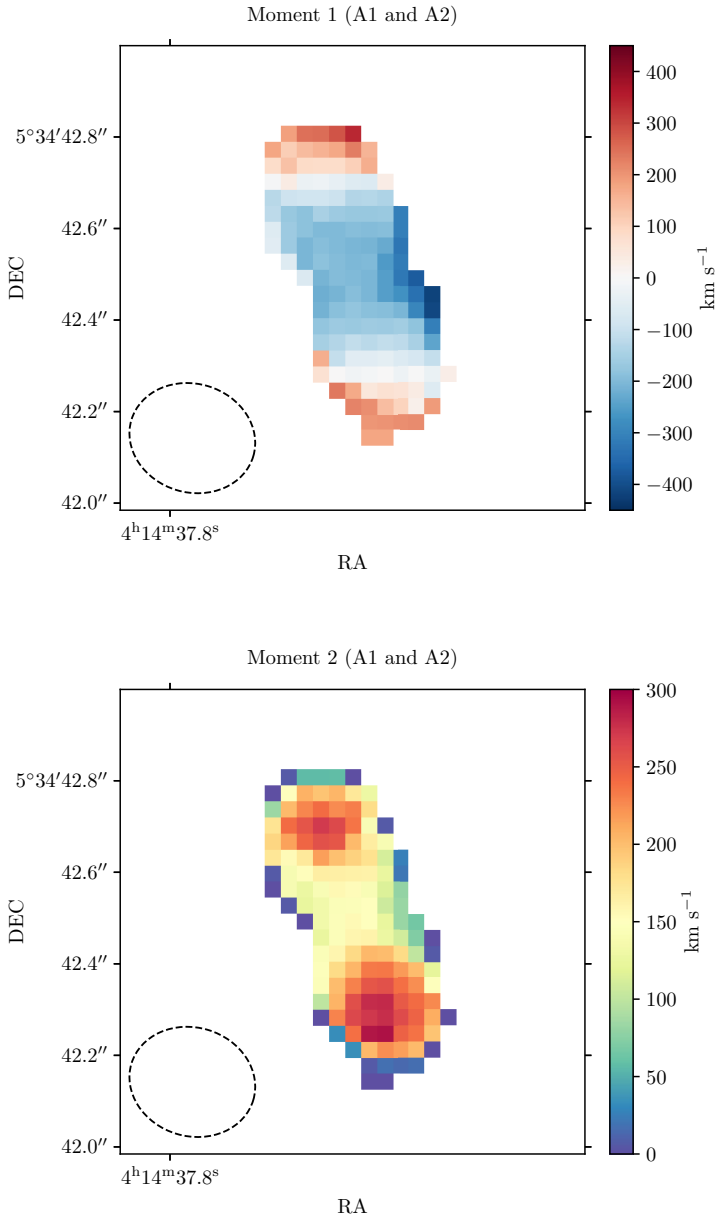

Figure 5.5 | The CO (11–10) velocity-field (moment one; upper) and velocity dispersion (moment two; lower), for the merging images A1 and A2. Pixels below the 5σ-level are masked out. The synthesised beam FWHM is shown in the lower left corner.

Acknowledgements

We thank Leon Koopmans and the anonymous referee for their comments on the letter on which this chapter is based. This work makes use of the following ALMA data: ADS/JAO.ALMA#2013.1.01110.S. ALMA is a partnership of ESO (representing its member states), NSF (USA) and NINS (Japan), together with NRC (Canada) and NSC and ASIAA (Taiwan) and KASI (Republic of Korea), in cooperation with the Republic of Chile. The Joint ALMA Observatory is operated by ESO, AUI/NRAO and NAOJ. This research made use of Astropy, a community-developed core Python package for Astronomy (The Astropy Collaboration et al., 2018).

Smoke on the water

40 ml mezcal
15 ml maraschino liqueur
15 ml crème de violette
25 ml lemon juice
15 ml agave syrup
20 ml aquafaba or egg white

Shake well all the ingredients with ice. Strain into a chilled coupe glass.

6

Resolving quasar lens systems at sub-mm wavelengths

III. Smoke on the water: CO and H_2O gas in a circumnuclear disc at redshift 2.64

H. R. Stacey, A. Lafontaine and J. P. McKean

Based on "Smoke on the water: CO emission and H_2O gas in a circumnuclear disc around a quasar at redshift 2.64"
H. R. Stacey, A. Lafontaine & J. P. McKean; in press with Monthly Notices of the Royal Astronomical Society

Abstract

We present an analysis of observations with the Atacama Large (sub-)Millimetre Array (ALMA) of the 380 GHz water emission line and CO (11–10) emission line from MG J0414+0534, a gravitationally lensed dusty star-forming galaxy that hosts a type 1 quasar. We also present observations at 1.6 GHz with global very long baseline interferometry (VLBI) of the radio source. We confirm the previously reported detection of the 380 GHz water line and that the flux density ratio between the two merging lensed images is reversed with respect to the radio/mm continuum. We further find tentative evidence of variability in the integrated line intensity on timescales of days. We show that the 380 GHz water line has two components of emission: a disc that is around 35 pc in diameter around the quasar, and another component of emission that is offset ~ 600 pc perpendicular to the disc that lies close to the lensing caustic. With lens modelling of the multi-wavelength data sets we construct a model for the quasar system, consisting of a circumnuclear disc of molecular gas with a size of about 60 pc bisected by radio jets extending to a distance of about 200 pc from the radio core. Our findings suggest that observations with ALMA of high-excitation molecular lines from strongly lensed quasars could allow detailed studies of AGN accretion and feedback at the cosmic peak of black hole and galaxy growth.

6.1. Introduction

Water is an abundant molecule in the Universe with a large number of observable transitions from cm to mm wavelengths, whose properties can provide valuable insights into the physical conditions of the interstellar medium (ISM) of galaxies. While H_2O emission is weak from the quiescent cold ISM, it is often associated with the dense, warm (or shock-heated) ISM in star-forming regions (e.g. van der Werf et al. 2011; Jarugula et al. 2019) or regions in the vicinity of active galactic nuclei (AGN; e.g. Moran et al. 1995). Collisional excitation or pumping from a strong radiation field can lead to population inversion, which can create the conditions needed for bright maser emission to occur (Neufeld et al., 1994). Extra-galactic H_2O masers can be produced by a large number of individual masers in an intense starburst (Cernicharo et al., 2006; König et al., 2017). However, they are more typically associated with AGN, where synchrotron emission from the radio core can penetrate the large column densities of dust and gas in the circumnuclear region, and provide sufficient continuum luminosity to reach the critical threshold for maser emission. These are termed 'megamasers', having luminosities $> 10^6$ times higher than Galactic masers (see Lo 2005, for review).

AGN megamasers have been localised with very long baseline interferometry (VLBI; 6_{16}–5_{23} transition; rest-frequency 22.23508 GHz) at cm-wavelengths to regions that are typically < 1 pc from the radio core. These can originate from illuminated gas near or in the accretion disc or torus, where they can be used to constrain the physical environment around the black hole (e.g. Moran et al. 1995; Herrnstein et al. 1998; Klöckner et al. 2003; Kuo et al. 2018). Studies of AGN disc masers have enabled accretion discs to be characterised as geometrically thin discs of dense molecular gas (Neufeld & Maloney, 1995; Herrnstein et al., 1996; Reid et al., 2009; Kuo et al., 2011) with evidence of substructure (Humphreys et al., 2008). AGN megamasers can also be produced by interactions between jet plasma and dense clouds of gas, and are therefore a useful probe of jet physics (Peck et al., 2003) and can trace jet-driven outflows of molecular gas (Greenhill et al., 2003). Observations of megamasers at high redshift are, therefore, especially of interest as they can be used to constrain the environment around AGN at the peak of cosmic star formation and AGN activity (Madau & Dickinson, 2014).

Thus far, only one 22 GHz H_2O megamaser has been detected at $z \gtrsim 1$, from the gravitationally lensed quasar system MG J0414+0534 ($z = 2.64$; Impellizzeri et al. 2008; Castangia et al. 2011). The next highest redshift detection is from a type 2 quasar at $z = 0.66$ (Barvainis & Antonucci, 2005), despite numerous searches of other systems at $z > 1$ (Wilner et al., 1999; Ivison, 2006; Wagg & Momjian, 2009; Bennert et al., 2009; McKean et al., 2011). The megamaser emission from MG J0414+0534 has not been localised, so the origin (whether disc, jet or starburst) has, thus far, been undetermined.

However, the bright synchrotron emission from the radio source and large isotropic line luminosity of $10^{3.9}$ $L_\odot$ strongly suggests the megamaser emission is associated with the AGN. The blueshifted, complex velocity profile, initially reported by Impellizzeri et al. (2008), suggested it originates in the radio jet. However, the later tentative detection of a redshifted satellite line by Castangia et al. (2011) may point to a nuclear disc origin.

Variability of 22 GHz H_2O megamasers that are associated with AGN can be caused by fluctuations in the luminosity of the seed photons, the radiative pumping source that causes population inversion (Neufeld et al., 1994; Gallimore et al., 2001), the movement of the masing region (such as in a disc; Moran et al. 1995), or from interstellar scintillation (Greenhill et al., 1997). These variations can occur on timescales of minutes, in the case of scintillation, to months, in the case of disc rotation. It has also been suggested that microlensing by stars in foreground lensing galaxies can result in significant (extrinsic) variability of lensed 22 GHz H_2O megamasers at high redshift (Garsden, Lewis & Harvey-Smith, 2011). The 15 month monitoring campaign of MG J0414+0534 with the Arecibo telescope that was reported by Castangia et al. (2011) revealed variations in the isotropic line luminosity over this timescale, consistent with an AGN origin. They did not find significant evidence of a velocity drift, indicative of rotation of any maser regions in a pc-scale accretion disc. However, high-velocity disc features found in nearby AGN, where megamasers originate from the mid-line of the disc (e.g. Bragg et al. 2000; Yamauchi et al. 2005; Humphreys et al. 2008), fall within the inferred upper limit for any velocity drift in the 22 GHz H_2O megamaser emission from MG J0414+0534.

The complex energy level structure of H_2O also results in a large number of rotational transitions emitted at far-infrared (FIR) to mm wavelengths, which can be spatially resolved with the new capabilities of sub-mm/mm interferometry. These higher frequency transitions of H_2O are associated with both extreme star-formation and AGN activity within FIR-luminous galaxies (Omont et al., 2011; van der Werf et al., 2011), and have been used to probe the physical conditions within the ISM at high redshift (González-Alfonso et al., 2014). Given the previous detection of the 22 GHz H_2O megamaser, observations of MG J0414+0534 with the Atacama Large (sub)Millimetre Array (ALMA) were recently carried out by Kuo et al. (2019), who made a tentative detection of the 4_{14}–3_{21} H_2O line (rest frequency 380.197 GHz). Surprisingly, this tentative detection finds the flux ratio between the two merging lensed images (A1 and A2) to be reversed relative to the radio/mm continuum and CO (11–10) line emission (Chapter 5), and counter to expectations of gravitational lensing theory (Kochanek & Dalal, 2004). Kuo et al. account for this with three regions of megamaser emission, where one component is coincident with the quasar and two components are separated by large distances (~ 1.5 kpc) from the quasar.

Here, we present a re-analysis of the ALMA observations of MG J0414+0534 re-

ported by Kuo et al., and use these in combination with archival 1.6 GHz VLBI data of the radio continuum and ALMA CO (11–10) imaging to investigate the emission properties of the 380 GHz H_2O line. We confirm a robust detection of the 380 GHz H_2O line emission and the reverse in the flux ratio of the two merging lensed images with respect to the other multi-wavelength data for this object. We localise the 380 GHz H_2O emission relative to the CO and radio jet components, from which we derive a model for the emission from the system. In Section 6.2 we describe the observations and data reduction of the ALMA and global VLBI data. In Section 6.3, we report the velocity structure and variability of the 380 GHz H_2O line, and describe our lens modelling analysis. Finally, in Section 6.4 we propose a source-plane model to describe the physical origin of the different H_2O components and consider the implications of our results for future searches for mm-wavelength H_2O line emission in the early Universe.

We assume the Planck Collaboration et al. (2016) model of flat ΛCDM cosmology with $H_0 = 67.8\ \mathrm{km\,s^{-1}\ Mpc^{-1}}$, $\Omega_M = 0.31$ and $\Omega_\Lambda = 0.69$. For this cosmology, 1 arcsec corresponds to 8.2 kpc at the source redshift of 2.64.

6.2. Observations and data reduction

In this section, we summarise the observations and data reduction of the ALMA and global VLBI data used in this analysis.

6.2.1. 1.6 GHz VLBI observations

MG J0414+0534 was observed with the global VLBI array on 2008 June 7, under project code GW019A (PI: Wucknitz). The observations were performed at a central frequency of 1.6 GHz in full circular polarisation (RR, LL, RL, LR). The data were correlated with a visibility integration time of 1 s, in 8 spectral windows each of 16 channels and 8 MHz bandwidth. A total of 21 antennas were used for the observation from the European VLBI Network and the Very Long Baseline Array, but only 18 antennas were found to have usable data.

Phase referencing to nearby calibrators (J0412+0438, J0422+0219, J0409+1217) was performed at intervals of 14 min and standard fringe finder calibrators (3C286, 3C48, DA193, 0528+134) were observed at regular intervals over the 20 h observation. The data were edited, calibrated and imaged using the Astronomical Image Processing Software (AIPS). The data were manually flagged to remove radio frequency interference

and off-source integrations. Observations of the fringe finders were used to remove the instrumental delays. The spectral bandpass was calibrated using observations of DA193 and 0528+134, and the relative amplitudes were set using measured system temperatures and gain curves. Observations of the phase-reference calibrator were used to determine the time-dependent phase delays and rates. Several iterations of self-calibration of the target were performed, down to a solution interval of 60 s for each spectral window, to correct for residual phase and amplitude errors. The target was imaged and deconvolved in AIPS using a Briggs weighting of the visibilities (shown in Fig. 6.1). The VLBI components appear structurally similar to those reported by Ros et al. (2000) at 8.4 GHz, and previous imaging of the same data by Volino et al. (2010).

The task IMFIT within the Common Astronomy Software Applications (CASA) package (McMullin et al., 2007) was used to fit 2-dimensional Gaussians to the sub-components of the four lensed images (in the image plane) to extract their positions and uncertainties (listed in Table 6.1). The radio components are measured relative to the brightest component in image B, for consistency with previous studies (e.g. MacLeod et al. 2013). The relative image positions of the brightest radio component (sub-component I) are consistent with the relative positions of the optical emission from the quasar (Falco et al., 1997), so this is likely emission from (or very close to) the radio core.

6.2.2. ALMA observations

The ALMA imaging of MG J0414+0534 was taken in two distinct data sets, which we describe separately. The first, taken at 100 GHz, targeted H_2O, whereas the second, taken at 340 GHz, targeted high-excitation CO.

100 GHz data

MG J0414+0534 was observed with ALMA in Band 3 under project code 2017.1.00316.S (PI: Kuo). The data were taken in four epochs on 2017 December 13, 15 (two observations) and 18 in an antenna configuration with a longest baseline of 2400 m. The data were correlated with a visibility integration time of 3 s, in four spectral windows of central frequency 92, 94, 104 and 106 GHz, respectively. The 94 and 104 GHz spectral windows covered the redshifted rest frequency of two H_2O emission lines (4_{14}–3_{21}, $\nu_{\rm rest}$ = 380.197 GHz, and 5_{23}–6_{16}, $\nu_{\rm rest}$ = 336.228 GHz). These spectral windows were each correlated with 1920 channels and 0.94 GHz bandwidth; the remaining spectral windows had 128 channels and 2 GHz bandwidth. J0423−0120 was used as the absolute

flux and spectral bandpass calibrator. Phase switching to J0427+0457 was performed to correct the time-dependent phase variations. The total time on-target was 160 min, with approximately 40 min per epoch.

The data were calibrated using the ALMA pipeline within CASA. After confirming the quality of the pipeline calibration, the data were averaged in frequency by a factor of 16 to increase the signal-to-noise ratio per channel and the computational speed during imaging. This resulted in a spectral resolution of 22.6 km s^{-1} channel^{-1}. Self-calibration was performed using the continuum spectral windows to spatially align the four epochs and correct for any residual time-dependent phase and amplitude errors. The continuum subtraction was performed by fitting a model to the continuum in the line-free spectral channels and subtracting it from the data in the visibility plane.

The 100 GHz continuum image (see Fig. 6.2) shows four point sources of emission, consistent with the findings of Kuo et al. (2019) and with the far-infrared–radio spectral energy distribution that shows synchrotron-dominated emission at this frequency (see Chapters 2 and 5). We find no significant variability in the continuum flux density between the four epochs. We do not detect the 5_{23}–6_{16} H_2O line, consistent with the results of Kuo et al. (2019)*. We confirm the detection of the 4_{14}–3_{21} H_2O line; the line intensity and line luminosity (uncorrected for lensing magnification) are given in Table 6.2. We detect lensed images A1, A2 and B, but do not detect image C (the least magnified image). Moment maps of the line emission from lensed images A1 and A2, using a signal-to-noise ratio cut of 3σ, are shown in Fig. 6.4.

340 GHz data

MG J0414+0534 was observed with ALMA in Band 7 under project code 2013.1.01110.S (PI: Inoue). The spectral coverage included the CO (11–10) emission line ($\nu_{\rm rest}$ = 1267.014 GHz). Details of the observations, data reduction and imaging are reported in Chapter 5. The continuum imaging reveals four point sources of emission from the quasar and an Einstein ring of thermal dust emission. Imaging of the CO (11–10) shows four compact components at the location of the quasar images. The resolved velocity field from the two merging images (A1 and A2) shows evidence of ordered rotation around ±500 km s^{-1} from the systemic velocity. The positions of the redshifted and blueshifted components of the line emission were extracted by creating images from selected channels on either side of the systemic velocity. The positions of these components were extracted by fitting 2-dimensional Gaussians using the task IMFIT within CASA.

*This non-detection is not surprising as the excitation conditions ($E_u \sim 3000$ K) mean that it is not likely to be detected from an extragalactic source.

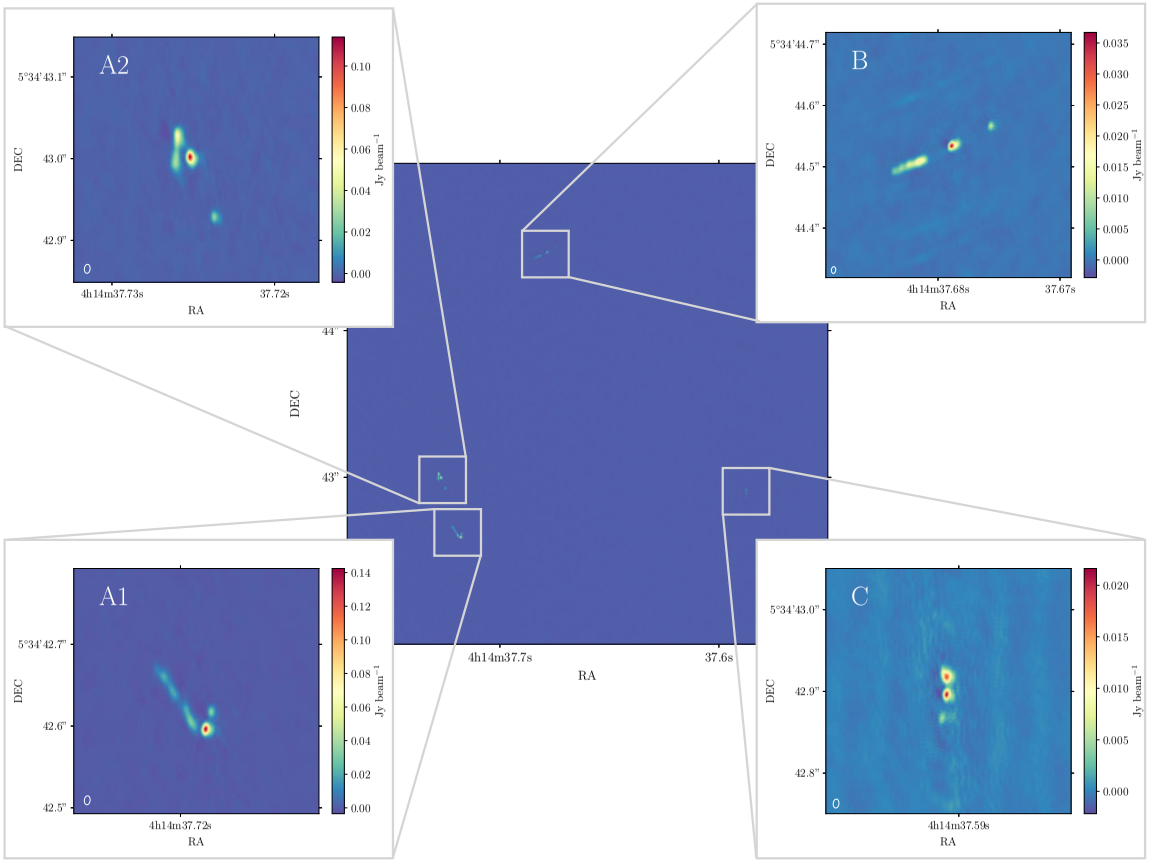

Figure 6.1 | 1.6 GHz global VLBI image of MG J0414+0534. Inset figures show cutouts of each lensed image. The beam size is shown in the lower-left corner of the inset images and is approximately 7 × 11 mas.

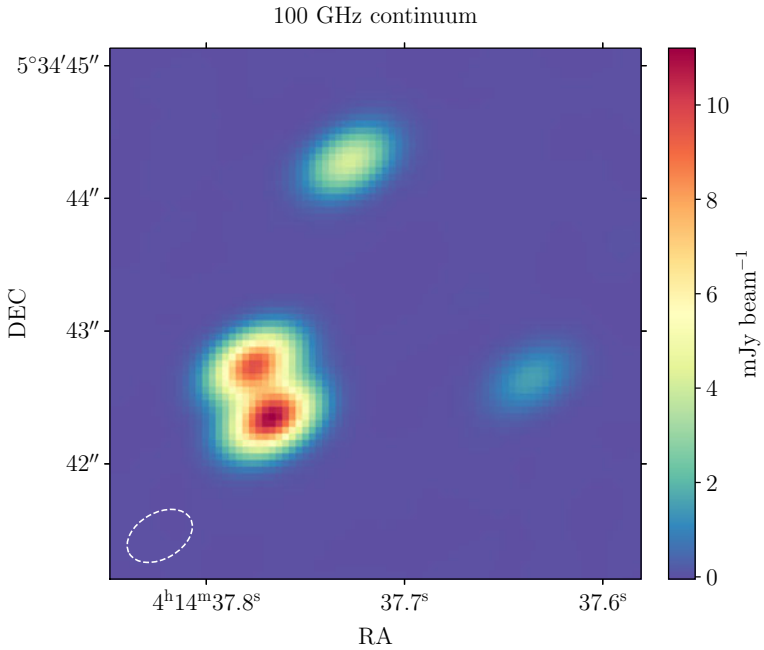

Figure 6.2 | Continuum emission from MG J0414+0534 at 100 GHz (360 GHz rest-frame frequency). The image shows four point sources of synchrotron emission from the AGN. The flux ratio between the merging lensed images is inconsistent with expectations for a smooth model, as reported in Chapter 5 with 340 GHz observations.

Table 6.1 | The radio VLBI and CO velocity components used in our lens modelling. The components are measured by fitting 2D Gaussians to the images using the task IMFIT within CASA. The positions are defined in arcsec relative to component B-I.

		VLBI				CO	
		I	II	III	IV	red	blue
A1	δx	-0.589932 ± 0.000005	-0.60892 ± 0.00004	-0.58320 ± 0.00002	-0.63538 ± 0.00010	-0.576 ± 0.003	-0.596 ± 0.005
	δy	-1.938372 ± 0.000009	-1.92669 ± 0.00008	-1.91770 ± 0.00005	-1.88383 ± 0.00017	-1.993 ± 0.003	-1.863 ± 0.005
A2	δx	-0.723891 ± 0.000006	-0.73902 ± 0.00001	-0.69423 ± 0.00003	-0.74172 ± 0.000016	-0.739 ± 0.003	-0.709 ± 0.005
	δy	-1.53326 ± 0.00001	-1.50852 ± 0.00004	-1.60586 ± 0.00005	-1.53706 ± 0.00008	-1.520 ± 0.003	-1.620 ± 0.005
B	δx	$\equiv 0.00000 \pm 0.00004$	-0.05185 ± 0.00010	$+0.06236 \pm 0.00006$	-0.72623 ± 0.00030	$\equiv 0.000 \pm 0.003$	$\equiv 0.000 \pm 0.005$
	δy	$\equiv 0.00000 \pm 0.00003$	-0.02566 ± 0.00007	$+0.03189 \pm 0.00010$	-0.03282 ± 0.00014	$\equiv 0.000 \pm 0.003$	$\equiv 0.000 \pm 0.005$
C	δx	$+1.3549 \pm 0.00002$	$+1.3549 \pm 0.0005$	$+1.34980 \pm 0.00004$	$+1.35486 \pm 0.00049$	$+1.345 \pm 0.003$	$+1.345 \pm 0.005$
	δy	-1.63822 ± 0.00005	-1.61619 ± 0.00005	-1.66682 ± 0.00013	-1.61619 ± 0.00080	-1.648 ± 0.003	-1.648 ± 0.005

Table 6.2 | Observed line intensities, line luminosities and continuum flux densities for the ALMA observations, uncorrected for lensing magnification. A 5 percent error in amplitude calibration should be assumed for the continuum flux density.

	$I_{\rm line}$ (Jy km s^{-1})	$L_{\rm line}$ ($L_\odot$)	$L'_{\rm line}$ (K km s^{-1} pc^2)	$S_{\rm cont}$ (mJy)	Reference
H_2O (4_{14}–3_{21})	1.0 ± 0.1	$(5.3 \pm 0.6) \times 10^7$	$(3.0 \pm 0.4) \times 10^{10}$	27	this work
H_2O (6_{16}–5_{23})	0.30 ± 0.03	$(9.5 \pm 0.9) \times 10^5$	$(2.7 \times 0.3) \times 10^{12}$	71	Castangia et al. (2011)
CO (11–10)	6.4 ± 0.3	$(1.16 \pm 0.06) \times 10^9$	$(1.78 \pm 0.09) \times 10^{10}$	24	this work; Chapter 5

6.3. Results

In this section, we present an analysis of the observed properties of the 380 GHz H_2O emission from MG J0414+0534, and the inferred source-plane properties of the various molecular gas components, relative to the quasar and the radio jets.

6.3.1. Velocity structure

Fig. 6.3 shows the line profile of the 380 GHz H_2O (4_{14}–3_{21}) emission, relative to the CO (11–10) line profile from Chapter 5, using an aperture including lensed images A1 and A2, and also from only lensed image A1 in the case of the former. The 380 GHz H_2O line profile obtained from only image A1 has a structure suggestive of a double horn profile, characteristic of emission from a disc. We fit two Gaussian components to the double-horn profile isolated from image A1, which are centred on -210 ± 20 km s^{-1} and 490 ± 20 km s^{-1}, with full width at half maximum (FWHM) of 630 ± 50 km s^{-1} and 420 ± 40 km s^{-1}, respectively. The CO line profile from both A1 and A2 is more peaked around the systemic velocity compared to the total 380 GHz H_2O emission, without a double-horn shape. The overall FWHM of the 380 GHz H_2O line profile is ~ 1000 km s^{-1}, comparable to that observed from the CO (11–10) line (i.e. 1100 ± 100 km s^{-1}, based on a Gaussian fit). The similar terminal velocities suggest that they are associated with the same region of the source.

The double-peaked 380 GHz H_2O profile from image A1, under the assumption that the emission is from a disc, suggests a correction to the systemic velocity of $+140 \pm 10$ km s^{-1}. The centre of the CO (11–10) profile also suggests a slightly redshifted systemic velocity. We note that the peaks in the 380 GHz H_2O line profile are consistent with the blue and redshifted components of the 22 GHz H_2O megamaser system reported by Castangia et al. (2011) (shown with black crosses in Fig. 6.3), but with larger associated dispersions.

From the moment maps of the 380 GHz H_2O line emission (see Fig. 6.4), we find that the line emission is only marginally resolved in total intensity for the two merging lensed images (which are also those with the highest magnification; see below). However, there is evidence of resolved structure in the velocity map, where we find a (red) component at around +100 km s^{-1}, that is, close to the systemic velocity, which is coincident with the peak in the line total intensity, and a spatially-offset (blue) component that is at a velocity of around -300 km s^{-1}. This velocity structure is markedly different from the CO (11–10), where there is evidence of only a disc component associated with the AGN. This could be, in part, due to the better angular

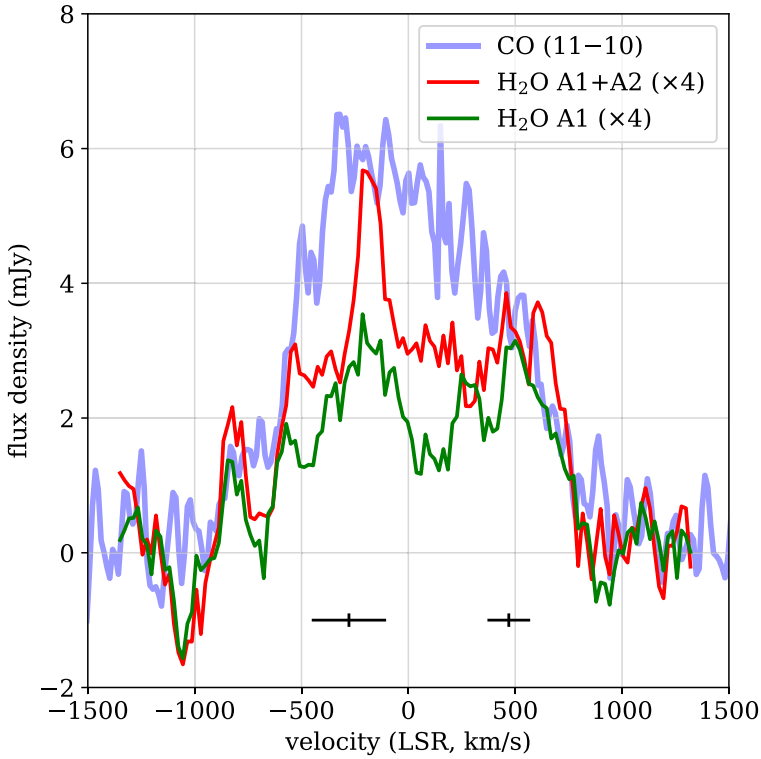

Figure 6.3 | Line profiles of CO (11–10) (blue) and H_2O (4_{14}–3_{21}). The H_2O line integrated over both A1 and A2 is shown in red, and the line from the peak of A1 is shown in green. The black crosses indicate the peak and FWHM of the 22 GHz H_2O megamaser components from Castangia et al. (2011). The H_2O line profiles are smoothed with a boxcar kernel of width 5 channels (113 km s^{-1}) and scaled by a factor of 4, for comparison. The systemic velocity is relative to $z = 2.639$, using the radio definition of velocity.

resolution of the CO (11–10) observations, where the overall velocity structure is less beam-smeared. We see that the velocity dispersion of the 380 GHz H_2O emission peaks at around 400 km s^{-1} and is co-spatial with the quasar, both of which are consistent with the properties of the CO (11–10) emission. This further suggests that the major component of these two molecular gas tracers are likely associated.

While the angular resolution of the 380 GHz H_2O line observations are around a factor of 2 lower than those of the CO (11–10), the water emission cannot be significantly more extended (as it would form an arc or ring), or be spatially offset (which would produce a different image configuration). Assuming a smooth distribution of mass in the lens, these merging images should be almost mirror images with a similar flux density. Consistent with Kuo et al. (2019), the H_2O line emission from image A2 appears around twice as bright as A1: this flux density ratio is reversed compared to the radio/mm continuum, CO (11–10) emission and multi-wavelength archival observations (see Chapter 5). As the 380 GHz H_2O emission is spatially coincident with the CO (11–10) and mm-continuum emission from the quasar, small-scale mass structure in the lens is unlikely to be responsible for the different flux ratio as the emission is subject to the same local lens potential. Therefore, the observed reversed flux ratio is more likely due to the effect of source structure rather than the mass distribution in the lens (see below).

We fit Gaussian components to the four lensed images in the 380 GHz H_2O line integrated intensity to determine at what level the emission is spatially resolved. Assuming the 380 GHz H_2O line emission that is coincident with the quasar images is unresolved and has image flux ratios consistent with the mm-continuum, we fix four Gaussian components to the size and position angle of the synthesised beam, and fix the component positions to the centroids of the mm-continuum emission. We initially allow the flux density of these components to optimise. We then fix the flux density of images A2, B and C using the flux ratios reported in Chapter 5, normalised relative to the optimised flux density of A1. As shown in Fig. 6.5, the residuals of this model fit have surface brightness features at the 4σ level, suggesting that some 380 GHz H_2O line emission is spatially resolved around image A2.

Fig. 6.6 shows position-velocity diagrams of a slice through images A1 to A2 for the 380 GHz H_2O line emission, with the contours of the CO (11–10) emission from the same region overlaid. A double-peak structure can be seen within the extent of the CO disc, as suggested by the line profile. The CO emission has a caret shape, due to the fact that the blueshifted emission is closer to the caustic and is more strongly magnified. An additional velocity component from the 380 GHz H_2O emission can be seen around image A2 that is more extended than the CO emission and does not have a mirror component in A1. This is the extended emission seen in the moment 0 image and contributes the narrow peak in the line profile at around -220 km s^{-1} (see

Fig. 6.3). The anomalous velocity component is not consistent with the caret shape of the CO (11–10) disc and is spatially offset. Therefore, this cannot be emission from the disc.

6.3.2. Variability

As the observations of the 380 GHz H_2O line were obtained in four epochs with separations between a few hours and 6 days, we examine the individual observations to look for short time-scale variability. The emission from the merging images (A1+A2) appears to increase by a factor 1.7 ± 0.8 between the observations taken on 2017 December 13 and 15, but this is not significant as the uncertainty is large. We find tentative evidence for variability when comparing the integrated flux from combining the two 2017 December 15 epochs with the combined preceding and succeeding epochs on 2017 December 13 and 18 (combined to match the signal-to-noise of 2017 December 15 epochs). The significance of this variability is at the 2σ level when we consider the total integrated emission (see Fig. 6.7, left panel). However, the significance rises to 3σ when we only consider the integrated flux from image A1 (Fig. 6.7, right panel). We do not find evidence that the continuum emission is variable over the observations, which is consistent with the results of Chapter 5 for the rest-frame 1267 GHz continuum emission from the AGN. We note that, although differences in amplitude scaling could mimic source variability, this would not affect the signal-to-noise ratio of the line emission.

The strongest evidence for variability in the 380 GHz H_2O line is seen in the position-velocity diagrams for these observations, which are also shown in Fig. 6.6. The emission can be seen to be quite different between the data sub-sets. The emission in the combined data from the epochs on 2017 December 15 is higher overall, but, in particular, the emission from image A1 shows the largest difference. The time delay between the merging images of the quasar is expected to be 0.4 days, based on our lens model (see below). When comparing the two epochs taken on 2017 December 15, the flux ratio appears to switch, with A2 brighter in the first epoch. This accords with our expectation from the lens model (image A2 is the leading image), but these measurements are within the overall uncertainties. Our findings could be interpreted as two components of 380 GHz H_2O line emission, one that is variable on timescales of less than a few days, as seen in image A1, and one that is constant over the timescale of the observations.

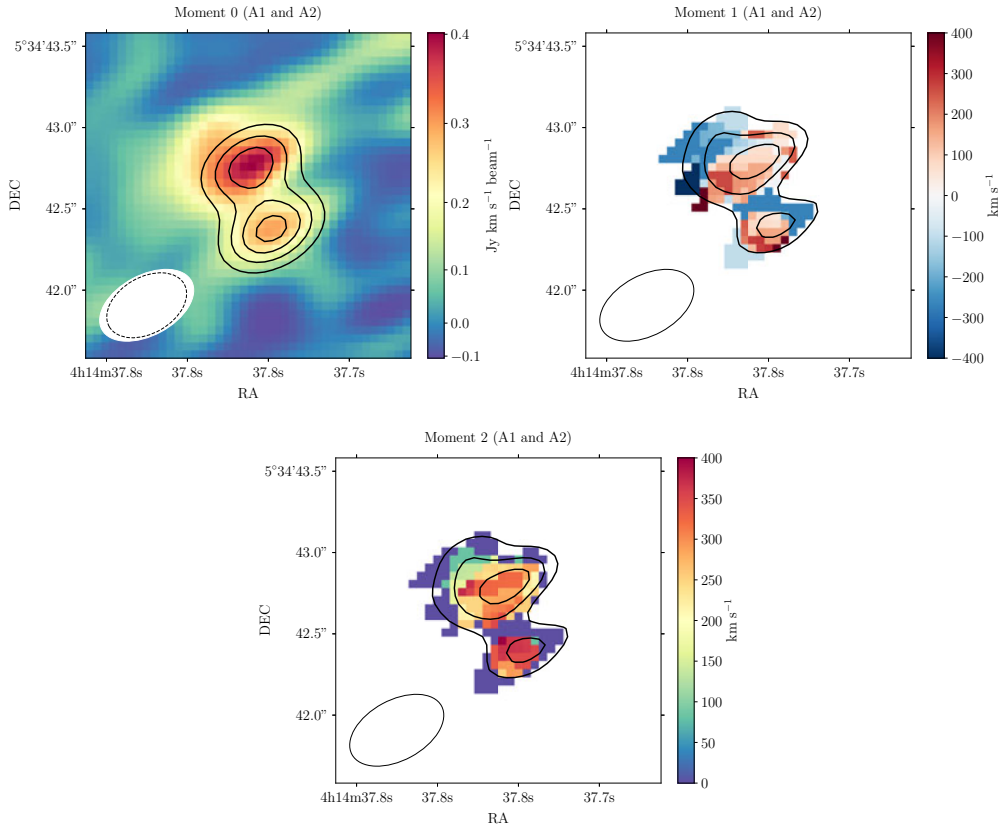

Figure 6.4 | Velocity integrated line intensity (moment 0), velocity field (moment 1) and velocity dispersion (moment 2) of the H_2O (4_{14}–3_{21} line emission. The moment 1 and 2 images are created by masking emission below 3σ, where σ is the mean rms noise per channel. In the moment 0 image, contours showing the continuum are over-plotted with peak fractions 0.3, 0.5, 0.7, 0.9. The moment 1 and 2 images show contours of the moment 0 image at 5, 7, 9σ (where σ is the rms noise). The synthesised beam is shown in the lower left corner and has a size of 0.4 arcsec × 0.6 arcsec.

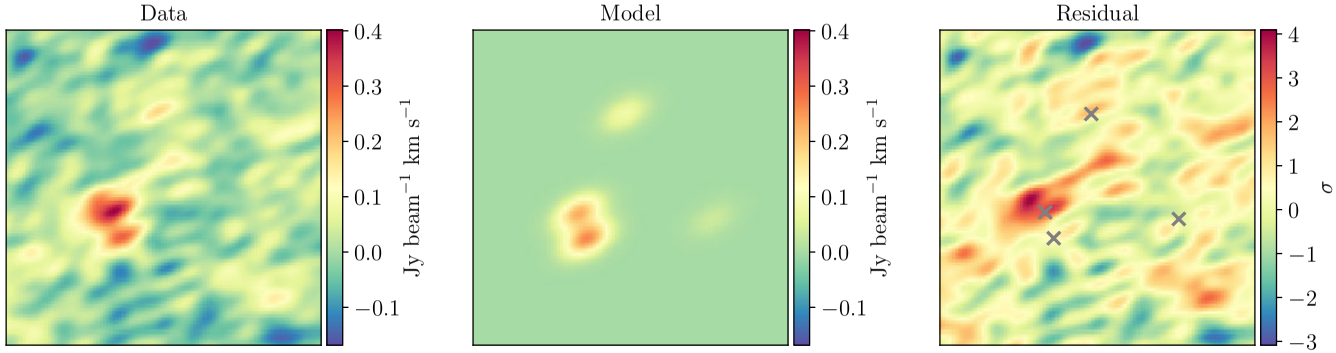

Figure 6.5 | Gaussian model fit to imaging of the 380 GHz H_2O line integrated line intensity. *Left to right*: the data; the model on the same colour scale as the data; and the residuals (data−model) in units of σ, where σ is the rms noise in the data. The Gaussian model components are fixed to the size of the synthesised beam (PSF) and their positions are fixed to the image positions in the continuum emission. The component flux densities are initially allowed to optimise, but afterwards are fixed to the continuum flux ratios reported in Chapter 5 relative to the optimised flux density of image A1. Residuals of this model fit show surface brightness features around image A2 at the 4σ level.

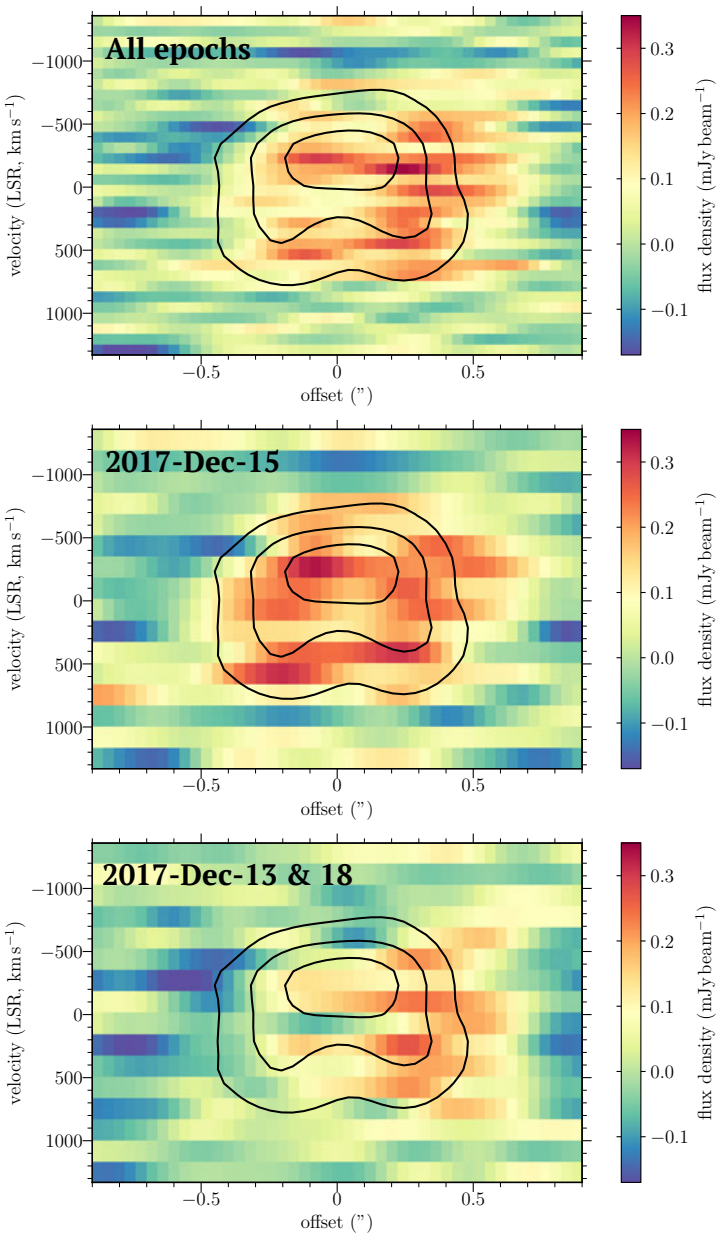

Figure 6.6 | Position-velocity diagrams for the 380 GHz H_2O line emission from the merging images in the direction A1 to A2 (left to right). The top image shows the data from all 4 epochs; the middle image is data only from two epochs on 2017 December 15; the bottom image is data combined from 2017 December 13 and 18. The contours show the CO (11–10) line emission from the same region, smoothed with a Gaussian kernel to match the angular resolution of the 380 GHz H_2O line emission.

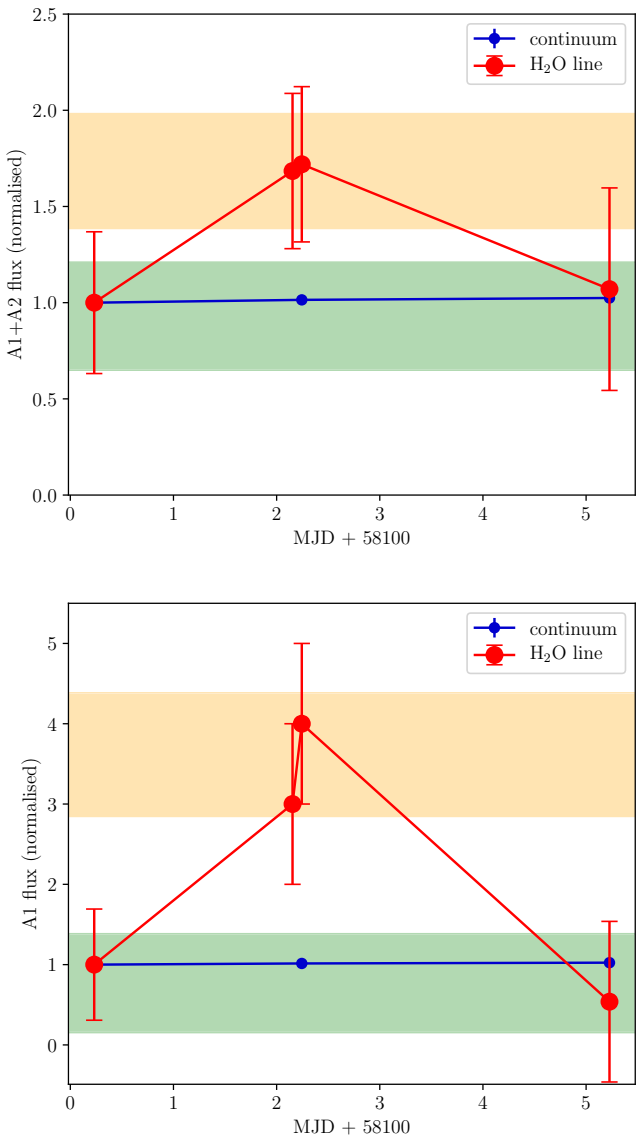

Figure 6.7 | The normalised, velocity-integrated flux density of the 380 GHz H_2O line emission and rest-frame continuum for the four epochs. We show the integrated flux density of both merging images (A1+A2; left) and for image A1 only (right). The 380 GHz H_2O line emission is shown in red and the continuum is shown in blue. The orange region shows the combined flux density and uncertainty for both epochs on 2017 December 15; the green region shows the combined flux and uncertainty for 2017 December 13 and 18.

6.3.3. Source-plane structure

In order to determine the structure of the various emission components from MG J0414+0534 in the source plane, we first determine a model for the lens. This was performed using the parametric lens modelling software GRAVLENS (Keeton, 2001a,b). We assume a simple model of a singular isothermal ellipsoid with external shear (SIE+γ) for the primary lens (G1), and a singular isothermal sphere (SIS) for the satellite galaxy (G2). The 1.6 GHz VLBI positions, having the highest precision and largest number of image components, were used to optimise for the best lens model parameters. The flux densities of the components were not used in the modelling, as these are known to deviate from a smooth lens model (e.g. MacLeod et al., 2013). While an improved fit to the image positions may also be obtained with more complex parametric models, such as an ellipsoidal power-law mass distribution (e.g. Spingola et al., 2018), this will not significantly change our interpretation here. The resulting best fit parameters are given in Table 6.3, and are found to be in good agreement with previous modelling of the system (e.g. Ros et al. 2000; MacLeod et al. 2013). As the absolute astrometry between the various data sets is lost after self-calibration, we align them using the compact core emission that is associated with synchrotron emission from the quasar. The consistent image separation of these components in each data set supports the assumption that the component we identify as the radio core is coincident with the quasar.

The reconstructed source-plane emission from the 1.6 GHz VLBI continuum and CO (11–10) velocity components are shown in Fig. 6.8. We find that the jet and counter jet (the components either side of the radio core) form an almost-linear structure that is extended in an East–West direction by around 200 pc in projection. The red and blue CO (11–10) velocity components are almost perpendicular to the radio jets, and form what we interpret as a molecular gas disc with a size that is 60 pc in projection around the quasar. Given the similarity in the position-velocity diagrams of the CO (11–10) and the 380 GHz H_2O emission, we assume that the molecular gas disc also contains part of the water emission observed from MG J0414+0534.

Assuming just half of the 380 GHz H_2O emission we detect originates in a disc, and assuming the total magnification of the radio core inferred from our lens modelling is representative of the magnification of the H_2O disc ($\mu_{\rm tot} \simeq 40$), we estimate the isotropic line luminosity is $\sim 7 \times 10^5$ $L_\odot$.

To constrain the origin of the anomalous velocity component in the 380 GHz H_2O line emission (i.e. emission not from the disc) we place a grid of mock sources on the source plane and compute the positions predicted by our lens model. Fig. 6.9 shows the image positions produced by the mock sources relative to the radio components. As the anomalous velocity feature is not detected from the emission peak of A1, we exclude

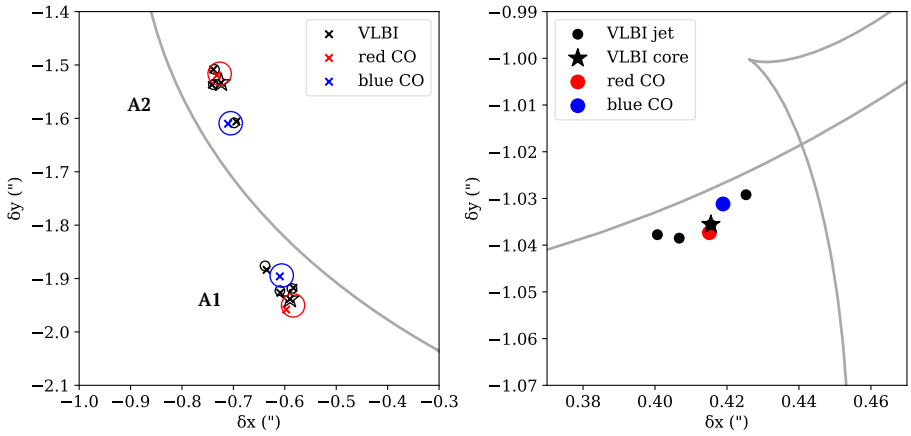

Figure 6.8 | Lens-plane (left) and source-plane (right) positions of the CO (11–10) and 1.6 GHz VLBI components. We show only the region of the lens plane around the merging images (A1 and A2). The grey lines trace the critical curve on the lens plane and tangential caustics on the source plane. The observed image positions are shown with crosses. The model-predicted positions on the lens and source plane are shown in red and blue circles for the respective CO (11–10) velocity components, and in black circles for the 1.6 GHz VLBI components. The source plane structure suggests a molecular gas disc of CO (11–10) emission bisected by two perpendicular radio jets.

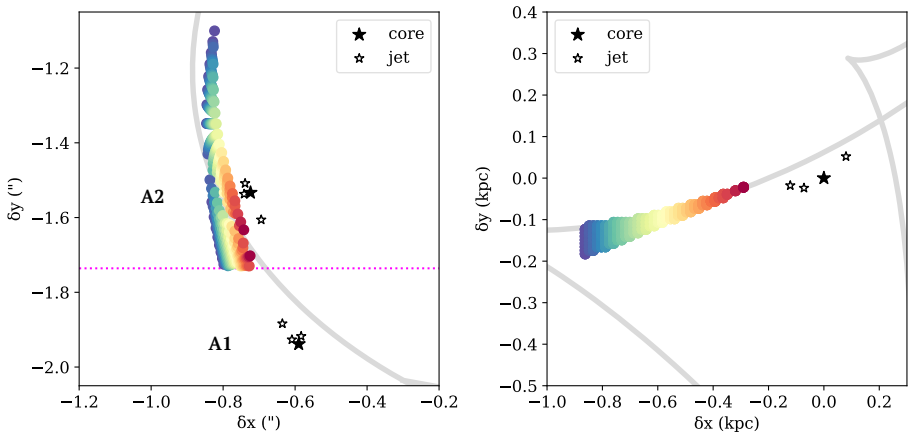

Figure 6.9 | Lens-plane images (left) corresponding to mock positions of the anomalous 380 GHz H_2O velocity component on the source plane (right). The radio core and jets are shown with filled and empty stars, respectively, and the grey lines trace the critical curve and tangential caustics. The source-plane positions are shown in kpc relative to the radio core. Sources that produce images below the midpoint of A1 and A2 (shown with the dotted magenta line) are excluded. We also exclude sources that produce fewer than four images, as they would not produce an image on the relevant area of the lens plane or would be a very large distance from the quasar.

Table 6.3 | The best parameters of the lens model, based on the positions of the VLBI image subcomponents. The primary lens, G1, is modelled with an SIE and external shear, and the secondary lens, G2, is modelled with an SIS. b is the Einstein radius of the lens. The positions (x,y) are given relative to the brightest component of image B. e and γ are the ellipticity and external shear, and θ_e and θ_γ are their respective position angles East of North.

	b (")	x (")	y (")	e	θ_e (°)	γ	θ_γ (°)
G1	1.076	+0.482	−1.279	0.235	−84.16	0.098	53.85
G2	0.196	+0.913	+0.150	-	-	-	-

all source positions that produce an image below the midpoint between image A1 and A2. We also exclude any positions that are doubly imaged (outside the tangential caustic), as these would not produce an image in the region of interest. Doubly imaged source positions that could produce an image near the merging images would be on the opposite side of the caustics (several kpc from the quasar, as suggested by Kuo et al. 2019), which we do not consider to be feasible. We find that the remaining viable source positions are very close to the lens caustic, which would produce a high magnification of the anomalous velocity component. However, as the position-velocity diagrams (see Fig. 6.6) and Gaussian source fitting to the images (see Fig. 6.5) show the anomalous feature is North of A2 and around 0.3–0.4 arcsec from the midpoint, only the green and blue source regions are in agreement with the observations. This suggests that the anomalous 380 GHz H_2O feature originates > 600 pc East of the quasar and perpendicular to the molecular gas disc.

Assuming that half of the 380 GHz H_2O emission originates in the anomalous feature, we take the highest combined magnification of the merging images produced by the mock sources (about 330) to infer a minimum intrinsic isotropic line luminosity of 8×10^4 $L_\odot$.

6.3.4. Size and structure of the molecular gas disc

From our lens modelling, we find that the CO (11–10) originates in a molecular gas disc with a size (diameter) of 60 pc around the quasar. From this, we estimate the enclosed dynamical mass ($M_{\rm dyn}$) of the system using

$$M_{\rm dyn} = \frac{RV_{\rm max}^2}{G}, \tag{6.1}$$

where R is the 30 pc radius (60 pc diameter) and $V_{\rm max}$ is the maximum rotational velocity. We assume the rotational velocity is the line velocity at the FWHM ($V_{\rm obs} = 550$ km s^{-1}), corrected with an inclination angle of 45 deg (i.e. $V_{\rm max} = V_{\rm obs}/\sin 45°$). We find a dynamical mass of $M_{\rm dyn}(< 30\ {\rm pc}) \sim 3 \times 10^9\ {\rm M}_\odot$, which is only three times larger than the black hole mass determined by Pooley et al. (2007) from a microlensing analysis of the X-ray emission from the quasar accretion disc. This suggests that the kinematics of the CO (11–10) emission are driven by the properties of the central supermassive black hole.

The resolved velocity structure of the CO (11–10) line, presented in Chapter 5, shows a radially increasing velocity profile and appears to show a very high central velocity dispersion. However, 2-dimensional velocity fields are strongly affected by beam-smearing effects that can lead to an incorrect interpretation of the global dynamical properties (Lelli, Fraternali & Sancisi, 2010). Therefore, we defer a more comprehensive investigation of the disc dynamics to a future work that will use higher resolution imaging of the CO (11–10) line.

Assuming the molecular gas disc also contains water emitting regions with a Keplerian rotation and whose enclosed mass is dominated by the black hole (e.g. Kuo et al. 2011), we use the same formalism as Eq. 6.1 to estimate the minimum size of the disc. Here, we assume the maximum rotational velocity is half the separation of the line peaks identified in Section 6.3, corrected for an assumed disc inclination angle of 45 deg. This implies the size (diameter) of the water emitting disc is around 35 pc, that is, about half the size of the CO (11–10) disc. Further high-resolution imaging of the 380 GHz H_2O emission with ALMA could confirm that the double peak structure is indeed part of a disc, as implied by the position-velocity diagrams shown in Fig. 6.6.

6.4. Discussion and conclusions

We have re-analysed spectral line imaging with ALMA of the rest-frame 380 GHz H_2O emission from MG J0414+0534 ($z = 2.639$), a gravitationally lensed dusty star-forming galaxy that hosts a type 1 quasar. These observations were first presented by Kuo et al. (2019), who reported a tentative detection of the line. Kuo et al. found that the broad line profile made the continuum subtraction challenging, and that the flux density ratio of the line emission in the two merging lensed images was reversed relative to multi-wavelength continuum and CO (11–10) observations for this object.

6.4.1. Origin of the H_2O emission

From a careful re-analysis of these data, we find strong evidence that the 380 GHz H_2O line detection is robust. We independently verified the calibration and imaging (of both the target and the calibrators), and compared the line profile and position-velocity diagram with those from the CO (11–10) and the 22 GHz H_2O megamaser that were previously reported for this object (Chapter 5; Castangia et al. 2011). We find that the line width ($\sim$ 1000 km s^{-1}) and velocity dispersion ($\sim$ 400 km s^{-1}) are almost identical to the CO (11–10) emission, and there are peaks in the line profile (at -210 and $+420$ km s^{-1}) that correspond to the velocities of 22 GHz H_2O megamaser components. Such similarities provide circumstantial evidence that the detection is robust. However, the strongest evidence comes from the position-velocity diagram, where there is evidence of a resolved velocity structure that is consistent with a rotating disc. This disc has an inferred size of around 35 pc, given the mass of the black hole, which is again similar to the resolved CO (11–10) emission. We also find evidence for an additional 380 GHz H_2O component of emission, which, with lens modelling, is estimated to be $\sim$ 600 pc from the quasar. The source of the offset feature is unclear; perhaps corresponding to a jet-cloud interaction or a dense region of star formation. Its location close to the lens caustic suggests it could be very highly magnified by a factor of > 100.

Our findings may imply that the host galaxy of MG J0414+0534 contains a significant number of water emitting regions, and our detection of this particular component is due to a chance lensing configuration. A similar scenario was suggested by Kuo et al. (2019) in their analysis of the same data set, however, they proposed three water-emitting regions separated by a larger distance of around 1.5 kpc that are doubly-imaged. While the model we propose suggests a chance high magnification for the anomalous component, the doubly-imaged regions in the model of Kuo et al. produce much lower magnifications corresponding to higher intrinsic luminosities. Future observations of 380 GHz line emission from dusty star-forming galaxies will determine the rarity of high-luminosity water-emitting regions and test which scenario is more probable.

6.4.2. Structure of the circumnuclear gas disc

We extend the investigation of the 380 GHz H_2O line emission in MG J0414+0534 by combining these data with the information provided by the CO (11–10) spectral line emission and global VLBI imaging of radio jet components to construct a model for the structure of the lensed quasar. Fig. 6.10 shows a toy model of the reconstructed

source emission (approximately to scale). This model consists of a molecular gas disc around the quasar with 22 GHz and 380 GHz H_2O line emission with a size of around 35 pc, with the CO (11–10) gas emission extending to a diameter of 60 pc. Bi-polar compact radio jets extend from the quasar radio core to a distance of about 200 pc, almost perpendicular to the gas disc. The other source of 380 GHz H_2O line emission is offset by ~ 600 pc East of the quasar.

We find tentative evidence for variability in the 380 GHz H_2O disc at the 3σ level on timescales of hours to days. Amplitude fluctuations were previously reported for the 22 GHz H_2O megamaser in long-term monitoring (Castangia et al., 2011), although the 1 month cadence could mask shorter-term variability. A high time variability is inconsistent with our estimate of > 35 pc for the diameter of the 380 GHz H_2O disc and suggests a much more compact region with a size of just a few light days. Such high time variability has been detected from compact maser discs in the local Universe (e.g. Braatz et al. 2003). Monitoring with a short-term cadence, such as with single dish observations, could determine whether the tentative variability is real.

The compact size of the molecular gas disc and the excitation conditions of the CO (11–10) and water lines ($n_{H_2} \sim 10^{6-8}$ cm^{-3}; $E_u \sim 300$–600 K) suggest that we are probing a dense and warm environment close the AGN. Around one third of the dynamical mass enclosed by the CO disc is in the central supermassive black hole, perhaps indicating that we resolve a circumnuclear disc or the outer AGN torus. High densities close to AGN are often associated with maser activity in the local Universe. However, we find no clear evidence that the 380 GHz H_2O line observed here originates from a population of masers: the extremely high integrated luminosity is more consistent with observations of thermally excited H_2O lines from dusty star-forming galaxies (e.g. Jarugula et al. 2019). The 380 GHz H_2O line is predicted to produce both thermal and non-thermal maser emission, and exhibits a sharp transition between these processes with density (Gray et al., 2016). Further investigations of the 380 GHz H_2O line are needed to determine whether it is expected to be associated with thermal emission from dusty star-forming galaxies at high redshift, rather than non-thermal maser emission (or a combination of both).

Circumnuclear discs of dust and molecular gas have been resolved on pc-scales around AGN in the local Universe, which provide insight into the nuclear structure of AGN and the mechanisms of black hole feeding (Gallimore et al., 2016; Imanishi et al., 2018; García-Burillo et al., 2016, 2019; Combes et al., 2019; Impellizzeri et al., 2019). A detection of a compact disc around the quasar of MG J0414+0534 could suggest that the 380 GHz H_2O line is a useful tool to investigate the nuclear structure of AGN at high redshift. However, the low surface brightness of this 380 GHz H_2O line emission and the chance lensing configuration we propose suggest that spatially resolving the source emission may be difficult. On the other hand, we find that the CO (11–10)

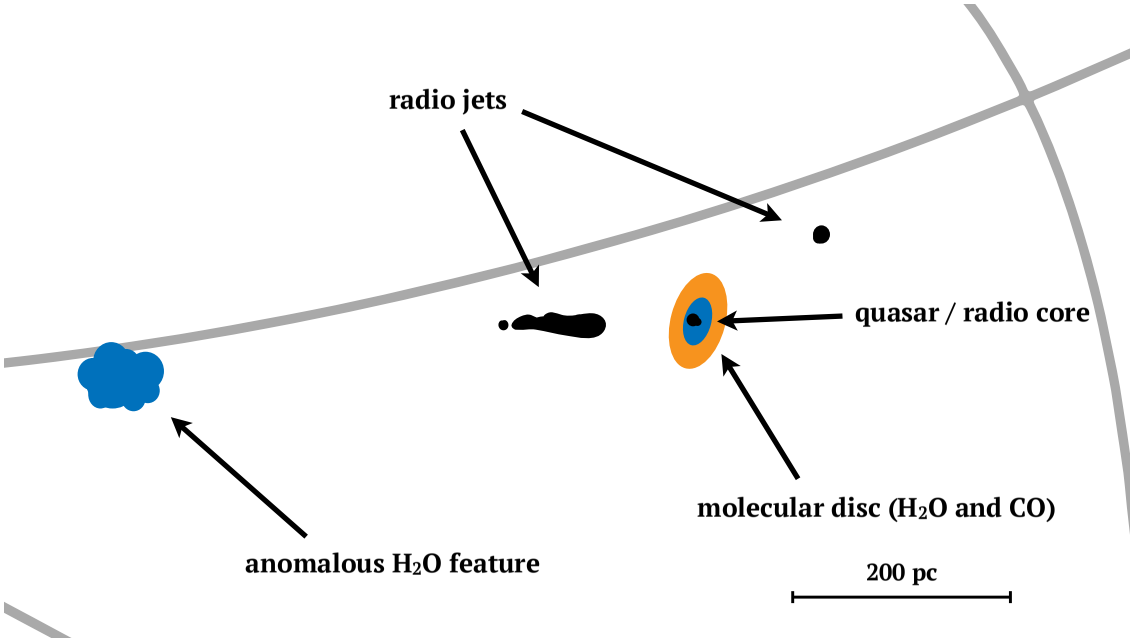

Figure 6.10 | Toy model (approximately to scale) to explain the observed H_2O (blue) and CO (11–10) (orange) line emission, relative to the radio core and jets (black) from MG J0414+0534. This model predicts a molecular gas disc around the AGN with a size of 60 pc, with the 22 and 380 GHz H_2O emission enclosed in a disc of around 35 pc diameter. An additional component of 380 GHz H_2O emission is predicted to form around 600 pc in projection from the quasar, and may be associated with a highly magnified star-forming region that happens to lie close to the lens caustics (grey lines). The radio jets extend out to 200 pc in projection from the radio core, and are not expected to be associated with the highly magnified region of water emission from the system.

emission probes similarly small physical scales and is significantly brighter than the 380 GHz H_2O emission. Observations of CO (11–10) (or even higher excitation CO lines), combining the spatial resolution possible with the long baselines of ALMA and a high gravitational lens magnification, will present a promising approach to spatially resolve molecular tori at high redshift. This could allow detailed studies of supermassive black hole accretion and feedback on 10-pc-scales at the cosmic peak of black hole and galaxy growth.

Acknowledgements

JPM acknowledges support from an NWO-CAS grant (project number 629.001.023).

This chapter makes use of the following ALMA data:
ADS/JAO.ALMA#2017.1.00316.S, ADS/JAO.ALMA#2013.1.01110.S.
ALMA is a partnership of ESO (representing its member states), NSF (USA) and NINS (Japan), together with NRC (Canada), MOST and ASIAA (Taiwan), and KASI (Republic of Korea), in cooperation with the Republic of Chile. The Joint ALMA Observatory is operated by ESO, AUI/NRAO and NAOJ.

The European VLBI Network is a joint facility of independent European, African, Asian, and North American radio astronomy institutes. Scientific results from data presented in this publication are derived from the following EVN project code(s): GW019. The National Radio Astronomy Observatory is a facility of the National Science Foundation operated under cooperative agreement by Associated Universities, Inc.

This research made use of Astropy and Matplotlib packages for Python (The Astropy Collaboration et al., 2018; Hunter, 2007).

Fire in the sky

60 ml whisky
30 ml lemon juice
15 ml ginger syrup
15 ml simple syrup
15 ml port

Shake the whisky, lemon and syrup with ice. Strain into an old-fashioned glass over fresh ice. Gently pour in the port over the back of a spoon so it floats on top.

7

Conclusions and future prospects

This thesis investigates the host galaxies of quasars in at redshift 1 to 4 by exploiting the magnifying effect of gravitational lensing in order to address open questions about the formation and evolution of galaxies. In this chapter, we summarise our main results and consider avenues of future work.

7.1. Surveying quasar hosts during the epoch of galaxy formation

Determining the level of star formation in quasar hosts is a key aspect of understanding the co-evolution of cosmic star formation and black hole accretion history, and their respective roles in the evolutionary sequence of massive galaxies. In Chapter 2 we have shown that surveys of lensed quasar systems at low resolution can efficiently probe emission from obscured star formation in the host galaxies of quasars at high redshifts. With these surveys, we were able to characterise the global properties of quasar hosts in a lower luminosity range than accessible with field sources. Our survey of 104 lensed quasars was the largest such sample ever studied. We found that at least 66 percent of quasar host galaxies have high levels of dust-obscured star formation ongoing in their host galaxies, with a median and distribution of 120^{+120}_{-80} $M_\odot$ yr^{-1}. Their overall far-infrared properties are similar to coeval dusty star-forming galaxies, and consistent with general expectations from hydro-dynamical and semi-analytic models. We find that the radio-quiet sub-sample of lensed quasars is broadly consistent

with the radio–infrared correlation for star-forming galaxies, but this is strongly limited by the lack of radio detections.

In Chapter 3, we investigated the low-frequency properties of three objects from the parent sample presented in Chapter 2 that fell within the field of the LOFAR Two-metre Sky Survey (LoTSS) first data release. This was the first study of gravitational lenses at very low radio frequencies. The radio detections enabled us to compare the radio emission for this sample to their far-infrared emission and add further evidence that star formation (at rates of 20 to 300 $M_\odot$ yr^{-1}) is the primary source of their radio emission, rather than emission from the AGN. While none of the sources were detected in the FIRST survey, all three of these systems were detected in LoTSS: due to the rising flux density towards lower frequencies (negative spectral slope) of optically thin synchrotron emission, LoTSS can detect emission 5 to 10 times below the detection limit of FIRST with equivalent resolution and sensitivity. We estimate that at least most of the parent sample will be detected in the full survey, which will enable the analysis of radio-quiet quasars with the radio–infrared correlation to be extended to lower luminosities.

The results of the survey reported in Chapter 2 have been useful to identify lens systems to investigate at sub-mm wavelengths with ALMA, which motivated the research of subsequent chapters and has helped guide the direction of future research. Chapters 4, 5 and 6 presented detailed investigations of individual quasars systems from the parent sample using ALMA observations. Both investigations of quasar host galaxies and the lens mass distributions will be expanded with ongoing ALMA programmes of systems selected from the sample in Chapter 2 and of newly discovered quasar lens systems. This consists of deep, high-resolution observations of objects from the pilot sample introduced in Chapter 2 and short observations ('snapshots') of newly-discovered lens systems whose dust emission at far-infrared/sub-mm/mm wavelengths and molecular gas properties are currently uncharacterised. We detect dust emission from 15 out of 18 of these systems in our observations (see Fig. 7.1) which also cover the rest-frequency of a high-excitation CO line. The initial results of the snapshot survey demonstrate that these short observations are effective at characterising the sub-mm dust emission.

Studies of gravitationally lensed galaxies, including those in this thesis, are strongly limited by small-sample statistics. However, by applying automated lens-finding algorithms (Metcalf et al., 2019), future large-scale surveys with Euclid (Laureijs et al., 2011) and the Large Synoptic Survey Telescope (LSST Science Collaboration et al., 2009) are expected to increase the number of known galaxy-scale gravitational lens systems from hundreds to around 100 000 (Serjeant, 2012; Collett, 2015). These forthcoming large samples will enable homogeneously selected samples of lensed galaxies that can be efficiently characterised with targeted far-infrared/sub-mm surveys (such as

with ALMA or the Atacama Compact Array) and radio surveys (such as with LOFAR or the Square Kilometre Array). With follow-up at high-resolution, these new lens systems can test models of galaxy formation (Section 7.2) and the nature of dark matter (Section 7.3).

7.2. Galaxy evolution, from formation to quiescence

7.2.1. Spheroid formation

The commonly accepted framework of galaxy evolution is that dusty star-forming galaxies are progenitors of local massive elliptical galaxies (Hopkins et al., 2008). Models propose that the formation of a compact spheroid follows from dynamical instabilities in a gas disc, which causes gas to be funnelled into a small region to generate a compact starburst. These dynamical instabilities may occur secularly within an unstable disc of star formation, or they may be induced by mergers or tidal interactions (Zolotov et al., 2015). Tests of the star formation history of quiescent galaxies finds that the compact starburst is rapidly quenched and remains suppressed, which may occur as a result of increasing dynamical stability, stellar feedback, AGN feedback, virial shock-heating or some combination of these phenomena. The mechanisms that drive the evolutionary process from formation of the star-forming disc to quiescent spheroid, are not well understood or observationally tested because it is practically difficult to achieve the resolution required to study these systems.

In Chapter 4 we have shown that gravitational lens modelling of high-resolution observations of gravitationally lensed galaxies can access the physical scales needed to probe morphology and gas kinematics during the epoch of galaxy assembly. We investigated six strongly lensed quasar systems from the parent sample introduced in Chapter 2. With the aid of visibility-plane lens modelling, we were able to resolve the dust and molecular gas in quasar host galaxies at $z \sim 2$ with an equivalent resolution 100 to 300 pc (around 1 to 3 kpc without lensing). The effective resolution of 100 pc we were able to achieve for some objects is more than a factor of 2 smaller than the resolution capability of ALMA with its longest baselines*, and can therefore only be achieved for gravitationally lensed sources: even then, we find that some objects are still only marginally resolved. Our investigation revealed that quasar host galaxies are more compact than coeval sub-mm-selected dusty star-forming galaxies: this suggests

*100 pc at $z \sim 2$ equates to 10–15 mas. If observations with the longest baselines of ALMA become feasible in bands 9 and 10, this resolution is possible, but will suffer from poor sensitivity.

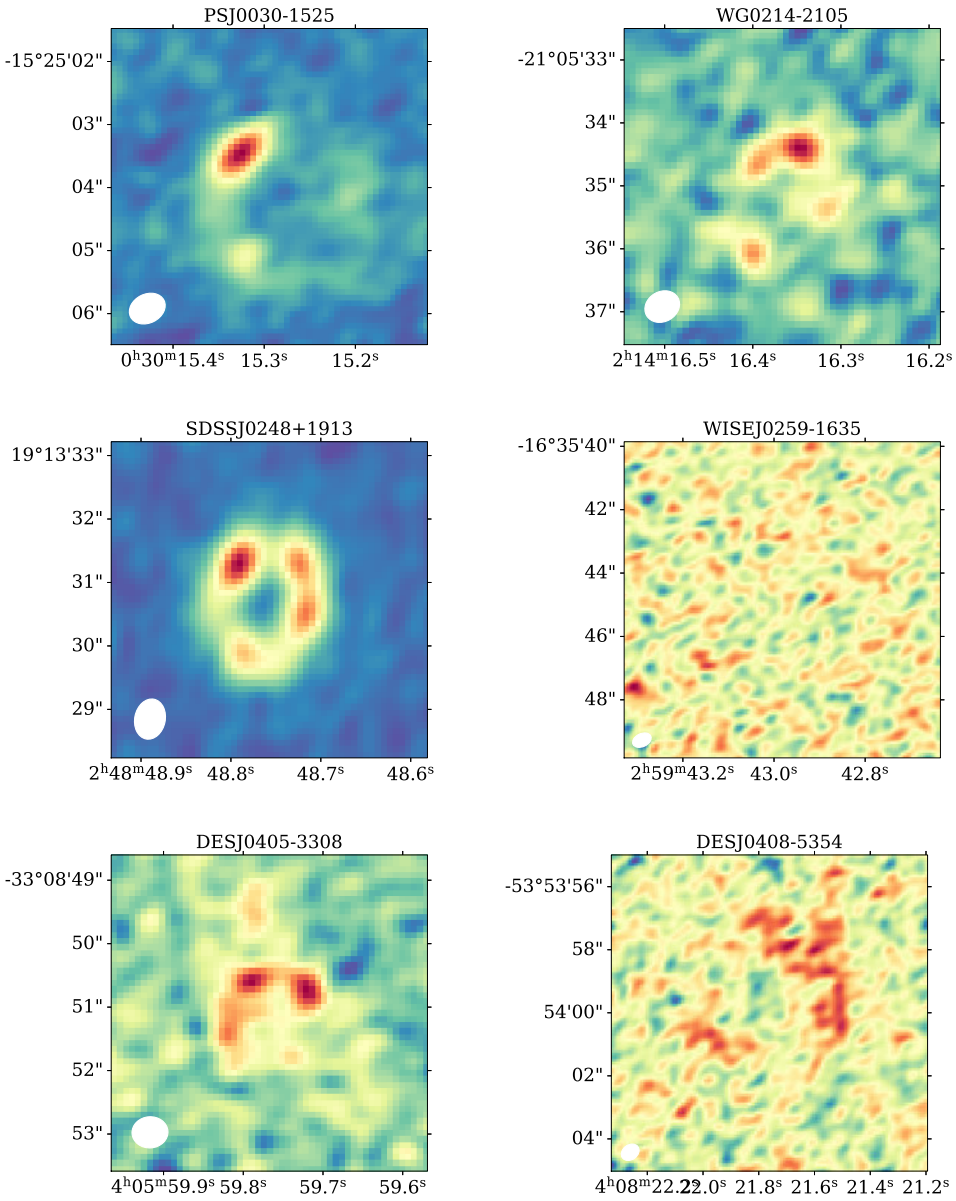

Figure 7.1 | ALMA 'snapshot' survey of new gravitational lens systems at around 0.5 arcsec resolution and 50 μJy rms noise level. We find a variety of sub-mm properties: some systems are strongly detected, whilst others are not detected at all.

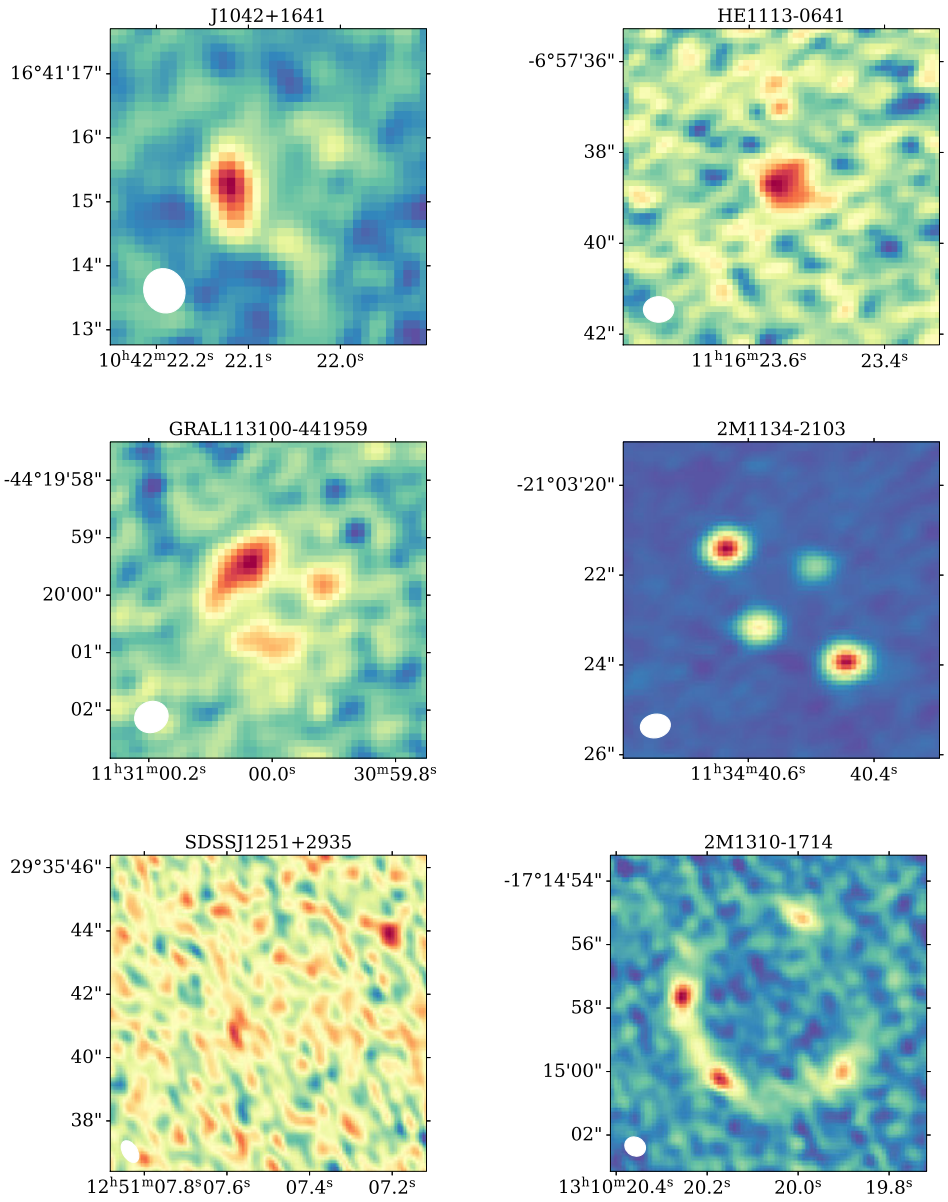

Figure 7.1 | (continued)

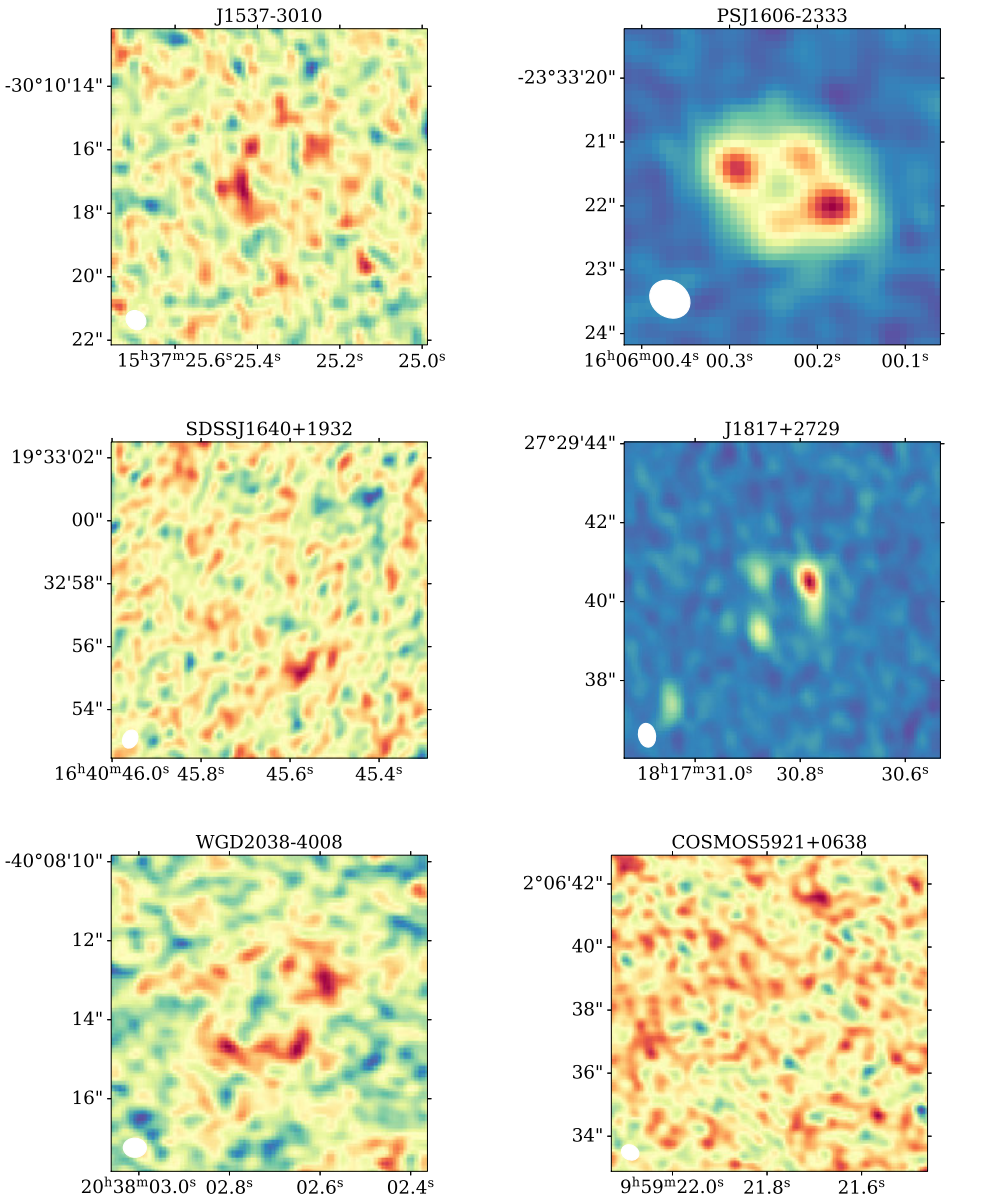

Figure 7.1 | (continued)

that the high dust temperatures we found for quasar hosts in Chapter 2 are not due to a significant AGN contribution, but because the star formation is concentrated within a smaller volume for the quasar hosts. We find that some quasar hosts are similar in size and morphology to dusty star-forming galaxies (effective diameter 3–6 kpc), with evidence of non-axisymmetric structures that are indicative of unstable discs, while some are extremely compact (effective diameter of 0.5–2 kpc) with star formation rates that are Eddington-limited. The similarity between the latter group and higher-redshift ($z > 4$) dusty star-forming galaxies may be due to the different biases between sub-mm-selected systems and optically-selected quasar hosts. The size and morphology of the quasar hosts are consistent with galaxies observed during stages of evolution into compact spheroids, where a high density of dynamically unstable gas leads to efficient star formation and black hole accretion.

An illustration of the evolutionary sequence we propose is shown in Fig. 7.2. There are still outstanding questions, including the origin of dynamical instabilities and gas infall, when and how AGN are triggered, and the mechanism by which compact galaxies quench and maintain a quenched state. Chapter 4 shows that investigations of the morphology of dust alone can give insights into galaxy dynamics: alone, the detection of non-axisymmetric features and extreme star formation rates show that the molecular gas must be globally unstable to gravitational collapse. This investigation was restrained by the small sample size, but forthcoming observations will test our proposed model with at least 10 more lens systems. Fig. 7.3 shows newly obtained high-resolution ALMA observations of lensed quasar system WFI J2026−4536: we detect bright, compact dust and CO (10–9) emission from this system, which is similar to the lens systems we study in Chapter 4.

Future work will also require investigation of the cold gas reservoir of both quasar hosts and dusty star-forming galaxies. Future or archival observations of cold gas diagnostics, such as CO (1–0) or CO (3–2), with sufficient resolution for the lens modelling analysis, will be an important line of investigation to determine the dynamical properties of the gas, the size of the gas reservoir, and the gas depletion timescales. In particular, the self-quenching of compact galaxies predicts an inside-out evolution in which gas in the inner region of the galaxy is consumed more rapidly than the outskirts: the resolutions we achieve with an analysis of lensed systems will allow the gas depletion time to be mapped as a function of radius (e.g. Spilker et al. 2019).

The analysis in Chapter 4 was limited to a crude 2D investigation of the gas kinematics, however more sophisticated methods allow the dynamics of high-redshift galaxies to be accurately constrained. Rizzo et al. (2018) introduced a new approach to simultaneously model lensed systems and galaxy kinematics, which both improves the fidelity of the reconstructed source and recovers the source kinematics using a 3D approach to minimise the beam-smearing bias that results from limited angular resolu-

tion. Resolution-matched observations of cold gas diagnostics, in combination with the kinematic-lensing technique, will allow for a joint investigation of the dynamics of dusty star-forming galaxies and quasar hosts. If the conclusions of Chapter 4 are correct, we should expect to see a global evolution of massive galaxies from quasi-stable discs, to compact systems in the process of quenching.

7.2.2. AGN feedback – or not?

In Chapter 4 we predicted that the maximum starbursts in our study will consume their cold gas supply within 20 Myr. The rapid gas consumption and increasing dynamic stability of the gas disc will make star formation inefficient, effectively quenching them. This suggests that AGN feedback is not a necessary component in the growth and morphological change of massive galaxies, apparently in conflict with predictions from cosmological simulations that find that stellar feedback alone is not sufficient to suppress the level of star formation in massive galaxies. At present, simulations have only a phenomenological implementation of AGN feedback due to computational limitations: it is therefore essential to observationally test their predictions of feedback and quenching.

For one system in Chapter 4, we found possible evidence of a galaxy-scale bipolar outflow of molecular gas. While we cannot determine its origin, our estimates suggest that the star formation is sufficiently energetic to drive an outflow of this degree. While the mass outflow rate implies that it will quench the host galaxy within 1–3 Myr, the velocity of this outflow is not sufficient to escape the galaxy so it will fall back into the galaxy to fuel further star formation. Such massive outflows of molecular gas have hitherto rarely been detected at high redshift. Evidence of a molecular outflow was only possible to detect with the resolution we achieved with gravitational lensing magnification and sub-mm interferometry: as the velocity of the outflow is low, it would likely not be distinguished in an analysis of the line profile. Therefore, future investigations of lensed quasar systems which can resolve cold molecular gas tracers on 100-pc-scales will determine whether these large-scale, low-velocity outflows are prevalent. If these outflows are too energetic to be driven by stellar feedback, this could be a strong indication that radiative feedback plays an important role in the rapid formation of quiescent galaxies at high redshift.

AGN feedback may not only occur in the form of outflows, but from radiative heating of the surrounding ISM. Quasars represent the most rapidly accreting AGN and produce strong X-ray emission. Chapter 4 and 6 investigated high-excitation transitions of CO, which probe the warm interstellar medium. While the low- and mid-excitations probe energy injection from stars, radiative transfer models of the

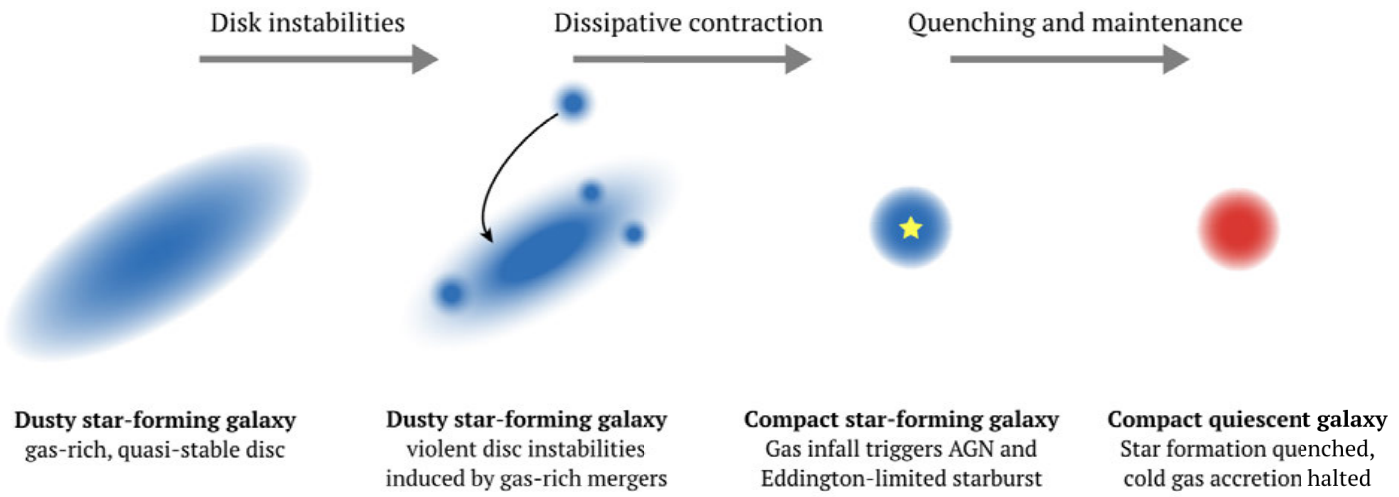

Figure 7.2 | A path to the formation of a compact quiescent galaxy, based on our investigation in Chapter 4. The mechanisms that lead to morphological change (mergers, or secular accretion and instabilities) and quenching of star formation (AGN feedback, stellar feedback and morphological quenching) are currently subject to debate.

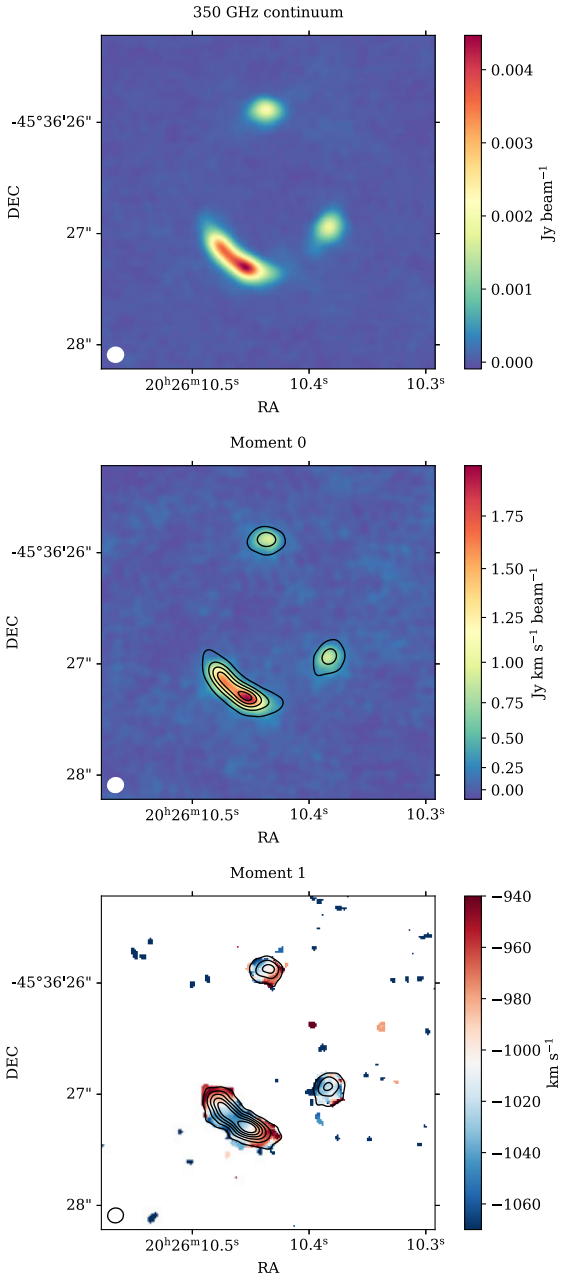

Figure 7.3 | Newly obtained ALMA imaging of gravitational lens system WFI J2026−4536 ($z = 2.23$) at about 0.15 arcsec resolution. *Top*: thermal dust emission at rest-frame (observed-frame) frequency 1.1 THz (350 GHz). *Middle*: velocity-integrated intensity of CO (10–9) emission. *Bottom*: CO (10–9) velocity field.

spectral line energy distribution of quasar hosts find that these transitions are likely enhanced by the AGN (Meijerink et al., 2007; Vallini et al., 2019). The small size of the quasar host galaxies may allow the X-ray radiation field of AGN to penetrate the entire gas disc and influence its conversion into stars. Due to the high frequency of these CO line transitions, these lines are only observable at sub-arcsecond resolution for objects in the distant Universe, where the lines are redshifted to lower frequencies in which they can be observed with ALMA. This can allow the warm molecular gas around quasars to be resolved with the aid of gravitational lensing.

In Chapter 6 we resolve highly excited CO emission originating in a compact disc of molecular gas around the radio-loud quasar MG J0414+0534. The 60 pc size of the disc suggests it falls within the black hole sphere of influence, at the outer torus of the AGN. The molecular gas in this region directly fuels the supermassive black hole and a compact nuclear starburst. Therefore, an investigation of the structure and dynamics of the gas can help understand one of the fundamental questions of galaxy evolution: how do supermassive black holes grow? In particular, why do galaxies and their central black holes grow so rapidly at high redshift? With the long-baseline capabilities of ALMA, combined with high lensing magnification, this disc has been imaged with an equivalent source-plane resolution of 10–20 pc (see Fig 7.4). The wealth of multi-frequency data for this system (including radio global-VLBI imaging of radio jets, optical *Hubble Space Telescope* imaging of the quasar and unobscured star formation, and an ongoing campaign with ALMA to resolve the physical conditions of the molecular ISM) combined with new developments in lens modelling techniques, will enable the most detailed investigation of a quasar system at high redshift. This study will provide new insights into feedback, supermassive black hole growth and star formation during the formation of a massive galaxy, with spatial resolution comparable to studies in the local Universe (e.g. Combes et al. 2019).

7.3. Testing models of dark matter

In the past few decades it has emerged that dark matter is a fundamental component to how galaxies form: cosmological simulations predict that galaxies form inside haloes of dark matter and grow hierarchically, through a series of mergers. The specifics of how galaxies form and evolve depend on the properties of the dark matter particle. The cold dark matter (CDM) model proposes that dark matter consists of massive, weakly interacting particles that have not yet been discovered in ground-based experiments. This model is successful in reproducing the large-scale structure of the Universe and has become the paradigm of cosmological structure formation. Simulations of CDM

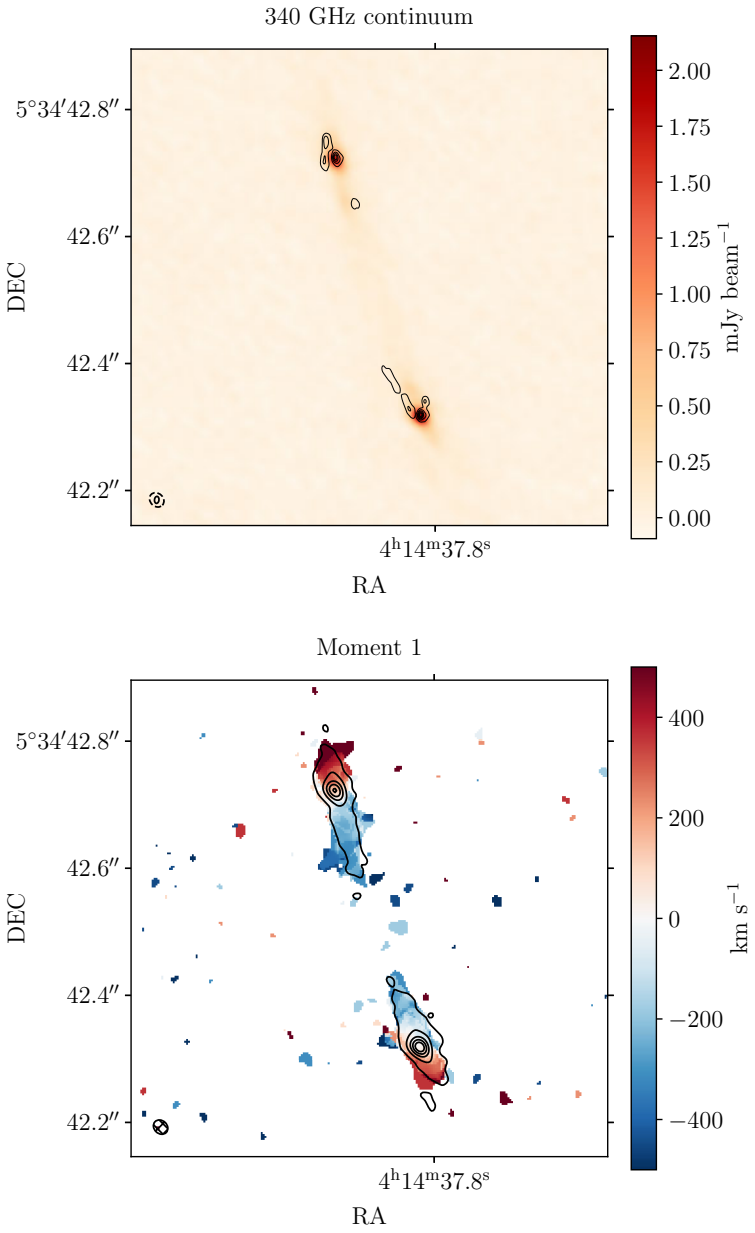

Figure 7.4 | The merging images of lens system MG J0414+0534 imaged with ALMA at 25 to 35 mas resolution. Top: the 340 GHz continuum overlaid with contours of 1.6 GHz global VLBI imaging. Bottom: the CO (11–10) velocity field overlaid with contours of the line intensity. The synthesised beam is shown in the lower-left corner.

find that a large number of small haloes of masses $< 10^{10}$ $M_\odot$ should survive the merger process, remaining around massive galaxies and in the field. Alternative models of dark matter (i.e. warm dark matter; WDM) propose a dark matter particle of lower mass, which results in the formation of fewer low-mass haloes. Therefore it is possible to constrain the mass of the dark matter particle by measuring the abundance of low-mass haloes. However, as these haloes may be devoid of stars or gas, they may be difficult or impossible to observe directly, making it difficult to discriminate between WDM and CDM. In the absence of an electromagnetic signature, the only way to detect low-mass haloes is through their gravitational influence. Strong lensing is a tool to investigate the abundance of low-mass haloes, either through the prevalence of flux ratio anomalies (e.g. Dalal & Kochanek 2002; Xu et al. 2015; Hsueh et al. 2019; Gilman et al. 2019a) or by detecting their effect on extended arcs or rings (e.g. Koopmans 2005; Vegetti & Koopmans 2009; Hezaveh et al. 2016b,a; Chatterjee & Koopmans 2018).

One of the major limitations in flux ratio analysis has been the small number of lens systems available for study. Observations at radio or mid-infrared wavelengths (e.g. Jackson et al. 2015; Minezaki et al. 2009), or of narrow-line emission (Nierenberg et al., 2019), have been used to measure flux ratios, but these can be difficult to obtain due to technical limitations or the properties of the lensed source. In Chapter 5, we proposed a new approach to increase to the number of lens systems for flux ratio analysis with observations at sub-mm wavelengths. MG J0414+0534 is a lens system that has long been established to have an anomalous flux ratio between its merging images. The flux ratio we measured in CO (11–10) is consistent with measurements from imaging of the compact radio synchrotron emission and mid-infrared torus emission. The CO line emission for MG J0414+0534 is luminous enough to achieve high enough significance for flux ratio analysis studies and therefore can provide a viable method to attain a statistically significant sample of flux ratio measurements to improve the constraints on dark matter models.

Chapter 4 showed that high-excitation CO lines can be detected with short observations of lensed quasar systems with ALMA, and could provide a sample for flux ratio analysis. However, we also found that the thermal dust emission is compact and usually detected at higher significance than the spectral line emission, which presents a more statistically useful measurement for flux ratio analysis. Fig. 7.5 shows the flux ratios measured in sub-mm emission, relative to predictions from the smooth lens modelling, for five fold-configuration lens systems investigated in this thesis. In some cases, the flux ratios measured in the sub-mm imaging are inconsistent with model predictions. The fact that flux ratio anomalies are observed at all may be somewhat surprising, as the extended source structure should wash out the effect of low-mass haloes. The source of the flux ratio anomalies (or rather, surface brightness anomalies), whether due to the effect of low-mass haloes or large-scale galactic substructure, will

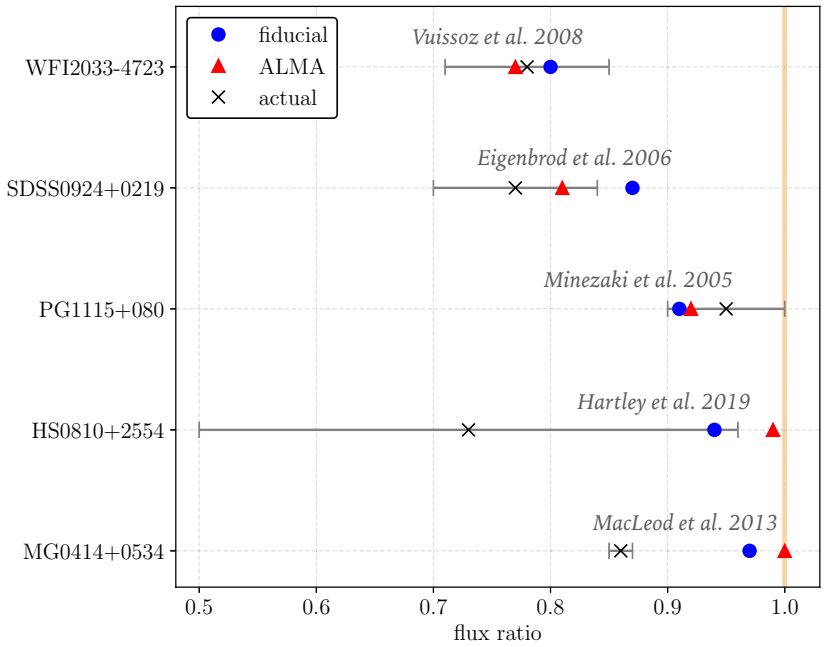

Figure 7.5 | Comparison of the predicted and observed flux ratios for the merging images of five fold-configuration lens systems in this thesis. We show the flux ratios predicted by the best lens model for the ALMA data (red triangles) and by previous studies in the literature (blue circles, shown with their respective reference). The observed flux ratios and uncertainties in the ALMA imaging are shown with black crosses. In some cases the model-predicted flux ratios are different from previous studies, and different from the observed flux ratios.

be a focus of future work.

As sub-mm observations often show arcs or rings of lensed emission, they provide many more constraints on the lens mass distribution. In Fig. 7.5 we show that this can result in different lens models and flux ratio predictions, relative to models based on optical, mid-infrared or radio imaging. With the additional constraints from extended source emission, we can also test the effect of small-scale mass perturbations using a gravitational imaging approach.

Fig. 7.6 shows a test of the gravitational imaging technique, adapted for visibility-plane data, on one of the data sets investigated in Chapter 4 of this thesis. The convergence (surface mass density) correction shows a feature that could be a low-mass halo (e.g. Vegetti et al. 2012), or part of a multi-pole feature caused by the effect of a galactic disc (e.g. Hsueh et al. 2018). Under the assumption of a low-mass halo,

the inclusion of an analytic halo profile in the lens model does not meet the level of statistical significance required for detection (as discussed in Ritondale et al. 2019). Regardless of whether or not this represents a true low-mass halo, the non-smoothness of galaxies is an important systematic to test. There are already hints from gravitational imaging investigations at optical wavelengths that the large-scale mass distribution of galaxies are complex (Ritondale et al., 2019). As sensitivity to the lensing signal of low-mass structures depends on the resolution of the data, its signal-to-noise ratio, and the complexity of the source surface brightness, the high angular resolution of ALMA in the long-baseline configurations (as in Fig. 7.4) can potentially allow us to detect low-mass haloes in the range $\sim 10^7$ $M_\odot$ (Asadi et al., 2017). This is a mass range that is currently probed with flux ratio analysis, where the expected number of halo detections differs significantly between WDM and CDM (e.g. Gilman et al. 2019a). As gravitational imaging does not assume the nature of the mass perturbation, we can take a synergistic approach between gravitational imaging and flux ratio analysis to test to what extent flux ratio anomalies reflect the effect of low-mass haloes, as opposed to galactic substructure. This investigation will be of vital importance to the interpretation of flux ratio anomalies, particularly in view of ongoing surveys that will find many new lensed quasars (e.g. Agnello & Spiniello 2019) and the expectation that only ~ 50 lens systems would be required to confirm a WDM scenario (Gilman et al., 2019b).

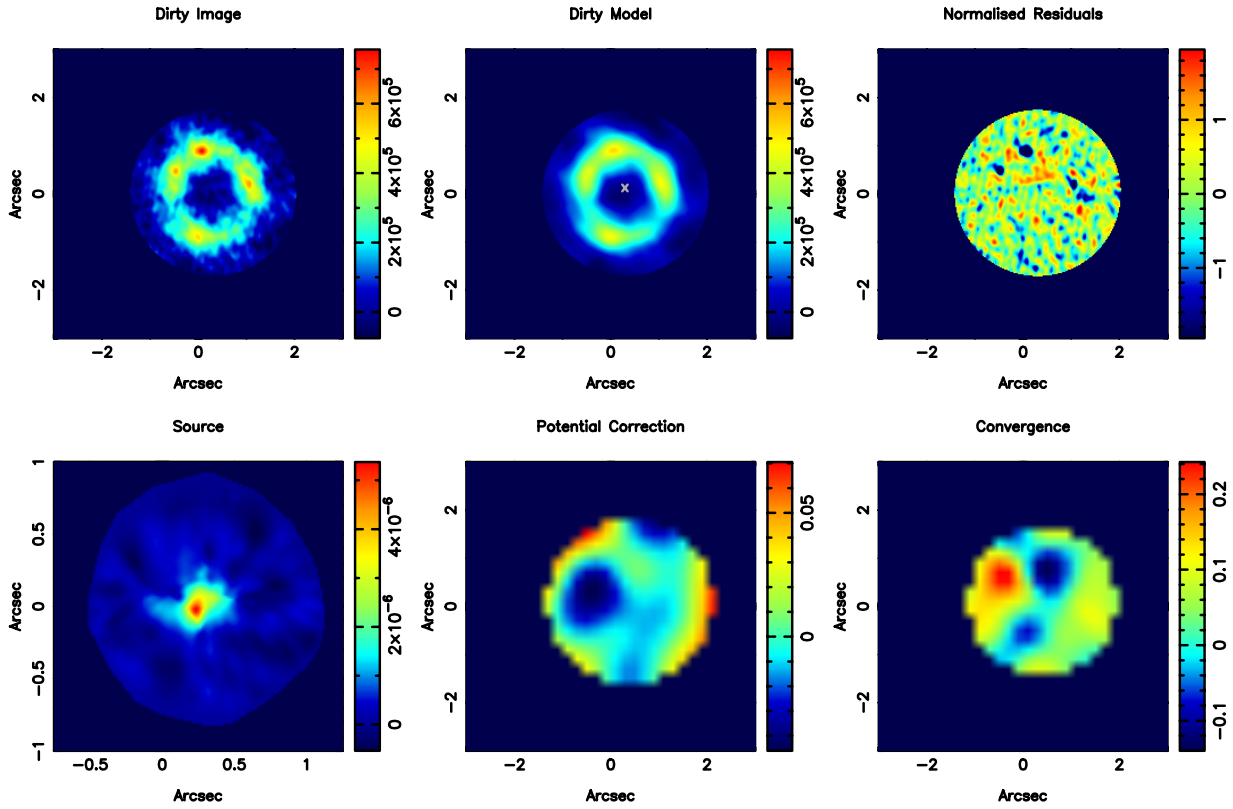

Figure 7.6 | Investigating low-mass structure of the lens system SDSS J0924+0219 with a visibility-plane analysis of ALMA data. Top row: dirty image of the data, dirty image of the model data and image of the residuals (model−data); bottom row: the reconstructed source, pixellated corrections to the lens potential and correction to the convergence. The convergence corrections show a localised feature that could be a low-mass halo, but this does not represent a statistically significant detection given the quality of the data.

Bibliography

ALMA Partnership et al., 2015, ApJ, 808, L4
Agnello A., Spiniello C., 2019, MNRAS, 489, 2525
Agnello A., et al., 2017, MNRAS, 472, 4038
Agudo I., Thum C., Wiesemeyer H., Krichbaum T. P., 2010, ApJS, 189, 1
Agudo I., Thum C., Gómez J. L., Wiesemeyer H., 2014, A&A, 566, A59
Alatalo K., et al., 2011, ApJ, 735, 88
Alatalo K., et al., 2015, ApJ, 798, 31
Alexander D. M., Hickox R. C., 2012, New A Rev., 56, 93
Alexandroff R. M., Zakamska N. L., van Velzen S., Greene J. E., Strauss M. A., 2016, MNRAS, 463, 3056
Alloin D., Guilloteau S., Barvainis R., Antonucci R., Tacconi L., 1997, A&A, 321, 24
Alloin D., Kneib J.-P., Guilloteau S., Bremer M., 2007, A&A, 470, 53
Andreani P., Franceschini A., Granato G., 1999, MNRAS, 306, 161
Andrews B. H., Thompson T. A., 2011, ApJ, 727, 97
Asadi S., Zackrisson E., Freeland E., 2017, MNRAS, 472, 129
Audibert A., et al., 2019, A&A, 632, A33
Auger M. W., Treu T., Bolton A. S., Gavazzi R., Koopmans L. V. E., Marshall P. J., Moustakas L. A., Burles S., 2010, ApJ, 724, 511
Augusto P., et al., 2001, MNRAS, 326, 1007
Azadi M., et al., 2015, ApJ, 806, 187
Baade W., Minkowski R., 1954, ApJ, 119, 206
Baldi R. D., et al., 2018, MNRAS, 476, 3478
Banerji M., Carilli C. L., Jones G., Wagg J., McMahon R. G., Hewett P. C., Alaghband-Zadeh S., Feruglio C., 2017, MNRAS, 465, 4390
Barcos-Muñoz L., et al., 2017, ApJ, 843, 117
Barro G., et al., 2013, ApJ, 765, 104
Barro G., et al., 2014, ApJ, 791, 52
Barro G., et al., 2016, ApJ, 827, L32
Barro G., et al., 2017, ApJ, 851, L40
Barthel P. D., 2006, A&A, 458, 107
Barvainis R., Antonucci R., 2005, ApJ, 628, L89
Barvainis R., Ivison R., 2002, ApJ, 571, 712

Barvainis R., Antonucci R., Coleman P., 1992, ApJ, 399, L19
Barvainis R., Antonucci R., Hurt T., Coleman P., Reuter H.-P., 1995, ApJ, 451, L9
Barvainis R., Antonucci R., Alloin D., Guilloteau S., 1997, in American Astronomical Society Meeting Abstracts. p. 103.02
Barvainis R., Alloin D., Bremer M., 2002, A&A, 385, 399
Becker R. H., White R. L., Edwards A. L., 1991, ApJS, 75, 1
Becker R. H., White R. L., Helfand D. J., 1995, ApJ, 450, 559
Beelen A., Cox P., Benford D. J., Dowell C. D., Kovács A., Bertoldi F., Omont A., Carilli C. L., 2006, ApJ, 642, 694
Bendo G. J., et al., 2013, MNRAS, 433, 3062
Benford D. J., Cox P., Omont A., Phillips T. G., McMahon R. G., 1999, ApJ, 518, L65
Bennert N., Barvainis R., Henkel C., Antonucci R., 2009, ApJ, 695, 276
Bennett C. L., Lawrence C. R., Burke B. F., Hewitt J. N., Mahoney J., 1986, ApJS, 61, 1
Bicknell G. V., Sutherland R. S., van Breugel W. J. M., Dopita M. A., Dey A., Miley G. K., 2000, ApJ, 540, 678
Biggs A. D., et al., 2003, MNRAS, 338, 1084
Blain A. W., Smail I., Ivison R. J., Kneib J. P., Frayer D. T., 2002, Phys. Rep., 369, 111
Bonzini M., Padovani P., Mainieri V., Kellermann K. I., Miller N., Rosati P., Tozzi P., Vattakunnel S., 2013, MNRAS, 436, 3759
Bonzini M., et al., 2015, MNRAS, 453, 1079
Bower R. G., Benson A. J., Malbon R., Helly J. C., Frenk C. S., Baugh C. M., Cole S., Lacey C. G., 2006, MNRAS, 370, 645
Braatz J. A., Wilson A. S., Henkel C., Gough R., Sinclair M., 2003, ApJS, 146, 249
Bradford C. M., et al., 2009, ApJ, 705, 112
Bragg A. E., Greenhill L. J., Moran J. M., Henkel C., 2000, ApJ, 535, 73
Brown R. L., Wild W., Cunningham C., 2004, Advances in Space Research, 34, 555
Browne I. W. A., et al., 2003, MNRAS, 341, 13
Burud I., et al., 1998, The Messenger, 92, 29
Burud I., et al., 2002, A&A, 391, 481
Bussmann R. S., et al., 2013, ApJ, 779, 25
Bussmann R. S., et al., 2015, ApJ, 812, 43
Cañameras R., et al., 2017, A&A, 604, A117
Calistro Rivera G., Lusso E., Hennawi J. F., Hogg D. W., 2016, ApJ, 833, 98
Calistro Rivera G., et al., 2017, MNRAS, 469, 3468
Carilli C. L., Bertoldi F., Omont A., Cox P., McMahon R. G., Isaak K. G., 2001, AJ, 122, 1679
Carilli C. L., Lewis G. F., Djorgovski S. G., Mahabal A., Cox P., Bertoldi F., Omont A., 2003, Science, 300, 773
Carilli C. L., et al., 2005, ApJ, 618, 586

Carollo C. M., et al., 2013, ApJ, 773, 112
Casey C. M., Narayanan D., Cooray A., 2014, Phys. Rep., 541, 45
Castangia P., et al., 2011, A&A, 529, A150
Cernicharo J., Pardo J. R., Weiss A., 2006, ApJ, 646, L49
Chapin E. L., et al., 2011, MNRAS, 411, 505
Chapman S. C., Scott D., Lewisi G. F., Borys C., Fahlman G. G., 1999, A&A, 352, 406
Chartas G., Cappi M., Hamann F., Eracleous M., Strickland S., Giustini M., Misawa T., 2016, ApJ, 824, 53
Chatterjee S., Koopmans L. V. E., 2018, MNRAS, 474, 1762
Chavushyan V. H., Vlasyuk V. V., Stepanian J. A., Erastova L. K., 1997, A&A, 318, L67
Chen G. C. F., et al., 2019, arXiv e-prints, p. arXiv:1907.02533
Collett T. E., 2015, ApJ, 811, 20
Combes F., et al., 2013, A&A, 558, A124
Combes F., et al., 2019, A&A, 623, A79
Condon J. J., Condon M. A., Broderick J. J., Davis M. M., 1983, AJ, 88, 20
Condon J. J., Anderson M. L., Helou G., 1991, ApJ, 376, 95
Condon J. J., Cotton W. D., Greisen E. W., Yin Q. F., Perley R. A., Taylor G. B., Broderick J. J., 1998, AJ, 115, 1693
Condon J. J., Kellermann K. I., Kimball A. E., Ivezić Ž., Perley R. A., 2013, ApJ, 768, 37
Congdon A. B., Keeton C., 2018, Principles of Gravitational Lensing: Light Deflection as a Probe of Astrophysics and Cosmology
Coppin K., Halpern M., Scott D., Borys C., Chapman S., 2005, MNRAS, 357, 1022
Coppin K. E. K., et al., 2008, MNRAS, 389, 45
Cox P., et al., 2002, A&A, 387, 406
Croton D. J., et al., 2006, MNRAS, 365, 11
Dalal N., Kochanek C. S., 2002, ApJ, 572, 25
Dale D. A., Helou G., Contursi A., Silbermann N. A., Kolhatkar S., 2001, ApJ, 549, 215
Damjanov I., et al., 2011, ApJ, 739, L44
Davé R., Finlator K., Oppenheimer B. D., Fardal M., Katz N., Kereš D., Weinberg D. H., 2010, MNRAS, 404, 1355
Davies M. L., et al., 2009, MNRAS, 400, 984
Deane R. P., Rawlings S., Garrett M. A., Heywood I., Jarvis M. J., Klöckner H.-R., Marshall P. J., McKean J. P., 2013, MNRAS, 434, 3322
Dekel A., Birnboim Y., 2006, MNRAS, 368, 2
Dekel A., et al., 2009, Nature, 457, 451
Delhaize J., et al., 2017, A&A, 602, A4
Delvecchio I., et al., 2017, A&A, 602, A3
Di Matteo T., Springel V., Hernquist L., 2005, Nature, 433, 604
Diamond-Stanic A. M., Moustakas J., Tremonti C. A., Coil A. L., Hickox R. C., Robaina

A. R., Rudnick G. H., Sell P. H., 2012, ApJ, 755, L26
Downes D., Neri R., Wiklind T., Wilner D. J., Shaver P. A., 1999, ApJ, 513, L1
Dunne L., Eales S. A., 2001, MNRAS, 327, 697
Dunne L., Eales S., Edmunds M., Ivison R., Alexander P., Clements D. L., 2000, MNRAS, 315, 115
Dutton A. A., et al., 2013, MNRAS, 428, 3183
Dye S., Warren S. J., 2005, ApJ, 623, 31
Dye S., et al., 2018a, MNRAS, 476, 4383
Dye S., et al., 2018b, MNRAS, 476, 4383
Eigenbrod A., Courbin F., Dye S., Meylan G., Sluse D., Vuissoz C., Magain P., 2006, A&A, 451, 747
Einstein A., 1916, Annalen der Physik, 354, 769
Ellingsen S. P., Voronkov M. A., Breen S. L., Lovell J. E. J., 2012, ApJ, 747, L7
Engel H., et al., 2010, ApJ, 724, 233
Fabian A. C., 2012, ARA&A, 50, 455
Falco E. E., Lehar J., Perley R. A., Wambsganss J., Gorenstein M. V., 1996, AJ, 112, 897
Falco E. E., Lehar J., Shapiro I. I., 1997, AJ, 113, 540
Falgarone E., et al., 2017, Nature, 548, 430
Fan L., Lapi A., De Zotti G., Danese L., 2008, ApJ, 689, L101
Fassnacht C. D., Xanthopoulos E., Koopmans L. V. E., Rusin D., 2002, ApJ, 581, 823
Faure C., Courbin F., Kneib J. P., Alloin D., Bolzonella M., Burud I., 2002, A&A, 386, 69
Ferkinhoff C., Brisbin D., Nikola T., Stacey G. J., Sheth K., Hailey-Dunsheath S., Falgarone E., 2015, ApJ, 806, 260
Feroz F., Hobson M. P., Cameron E., Pettitt A. N., 2013, arXiv e-prints, p. arXiv:1306.2144
Ferrarese L., Merritt D., 2000, ApJ, 539, L9
Feruglio C., Maiolino R., Piconcelli E., Menci N., Aussel H., Lamastra A., Fiore F., 2010, A&A, 518, L155
Foreman-Mackey D., Hogg D. W., Lang D., Goodman J., 2013, PASP, 125, 306
Gabor J. M., Bournaud F., 2014, MNRAS, 441, 1615
Gallimore J. F., Henkel C., Baum S. A., Glass I. S., Claussen M. J., Prieto M. A., Von Kap-herr A., 2001, ApJ, 556, 694
Gallimore J. F., et al., 2016, ApJ, 829, L7
Galvin T. J., et al., 2018, MNRAS, 474, 779
García-Burillo S., et al., 2006, ApJ, 645, L17
García-Burillo S., et al., 2016, ApJ, 823, L12
García-Burillo S., et al., 2019, arXiv e-prints, p. arXiv:1909.00675
Garrett M. A., Calder R. J., Porcas R. W., King L. J., Walsh D., Wilkinson P. N., 1994, MNRAS, 270, 457
Garsden H., Lewis G. F., Harvey-Smith L., 2011, MNRAS, 413, 1537

Gebhardt K., et al., 2000, ApJ, 539, L13
Gilman D., Agnello A., Treu T., Keeton C. R., Nierenberg A. M., 2017, MNRAS, 467, 3970
Gilman D., Birrer S., Treu T., Keeton C. R., 2018, preprint, (arXiv:1712.04945)
Gilman D., Birrer S., Nierenberg A., Treu T., Du X., Benson A., 2019a, arXiv e-prints, p. arXiv:1908.06983
Gilman D., Birrer S., Treu T., Nierenberg A., Benson A., 2019b, MNRAS, 487, 5721
Giommi P., et al., 2012, A&A, 541, A160
González-Alfonso E., Fischer J., Aalto S., Falstad N., 2014, A&A, 567, A91
Gray M. D., Baudry A., Richards A. M. S., Humphreys E. M. L., Sobolev A. M., Yates J. A., 2016, MNRAS, 456, 374
Greenhill L. J., Ellingsen S. P., Norris R. P., Gough R. G., Sinclair M. W., Moran J. M., Mushotzky R., 1997, ApJ, 474, L103
Greenhill L. J., Kondratko P. T., Lovell J. E. J., Kuiper T. B. H., Moran J. M., Jauncey D. L., Baines G. P., 2003, ApJ, 582, L11
Gregory P. C., Condon J. J., 1991, ApJS, 75, 1011
Griffin M. J., et al., 2010, A&A, 518, L3
Griffith M. R., Wright A. E., 1993, AJ, 105, 1666
Griffith M., Langston G., Heflin M., Conner S., Lehar J., Burke B., 1990, ApJS, 74, 129
Griffith M. R., Wright A. E., Burke B. F., Ekers R. D., 1994, ApJS, 90, 179
Griffith M. R., Wright A. E., Burke B. F., Ekers R. D., 1995, ApJS, 97, 347
Gürkan G., et al., 2018, MNRAS, 475, 3010
Gürkan G., et al., 2019, A&A, 622, A11
Hainline L. J., Scoville N. Z., Yun M. S., Hawkins D. W., Frayer D. T., Isaak K. G., 2004, ApJ, 609, 61
Hardcastle M. J., Evans D. A., Croston J. H., 2007, MNRAS, 376, 1849
Harris K., et al., 2016, MNRAS, 457, 4179
Harrison C. M., 2017, Nature Astronomy, 1, 0165
Harrison C. M., et al., 2012, ApJ, 760, L15
Harrison C. M., Alexander D. M., Mullaney J. R., Swinbank A. M., 2014, MNRAS, 441, 3306
Harrison C. M., Thomson A. P., Alexander D. M., Bauer F. E., Edge A. C., Hogan M. T., Mullaney J. R., Swinbank A. M., 2015, ApJ, 800, 45
Harrison C. M., et al., 2016, MNRAS, 457, L122
Harrison C. M., Costa T., Tadhunter C. N., Flütsch A., Kakkad D., Perna M., Vietri G., 2018, Nature Astronomy, 2, 198
Hartley P., Jackson N., Sluse D., Stacey H. R., Vives-Arias H., 2019, arXiv e-prints, p. arXiv:1901.05791
Hatziminaoglou E., Farrah D., Humphreys E., Manrique A., Pérez-Fournon I., Pitchford

L. K., Salvador-Solé E., Wang L., 2018, MNRAS, 480, 4974
Helou G., Khan I. R., Malek L., Boehmer L., 1988, ApJS, 68, 151
Henkel C., Braatz J. A., Menten K. M., Ott J., 2008, A&A, 485, 451
Herrera-Camus R., et al., 2019, ApJ, 871, 37
Herrera Ruiz N., Middelberg E., Norris R. P., Maini A., 2016, A&A, 589, L2
Herrera Ruiz N., et al., 2017, A&A, 607, A132
Herrnstein J. R., Greenhill L. J., Moran J. M., 1996, ApJ, 468, L17
Herrnstein J. R., Moran J. M., Greenhill L. J., Blackman E. G., Diamond P. J., 1998, ApJ, 508, 243
Hewett P. C., Wild V., 2010, MNRAS, 405, 2302
Hewitt J. N., Turner E. L., Lawrence C. R., Schneider D. P., Brody J. P., 1992, AJ, 104, 968
Hezaveh Y. D., Marrone D. P., Holder G. P., 2012, ApJ, 761, 20
Hezaveh Y., Dalal N., Holder G., Kuhlen M., Marrone D., Murray N., Vieira J., 2013, ApJ, 767, 9
Hezaveh Y., Dalal N., Holder G., Kisner T., Kuhlen M., Perreault Levasseur L., 2016a, J. Cosmology Astropart. Phys., 11, 048
Hezaveh Y. D., et al., 2016b, ApJ, 823, 37
Hezaveh Y. D., et al., 2016c, ApJ, 823, 37
Hickox R. C., Mullaney J. R., Alexander D. M., Chen C.-T. J., Civano F. M., Goulding A. D., Hainline K. N., 2014, ApJ, 782, 9
Hjorth J., et al., 2002, ApJ, 572, L11
Ho L. C., 2008, ARA&A, 46, 475
Hodge J. A., Riechers D., Decarli R., Walter F., Carilli C. L., Daddi E., Dannerbauer H., 2015, ApJ, 798, L18
Hodge J. A., et al., 2016, ApJ, 833, 103
Hodge J. A., et al., 2019, The Astrophysical Journal, 876, 130
Högbom J. A., 1974, A&AS, 15, 417
Holland W. S., et al., 1999, MNRAS, 303, 659
Hopkins P. F., Hernquist L., Cox T. J., Di Matteo T., Martini P., Robertson B., Springel V., 2005, ApJ, 630, 705
Hopkins P. F., Hernquist L., Cox T. J., Kereš D., 2008, ApJS, 175, 356
Hsueh J.-W., Fassnacht C. D., Vegetti S., McKean J. P., Spingola C., Auger M. W., Koopmans L. V. E., Lagattuta D. J., 2016, MNRAS, 463, L51
Hsueh J. W., et al., 2017, MNRAS, 469, 3713
Hsueh J.-W., Despali G., Vegetti S., Xu D., Fassnacht C. D., Metcalf R. B., 2018, MNRAS, 475, 2438
Hsueh J.-W., Enzi W., Vegetti S., Auger M., Fassnacht C. D., Despali G., Koopmans L. V. E., McKean J. P., 2019, arXiv e-prints, p. arXiv:1905.04182
Hughes D. H., Dunlop J. S., Rawlings S., 1997, MNRAS, 289, 766

Humphreys E. M. L., Reid M. J., Greenhill L. J., Moran J. M., Argon A. L., 2008, ApJ, 672, 800
Hunter J. D., 2007, Computing in Science & Engineering, 9, 90
Ikarashi S., et al., 2015, ApJ, 810, 133
Ikarashi S., et al., 2017, ApJ, 849, L36
Imanishi M., Nakanishi K., Izumi T., Wada K., 2018, ApJ, 853, L25
Impellizzeri C. M. V., McKean J. P., Castangia P., Roy A. L., Henkel C., Brunthaler A., Wucknitz O., 2008, Nature, 456, 927
Impellizzeri C. M. V., et al., 2019, ApJ, 884, L28
Inada N., et al., 2003, AJ, 126, 666
Inada N., et al., 2006, AJ, 131, 1934
Inada N., et al., 2007, AJ, 133, 206
Inada N., et al., 2009, AJ, 137, 4118
Inada N., et al., 2012, AJ, 143, 119
Inoue K. T., Matsushita S., Minezaki T., Chiba M., 2017, ApJ, 835, L23
Intema H. T., Jagannathan P., Mooley K. P., Frail D. A., 2017, A&A, 598, A78
Iono D., et al., 2016, ApJ, 829, L10
Irwin M. J., Ibata R. A., Lewis G. F., Totten E. J., 1998, ApJ, 505, 529
Isaak K. G., Priddey R. S., McMahon R. G., Omont A., Peroux C., Sharp R. G., Withington S., 2002, MNRAS, 329, 149
Ishibashi W., Fabian A. C., Canning R. E. A., 2013, MNRAS, 431, 2350
Ivison R. J., 2006, MNRAS, 370, 495
Ivison R. J., et al., 2002, MNRAS, 337, 1
Ivison R. J., et al., 2010, A&A, 518, L35
Jackson N., et al., 1995, MNRAS, 274, L25
Jackson N., Ofek E. O., Oguri M., 2008, MNRAS, 387, 741
Jackson N., Ofek E. O., Oguri M., 2009, MNRAS, 398, 1423
Jackson N., Tagore A. S., Roberts C., Sluse D., Stacey H., Vives-Arias H., Wucknitz O., Volino F., 2015, MNRAS, 454, 287
Jarugula S., et al., 2019, ApJ, 880, 92
Jethava N., Henkel C., Menten K. M., Carilli C. L., Reid M. J., 2007, A&A, 472, 435
Johnston D. E., et al., 2003, AJ, 126, 2281
Jones E., Oliphant T., Peterson P., et al., 2001, SciPy: Open source scientific tools for Python, `http://www.scipy.org/`
Juvela M., Ysard N., 2012a, A&A, 539, A71
Juvela M., Ysard N., 2012b, A&A, 541, A33
Juvela M., Ysard N., 2012c, A&A, 541, A33
Kalfountzou E., et al., 2014, MNRAS, 442, 1181
Katz C. A., Moore C. B., Hewitt J. N., 1997, ApJ, 475, 512

Kayo I., Inada N., Oguri M., Morokuma T., Hall P. B., Kochanek C. S., Schneider D. P., 2010, AJ, 139, 1614
Keeton C. R., 2001b, arXiv e-prints, pp astro–ph/0102341
Keeton C. R., 2001a, arXiv e-prints, pp astro–ph/0102340
Kellermann K. I., Pauliny-Toth I. I. K., 1973, AJ, 78, 828
Kennicutt Jr. R. C., 1998, ApJ, 498, 541
Kereš D., Katz N., Weinberg D. H., Davé R., 2005, MNRAS, 363, 2
King L. J., Browne I. W. A., Muxlow T. W. B., Narasimha D., Patnaik A. R., Porcas R. W., Wilkinson P. N., 1997, MNRAS, 289, 450
Kirkpatrick A., et al., 2012, ApJ, 759, 139
Kirkpatrick A., Sharon C., Keller E., Pope A., 2019, ApJ, 879, 41
Klamer I. J., Ekers R. D., Sadler E. M., Hunstead R. W., 2004, ApJ, 612, L97
Klöckner H.-R., Baan W. A., Garrett M. A., 2003, Nature, 421, 821
Kneib J.-P., Cohen J. G., Hjorth J., 2000, ApJ, 544, L35
Kocevski D. D., et al., 2017, ApJ, 846, 112
Kochanek C. S., Dalal N., 2004, ApJ, 610, 69
Kochanek C. S., Falco E. E., Impey C., Lehar J., McLeod B., Rix H.-W., 1999, The CASTLES Survey, `https://www.cfa.harvard.edu/castles/`
König S., et al., 2017, A&A, 602, A42
Koopmans L. V. E., 2005, MNRAS, 363, 1136
Koopmans L. V. E., et al., 1999, MNRAS, 303, 727
Koopmans L. V. E., et al., 2003, ApJ, 595, 712
Koopmans L. V. E., Treu T., Bolton A. S., Burles S., Moustakas L. A., 2006, ApJ, 649, 599
Koopmans L. V. E., et al., 2009, ApJ, 703, L51
Kormann R., Schneider P., Bartelmann M., 1994, A&A, 284, 285
Kormendy J., Ho L. C., 2013, ARA&A, 51, 511
Kratzer R. M., Richards G. T., Goldberg D. M., Oguri M., Kochanek C. S., Hodge J. A., Becker R. H., Inada N., 2011, ApJ, 728, L18
Kreysa E., et al., 1999, Infrared Physics and Technology, 40, 191
Krips M., Neri R., Eckart A., Downes D., Martín-Pintado J., Planesas P., 2005, A&A, 431, 879
Krips M., Peck A. B., Sakamoto K., Petitpas G. B., Wilner D. J., Matsushita S., Iono D., 2007, ApJ, 671, L5
Kühr H., Witzel A., Pauliny-Toth I. I. K., Nauber U., 1981, A&AS, 45, 367
Kuo C. Y., et al., 2011, ApJ, 727, 20
Kuo C. Y., Reid M. J., Braatz J. A., Gao F., Impellizzeri C. M. V., Chien W. T., 2018, ApJ, 859, 172
Kuo C.-Y., Suyu S. H., Impellizzeri V., Braatz J. A., 2019, PASJ, 71, 57
LSST Science Collaboration et al., 2009, arXiv e-prints, p. arXiv:0912.0201

Lagattuta D. J., Vegetti S., Fassnacht C. D., Auger M. W., Koopmans L. V. E., McKean J. P., 2012, MNRAS, 424, 2800
Langston G. I., Heflin M. B., Conner S. R., Lehar J., Carilli C. L., Burke B. F., 1990, ApJS, 72, 621
Larionov M. G., Parijskij Y. N., Zhuravlev V. I., Sidorenkov V. N., Berlin A. B., Nizhel'Skii N. A., 1994, A&AS, 106, 119
Laureijs R., et al., 2011, arXiv e-prints, p. arXiv:1110.3193
Lawrence A., et al., 1993, MNRAS, 260, 28
Lawrence C. R., Elston R., Januzzi B. T., Turner E. L., 1995, AJ, 110, 2570
Lee J. A., Sohn B. W., Jung T., Byun D.-Y., Lee J. W., 2017, ApJS, 228, 22
Lehar J., et al., 1997, AJ, 114, 48
Lelli F., Fraternali F., Sancisi R., 2010, A&A, 516, A11
Leung G. C. K., et al., 2017, ApJ, 849, 48
Lewis G. F., Chapman S. C., Ibata R. A., Irwin M. J., Totten E. J., 1998, ApJ, 505, L1
Lis D. C., Neufeld D. A., Phillips T. G., Gerin M., Neri R., 2011, ApJ, 738, L6
Lo K. Y., 2005, ARA&A, 43, 625
Lowe S. R., Gawroński M. P., Wilkinson P. N., Kus A. J., Browne I. W. A., Pazderski E., Feiler R., Kettle D., 2007, A&A, 474, 1093
MacLeod C. L., Kochanek C. S., Agol E., 2009, ApJ, 699, 1578
MacLeod C. L., Jones R., Agol E., Kochanek C. S., 2013, ApJ, 773, 35
Maccagni F. M., Morganti R., Oosterloo T. A., Oonk J. B. R., Emonts B. H. C., 2018, A&A, 614, A42
Madau P., Dickinson M., 2014, ARA&A, 52, 415
Magain P., Surdej J., Swings J. P., Borgeest U., Kayser R., 1988, Nature, 334, 325
Magnelli B., et al., 2012, A&A, 539, A155
Magnelli B., et al., 2015, A&A, 573, A45
Magorrian J., et al., 1998, AJ, 115, 2285
Maini A., Prandoni I., Norris R. P., Giovannini G., Spitler L. R., 2016, A&A, 589, L3
Maiolino R., et al., 2015, MNRAS, 452, 54
Mancuso C., Lapi A., Shi J., Cai Z.-Y., Gonzalez-Nuevo J., Béthermin M., Danese L., 2016, ApJ, 833, 152
Mandelbaum R., Li C., Kauffmann G., White S. D. M., 2009, MNRAS, 393, 377
Mao S., Schneider P., 1998, MNRAS, 295, 587
Marlow D. R., et al., 2001, AJ, 121, 619
Martí-Vidal I., et al., 2013, A&A, 558, A123
Martí-Vidal I., Vlemmings W. H. T., Muller S., Casey S., 2014, A&A, 563, A136
Marvil J., Owen F., Eilek J., 2015, AJ, 149, 32
Massardi M., et al., 2008, MNRAS, 384, 775
Massardi M., López-Caniego M., González-Nuevo J., Herranz D., de Zotti G., Sanz J. L.,

2009, MNRAS, 392, 733
Massardi M., et al., 2018, A&A, 610, A53
Mauch T., Murphy T., Buttery H. J., Curran J., Hunstead R. W., Piestrzynski B., Robertson J. G., Sadler E. M., 2003, MNRAS, 342, 1117
McKean J. P., et al., 2005, MNRAS, 356, 1009
McKean J. P., et al., 2007, MNRAS, 378, 109
McKean J. P., Impellizzeri C. M. V., Roy A. L., Castangia P., Samuel F., Brunthaler A., Henkel C., Wucknitz O., 2011, MNRAS, 410, 2506
McMullin J. P., Waters B., Schiebel D., Young W., Golap K., 2007, in Shaw R. A., Hill F., Bell D. J., eds, Astronomical Society of the Pacific Conference Series Vol. 376, Astronomical Data Analysis Software and Systems XVI. p. 127
Meijerink R., Spaans M., Israel F. P., 2007, A&A, 461, 793
Melbourne J., et al., 2012, AJ, 143, 125
Metcalf R. B., et al., 2019, A&A, 625, A119
Meylan G., Jetzer P., North P., Schneider P., Kochanek C. S., Wambsganss J., eds, 2006, Gravitational Lensing: Strong, Weak and Micro (`arXiv:astro-ph/0407232`)
Mihos J. C., Hernquist L., 1996, ApJ, 464, 641
Minezaki T., Chiba M., Kashikawa N., Inoue K. T., Kataza H., 2009, ApJ, 697, 610
Mohan N., Rafferty D., 2015, PyBDSF: Python Blob Detection and Source Finder, Astrophysics Source Code Library (ascl:1502.007)
Moran J., Greenhill L., Herrnstein J., Diamond P., Miyoshi M., Nakai N., Inque M., 1995, Proceedings of the National Academy of Science, 92, 11427
More A., McKean J. P., More S., Porcas R. W., Koopmans L. V. E., Garrett M. A., 2009, MNRAS, 394, 174
Morgan N. D., Dressler A., Maza J., Schechter P. L., Winn J. N., 1999, AJ, 118, 1444
Morgan N. D., Caldwell J. A. R., Schechter P. L., Dressler A., Egami E., Rix H.-W., 2004, AJ, 127, 2617
Morganti R., Oosterloo T., Oonk J. B. R., Frieswijk W., Tadhunter C., 2015, A&A, 580, A1
Moshir M., et al., 1990, in Bulletin of the American Astronomical Society. p. 1325
Mosquera A. M., Kochanek C. S., 2011, ApJ, 738, 96
Moustakas L. A., Metcalf R. B., 2003, MNRAS, 339, 607
Muller S., Guélin M., Dumke M., Lucas R., Combes F., 2006, A&A, 458, 417
Munroe R., 2005, XKCD, A webcomic of romance, sarcasm, math, and language., `http://xkcd.com/`
Muratov A. L., Kereš D., Faucher-Giguère C.-A., Hopkins P. F., Quataert E., Murray N., 2015, MNRAS, 454, 2691
Murphy T., et al., 2010, MNRAS, 402, 2403
Murray N., Quataert E., Thompson T. A., 2005, ApJ, 618, 569

Myers S. T., VLASS Survey Team S. S. G. ., 2018, in American Astronomical Society Meeting Abstracts #231. p. 231.08
Myers S. T., et al., 1995, ApJ, 447, L5
Myers S. T., et al., 1999, AJ, 117, 2565
Myers S. T., et al., 2003, MNRAS, 341, 1
Naab T., Johansson P. H., Ostriker J. P., Efstathiou G., 2007, ApJ, 658, 710
Naab T., Johansson P. H., Ostriker J. P., 2009, ApJ, 699, L178
Negrello M., et al., 2010, Science, 330, 800
Nesvadba N. P. H., et al., 2010, A&A, 521, A65
Neufeld D. A., Maloney P. R., 1995, ApJ, 447, L17
Neufeld D. A., Maloney P. R., Conger S., 1994, ApJ, 436, L127
Nieppola E., Tornikoski M., Valtaoja E., León-Tavares J., Hovatta T., Lähteenmäki A., Tammi J., 2011, A&A, 535, A69
Nierenberg A. M., Treu T., Menci N., Lu Y., Torrey P., Vogelsberger M., 2016, MNRAS, 462, 4473
Nierenberg A. M., et al., 2017, MNRAS, 471, 2224
Nierenberg A. M., et al., 2019, arXiv e-prints, p. arXiv:1908.06344
Nightingale J. W., Dye S., 2015, MNRAS, 452, 2940
Ofek E. O., Oguri M., Jackson N., Inada N., Kayo I., 2007, MNRAS, 382, 412
Oguri M., et al., 2008a, AJ, 135, 520
Oguri M., Inada N., Blackburne J. A., Shin M.-S., Kayo I., Strauss M. A., Schneider D. P., York D. G., 2008b, MNRAS, 391, 1973
Oldham L. J., Auger M. W., 2018, MNRAS, 476, 133
Oldham L., et al., 2017, MNRAS, 465, 3185
Omont A., Cox P., Bertoldi F., McMahon R. G., Carilli C., Isaak K. G., 2001, A&A, 374, 371
Omont A., Beelen A., Bertoldi F., Cox P., Carilli C. L., Priddey R. S., McMahon R. G., Isaak K. G., 2003, A&A, 398, 857
Omont A., et al., 2011, A&A, 530, L3
Oteo I., et al., 2016, ApJ, 827, 34
Oteo I., Zwaan M. A., Ivison R. J., Smail I., Biggs A. D., 2017, ApJ, 837, 182
Ott S., 2010, in Mizumoto Y., Morita K.-I., Ohishi M., eds, Astronomical Society of the Pacific Conference Series Vol. 434, Astronomical Data Analysis Software and Systems XIX. p. 139 (arXiv:1011.1209)
Padovani P., 2016, A&A Rev., 24, 13
Padovani P., Miller N., Kellermann K. I., Mainieri V., Rosati P., Tozzi P., 2011, ApJ, 740, 20
Padovani P., et al., 2017, A&A Rev., 25, 2
Page M. J., Stevens J. A., Ivison R. J., Carrera F. J., 2004, ApJ, 611, L85

Page M. J., et al., 2012, Nature, 485, 213
Paraficz D., et al., 2018, A&A, 613, A34
Patnaik A. R., Browne I. W. A., Wilkinson P. N., Wrobel J. M., 1992, MNRAS, 254, 655
Peck A. B., Henkel C., Ulvestad J. S., Brunthaler A., Falcke H., Elitzur M., Menten K. M., Gallimore J. F., 2003, ApJ, 590, 149
Pilbratt G. L., et al., 2010, A&A, 518, L1
Pitchford L. K., et al., 2016, MNRAS, 462, 4067
Planck Collaboration et al., 2016, A&A, 594, A13
Planesas P., Martin-Pintado J., Neri R., Colina L., 1999, Science, 286, 2493
Pooley D., Blackburne J. A., Rappaport S., Schechter P. L., 2007, ApJ, 661, 19
Priddey R. S., McMahon R. G., 2001, MNRAS, 324, L17
Priddey R. S., Isaak K. G., McMahon R. G., Omont A., 2003, MNRAS, 339, 1183
Querejeta M., et al., 2016, A&A, 593, A118
Radcliffe J. F., et al., 2018, A&A, 619, A48
Reid M. J., Braatz J. A., Condon J. J., Greenhill L. J., Henkel C., Lo K. Y., 2009, ApJ, 695, 287
Reimers D., Hagen H. J., Baade R., Lopez S., Tytler D., 2002, A&A, 382, L26
Richards J. L., et al., 2011, ApJS, 194, 29
Riechers D. A., et al., 2006, ApJ, 650, 604
Riechers D. A., Walter F., Carilli C. L., Lewis G. F., 2009, ApJ, 690, 463
Riechers D. A., Weiß A., Walter F., Wagg J., 2010, ApJ, 725, 1032
Riechers D. A., Walter F., Carilli C. L., Cox P., Weiss A., Bertoldi F., Menten K. M., 2011a, ApJ, 726, 50
Riechers D. A., et al., 2011b, ApJ, 739, L32
Riechers D. A., et al., 2011c, ApJ, 739, L32
Riechers D. A., et al., 2013, Nature, 496, 329
Riechers D. A., et al., 2014, ApJ, 796, 84
Riechers D. A., et al., 2017, ApJ, 850, 1
Ritondale E., Vegetti S., Despali G., Auger M. W., Koopmans L. V. E., McKean J. P., 2019, MNRAS, 485, 2179
Rizzo F., Vegetti S., Fraternali F., Di Teodoro E., 2018, MNRAS,
Ros E., Guirado J. C., Marcaide J. M., Pérez-Torres M. A., Falco E. E., Muñoz J. A., Alberdi A., Lara L., 2000, A&A, 362, 845
Rosario D. J., et al., 2013, ApJ, 763, 59
Rottgering H. J. A., et al., 2006, arXiv e-prints, pp astro–ph/0610596
Rowan-Robinson M., 2000, MNRAS, 316, 885
Rowan-Robinson M., et al., 1993, MNRAS, 261, 513
Rusin D., et al., 2001, AJ, 122, 591
Rusu C. E., et al., 2019, arXiv e-prints, p. arXiv:1905.09338

Rybak M., McKean J. P., Vegetti S., Andreani P., White S. D. M., 2015a, MNRAS, 451, L40
Rybak M., Vegetti S., McKean J. P., Andreani P., White S. D. M., 2015b, MNRAS, 453, L26
Salpeter E. E., 1955, ApJ, 121, 161
Sanders D. B., Soifer B. T., Elias J. H., Madore B. F., Matthews K., Neugebauer G., Scoville N. Z., 1988, ApJ, 325, 74
Savage R. S., Oliver S., 2007, ApJ, 661, 1339
Schaye J., et al., 2015, MNRAS, 446, 521
Schmidt M., 1963, Nature, 197, 1040
Schmidt M., Green R. F., 1983, ApJ, 269, 352
Schneider P., Kochanek C. S., Wambsganss J., 2006, Saas-Fee Advanced Course 33: Gravitational Lensing: Strong, Weak and Micro. Springer-Verlag: Berlin
Schober J., Schleicher D. R. G., Klessen R. S., 2017, MNRAS, 468, 946
Scholtz J., et al., 2018, MNRAS, 475, 1288
Schulze A., et al., 2019, MNRAS, 488, 1180
Serjeant S., 2012, MNRAS, 424, 2429
Serjeant S., 2014, ApJ, 793, L10
Sérsic J. L., 1963, Boletin de la Asociacion Argentina de Astronomia La Plata Argentina, 6, 41
Seyfert C. K., 1943, ApJ, 97, 28
Sharon C. E., Riechers D. A., Hodge J., Carilli C. L., Walter F., Weiß A., Knudsen K. K., Wagg J., 2016, ApJ, 827, 18
Shimwell T. W., et al., 2017, A&A, 598, A104
Siebenmorgen R., Heymann F., Efstathiou A., 2015, A&A, 583, A120
Sijacki D., Springel V., Di Matteo T., Hernquist L., 2007, MNRAS, 380, 877
Silverman J. D., et al., 2019, arXiv e-prints, p. arXiv:1910.14242
Simpson J. M., et al., 2012, MNRAS, 426, 3201
Simpson J. M., et al., 2015, ApJ, 799, 81
Sluse D., Chantry V., Magain P., Courbin F., Meylan G., 2012, A&A, 538, A99
Sluse D., Kishimoto M., Anguita T., Wucknitz O., Wambsganss J., 2013, A&A, 553, A53
Smolčić V., et al., 2017, A&A, 602, A1
Snellen I. A. G., de Bruyn A. G., Schilizzi R. T., Miley G. K., Myers S. T., 1995, ApJ, 447, L9
Solomon P. M., Vanden Bout P. A., 2005, ARA&A, 43, 677
Solomon P., Vanden Bout P., Carilli C., Guelin M., 2003, Nature, 426, 636
Somerville R. S., Davé R., 2015, ARA&A, 53, 51
Somerville R. S., Hopkins P. F., Cox T. J., Robertson B. E., Hernquist L., 2008, MNRAS, 391, 481

Sonnenfeld A., Treu T., Gavazzi R., Marshall P. J., Auger M. W., Suyu S. H., Koopmans L. V. E., Bolton A. S., 2012, ApJ, 752, 163
Sonnenfeld A., Treu T., Gavazzi R., Suyu S. H., Marshall P. J., Auger M. W., Nipoti C., 2013, ApJ, 777, 98
Sopp H. M., Alexander P., 1991, MNRAS, 251, 14P
Spilker J. S., et al., 2016, ApJ, 826, 112
Spilker J. S., et al., 2018, Science, 361, 1016
Spilker J. S., Bezanson R., Weiner B. J., Whitaker K. E., Williams C. C., 2019, arXiv e-prints, p. arXiv:1908.02294
Spingola C., McKean J. P., Auger M. W., Fassnacht C. D., Koopmans L. V. E., Lagattuta D. J., Vegetti S., 2018, MNRAS, 478, 4816
Spingola C., et al., 2019, arXiv e-prints, p. arXiv:1905.06363
Springel V., Di Matteo T., Hernquist L., 2005, MNRAS, 361, 776
Stacey H. R., 2015, Msc thesis, The University of Manchester
Stacey H. R., McKean J. P., 2018, MNRAS, 481, L40
Stacey H. R., et al., 2018, MNRAS, 476, 5075
Stacey H. R., et al., 2019, A&A, 622, A18
Stanley F., et al., 2017, MNRAS, 472, 2221
Stanley F., Harrison C. M., Alexander D. M., Simpson J., Knudsen K. K., Mullaney J. R., Rosario D. J., Scholtz J., 2018, MNRAS, 478, 3721
Stevens J. A., Page M. J., Ivison R. J., Carrera F. J., Mittaz J. P. D., Smail I., McHardy I. M., 2005, MNRAS, 360, 610
Strittmatter P. A., Hill P., Pauliny-Toth I. I. K., Steppe H., Witzel A., 1980, A&A, 88, L12
Suyu S. H., Marshall P. J., Hobson M. P., Blandford R. D., 2006, MNRAS, 371, 983
Suyu S. H., Marshall P. J., Auger M. W., Hilbert S., Blandford R. D., Koopmans L. V. E., Fassnacht C. D., Treu T., 2010, ApJ, 711, 201
Swinbank A. M., et al., 2010, Nature, 464, 733
Swinbank A. M., et al., 2014, MNRAS, 438, 1267
Sykes C. M., et al., 1998, MNRAS, 301, 310
Symeonidis M., Page M. J., 2018, MNRAS, 479, L91
The Astropy Collaboration et al., 2018, preprint, (arXiv:1801.02634)
Thomson A. P., et al., 2012, MNRAS, 425, 2203
Tingay S. J., Jauncey D. L., King E. A., Tzioumis A. K., Lovell J. E. J., Edwards P. G., 2003, PASJ, 55, 351
Tinti S., Dallacasa D., de Zotti G., Celotti A., Stanghellini C., 2005, A&A, 432, 31
Trujillo I., et al., 2006, ApJ, 650, 18
Tuan-Anh P., Boone F., Hoai D. T., Nhung P. T., Weiß A., Kneib J.-P., Beelen A., Salomé P., 2013, A&A, 552, L12
Tuan-Anh P., Hoai D. T., Nhung P. T., Diep P. N., Phuong N. T., Thao N. T., Darriulat

P., 2017, MNRAS, 467, 3513
Uzgil B. D., Bradford C. M., Hailey-Dunsheath S., Maloney P. R., Aguirre J. E., 2016, ApJ, 832, 209
Valentino F., et al., 2019, arXiv e-prints, p. arXiv:1909.10540
Vallini L., Tielens A. G. G. M., Pallottini A., Gallerani S., Gruppioni C., Carniani S., Pozzi F., Talia M., 2019, MNRAS, p. 2427
Vegetti S., Koopmans L. V. E., 2009, MNRAS, 392, 945
Vegetti S., Lagattuta D. J., McKean J. P., Auger M. W., Fassnacht C. D., Koopmans L. V. E., 2012, Nature, 481, 341
Venturini S., Solomon P. M., 2003, ApJ, 590, 740
Volino F., et al., 2010, arXiv e-prints, p. arXiv:1011.6652
Vollmer B., Krichbaum T. P., Angelakis E., Kovalev Y. Y., 2008, A&A, 489, 49
Vuissoz C., et al., 2008, A&A, 488, 481
Wagg J., Momjian E., 2009, AJ, 138, 895
Waldram E. M., Pooley G. G., Grainge K. J. B., Jones M. E., Saunders R. D. E., Scott P. F., Taylor A. C., 2003, MNRAS, 342, 915
Wales D., Doye J., 1998, The Journal of Physical Chemistry A, 101
Walsh D., Carswell R. F., Weymann R. J., 1979, Nature, 279, 381
Wang S. X., et al., 2013, ApJ, 778, 179
Warren S. J., Dye S., 2003, ApJ, 590, 673
Weinberger R., et al., 2018, MNRAS, 479, 4056
Weiß A., Henkel C., Downes D., Walter F., 2003, A&A, 409, L41
Weiß A., Downes D., Neri R., Walter F., Henkel C., Wilner D. J., Wagg J., Wiklind T., 2007, A&A, 467, 955
Wellons S., et al., 2015, MNRAS, 449, 361
Wellons S., Faucher-Giguère C.-A., Anglés-Alcázar D., Hayward C. C., Feldmann R., Hopkins P. F., Kereš D., 2019, arXiv e-prints, p. arXiv:1908.05274
Weymann R. J., Latham D., Angel J. R. P., Green R. F., Liebert J. W., Turnshek D. A., Turnshek D. E., Tyson J. A., 1980, Nature, 285, 641
White R. L., Becker R. H., 1992, ApJS, 79, 331
White R. L., Helfand D. J., Becker R. H., Glikman E., de Vries W., 2007, ApJ, 654, 99
White S. V., Jarvis M. J., Häußler B., Maddox N., 2015, MNRAS, 448, 2665
White S. V., Jarvis M. J., Kalfountzou E., Hardcastle M. J., Verma A., Cao Orjales J. M., Stevens J., 2017, MNRAS, 468, 217
Williams C. C., et al., 2014, ApJ, 780, 1
Wilner D. J., Bourke T. L., Ho P. T. P., Killeen N. E. B., Calabretta M., 1999, AJ, 117, 1139
Winn J. N., et al., 2000, AJ, 120, 2868
Winn J. N., Hewitt J. N., Patnaik A. R., Schechter P. L., Schommer R. A., López S., Maza J., Wachter S., 2001, AJ, 121, 1223

Winn J. N., et al., 2002, AJ, 123, 10
Winn J. N., Rusin D., Kochanek C. S., 2003, ApJ, 587, 80
Winn J. N., Rusin D., Kochanek C. S., 2004, Nature, 427, 613
Wong K. C., et al., 2019, arXiv e-prints, p. arXiv:1907.04869
Wright A. E., Wark R. M., Troup E., Otrupcek R., Hunt A., Cooke D. J., 1990, Proceedings of the Astronomical Society of Australia, 8, 261
Wright E. L., et al., 2009, ApJS, 180, 283
Wu J., Vanden Bout P. A., Evans II N. J., Dunham M. M., 2009, ApJ, 707, 988
Wucknitz O., Volino F., 2008, in The role of VLBI in the Golden Age for Radio Astronomy. p. 102
Xanthopoulos E., et al., 1998, MNRAS, 300, 649
Xanthopoulos E., Combes F., Wiklind T., 2001, MNRAS, 325, 273
Xu D. D., Mao S., Cooper A. P., Gao L., Frenk C. S., Angulo R. E., Helly J., 2012, MNRAS, 421, 2553
Xu D., Sluse D., Gao L., Wang J., Frenk C., Mao S., Schneider P., Springel V., 2015, MNRAS, 447, 3189
Yamauchi A., Sato N., Hirota A., Nakai N., 2005, PASJ, 57, 861
Yan H., Ma Z., 2016, The Astrophysical Journal, 820, L16
Yang C., et al., 2019, A&A, 624, A138
York T., et al., 2005, MNRAS, 361, 259
Yun M. S., Carilli C. L., 2002, ApJ, 568, 88
Zakamska N. L., et al., 2016, MNRAS, 455, 4191
Zeballos M., et al., 2018, MNRAS, 479, 4577
Zeiger B., Darling J., 2010, ApJ, 709, 386
Zhang Z.-Y., Romano D., Ivison R. J., Papadopoulos P. P., Matteucci F., 2018, Nature, 558, 260
Zolotov A., et al., 2015, MNRAS, 450, 2327
de Vries W. H., Hodge J. A., Becker R. H., White R. L., Helfand D. J., 2007, AJ, 134, 457
van Dokkum P. G., et al., 2008, ApJ, 677, L5
van Dokkum P. G., et al., 2015, ApJ, 813, 23
van Haarlem M. P., et al., 2013, A&A, 556, A2
van der Werf P. P., et al., 2011, ApJ, 741, L38

Acknowledgements

This thesis would not have been possible without the support, guidance, friendship and generosity that I have received over the past four years. Below is a list of people who have contributed in some way towards the completion of this thesis.

Matt Auger
Cecilia Bacchini
Lucile Boccon-Gibod
Leon Boschman
Debbie van den Brink
Joe Callingham
Annique Claringbould
Vincent Le Corre
Will Cowley
Giulia Despali
Chris Fassnacht
Desiree Goubert
Aaron Greenwood
Paolo Guerra
Julia Healy
Kelley Hess
Jen-Wei Hsueh
Kate Isaak
Rob Ivison
Neal Jackson
Nika Jurlin
Leon Koopmans
Niek de Klein
Helmer Koppelman
Arno Lafontaine
Anne-Grete Märston
John McKean
Vanessa Moss
Sharon Poort
Devon Powell
Jack Radcliffe
Landi Raubenheimer
Glen Rees
Elisa Ritondale
Francesca Rizzo
Matus Rybak
Joana Saldida
Alessandro Savino
Emma Sharples
Tejas Sherkar
Cristiana Spingola
Sarrvesh Sridhar
Paul Stacey
Pauline Stacey
Filippo Tosi
Simona Vegetti
Tadeja Veršič
Paul van der Werf

I don't know half of you half as well as I should like, and I like less than half of you half as well as you deserve.

— Bilbo Baggins

Thanks to Beth and Sean at Riddles in Altrincham and Erik at The Stockroom in Groningen for helping to create the cocktail pairings.